Control Theoretic Approach for Attitude Control of High Altitude Scientific Stationary Platforms

by

Yao-Ting Mao

A dissertation submitted in partial satisfaction of the
requirements for the degree of
Doctor of Philosophy

in

Engineering: Mechanical Engineering

in the

Graduate Division

of the

University of California, Berkeley

Committee in charge:

Professor David M. Auslander, Chair
Professor J. Karl Hedrick
Professor Shmuel S. Oren

Fall 2014

Control Theoretic Approach for Attitude Control of High Altitude Scientific Stationary Platforms

Abstract

Control Theoretic Approach for Attitude Control of High Altitude Scientific Stationary Platforms

by

Yao-Ting Mao

Doctor of Philosophy in Engineering: Mechanical Engineering

University of California, Berkeley

Professor David M. Auslander, Chair

Scientific exploration of near-earth space and high altitudes within earth's atmosphere greatly enhance our knowledge of how the earth functions and how it interacts with the sun. These missions have the platforms and need the controller to achieve the specific attitude necessary with limited sensors and actuators. This dissertation introduces the dynamics of the scientific platforms with suitable control rules under various environments and constraints. Three kinds of science platforms are discussed here: (1) the spin rate and the attitude control of a rigid body, (2) the strategy for the stabilization and the modeling of a multibody system in the space, and(3) the pointing control of a multibody system at the stratosphere. This dissertation also provides the designs and verification procedures for the control software in the embedded system. The simulations and experiments are presented to verify the performance of the attitude controllers.

To my wife and my son

Their support and bother make my life colorful.

Contents

List of Figures

List of Tables

Acknowledgments

I would like to thank my supervisor, Professor David M. Auslander. Previously I was confused with the direction of the research, the qualifying exam and job search. He provided me the deep overview from engineering to life and helped me pass the hardest time of my doctoral period. When I passed by his office, he was usually enjoying his coding work. His diligence influences me to catch up with rapid technology and keep curiosity alive for this universe.

I would also like to thank Dr. David Pankow. He is truly an experienced mechanical engineer and provided me lots wise advice. With his help and suggestions, my research was processed efficiently and effectively. I also appreciate his efforts in experiments and suggestions regarding funding.

I express my sincere gratitude to the late Professor Robert Lin. His kindness, intelligence and passion established an excellent model of the scientist for people to follow. He let me enroll his teams of CINEMA and GRIPS. Those interesting projects helped me develop the research and professional skills. I also want to thank Dr. Thomas Immel and Dr. Pascal Saint Hilaire for their help and management of the CINEMA and GRIPS experiment.

I would also like to thank Professor J. Karl Hedrick and Professor Shmuel Oren for serving on my dissertation committee and for valuable comments.

I am thankful to the CINEMA team; especially Karla Vega. Her simulation model and thesis guided me to start the attitude controls of a rigid body. Her patience for explaining her work helped me adapt to the PhD program.

I am also thankful to the GRIPS team, especially Eduardo Wiputra and Ben Dokko. We worked very closely and developed the control systems. I appreciate their intelligence and assiduous attitude during project's difficult times.

I also thank to my labmates: Daniel Arnold and Michael Sankur for sharing the research ideas in the controls system. They are nice and easy-going people and helped me a lot in many aspects, especially in preparing the qualifying exam.

I am really grateful to Shan Tang, Chi-Shen Tsai, Shih-Yuan Liu, Yung-Kan Chen, Jun-Chau Chien, Yenhao Chen, Yang Lin, Cong Wang, Chung Yen Lin, Yiwen Liao, Chen-Yu Chan, Cheng-Ju Wu, and all others for sharing many precious moments and invaluable aid.

I would like to acknowledge the financial support from the Space Science Laboratory of the University of California, Berkeley.

Lastly, I would like to thank my family, especially my mother who continuously encouraged me to pursue my dream and my wife for her endless patience, love and support.

Chapter 1

Introduction

1.1 Background and Motivations

The universe provides tons of puzzles for people to discover and explore. Various instruments are shipped to high altitude or space in order to obtain data free of atmospheric attenuation or distortion.

To collect high-quality data and images, precise tracking or attitude control is necessary. Normally, the attitude control of the platforms needs to consider the angular momentum conservation principle if there is no external torque. The energy conservation is not always true if damping exists in the connecting joints or in the mechanical structures. Even if the platforms have external torque, the internal angular momentum transferring between the mechanical structures may induce collapses or oscillations for some structures. Furthermore, the platforms may not be able to recover and the missions will be failures.

The aim of this dissertation is to analyze the dynamics and design attitude control for the stationary platforms at the high altitude.

1.2 Literature Review

The high altitude scientific stationary platforms have been developed for several decades. "Stationary" in this context means the platform has no actuator for the translation motions so its orbit cannot be changed. In other contexts, "stationary" can refer to geosynchronous satellites.

Based on the classes of the launch, there are two main types of stationary platforms operated at high altitude. One is the satellite; the other is the balloon.

1.2.1 Satellite

The development of the satellite has a long history. The first artificial satellite Sputnik I was successfully launched by the Soviet Union on October 4, 1957. [36] introduces the

earlier history of the satellite. Around 2,200 satellites were orbiting the planet by the end of 20th century and many of them offer scientific data. The histories of previous decades, case studies, and the lessons of the satellite industry can be found in [14]. Current and future launch vehicle capability, space law, and space policies can be found in [73].

1.2.1.1 CubeSat

For the purpose of education and because of cost [27, 59], some satellites are intended to be built at very small size (micro/nano/pico-satellite). Tab. 1.1 shows the comparison of the sizes [6]. Many nanosatellites are based on the CubeSat standard. This standard was

Table 1.1: Comparison Satellite Size

Satellite Class	Mass Range
Femtosatellite	10-100g
Picosatellite	<1kg
Nanosatellite	1-10kg
Microsatellite	10-100kg
Small Satellite	100-500kg

developed by California Polytechnic State University and Stanford University in 1999 [61]. The standard unit of the CubeSats is 1U: 10cm × 10cm × 10cm. The size could be extended only in one axis. For example, 2U: 20cm × 10cm × 10cm. 3U: 30cm × 10cm × 10cm. The design specification of CubeSat can be referred in [12, 50, 46]. Many science missions use the CubeSat as the platform. [66] introduces two mission architectures. The first is the plasma impedance probe/DC probe system. The second is GPS scintillation measurements. [44] studies plasma irregularities in the ionosphere. [51] studies Terrestrial Gamma ray Flashes (TGFs) and does so with 3U CubeSat.

1.2.1.2 Satellite Attitude Control

[33] discusses attitude control devices and presents a special problem. It also gives attention to a bias momentum satellite, detumbling of a space station and yaw sensing strategy in the control. [67] provides a framework of the attitude tracking control problem for a rigid body. [38] discusses the stabilization problem of the rigid body when the angular velocity is not available. [11, 62, 35] present the attitude control problem with the momentum exchange actuator. [18] provides the scheme of the adaptive control of a rigid body. [58, 49] present the attitude control with magnets. [71] discusses the stability with magnets and shows that attitude control can be achieved with magnetorquers as sole actuators in a low-Earth, near-polar orbit. [63] uses the momentum wheels for the attitude control and has a management

servo for avoiding the singularity in the computation. [22] studies two momentum wheel actuators using a genetic algorithm for the attitude control. [31] studies a stabilization control law with the reaction wheels and also includes the reaction wheels dynamics in the system model. [37] provides a model reference control with the reaction wheels. [52] discusses the technique for a single wheel with three-axis control of satellites. The attitude determination could be found in [24] which uses two pairs of the observations. It is very similar to the Triad algorithm. The statistical method could be used if there are more than two observations [25]. Basically, the statistical methods try to solve attitude estimation by minimization of cost function. q method of Davenport and Singular Value Decomposition (SVD) method are robust estimators for minimizing the cost function [41]. [55] uses QUEST algorithm to increase efficiency and estimate the solution to the eigenproblem. Estimators of the optimal quaternion (ESOQ) is like QUEST, which is a less robust estimator.

1.2.2 High-Altitude Balloon

For the past few years, the high-altitude balloon is very popular for science missions because the cost of missions with a balloon is less than with a satellite. Moreover, the launch has fewer constraints. [4] is a compilation for survey of international organizations which support the balloon flight to the scientific community. The advantages of the balloon are cost and fewer restrictions from authorities, like NASA. The platforms carried by the balloon could fly up to an altitude of around 60,000 to 120,000 feet. A helium balloon is launched from Antarctica [13] and verifies a hypothesis that balloon flights with stable altitude profiles up to 10-30 days are feasible. [15] introduces how to use the balloon for positioning a rocket above 20 km in the atmosphere. [43] shows the idea of using a parachute in the balloon mission for a safe landing.

1.2.2.1 Balloon Pointing Control

[10] uses the servo system for the azimuth and the elevation control. It uses two control loops with pole placement techniques and reduced order estimators. However, there is no further detail about the control and the dynamics analysis. [16] controls orientations of the mirrors for the imaging but not controlling the entire gondola. [45] uses the PID control and feed forward with a balloon borne telescope but doesn't consider the dynamics from the balloon and the ladders. [32] uses the adaptive PID control with a Balloon-borne gondola system but those PID gains are not in the sense of the optimization. [21] utilizes a differential GPS system for coarse pointing in the azimuth and uses a new solar aspect system for fine pointing. A shaft angle encoder plus inclinometer provides the coarse elevation.

1.3 Dissertation Contributions

This dissertation shows the attitude control designs of three kinds of high altitude scientific stationary platforms and also provides details of the control software design and

simulation structures. The relevant algorithms of astronomy and the modeling principle of each components are also presented in this dissertation. The following are details of the main contributions in the attitude control.

- **The attitude control strategies for a rigid body with limited resources**
  The attitude control needs to know the current orientation and the angular velocity of the rigid body. This dissertation shows a new estimation method with two local measurements. Three estimation methods of the angular velocity and their comparison are provided. In order to reduce the convergence rate, four new attitude control algorithms with coils moments and their comparison are provided. The stability of the detumble control and the sun normal controls principle are also provided.

- **The stabilization and the modeling for a multibody system in space**
  A new design spacecraft and a stabilization strategy are provided. Simulation methods of the orbit Earth's shadow perturbation, the unloading of the bus reaction wheels, fuel tanks, gear constraints and spin plane booms are presented.

- **The pointing control for a mulitbody system at the stratosphere**
  The derivations of the dynamics of the balloon-borne gondola are presented. A new model of the elevation dynamics is proposed. The strategy of the pointing control, the simulation, the control software design in the embedded system and the experiments are described. The self-tuning adaptive control structure is proposed. A new method for fast self-tuning gains is also presented.

1.4 Dissertation Outline

The outline of the dissertation is as follows:

- Chapter 2 provides the preliminary knowledge of the dynamics. It introduces the rotational coordinate systems, rotational kinematics attitude determination, rigid body dynamics, orbit dynamics and Euler-Lagrange equations. An efficient method for solving Euler-Lagrange equations to the linear state space is provided. All formulas with the relevant references are also presented.

- Chapter 3 explores the preliminary knowledge of the controls. The linear and nonlinear systems are compared with the following topics: controllability, observability, adaptive control and robustness criterion. Each topic is described shortly and the reader can appreciate the ideas quickly. Some of the algorithms introduced are not used in chapters 4, 5 and 6. They are still introduced in this chapter because the author wants to discuss the preliminary knowledge of the controls thoroughly.

- Chapter 4 presents the attitude control of a rigid body by introducing the CubeSat of the science mission (CINEMA). The sensors and the actuator characteristics are shown.

The disturbance, noise and uncertainties in space are described. The controllability and observability of the CubeSat are presented. The spin rate control, the ecliptic normal, and the sun normal control are derived in the sense of Lyapunov stability. Based on the available measurements, several estimation methods of the angular velocity are proposed. The simulation structure with the rigid body dynamics, the space environment, the sensors and actuator, and simulated ground station are presented.

- Chapter 5 is devoted to investigating the stabilization method of a multibody system by presenting the grotifer spacecraft of the science mission (Eggbeater). The spacecraft design and modeling methods are presented. The actuator is constructed of four reaction wheels and is shaped like a pyramid. The algorithm for distributing the control signals in the four reaction wheels is presented. Two servo control implementations described are necessary for the global stabilization.

- Chapter 6 introduces the pointing control system of a multibody system by presenting the balloon-borne gondola of the science mission (GRIPS). The azimuth and the elevation dynamics are proposed. Control flow and simulation methods are described. The simulation results and the experiments are also presented. In the end of this chapter, the curve fitting gains of the self-tuning is proposed to deal with the uncertain system parameters.

- Chapter 7 summarizes the conclusions and contributions of this dissertation and mentions the possible extensions for research in the future.

Chapter 2

Dynamics Basics

Feedback or feed forward information are important for aerospace vehicle control systems. The information must be specified in the coordinate system of the aerospace vehicle. Two-dimensional control problems are simpler and easier understood than a corresponding three-dimensional control problems. An approach for presenting vehicle dynamics for a three-dimensional space is to draw two coordinates dimensionless in time, like a phase plane.

A two-dimensional space implies only one direction of angular velocity of a rigid body. Therefore, consideration of the body's dynamics and Euler's equations of rotation is not necessary. A body's motion in three-dimensional space is dominated by rigid body dynamics and Newton's laws of motion. Linear momentum, angular momentum and energy are almost nearly conserved for an aerospace vehicle at high altitude as there is no ground friction or reaction force. By analyzing the law of conservation of energy, a deep insight into the attitude control of an aerospace vehicle can be gained. This can save much time and energy in analysis of the vehicle's controllability.

2.1 Rotational Coordinate Systems

We use the coordinate system to present coordinates. Each coordinate has the scalar value.

For an aerospace vehicle, the coordinates typically present its position or attitude. For the attitude control, we are more interested in the vehicle's rotation. The position may inform the controller the changes of the environment and the controller can use the information to deal with the attitude control. The vehicle's position may inform the controller of environmental changes and the controller control or rectify the vehicle's attitude.

The satellite is a good example of application of the attitude control. Its position can be found or derived from Kepler's laws of planetary motion. The attitude controller is only responsible for the control of the satellite's rotational status. It is not necessary for the satellite's dynamics to be in Cartesian coordinates. However, it is often convenient to

express or present physical properties, such as a magnetic or electric field, in a Cartesian coordinate system. This chapter introduces the well-known coordinate systems.

2.1.1 Inertial Frame

Inertial frame is the frame with right-hand rule in the Cartesian frame without the acceleration and rotation respect to the inertia origin. In the inertial frame, free motion has a constant magnitude and direction. Actually, there is no frame without acceleration in the universe. Depending on the interesting range, people take a quasi-inertial frame for different practical conditions. For example, if you want to study the motion on the ground, inertial frame is fixed with the earth. If you want to study the motion of Mars, the inertial frame is fixed with the solar system.

2.1.2 Body Frame

The body frame is the frame which is fixed with a rigid body. The moment of inertia (inertia matrix) which is expressed in inertial frame is not constant if the rigid body is rotating. The inertia matrix is from the definition of the angular momentum. The angular momentum h is a vector and could be expressed in any coordinate system. The angular momentum needs to specify the point for the origin. Choose center of mass (CM) as the origin, we have:

$$\vec{h}_{cm} = \int_{body} (\vec{r} \times \vec{v}) dm \tag{2.1}$$

The Inertia matrix is equal to:

$$\mathbf{I} = \int_{body} \begin{bmatrix} y^2 + z^2 & -xy & -xz \\ -xy & x^2 + z^2 & -yz \\ -xz & -yz & x^2 + y^2 \end{bmatrix} dm \tag{2.2}$$

where x, y and z in the integral are the distances of each particle which has mass: dm to the origin. If the coordinate system is not fixed to the body frame, x, y and z change in the rotating body and the inertia matrix also changes. Define $\vec{v}_{cm}$ the velocity of the center of the mass (CM). Then each particle has a relative velocity Δv to CM. The relative velocity of a particle, is due to the angular velocity.

$$\Delta v = \vec{\omega} \times \vec{r} \tag{2.3}$$

An Angular velocity can be also expressed in any coordinate frame. After some computation, we find the angular momentum can be expressed as:

$$\vec{h} = \mathbf{I}\vec{\omega} \tag{2.4}$$

In this absence of an external torque, the angular momentum expressed in the inertial frame remains constant, despite the inertia matrix changing.

2.1.3 Earth Center Inertia (ECI)

This coordinate system has the origin as the center of the Earth. The x-axis is the intersection of the equatorial and the ecliptic plane and is aligned with the vernal equinox. It is the first point the sun arise from the equator of the earth (First Point of Aries). Since the vernal equinox is changing, we need to specify the year for the vernal equinox. (J2000) The z-axis is the Earth's North pole. The direction of y-axis is determined by the right-hand rule.

2.1.4 Earth Center Earth Fixed (ECEF)

The origin is the center of the Earth. The x-axis is on the equator (0° latitude) and is aligned with the Prime Meridian (0° longitude). The z axis is aligned with the north pole. The direction of y-axis is determined by the right-hand rule.

2.1.5 Local Vertical/Local Horizontal (LVLH)

LVLH is usually defined in the spacecraft. The origin is the center of the mass. The x-axis is the along the orbit. The y-axis is perpendicular to the orbit plane. The z-axis is toward the Earth.

2.2 Rotational Kinematics

When the rigid body is rotating, the relation between different frames of reference can be described by the rotation matrix. A vector representing a physical quantity, such as a magnetic field or angular momentum, described in one frame can be described in other frames. When we study the attitude control, we are only interested in rotational control but not translational control. The rotational kinematics is a study of the angles, angular velocity, and the rotational matrix. It does not involve any forces, torques, mass, and the moment of inertia.

2.2.1 Direction Cosine Matrix

Two basis vectors of the frame $\vec{a}_i$ and $\vec{b}_i$ have the following relation [69].

$$\begin{aligned}\vec{b}_1 &= C_{11}\vec{a}_1 + C_{12}\vec{a}_2 + C_{13}\vec{a}_3 \\ \vec{b}_2 &= C_{21}\vec{a}_1 + C_{22}\vec{a}_2 + C_{23}\vec{a}_3 \\ \vec{b}_3 &= C_{31}\vec{a}_1 + C_{32}\vec{a}_2 + C_{33}\vec{a}_3\end{aligned} \tag{2.5}$$

$$\mathbf{C}^{B/A} = \begin{bmatrix} C_{11} & C_{12} & C_{13} \\ C_{21} & C_{22} & C_{23} \\ C_{31} & C_{32} & C_{33} \end{bmatrix} \tag{2.6}$$

$\mathbf{C}^{B/A}$ means the direction cosine matrix which transfers the frame $\{\vec{a}_i\}$ to the frame $\{\vec{b}_i\}$, the components of which are $C_{ij} = \vec{b}_i \cdot \vec{a}_j$. The direction cosine matrix is a way to present the rotation matrix. The following example introduces how to use the rotation matrix. **Scenario:** The body frames are aligned with the inertial frame at the one moment. After that moment, the rigid body is rotating its z axis ($\vec{b}_3$) counterclockwise θ with respect to the inertial frame. The rotation matrix becomes:

$$\mathbf{C}^{B/A} = \begin{bmatrix} \cos\theta & \sin\theta & 0 \\ -\sin\theta & \cos\theta & 0 \\ 0 & 0 & 1 \end{bmatrix} \tag{2.7}$$

We get two new basis vectors of the frame: $\vec{b}_1 = \cos\theta\vec{a}_1 + \sin\theta\vec{a}_2$. $\vec{b}_2 = \text{-}\sin\theta\vec{a}_1 + \cos\theta\vec{a}_2$. One basis vector is the same: $\vec{b}_3 = \vec{a}_3$. A basis vector for each frame is a unit vector and points to some direction. Fig. 2.1 shows the relation of $\vec{b}_1$, $\vec{a}_1$ and $\vec{a}_2$. If there is a magnetic field

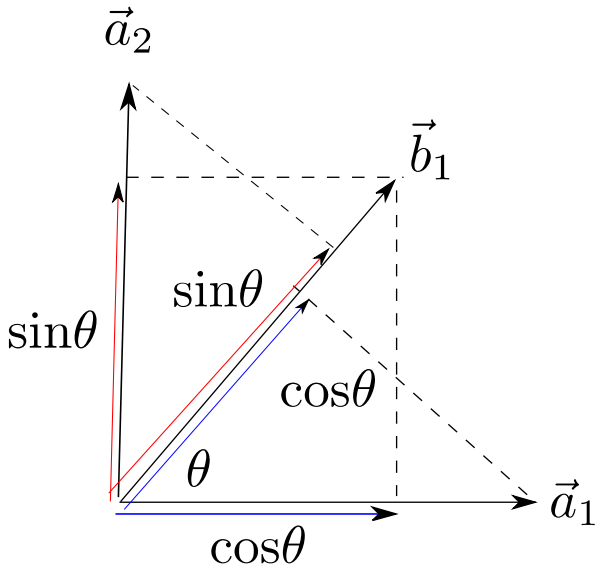

Figure 2.1: Relation of the $\vec{b}_1$, $\vec{a}_1$ and $\vec{a}_2$ After the Rotation

$\vec{M}$ with {1,0,0} direction and is fixed in the inertial frame, it should be with {$\cos\theta$,-$\sin\theta$, 0} direction in the body frame after the rotation of the body.

$$\begin{bmatrix} \cos\theta & \sin\theta & 0 \\ -\sin\theta & \cos\theta & 0 \\ 0 & 0 & 1 \end{bmatrix} \begin{bmatrix} 1 \\ 0 \\ 0 \end{bmatrix} = \begin{bmatrix} \cos\theta \\ -\sin\theta \\ 0 \end{bmatrix} \tag{2.8}$$

Fig. 2.2 shows the magnetic field in the body frame after the rotation of the body.

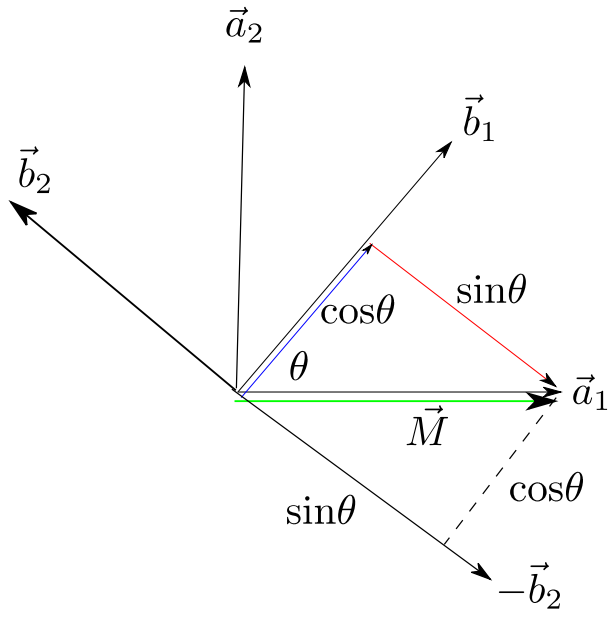

Figure 2.2: Magnetic Field Representation in the Body Frame

2.2.2 Quaternions

The Euler axis (eigenaxis) $\vec{e}$ is the axis fixed in the rigid body and that remains unchanged in the inertial frame after the rotation [69].

$$\begin{aligned}\vec{e} &= e_1\vec{a}_1 + e_2\vec{a}_2 + e_3\vec{a}_3 \\ &= e_1\vec{b}_1 + e_2\vec{b}_2 + e_3\vec{b}_3\end{aligned} \tag{2.9}$$

In other words, we can always present the rotation matrix with the Euler axis and the rotation angle θ. Define Euler parameters:

$$\begin{aligned}q_1 &= e_1\sin(\theta/2) \\ q_2 &= e_2\sin(\theta/2) \\ q_3 &= e_3\sin(\theta/2) \\ q_4 &= \cos(\theta/2)\end{aligned} \tag{2.10}$$

After lots manipulating the variables, we can represent the rotating matrix with the Euler parameters.

$$\mathbf{C}^{B/A} = \begin{bmatrix} 1-2(q_2^2+q_3^2) & 2(q_1q_2+q_3q_4) & 2(q_1q_3-q_2q_4) \\ 2(q_2q_1-q_3q_4) & 1-2(q_1^2+q_3^2) & 2(q_2q_3+q_1q_4) \\ 2(q_3q_1+q_2q_4) & 2(q_3q_2-q_1q_4) & 1-2(q_1^2+q_2^2) \end{bmatrix} \tag{2.11}$$

We know the eigenaxis has two possible directions. However, there is the only one set for the Euler parameter. The reason is that when we choose the negative direction of the axis,

the rotation angle θ is also negative. By checking Eqn. (2.10), those Euler parameters are independent of the direction of eigenaxis.

2.2.3 Gibber Parameters

The rotation matrix can also represent with the Gibber parameters. Define:

$$\begin{aligned} g_1 &= q_1/q_4 \\ g_2 &= q_2/q_4 \\ g_3 &= q_3/q_4 \end{aligned} \tag{2.12}$$

Then the rotation matrix can be represented as:

$$\mathbf{C}^{B/A} = \frac{1}{1+g_1^2+g_2^2+g_3^2} \begin{bmatrix} 1+g_1^2-g_2^2-g_3^2 & 2(g_1g_2+g_3) & 2(g_1g_3-g_2) \\ 2(g_2g_1-g_3) & 1-g_1^2+g_2^2-g_3^2 & 2(g_2g_3+g_1) \\ 2(g_3g_1+g_2) & 2(g_3g_2-g_1) & 1-g_1^2-g_2^2+g_3^2 \end{bmatrix} \tag{2.13}$$

When the rotation angel is 180° along the eigenaxis, each Gibber parameter in Eqn. (2.12) becomes infinity. This may prove disastrous in digital control. The controller needs to know the parameters to get the rotation matrix and compute the correct outputs. The effects of an infinity number in the digital system are unknown and possibly dangerous.

2.2.4 Kinematic Differential Equations

In spacecraft control attitude design, it is imperative to know the current attitude and the angular velocity. However, spacecrafts typically only have limited sensor resources, thus often have limited or incomplete state information. If there is no gyroscope or if the spacecraft gyroscope has particularly noisy measurements, we cannot tell the angular velocity of the spacecraft. However, with measurements of some targets fixed within the inertial frame then we can indirectly derive the angular velocity. It is convenient to use the *Triad* algorithm to get the rotation matrix. The time derivative of the rotation matrix can be used to derive the angular velocity.

Angular Velocity and Derivative Rotation Matrix

To find the relation of angular velocity and the rotation matrix, the derivative of the body frame in time must be found.

$$\dot{\vec{b}}_k = \mathring{\vec{b}}_k + \vec{\omega} \times \vec{b}_k \qquad k = 1, 2, 3 \tag{2.14}$$

Where " ° " means the time derivative w.r.t. the body frame and doesn't involve the changes of the coordinate system. Furthermore, amplitudes of all axes are unit vectors and therefore

the time derivative w.r.t the body frame is equal to zero. Based on this fact, Eqn. (2.14) becomes:

$$\frac{d\vec{b}_k}{dt} = \vec{\omega} \times \vec{b}_k \tag{2.15}$$

From Eqn. (2.5), we get:

$$\begin{bmatrix} \dot{\vec{b}}_1 \\ \dot{\vec{b}}_2 \\ \dot{\vec{b}}_3 \end{bmatrix} = \dot{\mathbf{C}} \begin{bmatrix} \vec{a}_1 \\ \vec{a}_2 \\ \vec{a}_3 \end{bmatrix} \tag{2.16}$$

Where $\vec{a}_k$ is in the inertial frame, so the time derivative to $\vec{a}_k$ is zero. For the rotation matrix, $\mathbf{C}^{-1} = \mathbf{C}^T$. Then we have:

$$\begin{bmatrix} \vec{\omega} \times \vec{b}_1 \\ \vec{\omega} \times \vec{b}_2 \\ \vec{\omega} \times \vec{b}_3 \end{bmatrix} = \dot{\mathbf{C}}\mathbf{C}^T \begin{bmatrix} \vec{b}_1 \\ \vec{b}_2 \\ \vec{b}_3 \end{bmatrix} \tag{2.17}$$

and

$$\begin{bmatrix} \vec{\omega} \times \vec{b}_1 \\ \vec{\omega} \times \vec{b}_2 \\ \vec{\omega} \times \vec{b}_3 \end{bmatrix} = - \begin{bmatrix} 0 & -\omega_3 & \omega_2 \\ \omega_3 & 0 & -\omega_1 \\ -\omega_2 & \omega_1 & 0 \end{bmatrix} \begin{bmatrix} \vec{b}_1 \\ \vec{b}_2 \\ \vec{b}_3 \end{bmatrix} = -\mathbf{\Omega} \begin{bmatrix} \vec{b}_1 \\ \vec{b}_2 \\ \vec{b}_3 \end{bmatrix} \tag{2.18}$$

So we have

$$(\dot{\mathbf{C}}\mathbf{C}^T + \mathbf{\Omega}) \begin{bmatrix} \vec{b}_1 \\ \vec{b}_2 \\ \vec{b}_3 \end{bmatrix} = \begin{bmatrix} 0 \\ 0 \\ 0 \end{bmatrix} \tag{2.19}$$

Since the body frame is arbitrarily chosen, so $\dot{\mathbf{C}}\mathbf{C}^T + \mathbf{\Omega} = 0$. Multiply $\mathbf{C}$ in both sides and use $\mathbf{C}^T\mathbf{C} = I$, I is the identity matrix. We can get:

$$\dot{\mathbf{C}} + \mathbf{\Omega}\mathbf{C} = 0 \tag{2.20}$$

There are nine equations from the matrix and only three unknowns in $\vec{\omega}$. After some manipulation of the linear equations, we can get:

$$\begin{aligned} \omega_1 &= \dot{C}_{21}C_{31} + \dot{C}_{22}C_{32} + \dot{C}_{23}C_{33} \\ \omega_2 &= \dot{C}_{31}C_{11} + \dot{C}_{32}C_{12} + \dot{C}_{33}C_{13} \\ \omega_3 &= \dot{C}_{11}C_{21} + \dot{C}_{12}C_{22} + \dot{C}_{13}C_{23} \end{aligned} \tag{2.21}$$

Angular Velocity and Quaternions

Taking the derivative in time of the components of Eqn. (2.11), and using Eqn. (2.21) we arrive at:

$$\begin{aligned}\omega_1 &= 2(\dot{q}_1 q_4 + \dot{q}_2 q_3 - \dot{q}_3 q_2 - \dot{q}_4 q_1)\\ \omega_2 &= 2(\dot{q}_2 q_4 + \dot{q}_3 q_1 - \dot{q}_1 q_3 - \dot{q}_4 q_2)\\ \omega_3 &= 2(\dot{q}_3 q_4 + \dot{q}_1 q_2 - \dot{q}_2 q_1 - \dot{q}_4 q_3)\end{aligned} \tag{2.22}$$

2.3 Attitude Determination

2.3.1 Triad Algorithm

If two measurements both in the body frame and in the inertial frame are available and they are not aligned, then we can use the *Triad* to generate the rotation matrix. Here is the idea of the *Triad* algorithm:

- Get two measurements and know the directions, for example the sun(s) and the direction of the magnetic field (m). Make them become unit vectors: $(\vec{s})^i$,$(\vec{s})^b$,$(\vec{m})^i$ and $(\vec{m})^b$. i means the expression in inertial frame. b means the expression in the body frame.

- Use those measurements, build coordinate systems. Choose $(\vec{s})^i = (\vec{x})^i$ as the x-axis, $(\vec{s})^i \times (\vec{m})^i = (\vec{y})^i$ as the y-axis, and $(\vec{s})^i \times (\vec{y})^i = (\vec{z})^i$ as the z-axis. It doesn't matter which measurement to be the x-axis or y-axis or z-axis. Just need to follow the right-hand rule for the cross product. Also do the same procedure for measurements in the body frame and get: $(\vec{x})^b$,$(\vec{y})^b$ and $(\vec{z})^b$ in the body frame.

- Build the rotation matrix. Define the frame which is built from the position of the sun and the direction of the magnetic field: *SM*, we have:

$$\begin{aligned}(\vec{x}) &= \begin{bmatrix}(\vec{x})^i \cdot \vec{E}_x\\ (\vec{x})^i \cdot \vec{E}_y\\ (\vec{x})^i \cdot \vec{E}_z\end{bmatrix}^i = \begin{bmatrix}(\vec{x})^b \cdot \vec{e}_x\\ (\vec{x})^b \cdot \vec{e}_y\\ (\vec{x})^b \cdot \vec{e}_z\end{bmatrix}^b\\ (\vec{y}) &= \begin{bmatrix}(\vec{y})^i \cdot \vec{E}_x\\ (\vec{y})^i \cdot \vec{E}_y\\ (\vec{y})^i \cdot \vec{E}_z\end{bmatrix}^i = \begin{bmatrix}(\vec{y})^b \cdot \vec{e}_x\\ (\vec{y})^b \cdot \vec{e}_y\\ (\vec{y})^b \cdot \vec{e}_z\end{bmatrix}^b\\ (\vec{z}) &= \begin{bmatrix}(\vec{z})^i \cdot \vec{E}_x\\ (\vec{z})^i \cdot \vec{E}_y\\ (\vec{z})^i \cdot \vec{E}_z\end{bmatrix}^i = \begin{bmatrix}(\vec{z})^b \cdot \vec{e}_x\\ (\vec{z})^b \cdot \vec{e}_y\\ (\vec{z})^b \cdot \vec{e}_z\end{bmatrix}^b\end{aligned} \tag{2.23}$$

  So the rotation matrix $\mathbf{C}^{SM/I}$ for the inertial frame: $\{\vec{E}_x,\vec{E}_y,\vec{E}_z\}$ to the intermediate frame $SM\{$ $(\vec{x})$,$(\vec{y})$,$(\vec{z})\}$ frame is:

$$\mathbf{C}^{SM/I} = \begin{bmatrix}(\vec{x})^i & (\vec{y})^i & (\vec{z})^i\end{bmatrix}^T \tag{2.24}$$

T means the transpose of a matrix. The rotation matrix from SM frame to the body frame $\{\vec{e}_x, \vec{e}_y, \vec{e}_y\}$ is:

$$\mathbf{C}^{B/SM} = \begin{bmatrix} (\vec{x})^b & (\vec{y})^b & (\vec{z})^b \end{bmatrix} \tag{2.25}$$

So the rotation matrix of the inertial frame to the body frame is:

$$\mathbf{C}^{B/I} = \mathbf{C}^{B/SM}\mathbf{C}^{SM/I} \tag{2.26}$$

2.4 Rigid-Body Dynamics

We have already known the math of the attitude, angular velocity and the rotation matrix. However, there is no dynamics involved in them. The dynamics of the rotation are governed by, the moment of inertia, initial states, external torques.

2.4.1 Angular Momentum of a Rigid Body

We are familiar with the liner momentum. The change of the linear momentum is depended on how much external forces to the system and don't care about the reference point. However, for the angular momentum, the reference point needs to be specified. Moreover, the change of the angular momentum for a fixed point in the inertial frame is from the point of view of the inertial frame. It is no meaning to make the same statement from the point of view of the body frame. If the rigid body has nonzero angular velocity for the general case, the angular momentum which is expressed in the body frame is continuously changing because of the rotation matrix changing. It is true even if there is no external torque. The time derivative of the angular momentum is equal to the external torque. $\vec{M}_o$ means the resultant torque to an arbitrary point o. The following equation uses same notion in [69].

$$\vec{M}_o = \int_{body} (\vec{r} \times \ddot{\vec{R}}) dm \tag{2.27}$$

$\vec{r}$ is the distance from o to the particle. $\vec{R}$ is the distance from the origin in the inertial frame to the particle. Let $\vec{R} = \vec{R}_o + \vec{r}$ and we know

$$\int_{body} \vec{r} dm = m\vec{r}_c \tag{2.28}$$

$\vec{r}_c$ is the vector from o to cm.

$$\int_{body} \vec{\rho} dm = 0 \tag{2.29}$$

$\vec{\rho}$ is the distance from cm to local particle. We have

$$\begin{aligned}\vec{M}_o &= \int_{body} (\vec{r} \times (\ddot{\vec{R}}_o + \ddot{\vec{r}}))dm \\ &= \int_{body} (\vec{r} \times \ddot{\vec{r}})dm + m\vec{r}_c \times \ddot{\vec{R}}_o\end{aligned} \tag{2.30}$$

Define the relative angular momentum.

$$\vec{h}_o = \int_{body} (\vec{r} \times \dot{\vec{r}})dm \tag{2.31}$$

$$\dot{\vec{h}}_o = \int_{body} (\dot{\vec{r}} \times \dot{\vec{r}})dm + \int_{body} (\vec{r} \times \ddot{\vec{r}})dm \tag{2.32}$$

We have:

$$\vec{M}_o = \dot{\vec{h}}_o + m\vec{r}_c \times \ddot{\vec{R}}_o \tag{2.33}$$

Relative angular momentum means the origin of the frame is set at the arbitrary point o. The o could be moving and is not necessarily fixed. Similar to the relative angular momentum, we can also define absolute angular momentum.

$$\vec{H}_o = \int_{body} (\vec{r} \times \dot{\vec{R}})dm \tag{2.34}$$

Since o is not fixed, the relative and the absolute momentum are different ($\dot{\vec{R}} = \dot{\vec{R}}_o + \dot{\vec{r}}$). From the time derivative of the absolute angular momentum, we get:

$$\begin{aligned}\dot{\vec{H}}_o &= \int_{body} (\dot{\vec{r}} \times \dot{\vec{R}})dm + \int_{body} (\vec{r} \times \ddot{\vec{R}})dm \\ &= \int_{body} (\dot{\vec{r}} \times (\dot{\vec{R}}_o + \dot{\vec{r}}))dm + \vec{M}_o \\ &= \int_{body} (\dot{\vec{r}} \times (\dot{\vec{R}}_o + \dot{\vec{r}}))dm + \vec{M}_o \\ &= \int_{body} (\dot{\vec{r}} \times \dot{\vec{R}}_o)dm + \vec{M}_o \\ &= m\dot{\vec{r}}_c \times \dot{\vec{R}}_o + \vec{M}_o\end{aligned} \tag{2.35}$$

If o is chosen as the center of the mass, we get: ($\dot{\vec{R}} = \dot{\vec{R}}_{cm} + \dot{\vec{r}}$) The absolute angular momentum is:

$$\begin{aligned}
\vec{H}_o &= \int_{body} \vec{r} \times (\dot{\vec{R}}_{cm} + \dot{\vec{r}}) dm \\
&= \int_{body} \vec{r} \times \dot{\vec{R}}_{cm} dm + \int_{body} \vec{r} \times \dot{\vec{r}} dm \\
&= \int_{body} \vec{r} \times \dot{\vec{R}}_{cm} dm + \vec{h}_o \\
&= m\vec{r}_c \times \dot{\vec{R}}_{cm} dm + \vec{h}_o
\end{aligned} \tag{2.36}$$

and $\vec{r}_c = 0$ for o is the center of mass. So $\vec{H}_o = \vec{h}_o$ and $\dot{\vec{M}}_o = \dot{\vec{H}}_o = \dot{\vec{h}}_o$ When we design the attitude controls for the spacecraft, it is convenient to choose the angular momentum to the center of the mass and eliminate the terms from $\vec{r}_c$. In this dissertation, if we talk about the angular momentum without the notification, it means the angular momentum to its center of the mass.

2.4.2 Rigid Body Equations of Motion

The angular momentum, the angular velocity and the torque are vectors and can be expressed in any frame. Specify the center of the mass of a rigid body for the angular momentum, then time derivative of the angular momentum equals resultant torque applied to this rigid body w.r.t. the inertial frame. The time derivative of the angular momentum w.r.t the body frame doesn't equal the resultant torque expressed w.r.t. the body frame because the resultant torque doesn't generate the additional term under different frames. The following equations use the same notion in [57]. Let $\boldsymbol{h_B}$, $\boldsymbol{h_I}$ mean the angular momentum expressed in the body frame and in the inertial frame. Let $\boldsymbol{\omega_B}$, $\boldsymbol{\omega_I}$ mean the angular velocity expressed in the body frame and in the inertial frame. Let $\boldsymbol{m_B}$, $\boldsymbol{m_I}$ mean the moment expressed in the body frame and in the inertial frame. Let $\boldsymbol{J_B}$, $\boldsymbol{J_I}$ mean the moment of inertia in the body frame and in the inertial frame. $\boldsymbol{H_B^I}$ means the rotation matrix from the body frame to the inertial frame and $\boldsymbol{H_I^B}$ means the rotation matrix from the inertial frame

to the body frame. We have the following equations:

$$\begin{aligned}
\boldsymbol{h_B} &= \boldsymbol{H_I^B h_I} = \boldsymbol{J_B \omega_B} \\
\boldsymbol{\omega_B} &= \boldsymbol{H_I^B \omega_I} \\
\boldsymbol{h_I} &= \boldsymbol{H_B^I h_B} = \boldsymbol{J_I \omega_I} \\
\boldsymbol{\omega_I} &= \boldsymbol{H_B^I \omega_B} \\
\boldsymbol{m_B} &= \boldsymbol{H_I^B m_I} \\
\boldsymbol{m_I} &= \boldsymbol{H_B^I m_B}
\end{aligned} \tag{2.37}$$

We know that the time derivative of the angular momentum is equal to the external torque. This statement is true under the expression in the inertial frame. That's why we start the time derivative for the angular momentum of $\boldsymbol{h_I}$. The time derivative of any vector $\boldsymbol{A}$ in a rigid body has this relation.[30]

$$\dot{\boldsymbol{A}} = (\dot{\boldsymbol{A}})_B + \boldsymbol{\omega} \times \boldsymbol{A} \tag{2.38}$$

The notion $()_B$ means the changing w.r.t.the body frame. It is important to know that Eqn. (2.38) just shows the relation of the vectors. We still need to decide which frames to express them. All the components in Eqn. (2.38) should use the unique frame.

$$\dot{\boldsymbol{h}}_{\boldsymbol{I}} = (\dot{\boldsymbol{h}}_{\boldsymbol{I}})_B + \boldsymbol{\omega_I} \times \boldsymbol{h_I} \tag{2.39}$$

The observer in the body frame can observe the time derivative of angular momentum $\dot{\boldsymbol{h}}_{\boldsymbol{B}}$ in his frame but cannot see the changes due to the time derivative of the frame. We also need to expressed the $\dot{\boldsymbol{h}}_{\boldsymbol{B}}$ in the correct frame and multiply it with $\boldsymbol{H_B^I}$.

$$\begin{aligned}
\dot{\boldsymbol{h}}_{\boldsymbol{I}} &= \boldsymbol{H_B^I} \dot{\boldsymbol{h}}_{\boldsymbol{B}} + \boldsymbol{\omega_I} \times \boldsymbol{h_I} \\
&= \boldsymbol{H_B^I} \dot{\boldsymbol{h}}_{\boldsymbol{B}} + \boldsymbol{\Omega_I h_I}
\end{aligned} \tag{2.40}$$

We also know that:

$$\dot{\boldsymbol{h}}_{\boldsymbol{I}} = \boldsymbol{H_B^I} \dot{\boldsymbol{h}}_{\boldsymbol{B}} + \dot{\boldsymbol{H}}_{\boldsymbol{B}}^{\boldsymbol{I}} \boldsymbol{h_B} \tag{2.41}$$

So we have:

$$\dot{\boldsymbol{H}}_{\boldsymbol{B}}^{\boldsymbol{I}} \boldsymbol{h_B} = \boldsymbol{\omega_I} \times \boldsymbol{h_I} = \boldsymbol{\Omega_I h_I} = \boldsymbol{\Omega_I H_B^I h_B} \tag{2.42}$$

and

$$\begin{aligned}
&\boldsymbol{H_B^I H_I^B} = \boldsymbol{I} \\
&\dot{\boldsymbol{H}}_{\boldsymbol{B}}^{\boldsymbol{I}} \boldsymbol{H_I^B} + \boldsymbol{H_B^I} \dot{\boldsymbol{H}}_{\boldsymbol{I}}^{\boldsymbol{B}} = \boldsymbol{0} \\
&\dot{\boldsymbol{H}}_{\boldsymbol{I}}^{\boldsymbol{B}} = -\boldsymbol{H_I^B} \dot{\boldsymbol{H}}_{\boldsymbol{B}}^{\boldsymbol{I}} \boldsymbol{H_I^B}
\end{aligned} \tag{2.43}$$

Then we can get:

$$\begin{aligned}\dot{\boldsymbol{h}}_{\boldsymbol{B}} &= \boldsymbol{H}_{\boldsymbol{I}}^{\boldsymbol{B}}\dot{\boldsymbol{h}}_{\boldsymbol{I}} + \dot{\boldsymbol{H}}_{\boldsymbol{I}}^{\boldsymbol{B}}\boldsymbol{h}_{\boldsymbol{I}} \\ &= \boldsymbol{H}_{\boldsymbol{I}}^{\boldsymbol{B}}\dot{\boldsymbol{h}}_{\boldsymbol{I}} - \boldsymbol{H}_{\boldsymbol{I}}^{\boldsymbol{B}}\dot{\boldsymbol{H}}_{\boldsymbol{B}}^{\boldsymbol{I}}\boldsymbol{H}_{\boldsymbol{I}}^{\boldsymbol{B}}\boldsymbol{h}_{\boldsymbol{I}} \\ &= \boldsymbol{H}_{\boldsymbol{I}}^{\boldsymbol{B}}\dot{\boldsymbol{h}}_{\boldsymbol{I}} - \boldsymbol{H}_{\boldsymbol{I}}^{\boldsymbol{B}}\dot{\boldsymbol{H}}_{\boldsymbol{B}}^{\boldsymbol{I}}\boldsymbol{h}_{\boldsymbol{B}} \\ &= \boldsymbol{H}_{\boldsymbol{I}}^{\boldsymbol{B}}\dot{\boldsymbol{h}}_{\boldsymbol{I}} - \boldsymbol{H}_{\boldsymbol{I}}^{\boldsymbol{B}}(\boldsymbol{\omega}_{\boldsymbol{I}} \times \boldsymbol{h}_{\boldsymbol{I}}) \\ &= \boldsymbol{H}_{\boldsymbol{I}}^{\boldsymbol{B}}\boldsymbol{m}_{\boldsymbol{I}} - \boldsymbol{\omega}_{\boldsymbol{B}} \times \boldsymbol{h}_{\boldsymbol{B}} \\ &= \boldsymbol{m}_{\boldsymbol{B}} - \boldsymbol{\omega}_{\boldsymbol{B}} \times \boldsymbol{J}_{\boldsymbol{B}}\boldsymbol{\omega}_{\boldsymbol{B}}\end{aligned} \tag{2.44}$$

We also have:

$$\begin{aligned}\dot{\boldsymbol{h}}_{\boldsymbol{B}} &= \boldsymbol{J}_{\boldsymbol{B}}\dot{\boldsymbol{\omega}}_{\boldsymbol{B}} + \dot{\boldsymbol{J}}_{\boldsymbol{B}}\boldsymbol{\omega}_{\boldsymbol{B}} \\ &= \boldsymbol{J}_{\boldsymbol{B}}\dot{\boldsymbol{\omega}}_{\boldsymbol{B}}\end{aligned} \tag{2.45}$$

The time derivative of moment of inertia expressed in the body frame is zero. So we have the governing equations for ω_B.

$$\begin{aligned}\boldsymbol{J}_{\boldsymbol{B}}\dot{\boldsymbol{\omega}}_{\boldsymbol{B}} &= \boldsymbol{m}_{\boldsymbol{B}} - \boldsymbol{\omega}_{\boldsymbol{B}} \times \boldsymbol{J}_{\boldsymbol{B}}\boldsymbol{\omega}_{\boldsymbol{B}} \\ \dot{\boldsymbol{\omega}}_{\boldsymbol{B}} &= \boldsymbol{J}_{\boldsymbol{B}}^{-\boldsymbol{1}}(\boldsymbol{m}_{\boldsymbol{B}} - \boldsymbol{\omega}_{\boldsymbol{B}} \times \boldsymbol{J}_{\boldsymbol{B}}\boldsymbol{\omega}_{\boldsymbol{B}})\end{aligned} \tag{2.46}$$

2.5 Orbit Dynamics

For the equation of the motion of two particles, assume one of them is the Earth, and the other is the satellite. $\vec{r}$ is the vector from the center of the satellite to the center of the Earth.

$$\begin{aligned}m_1\vec{a} &= \frac{GMm_1}{r^3}\vec{r} \\ \ddot{\vec{r}} &= \frac{\mu}{r^3}\vec{r}\end{aligned} \tag{2.47}$$

For the convenience, μ is a number to present all physical properties. From [69] and Eqn. (2.47), we can derive the energy conservation law ($\frac{v^2}{2} - \frac{\mu}{r}$=constant, per unit of mass) and the angular momentum conservation law ($\vec{h} = \vec{r} \times \vec{v}$=constant, per unit of mass). If we just apply the moment for the attitude controls in Eqn. (2.47), the equation of the motion will not change. Since the equation of the motion doesn't change, the energy and the angular momentum conservation are always true in the sense of a single particle. The total energy ($\frac{1}{2}mv^2 - \frac{\mu m}{r} + \frac{1}{2}\omega J\omega$) and the total angular momentum ($\vec{r}m \times \vec{v} + J\omega$) may not be conserved because $\frac{1}{2}\omega J\omega$ and $J\omega$ could be changed by the attitude controls. ω is from the rigid body rotation, J is measured w.r.t. the body frame, and the origin is the center of the mass. From Eqn. (2.47), we have:

$$\begin{aligned}\ddot{\vec{r}} + \frac{\mu}{r^3}\vec{r} &= 0 \\ \ddot{\vec{r}} \times \vec{h} + \frac{\mu}{r^3}\vec{r} \times \vec{h} &= 0\end{aligned} \tag{2.48}$$

$\vec{h}$ is constant and we know

$$\vec{r} \times \vec{h} = \vec{r} \times (\vec{r} \times \dot{\vec{r}}) = (\vec{r} \cdot \dot{\vec{r}})\vec{r} - (\vec{r} \cdot \vec{r})\dot{\vec{r}} \tag{2.49}$$

also,

$$\begin{aligned} \frac{d}{dt}(\frac{\mu}{r}) &= \frac{1}{2}\frac{\mu}{(x^2+y^2+z^2)^{3/2}}(2x\dot{x} + 2y\dot{y} + 2z\dot{z}) \\ &= \frac{\mu}{r^3}(\vec{r} \cdot \dot{\vec{r}}) \end{aligned} \tag{2.50}$$

Then we have:

$$\frac{d}{dt}[\dot{\vec{r}} \times \vec{h} - \frac{\mu}{r}\vec{r}] = 0 \tag{2.51}$$

Let

$$\dot{\vec{r}} \times \vec{h} - \frac{\mu}{r}\vec{r} = \mu\vec{e} \tag{2.52}$$

$\vec{e}$ is eccentricity vector. From the inner product in both sides, we have:

$$\vec{r} \cdot \dot{\vec{r}} \times \vec{h} - \vec{r} \cdot \frac{\mu}{r}\vec{r} = \vec{r} \cdot \mu\vec{e} \tag{2.53}$$

We know:

$$a \cdot (b \times c) = (a \times b) \cdot c \tag{2.54}$$

Then we get:

$$\vec{r} \cdot \dot{\vec{r}} \times \vec{h} = (\vec{r} \times \dot{\vec{r}}) \cdot \vec{h} = \vec{h} \cdot \vec{h} \tag{2.55}$$

and

$$h^2 - \mu r = \mu r e \cos\theta \tag{2.56}$$

The θ is called the true anomaly. e is the eccentricity of the orbit. We can get Kepler's first law:

$$r = \frac{h^2/\mu}{1 + e\cos\theta} \tag{2.57}$$

e and $h^2/\mu = p$ are constants and decide the shape of the orbit. From the Eqn. (2.47), the only path of the satellite is determined once the initial condition $\vec{r}(0)$ and $\vec{v}(0)$ are specified. There are six initial conditions and we can use another six classical orbital elements for describing the orbit [69]. a: semi-major axis; e: eccentricity; t_p: time of perigee passage; Ω: right ascension longitude of the ascending note; i: inclination of the orbit plane; ω: argument of the perigee. To get the initial conditions ($\vec{r}(0)$,$\vec{v}(0)$) from the orbit element, we determine the initial position and the velocity w.r.t. the perifocal reference frame and convert the position and the velocity w.r.t. the inertial frame. The original is in the center of the focus.

$(\vec{i},\vec{j},\vec{k})$ are the basis vectors for the perifocal reference frame. $(\vec{I},\vec{J},\vec{K})$ are the basis vectors for inertial frame. The rotation matrix is from 3->1->3 Euler angles rotation.

$$\begin{pmatrix}\vec{i}\\ \vec{j}\\ \vec{k}\end{pmatrix} = \begin{pmatrix}\cos\omega & \sin\omega & 0\\ -\sin\omega & \cos\omega & 0\\ 0 & 0 & 1\end{pmatrix}\begin{pmatrix}1 & 0 & 0\\ 0 & \cos i & \sin i\\ 0 & -\sin i & \cos i\end{pmatrix}\begin{pmatrix}\cos\Omega & \sin\Omega & 0\\ -\sin\Omega & \cos\Omega & 0\\ 0 & 0 & 1\end{pmatrix}\begin{pmatrix}\vec{I}\\ \vec{J}\\ \vec{K}\end{pmatrix}$$
$$\begin{pmatrix}\vec{i}\\ \vec{j}\\ \vec{k}\end{pmatrix} = C(\omega,i,\Omega)\begin{pmatrix}\vec{I}\\ \vec{J}\\ \vec{K}\end{pmatrix} \Rightarrow \begin{pmatrix}\vec{I}\\ \vec{J}\\ \vec{K}\end{pmatrix} = C(\omega,i,\Omega)^T\begin{pmatrix}\vec{i}\\ \vec{j}\\ \vec{k}\end{pmatrix} \tag{2.58}$$

In the perifocal frame, $x = r\cos\theta, y = r\sin\theta, z = 0$, $v_x = -(\sqrt{\mu/p})\sin\theta, v_y = \sqrt{\mu/p}(e + \cos\theta), v_z = 0$ [69]. From orbital elements $(a, e, t_p, \Omega, i, \omega)$, we can derive θ from

$$\tan\frac{\theta}{2} = \sqrt{\frac{1+e}{1-e}}\tan\frac{E}{2} \tag{2.59}$$

E could be obtained from:

$$\sqrt{\mu/a^3}(t - t_p) = E - e\sin E \tag{2.60}$$

The above equation needs the numerical iteration to find E. r can be obtained from:

$$r = \frac{p}{1 + e\cos\theta} = \frac{a(1-e^2)}{1 + e\cos\theta} \tag{2.61}$$

p is also called semilatus rectum. With the rotation matrix $C(\omega,i,\Omega)^T$ in Eqn. (2.58), we can get the initial position and velocity w.r.t. the inertial frame. Fig. 2.3 is a diagram of the satellite orbit and ECI frame. One of ellipse focus is the CM of the Earth. The inertial frame uses $3(\Omega)$->$1(i)$->$3(\omega)$ Euler angles to align with the perifocal frame. Actually, the starting point $\theta(0)$ usually doesn't matter if the orbit looks like a circle. We can directly set an arbitrary value for $\theta(0)$.

2.6 Euler-Lagrange Equation

All generalized coordinates (y) of the system (in the sense of the physics) would make Π have a "fixed" value with a fixed time interval (x).

$$\Pi = \int_a^b G(y, y', x)dx \tag{2.62}$$

Boundary conditions are $y(a) = \alpha$, $y(b) = \beta$. To prove Π has an extreme or a stable value, we just need to prove another modified function $\bar{y}$ makes the rate of change of Π zero.

$$\bar{y} = y(x) + \epsilon g(x) \tag{2.63}$$

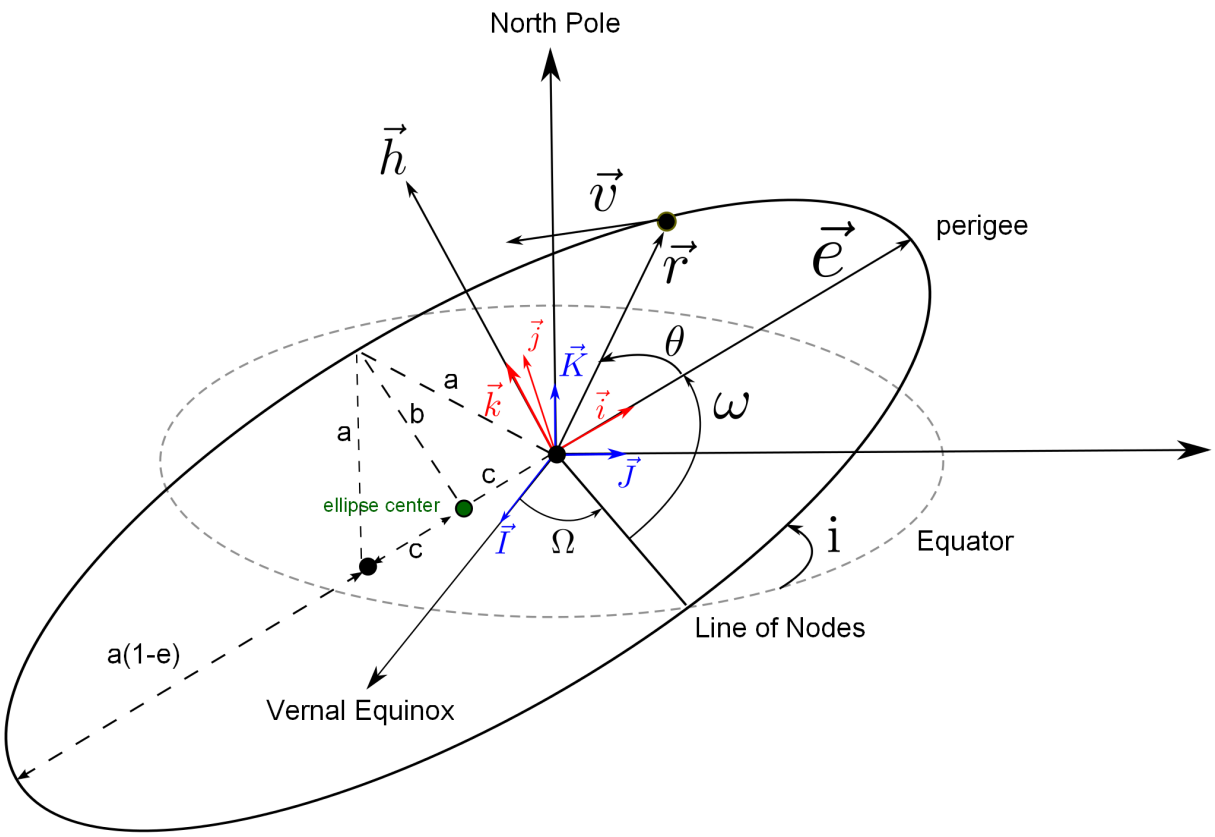

Figure 2.3: Satellite Ellipse Orbit and ECI Frame

The variation is: $\delta y = \bar{y} - y = \epsilon g(x)$. ϵ is a small scalar. δy means an arbitrary small change by y at point x. x is an independent variable and doesn't participate in the process of variation. We have:

$$\begin{aligned} &\delta x = 0 \\ &\delta y(a) = \delta y(b) = 0 \end{aligned} \tag{2.64}$$

We know

$$\frac{\partial}{\partial x}\delta y = \frac{\partial}{\partial x}\epsilon g(x) = \epsilon g' \tag{2.65}$$

and

$$\delta y' = \bar{y}' - y' = \epsilon g' \tag{2.66}$$

So we have:

$$\frac{\partial}{\partial x}\delta y = \delta y' \tag{2.67}$$

We also have:

$$\delta G(y, y', x) = G(y + \epsilon g, y' + \epsilon g', x) - G(y, y'x) = \epsilon(\frac{\partial G}{\partial y}g + \frac{\partial G}{\partial y'}g') \tag{2.68}$$

The variation of the stationary value of Π could be written as follows:

$$\delta\Pi = \delta \int_a^b G(y, y', x)dx = \int_a^b \delta G(y, y', x)dx = \epsilon \int_a^b (\frac{\partial G}{\partial y} g + \frac{\partial G}{\partial y'} g')dx \tag{2.69}$$

From the integration by parts, we have:

$$\int_a^b \frac{\partial G}{\partial y'} g' dx = \frac{\partial G}{\partial y'} g|_a^b - \int_a^b \frac{d}{dx}(\frac{\partial G}{\partial y'})g dx \tag{2.70}$$

The variation of y at the boundary (Eqn. (2.64)) is zero i.e. $g(a) = g(b) = 0$, we have: $\frac{\partial G}{\partial y'} g|_a^b = 0$. The rate of change of Π equals zero at $y = f(x)$. Substituting it to the variation of Π, we have:

$$\delta\Pi = \epsilon \int_a^b (\frac{\partial G}{\partial y} - \frac{d}{dx}\frac{\partial G}{\partial y'})g dx = 0 \tag{2.71}$$

$g(x)$ is determined arbitrarily. The following equation must be satisfied:

$$\frac{\partial G}{\partial y} - \frac{d}{dx}\frac{\partial G}{\partial y'} = 0 \tag{2.72}$$

In other words, any function which is satisfied Eqn. (2.72) could be the candidate for governing equations of generalized coordinates. Normally, G is replaced by the Lagrangian function (L). Traditionally, L has the following description.

$$L = T(\dot{q}, q) - U(q) \tag{2.73}$$

q is the generalized coordinates, not a single variable. For a single particle, we substitute L into Eqn. (2.72) for each coordinate and have:

$$\frac{d}{dt}(\frac{\partial T}{\partial \dot{q}_i}) - \frac{\partial T}{\partial q_i} + \frac{\partial U}{\partial q_i} = \vec{F}_{ncon} \cdot \vec{a}_i \tag{2.74}$$

$\vec{F}_{ncon}$ is the nonconservative force. $\vec{a}_i$ is the covariant basis vector.

$$\vec{a}_i = \frac{\partial \vec{r}}{\partial q^i} \tag{2.75}$$

More detail and the extended cases can be refereed in [47].

2.6.1 Governing Equations from the Symbolic Solver of MATLAB

Eqn. (2.72) provides a way to find the governing equations of the coordinate systems. However, it is very tedious in the process of the computation. This dissertation proposes a method which provides an efficient way for computation with symbolic solver of MATLAB.

This method could be also applied to the other software which has the similar feature. T is the kinetic energy, U is the potential energy. $r, z, \dot{z}, J, M, B, QT, QU$ are the intermediate variables. Set:

$$\begin{aligned} q &= \begin{pmatrix} q_1 & q_2 & \cdots & q_n \end{pmatrix} \\ \dot{q} &= \begin{pmatrix} \dot{q}_1 & \dot{q}_2 & \cdots & \dot{q}_n \end{pmatrix} \\ \ddot{q} &= \begin{pmatrix} \ddot{q}_1 & \ddot{q}_2 & \cdots & \ddot{q}_n \end{pmatrix} \\ z &= \begin{pmatrix} q & \dot{q}_1 & q_2 & \dot{q}_2 & \cdots & q_n & \dot{q}_n \end{pmatrix}^T \\ \dot{z} &= \begin{pmatrix} \dot{q}_1 & \ddot{q}_1 & \dot{q}_2 & \ddot{q}_2 & \cdots \dot{q}_n & \ddot{q}_n \end{pmatrix}^T \end{aligned} \tag{2.76}$$

Take jacobian operation (MATLAB supports "**jacobian**" function) of the kinematic energy T w.r.t. $\dot{q}$, we have:

$$r = \begin{pmatrix} \frac{\partial T}{\partial \dot{q}_1} & \cdots & \frac{\partial T}{\partial \dot{q}_n} \end{pmatrix} \tag{2.77}$$

$r(i)$ means the i-th components of r. Take jacobian operation of r w.r.t. z^T, we have:

$$J = \begin{pmatrix} \frac{\partial r(1)}{\partial q_1} & \frac{\partial r(1)}{\partial \dot{q}_1} & \cdots & \frac{\partial r(1)}{\partial q_n} & \frac{\partial r(1)}{\partial \dot{q}_n} \\ \frac{\partial r(2)}{\partial q_1} & \frac{\partial r(2)}{\partial \dot{q}_1} & \cdots & \frac{\partial r(2)}{\partial q_n} & \frac{\partial r(2)}{\partial \dot{q}_n} \\ \vdots & \vdots & \vdots & \vdots & \vdots \\ \frac{\partial r(n)}{\partial q_1} & \frac{\partial r(n)}{\partial \dot{q}_1} & \cdots & \frac{\partial r(n)}{\partial q_n} & \frac{\partial r(n)}{\partial \dot{q}_n} \end{pmatrix} = \begin{pmatrix} j_1 & j_2 & \cdots & j_n \end{pmatrix} \tag{2.78}$$

We can find that i-th row of J which takes the inner product with $\dot{z}$ is equal to $\frac{d}{dt}(\frac{\partial T}{\partial \dot{q}_i})$. Separate J into two matrices: M and B. M includes even columns of J. B includes odd columns of J. If n is an even number, we have:

$$\begin{aligned} M &= \begin{pmatrix} j_2 & j_4 & \cdots & j_n \end{pmatrix} \\ B &= \begin{pmatrix} j_1 & j_3 & \cdots & j_{n-1} \end{pmatrix} \end{aligned} \tag{2.79}$$

Take jacobian operation of the kinematic energy T w.r.t. q, we have:

$$QT = \begin{pmatrix} \frac{\partial T}{\partial q_1} & \cdots & \frac{\partial T}{\partial q_n} \end{pmatrix} \tag{2.80}$$

Take jacobian operation of the potential energy U w.r.t. q, we have:

$$QU = \begin{pmatrix} \frac{\partial U}{\partial q_1} & \cdots & \frac{\partial U}{\partial q_n} \end{pmatrix} \tag{2.81}$$

We have already got all components for Eqn. (2.74). Eqn. (2.74) can be written as:

$$M\ddot{q} = -B\dot{q} + QT^T - QU^T \tag{2.82}$$

If M^{-1} exists or the solver can find M^{-1}, we have,

$$\ddot{q} = M^{-1}(-B\dot{q} + QT^T - QU^T) \tag{2.83}$$

If we know the external force applied to the system, , Eqn. (2.82) could be modified as:

$$M\ddot{q} = -B\dot{q} + QT^T - QU^T + u \tag{2.84}$$

u is a matrix and includes the external inputs.

$$u = \begin{pmatrix} \vec{F}_{ncon} \cdot \vec{a}_1 \\ \vdots \\ \vec{F}_{ncon} \cdot \vec{a}_n \end{pmatrix} \tag{2.85}$$

We have:

$$\ddot{q} = M^{-1}(-B\dot{q} + QT^T - QU^T + u) \tag{2.86}$$

If there are other governing equations for the whole system, the additional rows could be applied in Eqn. (2.84) and the redundant rows should be subtracted. After the local linearization, if $\dot{q}$ doesn't appear on the right hand side of Eqn. (2.86) and coordinates are not coupled on the right hand side, we can use symbolic solver to extract the coordinates q and get:

$$\ddot{q} = Cq + Du \tag{2.87}$$

Let

$$\begin{aligned} x &= \begin{pmatrix} q & \dot{q} \end{pmatrix}^T \\ \dot{x} &= \begin{pmatrix} \dot{q} & \ddot{q} \end{pmatrix}^T \end{aligned} \tag{2.88}$$

The linearization state space is:

$$\dot{x} = \begin{pmatrix} 0_{n\times n} & I_{n\times n} \\ C & 0_{n\times n} \end{pmatrix} x + \begin{pmatrix} 0_{n\times 1} \\ D \end{pmatrix} u \tag{2.89}$$

Chapter 3

Control Basics

3.1 Linear System

A system is called a linear system if for every t_0 and every two state-input-output pairs

$$(x_i(t_0), u_i(t)) \rightarrow y_i(t) \quad \text{for i=1,2} \;\; t \geq t_0 \tag{3.1}$$

satisfy the additivity property and homogeneity property.

$$(x_1(t_0) + x_2(t_0), u_1(t) + u_2(t)) \rightarrow y_1(t) + y_2(t) \qquad t \geq t_0 \tag{3.2}$$

$$(\alpha x_i(t_0), \alpha u_i(t)) \rightarrow \alpha y_i(t) \quad \text{for i=1,2} \;\; t \geq t_0 \tag{3.3}$$

The additivity and homogeneity property can be combined as the superposition property [7].

3.2 Nonlinear System

If a system doesn't satisfy the superposition property, the system is called a nonlinear system. Euler's equations of rotation present a nonlinear system. The attitude control indeed deals with the nonlinear system. We can treat the nonlinear system as the linear system by the linearization at the interested point. However, the stability issue needs to be further studied. [26]

3.3 Stability

For the linear time-invariant system, the real parts of the eigenvalues of the state space matrix indicate if the system is stable or not. For the nonlinear system, we can use the Lyapunov theory [56] to investigate the stability

Definition 3.3.1. *The equilibrium state $x = 0$ is said to be stable, if for any $R > 0$, there exists $r > 0$, such that if $\|x(0)\| < r$, then $\|x(t)\| < R$ for all $t \geq 0$. Otherwise, the equilibrium point is unstable.*

Theorem 3.3.1 (**Local Stability**). *If, in a ball B_{R_o}, there exists a scalar function $V(x)$ with continuous first partial derivatives such that*

- *$V(x)$ is positive definite (locally in B_{R_o})*
- *$\dot{V}(x)$ is negative semi-definite (locally B_{R_o}) then the equilibrium point 0 is stable. If, actually, the derivative $\dot{V}(x)$ is locally negative definite in B_{R_o}, then the stability is asymptotic.*

When we prove the stability, Barbalat's lemma is useful.

Lemma 3.3.1. *(Barbalat)[56] If the differentiable function f(t) has a finite limit as $t \to \infty$, and if $\dot{f}$ is uniformly continuous, then $\dot{f}(t) \to 0$ as $t \to \infty$.*

Definition 3.3.2. *(Uniformly Continuous) A function g is said to be uniformly continuous on $[0, \infty)$, if $\forall R > 0, \exists \eta(R) > 0, \forall t_1 \geq 0, \forall t \geq 0, |t - t_1| < \eta \Rightarrow |g(t) - g(t_1)| < R$*

3.4 Controllability

3.4.1 Controllability for Linear Systems

Consider the n-dimensional p-input state equation[7]:

$$\dot{x} = Ax + Bu \tag{3.4}$$

where A and B are, respectively, $n \times n$ and $n \times p$ real constant matrices

Definition 3.4.1. *The state equation Eqn. (3.4) or pair (A, B) is said to be controllable if for any initial state $x(0) = x_0$ and any final state x_1, there exists the sequential inputs that transfers x_0 to x_1 in a finite time. Otherwise Eqn. (3.4) or (A,B) is said to be uncontrollable.*

3.4.2 Controllability for Nonlinear Systems

Define the system:

$$\dot{x} = f(x) + \sum_{i=1}^{m} g_i(x)u_i \tag{3.5}$$

is locally accessible about $x0$ if the accessibility distribution C spans n space, where n is the rank of x and C is defined by:

$$C = |g_1, g_2, ...g_m, [g_i, g_j], ..., [ad^k_{g_i}, g_j], ..., [f, g_i], ..., [ad^k_f, g_i], ...| \tag{3.6}$$

The g_i terms are analogous to the B terms. The $[g_i, g_j]$ terms are new terms from a nonlinear system. The $[f, g_i]$ terms is corresponding to the AB terms.
For any two column vectors, c_1 and c_2, the Lie bracket is defined:

$$\begin{bmatrix} c_1 & c_2 \end{bmatrix} := \frac{\partial c_2}{\partial x} c_1 - \frac{\partial c_1}{\partial x} c_2 \tag{3.7}$$

$\frac{\partial}{\partial x}$ means jacobian operation.

$$\frac{\partial c}{\partial x} = \begin{pmatrix} \frac{\partial c(1)}{\partial x_1} & \frac{\partial c(1)}{\partial x_2} & \cdots & \frac{\partial c(1)}{\partial x_n} \\ \cdots & \cdots & \cdots & \cdots \\ \frac{\partial c(n)}{\partial x_1} & \frac{\partial c(n)}{\partial x_2} & \cdots & \frac{\partial c(n)}{\partial x_n} \end{pmatrix} \tag{3.8}$$

Note: if $f(x) = 0$, then $\dot{x} = \sum_{i=1}^{m} g_i(x) u_i$ and if C has rank n, then the system is controllable.

3.5 Observability

3.5.1 Observability for Linear Systems

Consider the n-dimensional p-input q-output state equation [7]:

$$\begin{aligned} \dot{x} &= Ax + Bu \\ y &= Cx + Du \end{aligned} \tag{3.9}$$

Where A, B, C, and D are, respectively, $n \times n$, $n \times p$, $q \times n$ and $q \times p$ constant matrices.

Definition 3.5.1. *The state equation Eqn. (3.9) is said to be observable if for any unknown initial state x(0), there exits a finite $t_1 > 0$ such that the knowledge of the input u and the output y over $[0, t_1]$ suffices to determine uniquely the initial state x(0). Otherwise, the equation is said to be unobservable.*

3.5.2 Observability for Nonlinear Systems

Before the observability for nonlinear systems is defined, the mathematical tool must be introduced

Definition 3.5.2. *Let $f : \mathcal{R}^n \to \mathcal{R}^n$ be a vector field in $\mathcal{R}^n$, and $h : \mathcal{R}^n \to \mathcal{R}$ be a smooth scalar function. Then the Lie derivative of h with respect to f is:*

$$L_f h = \nabla h \cdot f = \frac{\partial h}{\partial x} \cdot f = \sum_{i=1}^{n} \frac{\partial h}{\partial x_i} f_i \tag{3.10}$$

$$f = [f_1(x), f_2(x), ..., f_n(x)]^T \tag{3.11}$$

$$\nabla h = [\frac{\partial h}{\partial x_1}, \frac{\partial h}{\partial x_2}, ..., \frac{\partial h}{\partial x_n}] \tag{3.12}$$

$$L_f^k h = \frac{\partial}{\partial x}[L_f^{k-1} h] \cdot f \tag{3.13}$$

For a nonlinear system [26]

$$\begin{aligned} \dot{x} &= f(x, u) \\ z &= h(x) = [h_1(x), h_2(x), ..., h_p(x)]^T \end{aligned} \tag{3.14}$$

The observability of a nonlinear system could be defined as the following statements.

Theorem 3.5.1. *Let G denote the set of all finite linear combinations of the Lie derivatives of $h_1, ..., h_p$ with respect to f for various values of u = constant. Let dG denote the set of all their gradients. If we can find n linearly independent vectors within dG, then the system is locally observable.*

The system is locally observable, that is distinguishable at a point x_0 if there exists a neighborhood of x_0 such that in this neighborhood , $x_0 \neq x_1 \Rightarrow z(x_0) \neq z(x_1)$ i.e. if the sensor readings are different, the states are different.

$$G = \begin{bmatrix} L_f^0 h_1 & ... & L_f^0 h_p \\ ... & ... & ... \\ L_f^{n-1} h_1 & ... & L_f^{n-1} h_p \end{bmatrix} \tag{3.15}$$

$$dG = \begin{bmatrix} dL_f^0 h_1 & ... & dL_f^0 h_p \\ ... & ... & ... \\ dL_f^{n-1} h_1 & ... & dL_f^{n-1} h_p \end{bmatrix} \tag{3.16}$$

Example: Assume ω_z is the only measurement of the rigid body and the moment of the inertia is diagonal. The observability is:

$$G = \begin{bmatrix} \omega_z \\ \dot{\omega}_z \\ \ddot{\omega}_z \end{bmatrix} = \begin{bmatrix} \omega_z \\ \frac{\omega_x \omega_y (J_1 - J_2)}{J_3} \\ \frac{\omega_y^2 \omega_z (J_1 - J_2)(J_2 - J_3)}{J_1 J_3} + \frac{\omega_x^2 \omega_z (J_1 - J_2)(J_3 - J_1)}{J_2 J_3} \end{bmatrix} \tag{3.17}$$

$$dG = \begin{bmatrix} 0 & 0 & 1 \\ \frac{\omega_y (J_1 - J_2)}{J_3} & \frac{\omega_x (J_1 - J_2)}{J_3} & 0 \\ \frac{2\omega_x \omega_z (J_1 - J_2)(J_3 - J_1)}{J_2 J_3} & \frac{2\omega_y \omega_z (J_1 - J_2)(J_2 - J_3)}{J_1 J_3} & \frac{\omega_y^2 (J_1 - J_2)(J_2 - J_3)}{J_1 J_3} + \frac{\omega_x^2 (J_1 - J_2)(J_3 - J_1)}{J_2 J_3} \end{bmatrix} \tag{3.18}$$

From Eqn. (3.18), we can find that if $J_1 = J_2$ or both ω_x and ω_y are zeros then the nonlinear system is unobservable.

3.5.3 Observer for Linear Systems

To design the observer for the linear system, just copy the original system [28]

$$\dot{\hat{x}} = A\hat{x} + Bu \tag{3.19}$$

The state estimation error is:

$$e := \hat{x} - x \tag{3.20}$$

From the time derivative of e, we have:

$$\dot{e} = A\hat{x} + Bu - (Ax + Bu) = Ae \tag{3.21}$$

If A is a stability matrix, no matter what input u, the error state converges. If A is not a stability matrix, we can construct Luenberger observer.

$$\begin{aligned} \dot{\hat{x}} &= A\hat{x} + Bu - L(\hat{y} - y) \\ \hat{y} &= c\hat{x} + Du \end{aligned} \tag{3.22}$$

L is also called output injection matrix gain $L \in \mathcal{R}^{n\times m}$[28]. We have:

$$\begin{aligned} \dot{e} &= A\hat{x} + Bu - L(\hat{y} - y) - (Ax + Bu) \\ \dot{e} &= (A - LC)e \end{aligned} \tag{3.23}$$

Theorem 3.5.2. *Consider the closed-loop state estimator Eqn (3.22). If the output injection matrix gain $L \in \mathcal{R}^{n\times m}$ makes $A - LC$ a stability matrix, then state error e converges to zero exponentially fast, for every input signal u*

3.5.4 Observer for Nonlinear Systems

General nonlinear observer methods are not used in the projects of this dissertation but the other methods to estimate the angular velocity are used. However, those general nonlinear observer methods are still mentioned for the completeness of this chapter. Several general categories of the nonlinear observer are [26]:

1. Stochastic nonlinear observer: a general method, also called "Extended Kalman Filter". Use a standard Kalman filter but with

$$\begin{aligned} A &= \frac{\partial f}{\partial x} \\ C &= \frac{\partial h}{\partial x} \end{aligned} \tag{3.24}$$

   at the operation point. The nonlinearities are treated as process noise.

2. Deterministic nonlinear observer:

a) Thau's method: Let the plant be:

$$\begin{aligned} \dot{x} &= Ax + g(t,u,z) + f(x) \\ z &= Mx \end{aligned} \tag{3.25}$$

Let the observer be:

$$\dot{\hat{x}} = A\hat{x} + g(t,u,z) + f(\hat{x}) + L(z - M\hat{x}) \tag{3.26}$$

Just tell us whether or not L gives asymptotically stable error dynamics.

- Raghavan's method: use the same observer structure of Thau's method but provide the constructive method for gains.

b) Geometric observers: observers with linearized error dynamics.

$$\begin{aligned} \dot{x} &= f(x) + g(x)u \\ y &= h(x) \end{aligned} \tag{3.27}$$

Find $z = \Phi(x)$ and convert the nonlinear system to:

$$\begin{aligned} \dot{z} &= Az + K(y,u) \\ y &= Cz \end{aligned} \tag{3.28}$$

The copy dynamics is:

$$\dot{\hat{z}} = A\hat{z} + K(y,u) + L(y - C\hat{z}) \tag{3.29}$$

The linear error dynamics is:

$$\begin{aligned} \dot{\tilde{z}} &= (A - LC)\tilde{z} \\ \hat{x} &= \Phi^{-1}(\hat{z}) \end{aligned} \tag{3.30}$$

We design $(A - LC)$ to make the error of z zero asymptotically. Then we can inverse the $\hat{z}$ to know x. [40] systematically presents the methods of finding the local diffeomorphism Φ

c) Sliding observers: It is the observer analog to sliding mode control and can deal with the imperfect models.

3.6 Linear Quadratic Regular

3.6.1 Feedback Invariants

Given a continuous-time LTI system

$$\begin{aligned} \dot{x} &= Ax + Bu \\ y &= Cx \\ x &\in \mathcal{R}^n, u \in \mathcal{R}^k, y \in \mathcal{R}^m \end{aligned} \tag{3.31}$$

[7] define a functional

$$H(x(\cdot); u(\cdot)) \tag{3.32}$$

that involves the control input and the system state. The value of this functional depends only on the initial condition $x(0)$ and not on the control input u.

Proposition 3.6.1. *(Feedback invariant) For every symmetric matrix P, the functional* $H(x(\cdot), u(\cdot)) := -\int_0^\infty (Ax(t)+Bu(t))'Px(t)+x(t)'P(Ax(t)+Bu(t)dt$ *is a feedback invariant for continuous time invariant system, as long as* $\lim_{t\to\infty} x(t) = 0$ *Proof:*

$$\begin{aligned} H(x(\cdot), u(\cdot)) &:= -\int_0^\infty (\dot{x}(t)'Px(t) + x(t)'P\dot{x}(t))dt \\ &= -\int_0^\infty \frac{d(x(t)'Px(t))}{dt}dt \\ &= x(0)'Px(0) - \lim_{t\to\infty} x(t)'Px(t) = x(0)'Px(0) \end{aligned} \tag{3.33}$$

Suppose a linear system with this structure[1]:

$$\begin{aligned} \dot{x} &= Ax + Bu \\ y &= Cx \\ z &= Gx + Hu \end{aligned} \tag{3.34}$$

$x \in \mathcal{R}^n, u \in \mathcal{R}^k, y \in \mathcal{R}^m$, and $z \in \mathcal{R}^l$. $z(t)$ is controlled output and is the interested state for the regulation. LQR control wants to make the cost function J_{LQR} as small as possible.

$$J_{LQR} := \int_0^\infty (z(t)'\bar{Q}z(t) + \rho u(t)'\bar{R}u(t))dt \tag{3.35}$$

J_{LQR} contains the energy of the controlled output: $z(t)$ and the energy of the control signal: $u(t)$. ρ is a trade-off between these two signals. Controller designer can decide which part $(z(t), u(t))$ needs more weighting. $\bar{Q}$ and $\bar{R}$ are the semi-definitive positive matrices ($\succeq 0$). Convert the general form with $z = Gx + Hu$. We have:

$$\begin{aligned} J_{LQR} &= \int_0^\infty ((Gx+Hu)'\bar{Q}(Gx+Hu) + \rho u(t)'\bar{R}u(t))dt \\ &= \int_0^\infty (x(t)'Qx(t) + u(t)'Ru(t) + 2x(t)'Nu(t))dt \end{aligned} \tag{3.36}$$

$$\begin{aligned} Q &= G'\bar{Q}G \\ R &= H'\bar{Q}H + \rho\bar{R} \\ N &= G'\bar{Q}H \end{aligned} \tag{3.37}$$

[1] H in Eqn. (3.34) is a matrix. $H(x(\cdot), u(\cdot))$ in Eqn. (3.33) is the feedback invariant. They have the different meanings.

Since $\bar{Q} \succeq 0$ and $\bar{R} \succeq 0$, we have $Q \succeq 0$ and $R \succeq 0$. The LQR criterion can be derived with the idea of the feedback invariant. $H(x(\cdot), u(\cdot))$

$$\begin{aligned} J_{LQR} &= \int_0^\infty (x'Qx + u'Ru + 2x'Nu)dt \\ &= H(x(\cdot), u(\cdot)) + \int_0^\infty (x'Qx + u'Ru + 2x'Nu + (Ax + Bu)'Px + x'P(Ax + Bu))dt \\ &= H(x(\cdot), u(\cdot)) + \int_0^\infty (x'(A'P + PA + Q)x + u'Ru + 2u'(B'P + N')x)dt \end{aligned} \tag{3.38}$$

and group the quadratic tern for u and x.

$$u'Ru + x'(PB + N)R^{-1}(B'P + N')x + 2u'(B'P + N')x = (u' + x'K')R(u + Kx) \tag{3.39}$$

$$K := R^{-1}(B'P + N') \tag{3.40}$$

J_{LQR} criterion becomes:

$$\begin{aligned} J_{LQR} = &H(x(\cdot), u(\cdot)) + \\ &\int_0^\infty (x'(A'P + PA + Q - (PB + N)R^{-1}(B'P + N'))x + (u' + x'K')R(u + Kx))dt \end{aligned} \tag{3.41}$$

If we can find the solution P for

$$A'P + PA + Q - (PB + N)R^{-1}(B'P + N') = 0 \tag{3.42}$$

Eqn. (3.42) is also called algebraic riccati equation (ARE), and the control signal is:

$$u = -Kx \tag{3.43}$$

then we have the minimum value of $J_{LQR} = H(x(\cdot), u(\cdot)) = x(0)'Px(0)$. The closed-loop system is:

$$\dot{x} = (A - BR^{-1}(B'P + N'))x \tag{3.44}$$

Theorem 3.6.1. *Assume that there exists a symmetric solution P to the Eqn. (3.42) for which $A - BR^{-1}(B'P + N')$ is a stationary matrix. Then the feedback law*

$$u := -Kx(t), \forall t \geq 0 \tag{3.45}$$

$$K := R^{-1}(B'P + N') \tag{3.46}$$

minimizes the LQR criterion and leads to

$$J_{LQR} = \int_0^\infty (x'Qx + u'Ru + 2x'Nu)dt = x(0)'Px(0) \tag{3.47}$$

3.6.2 Linear Quadratic Integrator

The state feedback control of LQR provides a good robust margin and has the optimal solution for the control output and the control signal. However, if the model is not perfect or there is a dead-zone for the actuator, the steady state error still happens. Using the strategy of the integral control can eliminate the steady state error. Linear quadratic integrator method (LQI) uses the concept of the LQR to find gains. The gains are computed from an augmented system with an additional state [72]. Fig. 3.1 shows the structure of LQI. The state and the integral of the error signal ($-y$) are feedback for the control signal. The new

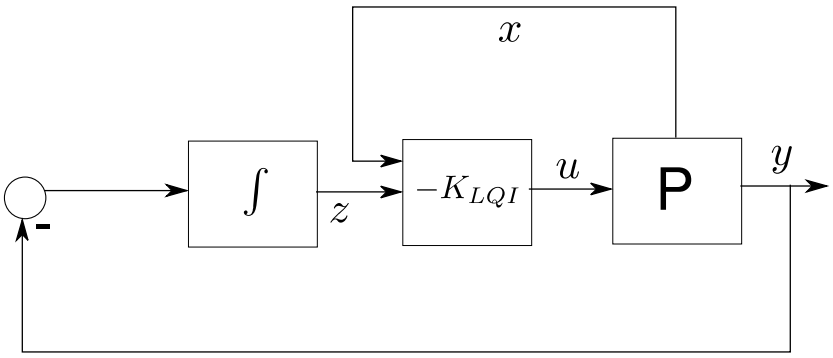

Figure 3.1: LQI Diagram

state space for the augmented system is in the Eqn. (3.48)

$$\begin{aligned}
\begin{pmatrix}\dot{x}\\ \dot{z}\end{pmatrix} &= \underbrace{\begin{pmatrix} A & 0_{3\times 1}\\ -C & 0\end{pmatrix}}_{A_{lqi}}\begin{pmatrix}x\\ z\end{pmatrix} + \underbrace{\begin{pmatrix}B\\ 0\end{pmatrix}}_{B_{lqi}} u\\
z &= -\int y\cdot dt \\
y &= \underbrace{\begin{pmatrix}C & 0\end{pmatrix}}_{C_{lqi}}\begin{pmatrix}x\\ z\end{pmatrix}
\end{aligned} \tag{3.48}$$

If the cross product tern N of ARE is zero, then ARE is:

$$A_{lqi}^T P + P A_{lqi} - P B_{lqi} R^{-1} B_{lqi}^T P + Q = 0 \tag{3.49}$$

and the controller gain K_{LQI} is:

$$K_{LQI} = R^{-1} B_{lqi}^T P \tag{3.50}$$

3.7 Adaptive Control

If the system has uncertain parameters and the controller is not adaptive to those parameters, the performance cannot be achieved as expected. Moreover, the system may have the

stability issue. The spirit of the adaptive control is to do the system identification and construct the adaptive controller on-line. The estimation of the parameters maybe not converge to the actual parameters but it still can regulate the controlled output (z). The adaptive control is more suitable for the unknown parameters drifting around nominal values or a slow time varying system.

3.7.1 Adaptive Control for Linear System

3.7.1.1 System Identification

3.7.1.1.1 Linear Regressor Form We have the uncertain parameters ΔA and ΔB in the system.

$$\dot{x} = (A + \Delta A)x + (B + \Delta B)u \tag{3.51}$$

Assume there is no issue for the observability, x and u are available. Since $\dot{x}$ is unavailable for the measurement, we can divide $\dot{x}$ a one order filer $\frac{1}{s+\lambda}$ to make the information of $\dot{x}$ available. s is the parameter for the Laplace transform. We have:

$$\frac{s}{s+\lambda}x = \frac{A + \Delta A}{s+\lambda}x + \frac{B + \Delta B}{s+\lambda}u \tag{3.52}$$

$$\frac{s}{s+\lambda}x = x - \frac{\lambda}{s+\lambda}x \tag{3.53}$$

Define:

$$\frac{1}{s+\lambda}x = x_f \tag{3.54}$$

$$\frac{1}{s+\lambda}u = u_f \tag{3.55}$$

We have:

$$\underbrace{x - \lambda x_f - Ax_f - Bu_f}_{\text{Define:}y} = \Delta A x_f + \Delta B u_f \tag{3.56}$$

For each "i" row,

$$\begin{aligned} y_i(t) &= \underbrace{\Delta A_i}_{\text{i-th row of}\Delta A} x_f + \underbrace{\Delta B_i}_{\text{i-th row of}\Delta B} u_f \\ &= \underbrace{\theta_i^T}_{\text{n unknow paremeters}} \phi(t) \end{aligned} \tag{3.57}$$

We want to estimate θ_i of i-th row for uncertain parameters. Take n measurement

$$\begin{aligned} Y_i = \begin{pmatrix} y_i(t_1) \\ \vdots \\ y_i(t_n) \end{pmatrix} &= \underbrace{\begin{pmatrix} \phi(t_1)^T \\ \vdots \\ \phi(t_n)^T \end{pmatrix}}_{n \times n} \underbrace{\theta_i}_{n \times 1} \\ &= \Phi \theta_i \end{aligned} \tag{3.58}$$

The uncertain parameter θ_i is:

$$\theta_i = \Phi^{-1} Y \tag{3.59}$$

Eqn. (3.59) could be used to get the uncertain parameters directly. However, this method takes the time and cannot be achieved on-line and needs to estimate each row. We can rewrite a more general form of the regressor for SISO system. $G(s)$ is the transfer function.

$$y = G(s)u = \frac{b_{n-1}s^{n-1} + \cdots + b_0}{s^n + a_{n-1}s^{n-1} + \cdots + a_1 s + a_0} u = \frac{B(s)}{A(s)} u \tag{3.60}$$

We have:

$$A(s)y = B(s)u \tag{3.61}$$

Design a linear system:

$$\dot{\zeta} = \Lambda\zeta + \mathcal{B}\xi \tag{3.62}$$

Where Λ and $\mathcal{B}$ are:

$$\Lambda = \begin{pmatrix} 0 & 1 & 0 & \cdots & 0 \\ 0 & 0 & 1 & \cdots & 0 \\ \vdots & \vdots & \vdots & \vdots & \vdots \\ -\lambda_0 & -\lambda_1 & -\lambda_2 & \cdots & -\lambda_{n-1} \end{pmatrix} \in \mathcal{R}^{n\times n} \quad \mathcal{B} = \begin{pmatrix} 0 \\ \vdots \\ \vdots \\ 1 \end{pmatrix} \in \mathcal{R}^{n\times 1} \tag{3.63}$$

Its characteristic equation is:

$$F(s) = det(sI - \Lambda) = s^n + \lambda_{n-1}s^{n-1} + \cdots + \lambda_1 s + \lambda_0 \tag{3.64}$$

We have:

$$\zeta = (sI - \Lambda)^{-1}\mathcal{B}\xi = \begin{pmatrix} \frac{1}{F(s)}\xi \\ \frac{s}{F(s)}\xi \\ \vdots \\ \frac{s^{n-1}}{F(s)}\xi \end{pmatrix} \tag{3.65}$$

Divide Eqn. (3.61) with a stable polynomial $F(s)$.

$$\frac{A(s)}{F(s)}y = \frac{B(s)}{F(s)}u \tag{3.66}$$

$$\begin{aligned} y &= \frac{F(s) - A(s)}{F(s)}y + \frac{B(s)}{F(s)}u \\ &= \frac{(\lambda_{n-1} - a_{n-1})s^{n-1} + \cdots + (\lambda_0 - a_0)}{F(s)}y + \frac{b_{n-1}s^n - 1 + \cdots + b_0}{F(s)}u \end{aligned} \tag{3.67}$$

Arranging the coefficients, we have:

$$y = (\lambda_0 - a_0, \cdots, \lambda_{n-1} - a_{n-1}, b_0, \cdots, b_{n-1}) \begin{pmatrix} \frac{1}{F(s)}y \\ \vdots \\ \frac{s^{n-1}}{F(s)}y \\ \frac{1}{F(s)}u \\ \vdots \\ \frac{s^{n-1}}{F(s)}u \end{pmatrix} \tag{3.68}$$

$$\begin{aligned} \theta_y &= (\lambda_0 - a_0, \cdots, \lambda_{n-1} - a_{n-1})^T \\ \theta_u &= (b_0, \cdots, b_{n-1})^T \\ \phi_y &= \begin{pmatrix} \frac{1}{F(s)}y & \cdots & \frac{s^{n-1}}{F(s)}y \end{pmatrix}^T \\ \phi_u &= \begin{pmatrix} \frac{1}{F(s)}u & \cdots & \frac{s^{n-1}}{F(s)}u \end{pmatrix}^T \\ \theta &= \begin{pmatrix} \theta_y \\ \theta_u \end{pmatrix} \\ \phi &= \begin{pmatrix} \phi_y \\ \phi_u \end{pmatrix} \end{aligned} \tag{3.69}$$

We can get:

$$y = \begin{pmatrix} \theta_y^T & \theta_u^T \end{pmatrix} \begin{pmatrix} \phi_y \\ \phi_u \end{pmatrix} = \theta^T \phi \tag{3.70}$$

ϕ is available with the idea of Eqn. (3.65). We can get:

$$\begin{aligned} \dot{\phi}_y(t) &= \Lambda \phi_y(t) + \mathcal{B} y \\ \dot{\phi}_u(t) &= \Lambda \phi_u(t) + \mathcal{B} u \end{aligned} \tag{3.71}$$

$$\Rightarrow \dot{\phi} = \begin{pmatrix} \Lambda + \mathcal{B}\theta_y^T & \mathcal{B}\theta_u^T \\ 0 & \Lambda \end{pmatrix} \begin{pmatrix} \phi_y \\ \phi_u \end{pmatrix} + \begin{pmatrix} 0 \\ \mathcal{B} \end{pmatrix} u \quad \text{For the convenience, set} \quad \phi(0) = 0 \tag{3.72}$$

3.7.1.1.2 On Line Identification Methods $\hat{\theta}$ could be updated from the following methods.

1. **Gradient Algorithm:**

$$\dot{\hat{\theta}} = \rho(y(t) - \hat{y}(t))\phi(t), \quad \rho > 0, \quad \hat{\theta}(0), \text{ arbitrary} \tag{3.73}$$

Eqn. (3.73) guarantees

$$\lim_{t \to \infty} \hat{y}(t) = y(t) \tag{3.74}$$

If regressor $\phi \in \mathcal{R}^n$ is persistently exciting (PE):

$$\int_t^{t+\Delta} \phi(\tau)\phi(\tau)^T d\tau \geq \alpha I > 0 \quad \text{for some } \Delta \text{ and } \alpha > 0 \tag{3.75}$$

, where I is the identity matrix, then $\lim_{t\to\infty} \hat{\theta} = \theta$ converges exponentially.

2. **Normalized Gradient Algorithm:**

$$\dot{\hat{\theta}} = \frac{\rho(y - \hat{y})\phi}{1 + \alpha \left\|\phi\right\|^2} \quad \alpha > 0 \tag{3.76}$$

3. **Batch Algorithm (off-line):** We can also use Batch algorithm to estimate θ. Batch algorithm is one kind of the least square (LS) algorithm. Define the cost function $J(\hat{\theta})$:

$$\begin{aligned} J(\hat{\theta}) &= \int_0^t |y(\tau) - \hat{\theta}^T\phi|^2 d\tau \\ &= \int_0^t |\theta^T\phi - \hat{\theta}^T\phi|^2 d\tau \end{aligned} \tag{3.77}$$

Take the derivative w.r.t $\hat{\theta}$ for $J(\hat{\theta})$ and find the extreme value.

$$\frac{\partial J(\hat{\theta})}{\partial \hat{\theta}} = 0 \tag{3.78}$$

$$\Rightarrow \int_0^t \phi(\tau)(y(\tau) - \phi(\tau)^T\hat{\theta})d\tau \tag{3.79}$$

$$\Rightarrow \hat{\theta}(t) = (\int_0^t \phi(t)\phi(t)^T d\tau)^{-1}(\int_0^t y(\tau)\phi(\tau)d\tau) \tag{3.80}$$

4. **Recursive algorithm:** Set

$$P(t)^{-1} = \int_0^t \phi(\tau)\phi(\tau)^T d\tau \tag{3.81}$$

We know:

$$\begin{aligned} PP^{-1} &= I \\ \dot{P}P^{-1} + P\dot{P}^{-1} &= 0 \\ \dot{P} &= -P\dot{P}^{-1}P \\ \dot{P} &= -P\phi(t)\phi(t)^T P \end{aligned} \tag{3.82}$$

With the idea of Batch algorithm, we have:

$$\hat{\theta}(t) = P(t) \int_0^t y(\tau)\phi(\tau)d\tau \tag{3.83}$$

$$\begin{aligned}
\dot{\hat{\theta}}(t) &= \dot{P}(t) \int_0^t y(\tau)\phi(\tau)d\tau + P(t)y(t)\phi(t) \\
&= -P(t)\dot{P}(t)^{-1}P(t) \int_0^t y(\tau)\phi(\tau)d\tau + P(t)y(t)\phi(t) \\
&= -P(t)\dot{P}(t)^{-1}\hat{\theta}(t) + P(t)y(t)\phi(t) \\
&= -P(t)\phi(t)\phi(t)^T(t)\hat{\theta}(t) + P(t)y(t)\phi(t) \\
&= P(t)\phi(t)(y - \phi(t)^T\hat{\theta})
\end{aligned} \tag{3.84}$$

If we design a scalar r for controlling the amount of $\dot{\theta}$, the updated law for the recursive algorithm is:

$$\begin{aligned}
\dot{\hat{\theta}}(t) &= rP(t)\phi(t)(y - \phi(t)^T\hat{\theta}) \\
\dot{P} &= -rP\phi(t)\phi(t)^T P
\end{aligned} \tag{3.85}$$

Eqn .(3.85) has the problem in the rate of the convergence. We can reset covariance matrix $P(t)$ periodically.

$$P(kT^+) = P_0 \tag{3.86}$$

If $\theta(t)$ is time varying, we can set a window and weight the current measurement.

$$\hat{\theta}(t) = P(t) \int_0^t e^{-\alpha(t-\tau)} y(\tau)\phi(\tau)d\tau \tag{3.87}$$

$$P(t)^{-1} = \int_0^t e^{-\alpha(t-\tau)} \phi(\tau)\phi(\tau)^T d\tau \tag{3.88}$$

The recursive algorithm becomes:

$$\begin{aligned}
\dot{\hat{\theta}}(t) &= rP(t)\phi(t)(y - \phi(t)^T\hat{\theta}) \\
\dot{P} &= \alpha P - rP\phi(t)\phi(t)^T P \\
P(kT^+) &= P_0
\end{aligned} \tag{3.89}$$

To prevent unbounded regressor $\phi(t)$, we can use the normalized recursive algorithm:

$$\begin{aligned}
\dot{\hat{\theta}}(t) &= \frac{rP(t)\phi(t)(y - \phi(t)^T\hat{\theta})}{1 + \beta\phi^T P\phi} \\
\dot{P} &= \frac{-rP\phi(t)\phi(t)^T P}{1 + \beta\phi^T P\phi} \\
P(kT^+) &= P_0 \quad \beta > 0
\end{aligned} \tag{3.90}$$

5. **Kalman Filter Estimation:** Kalman filter can estimate the state of the linear time variant (LTV) system.

$$\begin{aligned} \dot{x}(t) &= A(t)x + B(t)u + n_1 \\ y &= C(t)x + n_2 \end{aligned} \tag{3.91}$$

n_1 and n_2 are noise. The covariance are:

$$\begin{aligned} V_1 &= E\{n_1(t)n_1(t)^T\} \\ V_2 &= E\{n_2(t)n_2(t)^T\} \end{aligned} \tag{3.92}$$

The observer design is:

$$\begin{aligned} \dot{\hat{x}} &= A(t)\hat{x} + B(t)u + L(t)(y - C(t)\hat{x}) \\ L(t) &= Q(t)C(t)^T V_2^{-1} \end{aligned} \tag{3.93}$$

Forward riccati equation:

$$\begin{aligned} \dot{Q}(t) &= A(t)Q(t) + Q(t)A(t)^T + V_1 - Q(t)C(t)^T V_2^{-1} C(t)Q(t) \\ Q(0) &= Q_0 > 0 \end{aligned} \tag{3.94}$$

Using the Kalman filter to estimate $\hat{\theta}$, set $A(t) = 0$, $B(t) = 0$ and $C(t) = \phi^T(t)$, we have:

$$\begin{aligned} \dot{\hat{\theta}} &= Q(t)\phi V_2^{-1}(y - \phi^T\hat{\theta}) \\ L &= QC(t)^T V_2^{-1} \\ \dot{Q} &= V_1 - Q\phi V_2^{-1}\phi^T Q \\ Q(0) &= Q_0 > 0 \end{aligned} \tag{3.95}$$

3.7.1.2 Self-Tuning Control

The self-tuning control uses the linear regressor to update the unknown parameters of the system and the controller recalculated gains based on those estimated parameters. The self-tuning doesn't need the minimum phase of the system but the system may be unstabilizable.

3.7.1.2.1 Adaptive LQ Control [8] Assume the system has the structure in Eqn. (3.51), updated gains of LQ control is based on the updated system: $(A + \Delta\hat{A}, B + \Delta\hat{B}) = (\hat{A}, \hat{B})$.

$$\begin{aligned} u &= -\hat{K}x \\ \hat{K} &= R^{-1}\hat{B}^T\hat{P} \end{aligned} \tag{3.96}$$

The system can be written as:

$$\begin{aligned}\dot{x} &= (A+\Delta A-(B+\Delta B)\hat{K})x \\ &= (A+\Delta\hat{A}-(B+\Delta\hat{B})\hat{K})x+((\Delta A-\Delta\hat{A})-(\Delta B-\Delta\hat{B})\hat{K})x \\ &= \underbrace{(A+\Delta\hat{A}-(B+\Delta\hat{B})\hat{K})}_{\hat{A}_k}x+((\Delta A-\Delta\hat{A})x+(\Delta B-\Delta\hat{B})u) \\ &= \hat{A}_k x+\tilde{\theta}^T\phi_0(t)\end{aligned} \tag{3.97}$$

$$\phi_0=\begin{pmatrix}x\\u\end{pmatrix} \quad \text{and let } (\phi_0)_f=\phi=\frac{1}{s+\lambda}\begin{pmatrix}x\\u\end{pmatrix} \tag{3.98}$$

$\tilde{\theta}^T$ is not single row but a $n\times(n+1)$ matrix. To study the stability, we need to use swapping lemma [53].

Lemma 3.7.1. *Swapping lemma*
Let ϕ,w: $\mathcal{R}_+\to\mathcal{R}^n$ and ϕ be differentiable. Let $\hat{H}$ be a proper rational transfer function. If $\hat{H}$ is stable, with minimal realization

$$\hat{H}=c^T(sI-a)^{-1}b+d \tag{3.99}$$

then

$$\hat{H}(w^T\phi)-\hat{H}(w^T)\phi=\hat{H}_c(\hat{H}_b(w^T)\dot{\phi}) \tag{3.100}$$

where

$$\hat{H}_b=(sI-a)^{-1}b \quad \hat{H}_c=-c^T(sI-a)^{-1} \tag{3.101}$$

Define a stable transfer function:

$$\hat{H}=\frac{1}{s+\lambda} \quad ,a=-\lambda,b=1,c=1,d=0 \tag{3.102}$$

$$v_f=\frac{1}{s+\lambda}v=\hat{H}(v) \tag{3.103}$$

Although $\hat{A}$ is not a row vector, we use the swapping lemma row by row and get Eqn. (3.104):

$$\frac{1}{s+\lambda}(\hat{A}x)=\hat{A}\frac{1}{s+\lambda}x-\frac{1}{s+\lambda}[\dot{\hat{A}}\frac{1}{s+\lambda}x] \tag{3.104}$$

Let $()_f$ is a linear operator for $\frac{1}{s+\lambda}$. Eqn. (3.104) can be modified as:

$$(\hat{A}x)_f=\hat{A}x_f-\frac{1}{s+\lambda}[\dot{\hat{A}}x_f] \tag{3.105}$$

Lemma 3.7.2. *Let $\hat{H}$ is stable. If $u \in L_2$ or $u \in L_1$, then $y = \hat{H}(u) \to 0$ as $t \to \infty$*

With Lemma. (3.7.2), we can prove that if $\left\| \dot{\hat{A}}(\tau) \right\| \in L_1$ or L_2

$$(\hat{A}x)_f = \hat{A}x_f + \beta(t) \left\| x_f \right\|_{\infty,t} \quad t \to \infty \quad \beta(t) \to 0 \tag{3.106}$$

$\left\| x_f \right\|_{\infty,t}$ means the infinity norm of x_f during the interval $[0, t]$. We can also show that:

$$\frac{e}{1 + \left\| \phi \right\|_{\infty,t}} = \frac{\tilde{\theta}^T \phi}{1 + \left\| \phi \right\|_{\infty,t}} \in L_2 \tag{3.107}$$

We can use Barbalat lemma to prove:

$$e \in L_2 \quad \text{and} \quad \dot{e} \in L_\infty \quad e \to 0, \;\; t \to \infty \tag{3.108}$$

We can also prove:

$$\begin{aligned} u &= -\hat{K}x \\ \to u_f &= (-\hat{K}x)_f \\ &= -\hat{K}x_f + \alpha_3 \left\| x_f \right\|_{\infty,t} \end{aligned} \tag{3.109}$$

$$\dot{\hat{K}} = R^{-1}\dot{\hat{B}}\hat{P} + R^{-1}\hat{B}\dot{\hat{P}} \in L_2 \;\; \text{so we have } \alpha_3 \to 0, t \to \infty \tag{3.110}$$

and

$$\left\| \phi \right\|_{\infty,t} = \left\| \begin{pmatrix} x_f \\ u_f \end{pmatrix} \right\|_{\infty,t} \leq \left\| \begin{pmatrix} 1 \\ -\hat{K} + \alpha_3 \end{pmatrix} \right\|_\infty \left\| (x_f) \right\|_{\infty,t} \leq M \left\| (x_f) \right\|_{\infty,t} \tag{3.111}$$

M is some boundary for a $\left\| . \right\|_\infty$. Dividing Eqn. (3.97) with a stable filter $\frac{1}{s+\lambda}$ and use Eqn. (3.106) Eqn. (3.110), we have:

$$\begin{aligned} (\dot{x})_f &= (\hat{A}_k x)_f + (\tilde{\theta}^T \phi_0)_f \\ &= \hat{A}_k x_f + \alpha_1(t) \left\| x_f \right\|_{\infty,t} + \tilde{\theta}^T \phi + \alpha_2(t) \left\| \phi \right\|_{\infty,t} \end{aligned} \tag{3.112}$$

Set a Lyapunov candidate:

$$V(t) = x_f^T \hat{P} x_f \tag{3.113}$$

After lots of computation and using the results of Eqn. (3.112), Eqn. (3.107),Eqn. (3.112) we get:

$$V(t) \leq e^{-\sigma t} V(0) + \gamma_1 \left\| V \right\|_{\infty,t} + \gamma_2 \left\| V \right\|_{\infty,t}^{\frac{1}{2}} \tag{3.114}$$

As $t \to \infty$, $e^{-\sigma t} \to 0$ $\gamma_1 \to 0$ and $\gamma_2 \to 0$, we have $V(t) \to 0$. That shows $x_f \to 0$. We know $x_f = \frac{1}{s+\lambda}$x. Using Eqn. (3.111), Eqn. (3.112), we have

$$\begin{aligned} x &= \dot{x}_f + \lambda x_f \\ &= \hat{A}_k x_f + \tilde{\theta}^T \phi + \alpha_1 \left\| x_f \right\|_{\infty,t} + \alpha_2 \left\| \phi \right\|_{\infty,t} + \lambda x_f \\ &= 0 \quad \text{for } t \to \infty \end{aligned} \tag{3.115}$$

It shows with adaptive LQ control, x converges to zero.

3.7.1.3 Model Reference Adaptive Control (MRAC)

The model reference control directly changes the controller gains and the system is always stabilizable but needs minimum phase of the system. The stability for the MRAC can be referred to in [60]. For a linear system:

$$y = \frac{K_p B(s)}{A(s)} u \tag{3.116}$$

$dim(A) = n$ and $dim(B) = m$, A and B are monic polynomial. Assume the plant satisfies the following conditions:

1. minimum phase, system zeros $\in C^-$, C^{-1} means the field which is in the complex plane with the negative real part.
2. the sign of K_p is known.
3. The relative degree r is known.
4. An upper bound of n is known

The reference model is:

$$y_m = \frac{K_m B_m(s)}{A_m(s)} u_m \tag{3.117}$$

Assume the reference model satisfied the following conditions:

1. the reference model is the minimum phase
2. The reference model is asymptotic stable
3. $dim(A_m) - dim(B_m) \geq dim(A) - dim(B)$
4. u_m is bounded.

Fig. 3.2 shows the model reference structure. The plant transfer function is $w_p(s)$. We design $w_1(s)$, $w_2(s)$ and r_o and make the final transfer function from u_m to y as the transfer function $w_m(s)$. F is a stable polynomial.

$$\begin{aligned} w_1 &= \frac{D}{F} = \frac{D'}{F} + h = \frac{d_{n-2}s^{n-2} + \cdots + d_1 s + d_0}{s^{n-1} + f_{n-2}s^{n-2} + \cdots + f_1 s + f_0} + h \\ w_2 &= \frac{C}{F} = \frac{c_{n-2}s^{n-2} + \cdots + c_1 s + c_0}{s^{n-1} + f_{n-2}s^{n-2} + \cdots + f_1 s + f_0} \end{aligned} \tag{3.118}$$

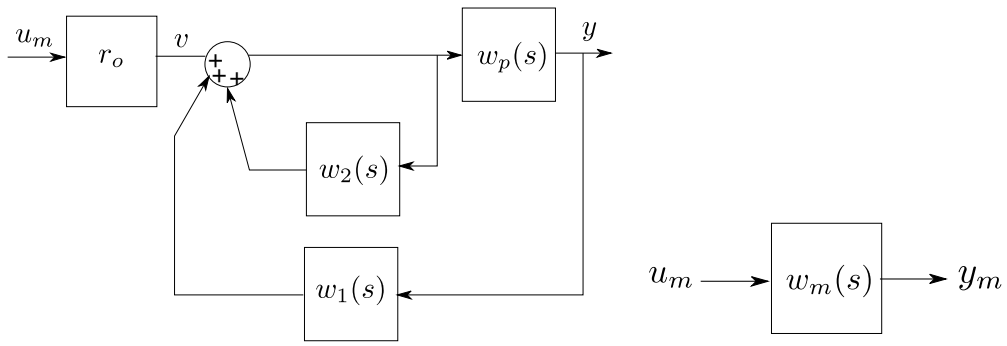

(a) Model Reference Structure (b) Reference Model

Figure 3.2: Model Reference Diagram

The transfer function from v to y is:

$$\begin{aligned} y &= \frac{\frac{1}{1-w_2}w_p}{1-\frac{w_p}{1-w_2}w_1}v \\ &= \frac{w_p}{1-w_2-w_1w_p}v \\ &= \frac{FBK_p}{A(F-C)-DBK_p}v \end{aligned} \tag{3.119}$$

If we can design:

- $F = B_m\lambda$, λ is a stable polynomial, $dim(\lambda) = n-m-1$. B_m is the desired zero.
- $A(F-C) - DBK_p = A_mB\lambda$
- $r_o = \frac{K_m}{K_p}$

Then we can have:

$$y = \frac{B_m\lambda BK_p}{A_mB\lambda}v = \frac{B_m}{A_m}K_pv = \frac{B_m}{A_m}K_pr_ou_m = w_m(s)u_m \tag{3.120}$$

To realize the controller and construct the linear regressor form, we can build ϕ_1 and ϕ_2 from Eqn. (3.71). and

$$\Lambda = \begin{pmatrix} 0 & 1 & 0 & \cdots & 0 \\ 0 & 0 & 1 & \cdots & 0 \\ \vdots & \vdots & \vdots & \vdots & \vdots \\ -f_0 & -f_1 & -f_2 & \cdots & -f_{n-2} \end{pmatrix} \in \mathcal{R}^{(n-1)\times(n-1)} \quad \mathcal{B} = \begin{pmatrix} 0 \\ \vdots \\ 1 \end{pmatrix} \in \mathcal{R}^{(n-1)\times 1} \tag{3.121}$$

$$\begin{aligned}\phi_1 &= \begin{pmatrix}\frac{1}{F(s)}y & \cdots & \frac{s^{n-2}}{F(s)}y\end{pmatrix}^T \\ \phi_2 &= \begin{pmatrix}\frac{1}{F(s)}u & \cdots & \frac{s^{n-2}}{F(s)}u\end{pmatrix}^T\end{aligned} \tag{3.122}$$

We get:

$$\begin{aligned}w_1 y &= (\frac{d_{n-2}s^{n-2}+\cdots+d_1 s+d_0}{s^{n-1}+f_{n-2}s^{n-2}+\cdots+f_1 s+f_0})y + hy = [d_0, d_1, \cdots, d_{n-2}]\phi_1 + hy = d^T\phi_1 + hy \\ w_2 u &= (\frac{c_{n-2}s^{n-2}+\cdots+c_1 s+c_0}{s^{n-1}+f_{n-2}s^{n-2}+\cdots+f_1 s+f_0})u = [c_0, c_1, \cdots, c_{n-2}]\phi_2 = c^T\phi_2\end{aligned} \tag{3.123}$$

control signals

$$\begin{aligned}u &= v + w_1 y + w_2 u \\ &= v + hy + d^T\phi_1 + c^T\phi_2 \\ &= r_o u_m + \begin{pmatrix}h^T & d^T & c^T\end{pmatrix}\begin{pmatrix}y & \phi_1 & \phi_2\end{pmatrix}^T \\ &= \theta^T\phi\end{aligned} \tag{3.124}$$

Where:

$$\theta = \begin{pmatrix}r_o \\ h \\ d \\ c\end{pmatrix} = \begin{pmatrix}r_0 \\ \theta_0\end{pmatrix} \quad \text{and} \quad \phi = \begin{pmatrix}u_m \\ y \\ \phi_1 \\ \phi_2\end{pmatrix} = \begin{pmatrix}u_m \\ \phi_0\end{pmatrix} \tag{3.125}$$

The state space $(A, B, C, 0)$ of the plant is:

$$\begin{aligned}\dot{x} &= Ax + Bu \\ y &= Cx\end{aligned} \tag{3.126}$$

Include the dynamics of ϕ_1 and ϕ_2, we can get:

$$\begin{aligned}\dot{\tilde{x}} &= \begin{pmatrix}\dot{x} \\ \dot{\phi}_1 \\ \dot{\phi}_2\end{pmatrix} = \begin{pmatrix}A & 0 & 0 \\ \mathcal{B}C & \Lambda & 0 \\ 0 & 0 & \Lambda\end{pmatrix}\begin{pmatrix}x \\ \phi_1 \\ \phi_2\end{pmatrix} + \begin{pmatrix}B \\ 0 \\ \mathcal{B}\end{pmatrix}u \quad \text{,insert} \quad u = v + hy + d^T\phi_1 + c^T\phi_2 \\ &= \underbrace{\begin{pmatrix}A+BhC & Bd^T & BC^T \\ \mathcal{B}C & \Lambda & 0 \\ \mathcal{B}hc & \mathcal{B}d^T & \mathcal{B}c^T+\Lambda\end{pmatrix}}_{\bar{A}}\begin{pmatrix}x \\ \phi_1 \\ \phi_2\end{pmatrix} + \underbrace{\begin{pmatrix}B \\ 0 \\ \mathcal{B}\end{pmatrix}}_{\bar{B}}v \\ y &= \underbrace{\begin{pmatrix}c & 0 & 0\end{pmatrix}}_{\bar{C}}\begin{pmatrix}x \\ \phi_1 \\ \phi_2\end{pmatrix} = \bar{C}(sI-\bar{A})^{-1}\bar{B}v\end{aligned} \tag{3.127}$$

if there are no uncertain parameters $y = w_m(s)u_m = w_m(s)\frac{K_p}{K_m}v$, then $\bar{C}(sI - \bar{A})^{-1}\bar{B} = w_m(s)\frac{K_p}{K_m}$. Right now, the plant includes the dynamics of x, ϕ_1 and ϕ_2.

Insert the dynamics of the control signal $u = \hat{r}_0 u_m + \hat{\theta}_0^T \phi_0$ and let $\tilde{\theta}_0 = \hat{\theta}_0 - \theta_0$, we have the new state space for the plant:

$$\begin{aligned} \dot{\bar{x}} &= \bar{A}\bar{x} + \bar{B}(\hat{r}_0 u_m + \tilde{\theta}_0^T \phi_0) \\ y &= \bar{C}\bar{x} \end{aligned} \tag{3.128}$$

The reference model is:

$$\begin{aligned} \dot{\bar{x}}_m &= \bar{A}\bar{x}_m + \bar{B}v_m \\ y_m &= \bar{C}\bar{x}_m \end{aligned} \tag{3.129}$$

Choose $v_m = r_0 u_m$. The error dynamics is:

$$\dot{\tilde{x}} = \bar{A}\tilde{x} + \bar{B}\tilde{\theta}^T \phi \tag{3.130}$$

The definition of θ and ϕ is the same in Eqn. (3.125). The plant has the parameters with Λ, c^T, d^T and uses $\tilde{\theta}$ in control signals to compensate for the uncertainty.

Definition 3.7.1. *(Strictly Positive Real(SPR))[56] A transfer function $h(p)$ is positive real if $Re[h(p)] \geq 0$ for all $Re[p] \geq 0$ It is strictly positive real if $h(p-\epsilon)$ is positive real for some $\epsilon > 0$*

$$h(p) = \frac{b_m p^m + \cdots + b_0}{p^n + a_{n-1}p^{n-1} + \cdots + a_0} \tag{3.131}$$

$h(p)$ is for single input and single output and $n \geq m$

The update law of $\hat{\theta}$ depends on the relative degree of the plant in Eqn. (3.127).

1. $r = 1$, make $w_m(s)$ SPR

$$\dot{\hat{\theta}} = -M\tilde{y}\phi \tag{3.132}$$

   M is a positive definite matrix.

2. $r = 2$, design $L(s) = s + \lambda$ and make $w_m(s)L(s)$ SPR, control signal:

$$u = L(s)\hat{\theta}^T L(s)^{-1}\phi \tag{3.133}$$

$$\dot{\hat{\theta}} = -M\tilde{y}\psi \tag{3.134}$$

$$\dot{\psi} = -\lambda\psi + \phi \tag{3.135}$$

3. $r \geq 2$, let:

$$\varepsilon = \hat{\theta}^T w_m(s)\phi - w_m(s)\hat{\theta}^T\phi \tag{3.136}$$

$$\zeta = w_m(s)\phi \tag{3.137}$$

Tracking error is:

$$e = r_0\tilde{\theta}^T\zeta - r_0\varepsilon \tag{3.138}$$

$$\epsilon = r_0\tilde{\theta}^T\zeta + \tilde{r}\varepsilon \quad \tilde{r} = \hat{r} - r_0 \tag{3.139}$$

$$m = 1 + \|\zeta\|^2 + \varepsilon^2 \tag{3.140}$$

The updated law is:

$$\dot{\hat{\theta}} = -sgn(r_0)M\epsilon\zeta/m^2 \tag{3.141}$$

$$\dot{\hat{r}} = -\alpha\epsilon\varepsilon/m^2 \quad \alpha > 0 \tag{3.142}$$

Note: $\hat{\theta}$ includes the estimation of r_0 and $\hat{r}$ also estimates r_0.

3.7.2 Adaptive Control for Nonlinear System

Consider a SISO nonlinear system [26]

$$\begin{aligned} \dot{x} &= f(x) + g(x)u \\ y &= h(x) \ \text{ relative degree } = r \end{aligned} \tag{3.143}$$

The relative degree means that control signals appear in the ordinary differential equation after y takes r time derivatives.

$$\frac{d^r y}{dt} = a(x) + b(x)u \tag{3.144}$$

Design a sliding surface S which includes the dynamics of y and the control signals u appears after the first time derivative.

$$\epsilon = y - y_d \tag{3.145}$$

y_d is the desired setting point. λ is a zero of the stable polynomial. The candidate of S could be:

$$\begin{aligned} S &:= c_1\epsilon + c_2\dot{\epsilon} + c_3\ddot{\epsilon}\cdots + c_r\epsilon^{(r-1)} \\ &= (\frac{d}{dt} + \lambda)^{r-1}\epsilon \\ c_1 &= \lambda^{r-1} \quad c_r = 1 \quad c_k = \frac{(r-1)!\lambda^{r-k}}{(r-k)!(k-1)!} \quad k = 1\cdots r \end{aligned} \tag{3.146}$$

Taking the time derivative of S:

$$\dot{S} = a(x) + b(x)u - y_d^{(r)} + CE(\epsilon) \tag{3.147}$$

Where:

$$CE(\epsilon) = c_1\dot{\epsilon} + c_2\ddot{\epsilon} + \cdots + c_{r-1}\epsilon^{(r-1)} \tag{3.148}$$

Let

$$u = \frac{1}{\hat{b}(x)}(-\hat{a}(x) + v) \tag{3.149}$$

In order to estimate unknown parameters, $a(x)$ and $b(x)$ are presented as:

$$\begin{aligned} a(x) &= a_1^T a_2 \\ &= \begin{pmatrix} a_{11}(x) & \cdots & a_{1p}(x) \end{pmatrix} \begin{pmatrix} a_{21} \\ \vdots \\ a_{2p} \end{pmatrix} \end{aligned} \tag{3.150}$$

$$\begin{aligned} b(x) &= b_1^T b_2 \\ &= \begin{pmatrix} b_{11}(x) & \cdots & b_{1q}(x) \end{pmatrix} \begin{pmatrix} b_{21} \\ \vdots \\ b_{2q} \end{pmatrix} \end{aligned} \tag{3.151}$$

a_1 and a_2 are known vectors. a_2 are b_2 are unknown vectors but constants. p and q are numbers of the unknown parameters in $a(x)$ and $b(x)$. Let $\tilde{a}_2 = a_2 - \hat{a}_2$ and $\tilde{b}_2 = b_2 - \hat{b}_2$ Eqn. (3.147) becomes:

$$\begin{aligned} \dot{S} &= a_1^T a_2 + \frac{b_1^T b_2}{b_1^T \hat{b}_2}(-a_1^T \hat{a}_2 + v) - y_d^{(r)} + CE(\epsilon) \\ &= a_1^T a_2 + \frac{b_1^T (b_2 - \hat{b}_2 + \hat{b}_2)}{b_1^T \hat{b}_2}(-a_1^T \hat{a}_2 + v) - y_d^{(r)} + CE(\epsilon) \\ &= a_1^T \tilde{a}_2 + \frac{b_1^T \tilde{b}_2}{b_1^T \hat{b}_2}(-a_1^T \hat{a}_2 + v) + v - y_d^{(r)} + CE(\epsilon) \\ &= \underbrace{\begin{pmatrix} a_1^T & \frac{b_1^T (v - a_1^T \hat{a}_2)}{b_1^T \hat{b}_2} \end{pmatrix}}_{w^T} \underbrace{\begin{pmatrix} \tilde{a}_2 \\ \tilde{b}_2 \end{pmatrix}}_{\tilde{\theta}} + v - y_d^{(r)} + CE(\epsilon) \end{aligned} \tag{3.152}$$

Let $v = y_d^{(r)} - CE(\epsilon) - Ksat(\frac{S}{\Phi})$. Φ is a scalar for a boundary layer for the sliding surface. This layer can smooth the discontinuity instead of $sgn(S)$. Eqn. (3.147) becomes:

$$\dot{S} = w^T \tilde{\theta} - Ksat(\frac{S}{\Phi}) \tag{3.153}$$

Choose a Lyapunov candidate:

$$V = \frac{S^2}{2} + \frac{\rho \tilde{\theta}^T \tilde{\theta}}{2} \quad \rho > 0 \tag{3.154}$$

Inside the boundary layer:

$$\dot{V} = -K\frac{S^2}{\Phi} + \tilde{\theta}^T(wS - \rho\dot{\hat{\theta}}) \tag{3.155}$$

So the update law is:

$$\dot{\hat{\theta}} = \frac{1}{\rho}wS \tag{3.156}$$

V is lower bounded. $\dot{V}$ is semi negative definite. S, $\tilde{\theta}$ are bounded. So $\ddot{V} = -\frac{2KS\dot{S}}{\Phi}$ is bounded. By the Barbalat lemma, we have V is uniform continuous and get $\dot{V} \to 0$ and $S \to 0$ as $t \to \infty$. Actually, it is very hard to get the measurement of $\dot{y}, \cdots, y^{(r-1)}$ in $CE(\epsilon)$.

3.8 Robustness

The uncertain parameters, the disturbance, and the noise may make the system which has a specified controller unstable. The robustness of the system means an ability to resist the disturbance of uncertain factors without changing the initial stable configuration.

Gain margin (GM) and phase margin (PM) are the traditional ways in the industry to evaluate the robustness. They are used in the SISO closed loop system. GM is a factor for a gain increased before making the system unstable. PM is a factor for how much additional phase lag or time delay before making the system unstable [19]. Vector gain margin (VGM) is another factor similar the gain margin to indicate the worst possible phase. VGM is normally used in the industry of the hard disk drive (HDD) to check the robustness. The idea is to find the minimum distance of the Nyquist plot and -1 (i.e. $\min|1 + CG| = |\frac{1}{S}|$). C is the controller. G is the plant. S is the sensitivity function.

$$S_\infty = \max_\omega |S| \tag{3.157}$$

$$VGM = \frac{S_\infty}{S_\infty - 1} \tag{3.158}$$

It can be shown that:

$$\int_0^\infty \ln(|S|)d\omega = \pi\sum_{i=1}^{n_p} Re\{p_i\} \tag{3.159}$$

n_p is the number of the total poles at rhp. If the loop gain is stable, the integral is zero. We cannot design the controller to make S_∞ at all frequencies as small as possible. The plant may be changed due to the environment and has large variation at a special frequency range. S_0 is the sensitivity function with a nominal loop gain. $\Delta = CG - CG_0$ means the variation of the loop gain. G_0 is the nominal plant. We can test many the bode plots of the loop gain in the environment and use Eqn. (3.160) for evaluating the robustness.

$$\|S_0\Delta\| < 1 \tag{3.160}$$

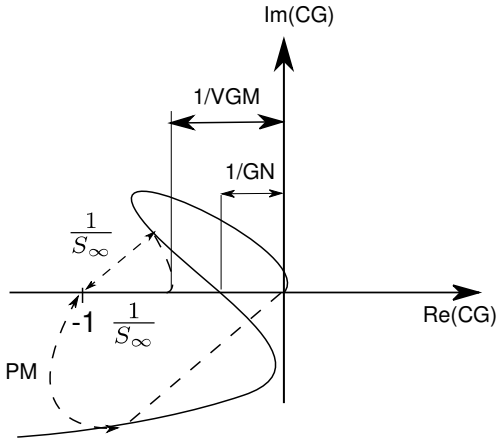

Figure 3.3: VGM, GM, PM diagram

To check the internal stability due to the unknown model, we need to analyze the block diagram and extract the unknown transfer function. Fig. 3.4 provides an example. $Q(s)$ is the uncertain dynamics and is feedback to the nominal plant $G_0(s)$. In the real mechanical system, the output of the plant indirectly indicates the mechanical vibration. This vibration affects the input of the plant through the casing.

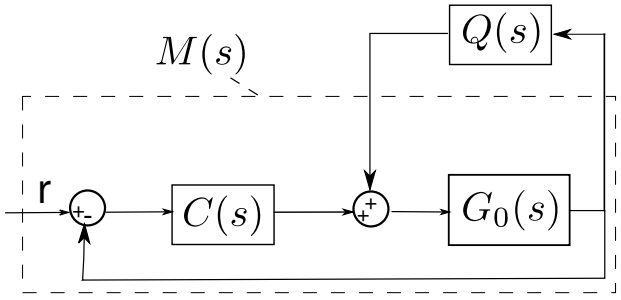

(a) Uncertain Dynamics Feedback

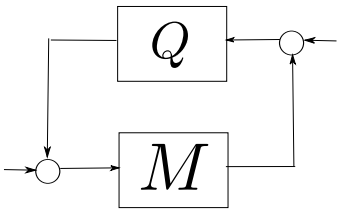

(b) Structure for the Internal Stability

Figure 3.4: Internal Stability

$$M(s) = \frac{G_0}{1 + CG_0} \tag{3.161}$$

Theorem 3.8.1. *(Small Gain Theorem)[74] Suppose $M \in RH_\infty$. Then the interconnected system shown in Fig. 3.4 (b) is well posed and internally stable for all $Q(s) \in RH_\infty$ with*
(a)$\|Q\|_\infty \leq \frac{1}{\gamma}$ if and only if $\|M(s)\|_\infty < \gamma$
(b)$\|Q\|_\infty < \frac{1}{\gamma}$ if and only if $\|M(s)\|_\infty \leq \gamma$

RH_∞ is the space which consists of all proper and real rational stable transfer matrices [74]. $\|G(s)_\infty\|$ means the largest single value of $G(j\omega)$. For the SISO system, that is the peak of the magnitude of $G(j\omega)$. For the MIMO system, it is largest eigenvalue of $\sqrt{G(s)'G(s)}$ among all $\omega \in R^+$. Actually, lemma. (3.8.1) is too conservative. In the real case, the bode plot of loop gain may indirectly be got from the sensitivity function and have a numerical error due to the division. The number of the sampling is another issue for the low frequency. The bode plot is also not accurate at high frequency due to Nyquist frequency.

Chapter 4

The Attitude Control of a Rigid Body - Three Units CubeSat

4.1 Mission Initiation

We begin our investigation about the attitude control by a real science mission. In this chapter, the spin rate and the attitude control of a rigid body are introduced.

CINEMA (CubeSat for Ions, Neutrals, Electrons and MAgneticfields) will image energetic neutral atoms (ENAs) in the magnetosphere, and make measurements of electrons, ions, and magnetic fields at high latitudes. To satisfy the mission requirements, the three unit CubeSat was designed. The spin axis needs to be in the ecliptic normal and the spin rate needs to be 4 rpm. The only power source for CINEMA is the solar panels. External torques are generated by an orthogonal pair of coils acting with the Earths magnetic field. This chapter provides the control strategy, given the limited power and available sensors, to optimize the convergence of the spin and attitude control. Fig. 4.1 shows the diagram of the ecliptic normal. The direction of the orbit of the Earth is the ecliptic normal. The tilted angle of the spin axis of the Earth makes the season changing when the Earth in the different location.

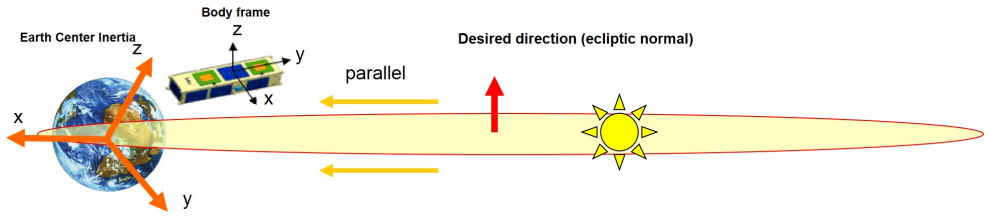

Figure 4.1: Ecliptic Normal

4.2 System Overview

CINEMA in space will have science instruments to measure solar wind induced activity. It has a preferred spin rate and attitude for best instrument operation. The spin axis should be collinear with the body frame Z axis. The spin axis should point to an ecliptic pole which also positions the sun in the body XY plane. (Fig. 4.2, [34]) The selected spin rate is 4 rpm.

4.2.1 Slit Sun Sensors

Both slit sun sensors are oriented in the YZ plane and form a V shape.(Fig. 4.3, [34]). As the satellite rotates, the sun produces pulses in each sun sensor. The pulse repetition rate in each sensor provides a measure of the Z axis spin period. The short variable delay between the sensor pair pulses is caused by the "V" shape geometry. This delay provides data needed to determine the elevation of the sun relative to the body spin plane. In Fig. 4.3, T_1 is the first impulse of one of two sun sensors. $\delta t = T$ is the time corresponding to the zero azimuth.

$$\delta t = \frac{T_1 + T_2}{2} = T \tag{4.1}$$

The period T_p is the inverse of the spin frequency.

$$T_p = \frac{T_3 + T_4}{2} - \frac{T_1 + T_2}{2} \tag{4.2}$$

t is the current time. The azimuth α and the elevation β are:

$$\alpha = \frac{t - T}{P} \tag{4.3}$$

$$\beta = k_{ss} \frac{T_2 - T_1}{P} \tag{4.4}$$

k_{ss} which can be derived geometrically and through the simulation or the experiments.

4.2.2 Magnetometers

CINEMA has two three-axis science magnetometers [34] that also provide the additional relative orientation data needed for operating the torque coils. In order to simulate the magnetic field, the international geomagnetic reference field (IGRF) is used. The model of the magnetic field is provided w.r.t. the ECEF. The simulation needs to convert the expression frame of the model w.r.t. the ECI frame with the fraction of the day. Then convert the modified model w.r.t. the body frame for the simulated measurement of the magnetic field.

4.2.3 Solar Panels

CINEMA also has six solar power panels which are also used to deduce the coarse attitude of the sun with respect to the body frame. Measuring the currents of these six panels surfaces provides the initial coarse orientation and roll information. The solar panels and the sun sensors provide similar information. The sun sensors provide far greater precision with a very limited field of view(FOV), while the solar panels afford full FOV coverage.

4.2.4 Torque Coils

Two wire wound torque coils serve as the control actuators. One of these coils is orthogonal to the spin axis (Z axis) and located in the XY plane, the other is co-planar with the spin axis(+Z). Torques are generated by the coil currents reacting with the magnetic field of the Earth. A more detailed description of the CINEMA structure is provided in [34]. When we talk about the total external torque, we also need to specify the point. However, since the torque which is generated by a coil is coupling, it doesn't matter the location of the center of the mass to the coil.

In this chapter, we describes how the orientation information is processed for spin rate and attitude control with a goal of rapid settling times. These simulations address the limited FOV of the sun sensors, as compared to the coarse solar panel data. The three strategies for angular velocity and two orientation computations are also discussed.

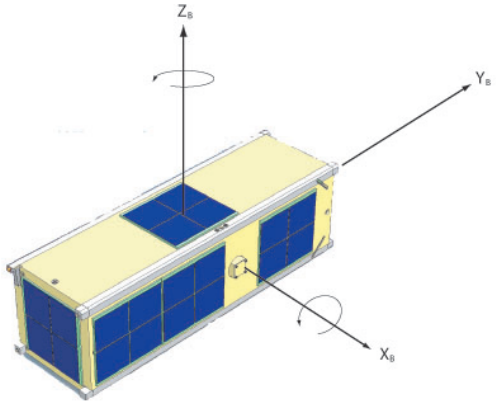

Figure 4.2: The Body Frame of CINEMA. Z axis is the spin axis.

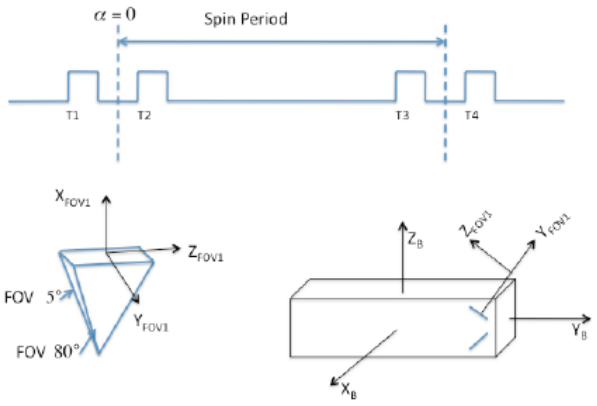

Figure 4.3: The Principle of the Sun Sensor. When the sun passes the slits, two impulses are generated.

4.3 Disturbance, Noise and Uncertainty

4.3.1 Albedo Effects

CINEMA uses the solar panels for the orientation of the sun. However, when the satellite passes the Antarctic, the solar panels receive more reflection of the ground. The simulation meshes the surface of the Earth. The idea of the albedo effect is from [17]. Each piece of the surface has its own direction. I assumes the reflectivity equals one. Each meshed surface receives the power of the sun with a fraction by an angle θ. Ignore the effects of the distance between the satellite and the ground. The power emitted by the meshed surface is strongest in direction of the meshed surface. So the power of a meshed surface also has a fraction to the satellite by an angle Φ. Assume each solar panel has the strongest acceptance in the direction of the surface. So the light reflected from the ground to a solar panel has a fraction by an angle Ψ. Collecting the fractions from all meshed surface in a solar panel and computing all power received in six surface, we can get the albedo effects to the orientation of the sun. Fig. 4.4 (a) is a diagram for two meshed surface reflecting the power to a solar panel.

4.3.2 Gravity gradient disturbance

The gravity-gradient (Fig. 4.4 (b)) is the largest disturbance in space. The derivation can be referred in [69]. Each piece of the satellite feels different gravity. The difference of the gravity generates the gravity-gradient torque.

$$\vec{M} = 3n^2 a_3 \times \hat{J} a_3 \tag{4.5}$$

Where $n = \sqrt{\mu / R_c^3}$ R_c is the real distance between CM of the Earth to the CM of the satellite and $a_3 = -\vec{R_c}/R_c$. M is the gravity-gradient torque. $\hat{J}$ is the moment of the inertia. μ

is the gravitational parameter. The gravity-gradient tries to make the satellite aligned to a special axis and $a_3 \times \hat{J}a_3 \approx 0$ in the end.

4.3.3 Solar panels acceptance

If the elevation of the sun is below 10 degree for a solar panel (Fig. 4.5 (a)), this solar panel cannot receive any power of the sun. Since the orientation of the sun in the body frame is computed by total power of the six panels, there exists a small bias (≤ 10 degree) to the position of the sun.

4.3.4 Shadow effects

When the satellite pass the shadow of the Earth (Fig. 4.5(b)), the satellite loses its power from the sun. At this moment, the satellite immediately stops the control. The shadow makes the settling time longer. S is the distance from CM of the Earth to CM of the sun. C is the distance from CM of the Earth to the vertex is formed by the eclipse. R_p is the radius of the Earth. R_s is the radius of the sun. ρ_c is the solid angle formed by the total eclipse. From the geometry, we can get:

$$\begin{aligned} C &= \frac{R_p S}{R_s - R_p} \\ \rho_c &= \sin^{-1}(\frac{R_s - R_p}{S}) \approx \sin^{-1}(\frac{R_s}{S}) \end{aligned} \tag{4.6}$$

For the Earth, $C = 1.385 \times 10^6$ km and $\rho_c = 0.266°$. Let $\vec{D}_s$ and $\vec{D}_p$ be the vector from the satellite to CM of the sun and CM of the Earth respectively. $\rho_s = \sin^{-1}(R_s/|D_s|)$ is the angle radius of the sun, $\rho_p = \sin^{-1}(R_p/|D_p|)$ is the angle radius of the Earth. θ is the interior angle between $\vec{D}_p$ and $\vec{D}_s$. $\theta = \cos^{-1}(\vec{D}_s \cdot \vec{D}_p/(|\vec{D}_s||\vec{D}_p|))$. The necessary and sufficient conditions of the eclipse are:

- Partial Eclipse:
$$|\vec{D}_s| > S \quad \text{and} \quad \rho_p + \rho_s > \theta > |\rho_p - \rho_s| \tag{4.7}$$
- Total Eclipse:
$$S < |\vec{D}_s| < S + C \quad \text{and} \quad \rho_s - \rho_p > \theta \tag{4.8}$$

4.3.5 Orbit precession

The ecliptic normal control needs the up-link package of the magnetic field for the reference. The preceesion of the orbit is around 1 deg per day. If the satellite passes the ground station around every 16 hours, the error is around 0.67 deg. When the precession happens, Ω in Fig. 2.3 changes.

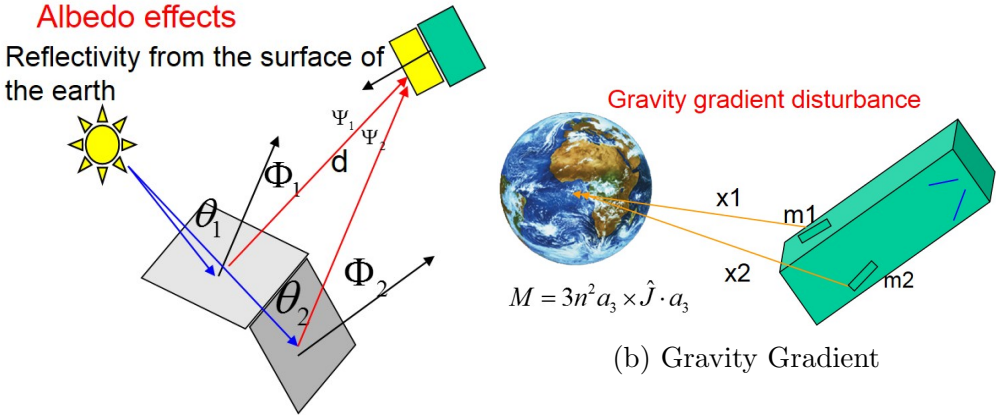

(a) Albedo Effects

(b) Gravity Gradient

Figure 4.4: Albedo Effects and Gravity Gradient Disturbance

4.3.6 Slit sun sensor extrapolation

The silt sun sensor (Fig. 4.3) only has 24 deg FOV and the controller needs to do the extrapolation of the position of the sun during the period of the impulse. Since the sun sensor only is operated after the spin rate control finished, the elevation doesn't change much during the period and the spin rate is assumed a constant. The azimuth is estimated by a simple sinusoidal function.

$$\begin{aligned} x &= \sin(\omega t + \alpha) \\ y &= \cos(\omega t + \alpha) \end{aligned} \tag{4.9}$$

x and y are the components of the estimated position of the sun w.r.t. the body frame. ω is the spin rate and α is the initial offset.

4.4 Controllability and Observability

4.4.1 Controllability of Three Units CubeSat

The torque coils can generate the coupling external torque and we want to change the angular velocity and have the desired spin rate. The controllability is a way to check if the linear system is controllable. For a nonlinear system, the controllability condition becomes the accessibility condition. Assume the moment of inertia is diagonal. From Euler equations

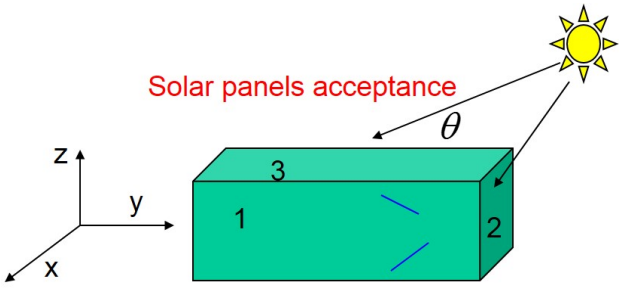

(a) Solar Panel Acceptance

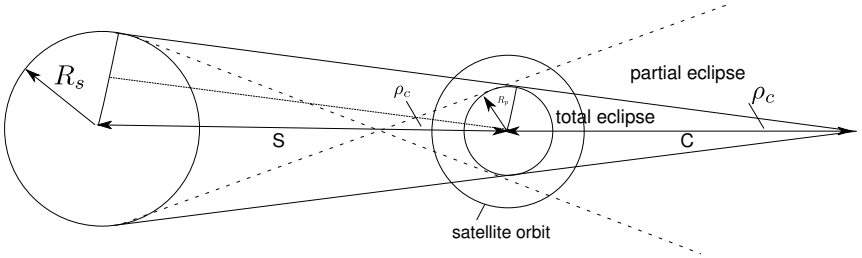

(b) Shadow Analysis

Figure 4.5: Solar Panels Acceptance and Shadow Analysis

of the rotation in Eqn. (2.46) and the structure of the coupling torque coils, we have:

$$\begin{pmatrix}\dot{\omega}_x\\ \dot{\omega}_y\\ \dot{\omega}_z\end{pmatrix} = \underbrace{\begin{pmatrix}\frac{w_y w_z(J_2-J_3)}{J_1}\\ \frac{w_x w_z(J_3-J_1)}{J_2}\\ \frac{w_x w_y(J_1-J_2)}{J_3}\end{pmatrix}}_{f} + \underbrace{\begin{pmatrix}\frac{-b_y}{J_1}\\ \frac{b_x}{J_2}\\ 0\end{pmatrix}}_{g_1}\bar{U} + \underbrace{\begin{pmatrix}0\\ -\frac{b_z}{J_2}\\ \frac{b_y}{J_3}\end{pmatrix}}_{g_2}\bar{V} \tag{4.10}$$

From Eqn. (3.6):

$$\begin{aligned} C &= \begin{bmatrix} g_1 & g_2 & [f & g_1] & [f & g_2] \end{bmatrix} \\ &= \begin{bmatrix} \frac{-b_y}{J_1} & 0 & \frac{\omega_z(J_2-J_3)b_x}{J_1J_2} & \frac{\omega_z(J_2-J_3)(-b_z)}{J_1J_2} + \frac{\omega_y(J_2-J_3)b_y}{J_1J_3} \\ \frac{b_x}{J_2} & \frac{-b_z}{J_2} & \frac{\omega_z(J_3-J_1)(-b_y)}{J_1J_2} & \frac{\omega_x(J_3-J_1)(b_y)}{J_2J_3} \\ 0 & \frac{b_y}{J_3} & \frac{\omega_2(J_1-J_2)(-b_y)}{J_1J_2} + \frac{\omega_1(J_1-J_2)b_x}{J_2J_3} & \frac{\omega_1(J_1-J_2)(-b_z)}{J_2J_3} \end{bmatrix} \end{aligned} \tag{4.11}$$

From Eqn. (4.11), the following condition makes the three units CubeSat inaccessible.
Remark 1: At the equilibrium point around the origin. The setting point of the three units CubeSat is four rpm. The loss of the accessibility around the origin doesn't happens in the normal operation.
Remark 2: In the direction of the magnetic field where $b_y = 0$.

We already show the accessibility of the angular velocity and want to prove the accessibility of the attitude. The angular velocity is assumed to be input for the attitude dynamics. The rotation matrix is constructed with $\theta_3 \rightarrow \theta_2 \rightarrow \theta_1$ Euler angles. The dynamics equation is:

$$\begin{bmatrix} \dot{\theta}_1 \\ \dot{\theta}_2 \\ \dot{\theta}_3 \end{bmatrix} = \begin{bmatrix} 1 & \frac{\sin\theta_1 \sin\theta_2}{\cos\theta_2} & \frac{\cos\theta_1 \sin\theta_2}{\cos\theta_2} \\ 0 & \cos\theta_1 & -\sin\theta_1 \\ 0 & \frac{\sin\theta_1}{\cos\theta_2} & \frac{\cos\theta_1}{\cos\theta_2} \end{bmatrix} \begin{bmatrix} \omega_1 \\ \omega_2 \\ \omega_3 \end{bmatrix} \tag{4.12}$$

The input matrix already has 3 independent columns and $f(x) = 0$, so the system is controllable.

4.4.2 Observability of Three Units Cubesat

The sun sensor uses the period of the impulse for the spin rate estimation. Between the impulses, the spin rate is assumed to be a constant. The drift of the estimation happens. Besides, the sun sensor provides the limited FOV. The solar panels also can provide rough estimation but with wider FOV. Both sensors have their pros and cons. The magnetometer provides the other reference for attitude. The ground station also provides another magnetic field w.r.t. the inertial frame. The sun table computation provides the position of the sun w.r.t. the inertial frame. For the three units CubeSat with its available resource, each control task is no issue for the observability.

4.5 Control Algorithm

The attitude or the spin rate control of the rigid body can be achieved by different types of actuators. [54] discussed methods of the attitude and the spin rate control for the axisymmetric spinning satellite with the electromagnetic dipole moments. The approach for both controllers lies in the context of the stability of Lyapunov function. [56] chapters three and four describe the details for stability of the Lyapunov function. From the analysis of the control law for CINEMA, the Lyapunov function was semidefinite. Which implies the control law cannot converge asymptotically. In this chapter, we describe the modified control laws to improve the convergence rate. Moreover, [54] converted the body frame to the inertial frame for attitude control. The tedious and sometimes annoying Euler angle were derived. Singularities in the Euler angles need to be considered for a proper algorithm. This singularity issue can be easily avoided with the *Triad* algorithm.

When the CubeSat is first released from its launcher, it needs some initial control to reduce residual tumbling angular velocity and later progress to the spin and the attitude control. [68] provided the control rules with two coils for this initial detumbling. [34] used z coil for detumbling using the derivative of magnetic fields in X direction. However, if the initial angular velocity only exists in the X direction, this detumbling doen't work. This study provides proof that only the Z coil is needed for detumble control of CINEMA. This is achieved by evaluating the z derivative of the local magnetic field. Before CINEMA

receives ground station local magnetic data in ECI format, the desired attitude is the spin axis perpendicular to the local sun line. This set point is called the sun normal direction where there are infinite possible rotations about the sun line. All of these candidates for sun normal directions are constrained to a plane. This study provides an algorithm for sun normal control which will tilt the spin axis using the shortest rotation directions to sun normal.

4.5.1 Spin Rate Control

The objective is to choose a Lyapunov function that describes the desired angular momentum. [54] used a bang-bang approach for spin rate control. He also described the effective torque used to reduce the spin rate error w.r.t. the inertial frame. We can establish a similar approach using the Lyapunov analysis. In spin rate control, we use the X coil to establish the desired spin rate. It must be commuted in magnetic X & Y to provide the desired Z torques. The Z coil can not produce Z torques, so it is not used in spin up. Eqn. (4.13) is angular momentum error vector. Eqn. (4.14) is called the candidate of the Lyapunov function. Our goal is to reduce this candidate of the Lyapunov function to zero. $(\cdot)_I$ means the object is expressed in the inertial frame. $(\cdot)_B$ means the object is expressed in the body frame. R_B^I means the rotation matrix from body frame to the inertial frame. $(R_B^I)^T R_B^I = I$

$$(E)_I = (\vec{h_f})_I - (\vec{h})_I \tag{4.13}$$

$$V = (E)_I \cdot (E)_I = (h_{xf} - h_x)_I^2 + (h_{yf} - h_y)_I^2 + (h_{zf} - h_z)_I^2 \tag{4.14}$$

$$\begin{aligned} \dot{V} = 2(h_{xf} - h_x)_I(\dot{h}_{xf} - \dot{h_x})_I + 2(h_{yf} - h_y)_I(\dot{h}_{yf} - \dot{h_y})_I + \\ 2(h_{zf} - h_z)_I(\dot{h}_{zf} - \dot{h_z})_I \end{aligned} \tag{4.15}$$

The desired settling point is constant angular momentum with its vector fixed in some desired orientation in inertial space. Eqn. (4.15) becomes:

$$\begin{aligned} \dot{V} = 2(h_{xf} - h_x)_I(-\dot{h_x})_I + 2(h_{yf} - h_y)_I(-\dot{h_y})_I + 2(h_{zf} - h_z)_I(-\dot{h_z})_I \\ = -2\bar{V}E_I \cdot (\vec{i_x} \times \vec{B})_I \\ = -2\bar{V}(R_B^I E_B) \cdot (R_B^I(\vec{i_x} \times \vec{B})_B) \\ = -2\bar{V}E_B \cdot (\vec{i_x} \times \vec{B})_B \end{aligned} \tag{4.16}$$

The remainder equations which have vectors in this chapter ignore the notation $(\cdot)_B$. The reader will recognize Eqn. (4.16) from the knowledge of external torques:

$$\vec{M} = \bar{V}\vec{i_x} \times \vec{B} \tag{4.17}$$

Here, we follow [54] to define the switching function as:

$$S = E \cdot (\vec{i_x} \times \vec{B}) \tag{4.18}$$

For the spin rate control, the error angular momentum is:

$$E = \begin{pmatrix} 0 \\ 0 \\ \Omega_f \end{pmatrix} - \begin{pmatrix} I_{xx}\omega_x \\ I_{yy}\omega_y \\ I_{zz}\omega_z \end{pmatrix} \tag{4.19}$$

Ω_f is the desired spin rate. And

$$\vec{i_x} \times \vec{B} = \begin{pmatrix} 0 \\ -b_z \\ b_y \end{pmatrix} \tag{4.20}$$

Control $\bar{V}$ is based on the switching function.

$$\begin{aligned} \bar{V} =& \beta^2 \quad if \quad S > 0 \\ \bar{V} =& -\beta^2 \quad if \quad S < 0 \end{aligned} \tag{4.21}$$

We only control the polarity of the magnetic moment(Bang-bang control) so $\dot{V}$ is semi definite. From [56], the system is stable but not necessary asymptotically stable. This candidate will not decrease to zero in some conditions. Fortunately, the local magnetic field changes periodically. It inertially rotates twice per orbit to provide persistent extinction for $\dot{V}$.

4.5.2 Ecliptic Normal Control

In the spin rate control, the set point is the desired spin but the direction of the spin axis is random in space. The objective for CINEMA is to align the spin axis with the ecliptic normal with a 4 rpm spin rate. [54] provided a solution for attitude control with only one coil where the magnetic moment is parallel to the spin axis. The attitude control should start after the spin rate control is finished because the spin axis will drift by the X coil disturbances.

4.5.2.1 Ecliptic Normal Control With Single Coil

We follow the method in [54] using the Z coil for the attitude control. The desired attitude in Eqn. (4.13) is modified for an angular momentum corresponding to 4 rpm and the direction is in the ecliptic normal. Eqn (4.18) is modified to:

$$S = E \cdot (\vec{i_z} \times \vec{B}) \tag{4.22}$$

For the ecliptic normal control, the error angular momentum is:

$$E = \begin{pmatrix} e_1 \\ e_2 \\ e_3 \end{pmatrix} I_{zz}\Omega_f - \begin{pmatrix} I_{xx}\omega_x \\ I_{yy}\omega_y \\ I_{zz}\omega_z \end{pmatrix} \tag{4.23}$$

$$\vec{i_z} \times \vec{B} = \begin{pmatrix} -b_y \\ b_x \\ 0 \end{pmatrix} \tag{4.24}$$

$\begin{pmatrix} e_1 & e_2 & e_3 \end{pmatrix}^T$ is ecliptic normal unit vector w.r.t. the body frame. Control $\bar{U}$ based on the switching function.

$$\begin{aligned} \bar{U} =& \alpha^2 \quad if \quad S > 0 \\ \bar{U} =& -\alpha^2 \quad if \quad S < 0 \end{aligned} \tag{4.25}$$

4.5.2.2 Ecliptic Normal Control With Two Coils

The derivative of the Lyapunov function is semi definite which means the error can not converge to zero for some states. Eqn. (4.22) has the same issue as the Eqn. (4.18). I propose several algorithms to use two coils to improve the convergence of the Lyapunov function.

4.5.2.2.1 Switching Coils by the Angle Between E & $(\vec{i_n} \times \vec{B})$ The first method uses the same set point as the single coil, but the switching function is modified to

$$S = E \cdot (\vec{i_n} \times \vec{B}) \tag{4.26}$$

and n is the index for the magnetic moment. The primary coil is the Z coil which operates almost continuously during the attitude control. We commute the X coil to improve the convergence when the angle θ_1 is near 90 degrees. θ_1 is the angle between the error function and cross product of the X coil magnetic moment and the local magnetic field. θ_2 is the angle between the error function and cross product of the X coil magnetic moment and local magnetic field. If the angle θ_2 is near 90 degrees, the ecliptic normal attitude control is suspended to avoid wasting power. The Z coil is designated as the primary coil for attitude control because of the X coil effects to the spin rate. The ranges of θ_1 and θ_2 are selected from simulation results. We need to set some bounds for swapping coils and avoid frequent changes.

4.5.2.2.2 Switching Coils by the Angle Between E & $(\vec{i_n} \times \vec{B})$, Turn on X coil for Half Rotations The next method may save power but has slower convergence rate. The X coil is actuated for half rotations because any torque produced in the opposite half would have a canceling effect. The algorithm is[1]:

$$\begin{aligned} S =& E \cdot (\vec{i_x} \times \vec{B}) \\ \bar{V} =& \beta^2 \quad if \quad S > 0 \\ \bar{V} =& 0 \quad if \quad S < 0 \end{aligned} \tag{4.27}$$

[1]Here E is the difference of the spin axis in the ecliptic normal with four rpm and current angular momentum.

4.5.2.2.3 Switching Coils with the Least Square Method The third method is an optimal combination of coils based on the present local magnetic field. Two coils are operated at the same time. The previous algorithms for ecliptic normal control are based on a bang-bang approach which cannot be used for both coils. In this method, the controller knows the local magnetic field and computes the optimal combination of magnetic moments. The simulations show that this best convergence rate. A magnetic moment is added in x direction.

$$\dot{V} = -2E \cdot (\bar{U}\vec{i_z} \times \vec{B} + \bar{V}\vec{i_x} \times \vec{B}) \tag{4.28}$$

The external torque is determined by:

$$\bar{U}\vec{i_z} \times \vec{B} + \bar{V}\vec{i_x} \times \vec{B} \tag{4.29}$$

We intend to find proper $\bar{U}$ and $\bar{V}$ to make Eqn. (4.28) as small as possible. If Eqn. (4.29) is in the same direction of E, then Eqn. (4.28) is a minimum value. We use the least square method to make the approximation E get a proper magnetic moment combination. Eqn. (4.29) can be written explicitly:

$$E \approx \bar{U}\vec{i_z} \times \vec{B} + \bar{V}\vec{i_x} \times \vec{B} = \bar{V}\begin{pmatrix} 0 \\ -b_z \\ b_y \end{pmatrix} + \bar{U}\begin{pmatrix} -b_y \\ b_x \\ 0 \end{pmatrix} \tag{4.30}$$

$$E \approx \begin{pmatrix} 0 & -b_y \\ -b_z & b_x \\ b_y & 0 \end{pmatrix}\begin{pmatrix} \bar{V} \\ \bar{U} \end{pmatrix} = A\begin{pmatrix} \bar{V} \\ \bar{U} \end{pmatrix} \tag{4.31}$$

A is the matrix composed of the components of the magnetic field. From the least square method, we can get:

$$\begin{pmatrix} \bar{V} \\ \bar{U} \end{pmatrix} = inv(A^T A)A^T E \tag{4.32}$$

$$\begin{pmatrix} \bar{V} \\ \bar{U} \end{pmatrix} = \frac{1}{b_y(b_x^2 + b_y^2 + b_z^2)}\begin{pmatrix} -b_x b_z & -b_z b_y & b_x^2 + b_y^2 \\ -(b_y^2 + b_z^2) & b_x b_y & b_x b_z \end{pmatrix} E \tag{4.33}$$

$\bar{V}$ and $\bar{U}$ need to be adjusted for the coil constraints. For example, the level of $\bar{U}$ and $\bar{V}$ are α^2 and β^2 respectively. If the larger amplitude of the components in Eqn. (4.33) is $\bar{U}$, we choose $\bar{U} = (sign)\alpha^2$ and $\bar{V} = C\bar{U}$. C is the scalar which is the ratio between $\bar{U}$ and $\bar{V}$ in Eqn. (4.33). Moreover, we only use this least square when the z coil could have the maximum effects. When the x coil could produce larger effects, we use first method to avoid lots the spin rate decreasing.

4.5.3 Sun Normal Control

Ecliptic normal control requires the absolute magnetic field vector and the sun direction vector. The controller will keep the spin axis perpendicular to the sun vector before receiving

the orbit ephemeris data from the ground station. The sun normal spin attitude does not fulfill the desired ecliptic normal attitude. One of these determinations is described by [65]. With incomplete attitude data, the spin vector can still drift in the plane orthogonal to the sun line. To avoid these unnecessary drift torques, control is suspended when the set point is achieved. When the sun elevation exceeds +-5 degrees (due to gravity gradient) the controller is re-started. The sun normal mode starts after the spin rate control finishes. The sun normal mode uses only the Z coil to avoid spin rate changes. The control algorithm is very similar to ecliptic normal control. The difference is that the spin vector set point is determined by on board data only. The control rules are the same in the Eqn. (4.23) and Eqn. (4.25) but $\begin{pmatrix} e_1 & e_2 & e_3 \end{pmatrix}^T$ is determined from Fig. 4.6.

4.5.4 Detumble Control

There will be modest (unknown) tumbling angular velocity when CINEMA is first released from its launch vehicle carrier. These may cause unknown instabilities in spin and pointing control if they are large. [68] introduced the concept of first reducing angular velocity with bang-bang control based on the derivative of measured magnetic field data. [34] used the derivatives of the magnetic filed in the x direction. If there are only X direction residual angular velocity, they will not be reduced. In contrast, we plan to use only Z coil data which may leave residual Z angular velocity. This is acceptable because the next control phase increases the Z axis spin. Our verification uses the following equations.

Select the candidate Lyapunov function:

$$V = w_x^2 + w_y^2 + w_z^2 \tag{4.34}$$

$$\dot{V} = 2w_x\dot{w_x} + 2w_y\dot{w_y} + 2w_z\dot{w_z} \tag{4.35}$$

From the single body rigid dynamics [29], we know:

$$\begin{aligned} J_1\dot{w_x} - (J_2 - J_3)w_y w_z &= M_x \\ J_2\dot{w_y} - (J_3 - J_1)w_z w_x &= M_y \\ J_3\dot{w_z} - (J_1 - J_2)w_x w_y &= M_z \end{aligned} \tag{4.36}$$

M_i is the components of the external torque. J_i is the diagonal components of the moment of inertia. ω_i is the components of angular velocity. Substitute Eqn. (4.36) to Eqn. (4.35), we have:

$$\begin{aligned} \dot{V} =& 2w_x(\frac{w_y w_z(J_2 - J_3)}{J_1}) + 2w_y(\frac{w_x w_z(J_3 - J_1)}{J_2}) + \\ & 2w_z(\frac{w_x w_y(J_1 - J_2)}{J_3}) + 2w_y(\frac{b_x}{J_2})\bar{U} - 2w_x(\frac{b_y}{J_1})\bar{U} \end{aligned} \tag{4.37}$$

Assume the initial angular velocity is quite small. The high order terms can be eliminated.

$$\dot{V} \approx 2w_y(\frac{b_x}{J_2})\bar{U} + 2w_x(-\frac{b_y}{J_1})\bar{U} \tag{4.38}$$

Without loss the generality and follow the similar assumption from [68], instant magnetic field b_y and b_z can be assumed:

$$\begin{aligned} b_y &= B_0 cos(w_x t) \\ b_z &= -B_0 sin(w_x t) \\ \dot{b_z} &= -B_0 w_x cos(w_x t) \end{aligned} \tag{4.39}$$

B_0 is some scalar at this moment and Eqn. (4.38) becomes:

$$\begin{aligned} \dot{V} &\approx 2\bar{U}(\frac{b_x}{J_2}w_y - \frac{b_y}{J_1}w_x) \\ &\approx 2\bar{U}(\frac{b_x}{J_2}w_y - \frac{B_0 cos(w_x t)}{J_1}w_x) \\ &= 2\bar{U}(\frac{b_x}{J_2}w_y + \frac{\dot{b_z}}{J_1}) \end{aligned} \tag{4.40}$$

The moment of the inertia of CINEMA has largest component in z direction and components in x and y are almost equal. Based on this, w_y is expected to oscillate and small. In the end, the dominant term of Eqn. (4.40) is the second term. The rules for the detumble control are:

$$\begin{aligned} \bar{U} &= -\alpha^2 \quad if \quad \dot{b_z} > 0 \\ \bar{U} &= \alpha^2 \quad if \quad \dot{b_z} < 0 \end{aligned} \tag{4.41}$$

That makes $\dot{V}$ in Eqn. (4.40) smaller or equal zero. Since switching function is based on the derivative of the b_z. We estimate the largest angular velocity about 2π per orbit.

4.6 State Estimation

CINEMA has limited sensors. There is no GPS and the ground reference ECI magnetic field is not always available. Before receiving data packets from the ground station, the spin rate control needs the angular velocity and Sun normal control needs its local orientation. "Local" means CINEMA must determine its attitude relative to the sun using the sun sensor or solar panels. When CINEMA receive ephemeris packets from the ground station, the *Triad* algorithms will determine the desired spin axis. The next sections describe states estimation using various available attitude sensors.

4.6.1 Spin Axis Orientation

4.6.1.1 Triad Algorithm In the Ecliptic Normal Control

In [64], the algorithm called the *Triad* algorithm. It uses two onboard sensors and the two corresponding ground values in ECI frame. [23] used a similar method to compute the

rotation matrix but it must evaluate the inverse of a 3x3 matrix. This method requires four spacial vectors. CINEMA uses this *Triad* algorithm with the local magnetic field and the sun vector data from the sun sensor or solar panels. The ECI magnetic field data is periodically uploaded from the ground station. The sun position in the ECI frame is computed from the *Julian date*. This algorithm is described in [25]. CINEMA uses deterministic attitude methods when only two observations are available. When more than two observations are available, statistical attitude determination is used, as described by [25]

4.6.1.2 Position of the Sun w.r.t. the Earth Centered Inertial Frame

The position of the sun is determined by the Julian date (JD). The distance between the Earth and the sun is far longer than the distance between the Earth and the satellite. So we take the position of the sun w.r.t. the position of the Earth as the same position w.r.t. the satellite. JD is a continuously running counting system for days and is used in astronomy [5]. "Int" is the floor function $\lfloor x \rfloor$. Gregorian calendar is a modification for the leap years which could be divisible by 100 but not by 400. UT means the fraction time which elapsed since midnight in the Greenwich time zone. The formula for JD with Gregorian calendar [5] from 1901 to 2099 is:

$$\text{JD} = 367 * \text{year} - \text{Int}\Big\{\frac{7[\text{year}+\text{Int}(\frac{\text{month}+9}{12})]}{4}\Big\} + \text{Int}(\frac{275 * \text{month}}{9}) + day + 1,721,013.5 + \text{UT}/24 \tag{4.42}$$

[64] has an example for the JD (year, month, day, UT) in chapter 3. For August 20, 1992, 12:14 P.M $JD = 2,448,855.099\ 722$. The algorithm for the unit vector (s_i) w.r.t. the ECI frame [25] is:

- T_{UT1}=$\frac{JD-2{,}451{,}545.0}{36{,}525}$
- $\lambda_{M_{Sun}} = 280.460\ 618\ 4^\circ + 36,000.770\ 053\ 61 \cdot T_{UT1}$
- Let $T_{TDB} \approx T_{UT1}$
  mean longitude of the sun
- $M_{Sun} = 357.527\ 723\ 3^\circ + 35,999.050\ 34 \cdot T_{TDB}$
  mean anomaly of the sun
- $\lambda_{ecliptic} = \lambda_{M_{Sun}} + 1.914\ 666\ 471^\circ \cdot \text{sind}(M_{Sun}) + 0.918\ 994\ 643 \cdot \text{sind}(2 * M_{Sun})$
  ecliptic longitude of the sun
- $\epsilon = 23.439\ 291^\circ - 0.013\ 004\ 2 \cdot T_{TDB}$
- position of the sun $s_i = \begin{bmatrix} \text{cosd}(\lambda_{ecliptic}) \\ \text{cosd}(\epsilon)\text{sind}(\lambda_{ecliptic}) \\ \text{sind}(\epsilon)\text{sind}(\lambda_{ecliptic}) \end{bmatrix}$

sind and cosd mean the sin(·) operation and cos(·) but the unit for the variable is degree (°).

The algorithm is verified with the data base of Jet Propulsion Laboratory (JPL) Solar System Dynamics[2]. However, readers will need to check the official organization if they require more precise results or the algorithm may be updated.

4.6.1.3 Spin Axis determination In the Sun Normal Mode

Fig. 4.6 establishes a method for evaluating the spin vector set point. The desired sun position is perpendicular to the body frame Z axis. Sun normal control is used to achieve this attitude.

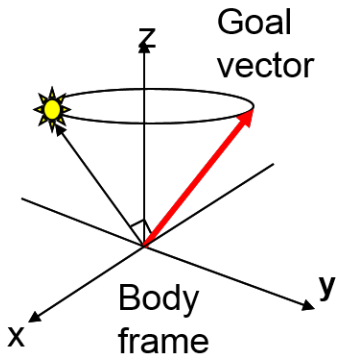

Figure 4.6: The Set Vector and the Current Spin Axis

4.6.2 Angular Velocity

The candidate Lyapunov function is based on the error in angular momentum. This subsection describes how the various data sets are used to compute angular velocity.

4.6.2.1 Angular Velocity From Derivative of Rotation Matrix

The angular velocity can be computed from the derivative of the rotation matrix. From rotation kinematics[69]:

$$\begin{aligned} w_x &= \dot{C}_{21}C_{31} + \dot{C}_{22}C_{32} + \dot{C}_{23}C_{33} \\ w_y &= \dot{C}_{31}C_{11} + \dot{C}_{32}C_{12} + \dot{C}_{33}C_{13} \\ w_z &= \dot{C}_{11}C_{21} + \dot{C}_{12}C_{22} + \dot{C}_{13}C_{23} \end{aligned} \tag{4.43}$$

The rotation matrix C_{ij} is obtained from the *Triad* algorithm.

[2]JPL Solar System Dynamics: http://ssd.jpl.nasa.gov/

4.6.2.2 Two Vectors For Angular Velocity

CINEMA will need spin rate control before it receives ECI data from the ground. We developed an algorithm that uses only onboard data to estimate the angular velocity. From the kinematics of a rigid body[47]:

$$\dot{\boldsymbol{r}} = \mathring{\boldsymbol{r}} + \boldsymbol{\omega} \times \boldsymbol{r} \tag{4.44}$$

$\boldsymbol{r}$ is an arbitrary vector and $\boldsymbol{\omega}$ is the angular velocity vector. $\mathring{\boldsymbol{r}}$ is the derivative w.r.t. the body frame. We assume two observations, the position of the sun and the magnetic field with small derivatives. The sun vector rotates once per year while the magnetic vector rotates once per ninety minute orbit. Given these low rates, Eqn. (4.44) can be modified to:

$$\mathbf{0} \approx \mathring{\boldsymbol{r}} + \boldsymbol{\omega} \times \boldsymbol{r} \tag{4.45}$$

When only one observation is available, Eqn. (4.45) encounters singularities. To avoid this, we replace some elements in the matrix. Eqn. (4.45) can be modified to:

$$\begin{pmatrix} \mathring{r}_1 \\ \mathring{r}_2 \\ \mathring{r}_3 \end{pmatrix} = \begin{pmatrix} 0 & r_3(t) & -r_2(t) \\ -r_3(t) & 0 & r_1(t) \\ r_2(t) & -r_1(t) & 0 \end{pmatrix} \begin{pmatrix} w_x \\ w_y \\ w_z \end{pmatrix} \tag{4.46}$$

r_i is the component of $\boldsymbol{r}$ in the body frame. To estimate ω_x, ω_y and ω_z, we extract data from available observations. For example, two components may be from the magnetic field and the other from the position of the sun. Eqn. (4.46) can be rewritten as:

$$\begin{pmatrix} \mathring{b}_x \\ \mathring{b}_y \\ \mathring{s}_z \end{pmatrix} = \begin{pmatrix} 0 & b_z & -b_y \\ -b_z & 0 & b_x \\ s_y & -s_x & 0 \end{pmatrix} \begin{pmatrix} w_x \\ w_y \\ w_z \end{pmatrix} \tag{4.47}$$

Then the angular velocity can be evaluated:

$$\begin{pmatrix} w_x \\ w_y \\ w_z \end{pmatrix} = \frac{-1}{b_z(b_x s_y - b_y s_x)} \begin{pmatrix} b_x s_x & b_y s_x & b_x b_z \\ b_x s_y & b_y s_y & b_y b_z \\ b_z s_x & b_z s_y & b_z b_z \end{pmatrix} \begin{pmatrix} \mathring{b}_x \\ \mathring{b}_y \\ \mathring{s}_z \end{pmatrix} \tag{4.48}$$

To avoid the singularity in the denominator of Eqn. (4.48), we replace the other components of the magnetic field and sun position. There are eighteen possible data combinations to produce smooth estimations.

4.6.2.3 One Vector For Angular Velocity

CINEMA may need to be operated in the shadow of the Earth where the only available data is the local magnetic field. This control system includes an option for estimating the

angular velocity with only one measurement. The algorithm is based on [48] and it assumes the second derivative of the observing object is zero in space.

$$\frac{\partial}{\partial t}S = -\Omega S \tag{4.49}$$

We can have this relation:

$$\begin{aligned}\Omega_y &= \frac{\Omega_x S_y + \dot{S}_z}{S_x} \\ \Omega_z &= \frac{\Omega_x S_z - \dot{S}_y}{S_x}\end{aligned} \tag{4.50}$$

The second derivative of S is zero:

$$\frac{\partial^2}{\partial t^2}S - I^{-1}[\Omega \times (I\Omega + h)] \times S - \Omega \times (\Omega \times S) = 0 \tag{4.51}$$

We have:

$$\begin{aligned}\alpha_1\Omega_x^2 + \beta_1\Omega_x + \gamma_1 = 0 \\ \alpha_2\Omega_x^2 + \beta_2\Omega_x + \gamma_2 = 0 \\ \alpha_3\Omega_x^2 + \beta_3\Omega_x + \gamma_3 = 0\end{aligned} \tag{4.52}$$

Define:

$$A \triangleq \begin{pmatrix}\alpha_1 & \beta_1 & \gamma_1 \\ \alpha_2 & \beta_2 & \gamma_2 \\ \alpha_3 & \beta_3 & \gamma_3\end{pmatrix} = \begin{pmatrix}\vec{r}_1 & \vec{r}_2 & \vec{r}_3\end{pmatrix}^T \tag{4.53}$$

and

$$\vec{\Omega}_x \triangleq \begin{pmatrix}\Omega_x^2 & \Omega_x & 1\end{pmatrix}^T \tag{4.54}$$

$\vec{\Omega}_x$ belongs the null space of A. We can find the null space by cross product operation.

$$\begin{aligned}\vec{n}_1 = \vec{r}_2 \times \vec{r}_3 \\ \vec{n}_2 = \vec{r}_3 \times \vec{r}_1 \\ \vec{n}_3 = \vec{r}_1 \times \vec{r}_2\end{aligned} \tag{4.55}$$

For the purpose of the noise rejection, we can choose a vector $\vec{n}_i$, where $\vec{n}_i$ is one of the vectors $(\vec{n}_1, \vec{n}_2, \vec{n}_3)$ which has the maximum norm and let $\vec{\Omega}_x \in \vec{n}_i$ for computing Ω_x. This is another method for the estimating of the angular velocity. The location of CINEMA is not fixed in space but has an orbit period of ninety minutes which means magnetic field changing is slow. Our simulations also revealed a smooth second derivative of the magnetic field. [48] also uses extended Kalman filter (EKF) for the noise rejection.

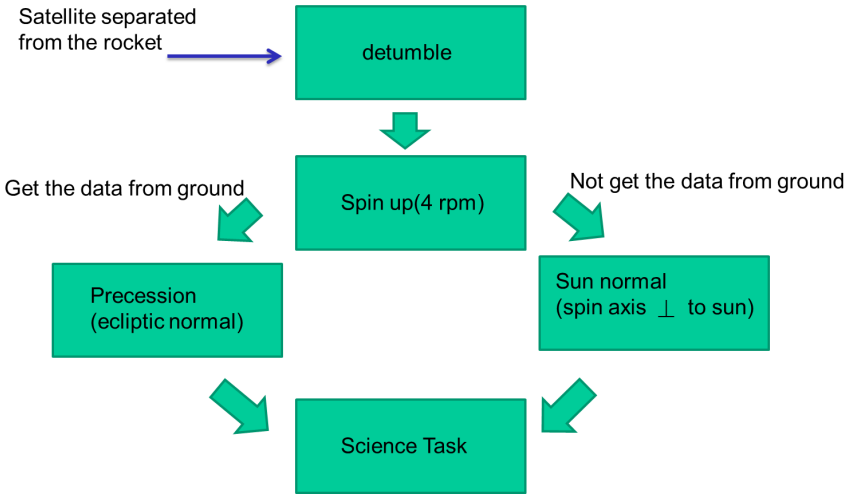

Figure 4.7: ACS Control Flow

4.7 Control Flow

Fig. 4.7 shows the control flow. The rocket carries several satellites. Those satellite are separated from the rocket by the force of the spring and have some initial velocity. For CINEMA, the detumble control is executed for reducing the initial angular velocity. In the end, only ω_z of the angular velocity remains. After the detumble control, the spin up control is executed for 4 rpm spin rate. After that, if the satellite receives the magnetic field w.r.t. the inertial frame. The precession control is executed and controls the spin axis aligned with the ecliptic normal - otherwise the sun normal control is executed and controls the spin axis perpendicular to the position of the sun. When the error of the attitude is smaller than a threshold, the controls is turned off and the science task begins. The science task and control tasks cannot be executed simultaneously because the conducting of the coil moments influences the science tasks.

4.8 Simulation Methods

These simulations were constructed in the simulink environment using the SimMechanics toolbox[3]. Fig. 4.8 presents the structure of these simulations. There are three parts, the physical environment, the sensors and the actuators. The control logic includes the controller and the ground station data. The arrows in the figure show the direction of data flow.

[3]detail: Mathworks:http://www.mathworks.com/index.html

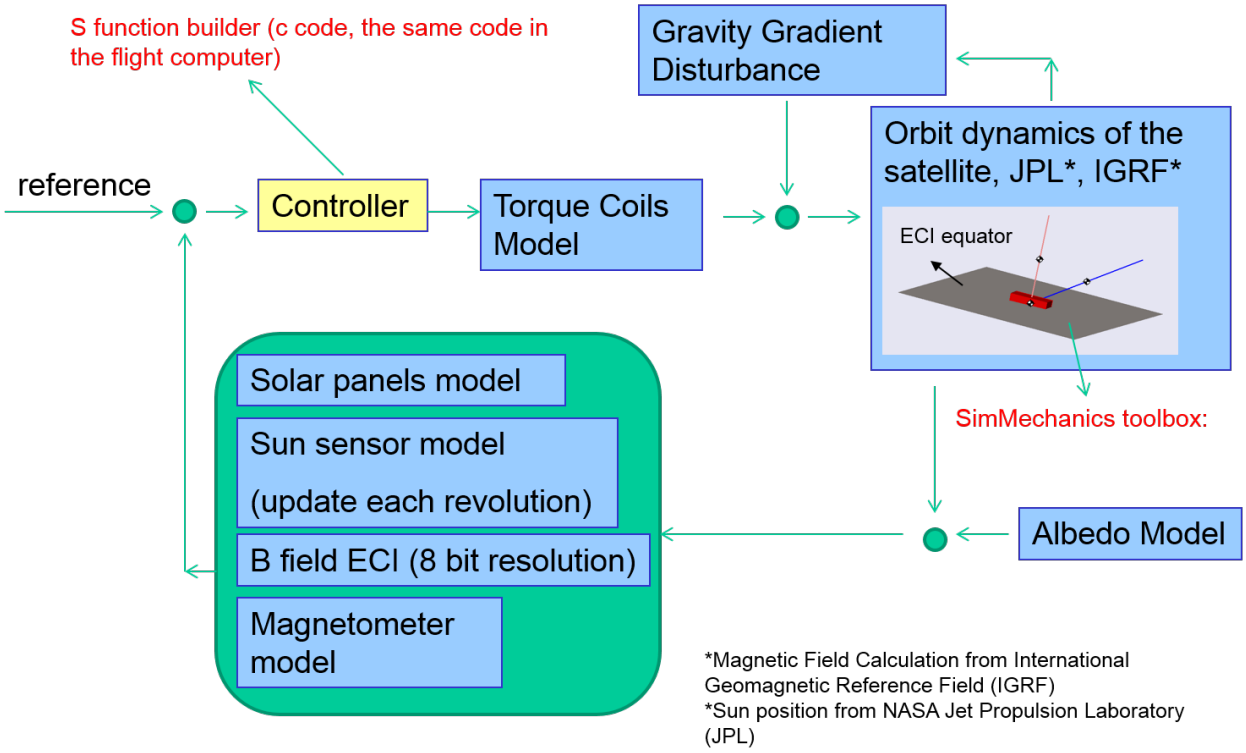

Figure 4.8: Simulation Setup

4.8.1 Physical Environment

The physical model includes orbit shadow, orbit dynamics, the magnetic field, the sun, the gravity gradient disturbances, and albedo[17]. A single rigid body is used for CINEMA constructed in the SimMechanics toolbox. In this model, best estimates of the mass and the moment of the inertia are used.

4.8.2 Sensor Models and the Actuators

The properties of the sun and magnetic field in the ECI frame are transformed to the ECEF frame and to the body frame. The solar panels model uses sun position to evaluate the corresponding panel currents. The sun sensor model transforms sun position to the rotating body on a continuing basis. When the sun is out of the FOV, the sun sensor simply does not respond. The actuators receive the controller commands to generate the external torques using the magnetic field model.

4.8.3 Controller And Ground Station

The attitude controller system (ACS) is one module on the flight software computer. This controller is implemented in C code and uses the S function builder in Simulink. A benefit of using S function builder is that the code can be copied into the flight software computer with few modifications. This greatly simplifies the tasks of building simulations and real time software. The ground station model provides uplink ECI magnetic field data to CINEMA. In the actual flight, the ground station uplinks data blocks during three minute ground passes. CINEMA uses the uplink magnetic field data for ecliptic normal control. Each time tagged magnetic field data value has two bytes, one is the desired relative azimuth and the other is elevation. Ground station protocol synchronizes the ground with the flight computer real time clock. The ACS software then selects the needed time tagged data. The uplink data blocks are generated to cover the next two ground passes. In this context, There is no concern over transmission delays.

4.8.4 Orbit Equation

The orbit is determined by:

$$\vec{a} = \frac{GM}{r^3}\vec{r} \tag{4.56}$$

$\vec{r}$ is from the center of the satellite to the center of the Earth. The unit of $\vec{r}$ is meter. GM=3.9860e+014. The initial condition could be determined from semi-major axis, eccentricity inclination, longitude of ascending node; argument of periapsis and true anomaly. The detail can be referred in [69] or chapter 2.

4.9 Simulation Results

Figure. 4.9 provides the spin up mode results using all available angular velocity computation methods. The one and two vector methods show similar convergence. The one vector method is a bit faster because it does not need a vector alignment criteria. The four vector method uses a derivative of the rotation matrix generated by *Triad* algorithm. It has slower convergence because of its vector alignment criteria and numerical discontinuities in the rotation matrix derivative. Each solar panel has a 2π field of view. The two vector method relies on these solar panel derivatives, and the four vector method contains nine of these derivatives. The one vector method uses magnetometer data which does not have these discontinuities. Fig. 4.10, Fig. 4.11 and Fig. 4.12 provide histograms of the angular velocity error. The two vector method provides the best estimation while the one vector method has data in the denominator that causes discontinuities.

Figure. 4.13 presents the convergence rates for various control schemes. The least squares and one vector methods produce the quickest convergence. The Z coil only shows the slowest response, but it does have a steady spin rate. The least squares method causes the largest spin rate changes. Fig. 4.14 provides histograms of the convergence rate as a function of the

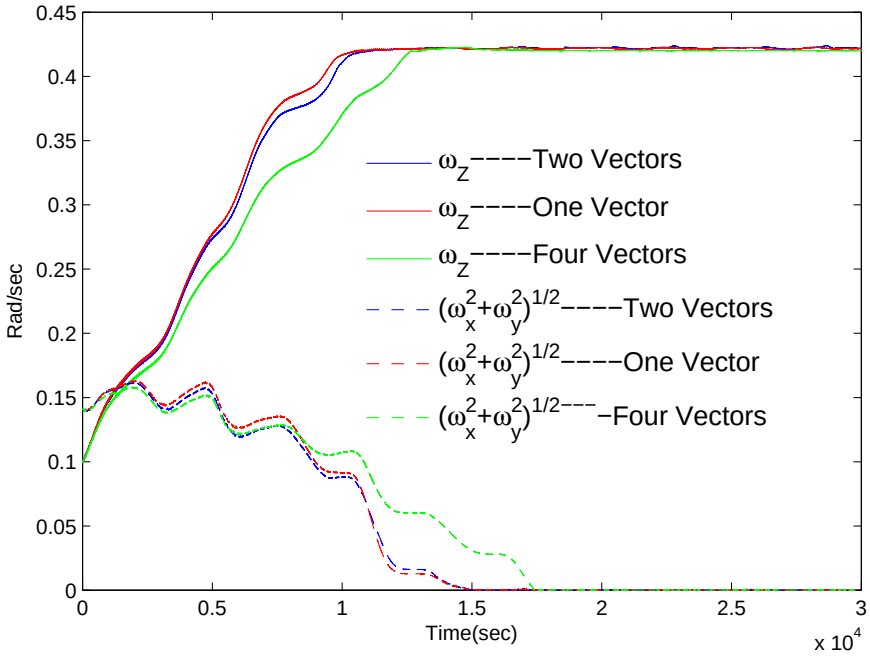

Figure 4.9: Spin Up Mode

initial argument of periapsis from 0-359 degrees. These results represent the time needed to reduce the pointing error from 5 degrees to one. Performance variations are largely due to the magnetic fields direction. The least square method has fastest convergence in Fig. 4.14

Fig. 4.15 shows the angular velocity changes and histogram in the detumble mode. The initial angular velocity of ω_x, ω_y and ω_z are 0.1 rad/sec. ω_x and ω_y are converge to the zero and the ω_z maintains its amplitude. The bottom of this figure is the histogram with different initial argument of periapsis. The mean is 2114 seconds. Figure. 4.16 shows the angular velocity changes and histogram in the sun normal mode. The converge rate of the sun normal mode is usually faster than the precession mode because of the infinite options for the spin axis. The bottom of this figure is the histogram with different initial argument of periapsis. The mean is 1130 second for four degrees error.

4.10 Implementation and Verification of Flight Computer and Software

Figure. 4.17 shows the arrangements used to verify the hardware and software. The single board flight computer is a dsPIC33FJ256GP710 from microchip[4]. A simulink physical model of CINEMA runs in a periphial laptop to generate the simulated sensor inputs. The data is transferred to the dsPIC by a RS232 port. The laptop also runs the same control

[4]microchip:http://www.microchip.com/

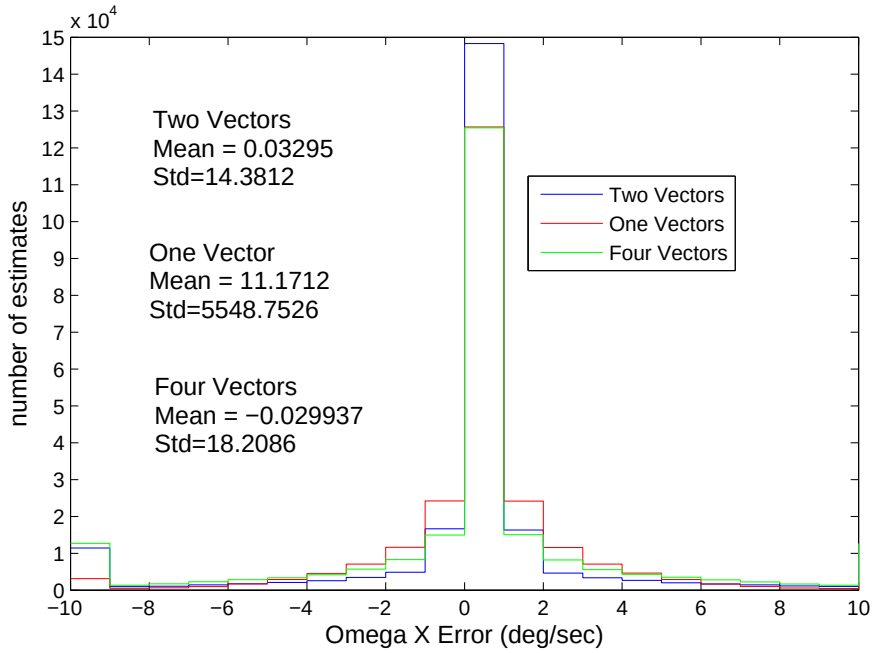

Figure 4.10: Histogram for Spin Up Omega X Error

software so it can be compared to the dsPIC. All of the sensor data is "float"data type and each signal is composed of four bytes. The flight computer decodes these serial packets and passes them to the controller software. These software/hardware loops also verified that the dsPIC will operate correctly in real time.

4.11 Summary

This chapter describes the development and testing of the attitude control modes needed for the CINEMA CubeSat. These control modes include detumble, spin rate, sun normal, and ecliptic normal control. In the spin control simulations, the comparison shows that four vectors method has slowest convergence rate. One vector method has the fastest convergence rate. However, the two vectors method has the best estimation from the view of the statistic. One vector method has the worst estimation. In the precession simulations, the least square method has the fastest converging rate. However, the least square method needs to change the amount of the current. If the coils moment has the hysteresis, the control signals will not be as expected. Using two coils for the ecliptic normal control, the spin rate will be affected and be compensated with some amount when the error of the attitude become small enough. In the interest of conserving power, this mode was modified to use the Z coil with a half time X coil. The detumble mode simulations performed as expected, based on Eqn. (4.41). The sun and ecliptic normal mode simulations also performed as expected and also satisfied Lyapunov's second stability method.

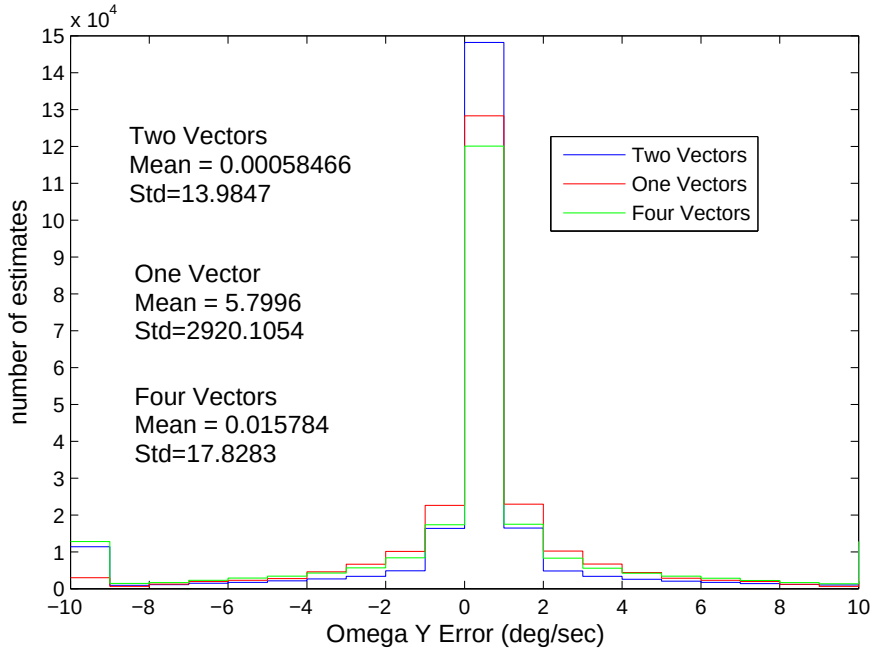

Figure 4.11: Histogram for Spin Up Omega Y Error

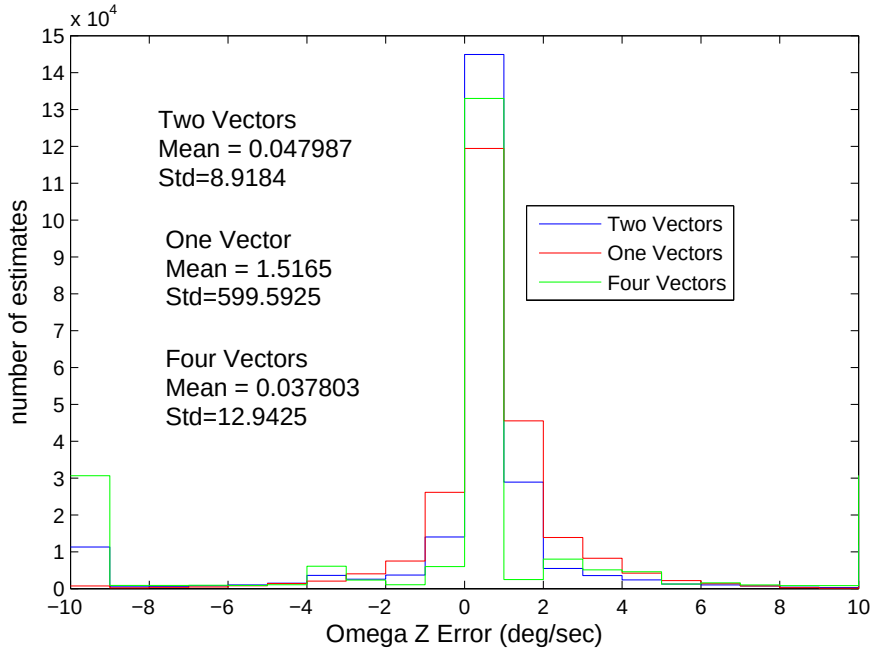

Figure 4.12: Histogram for Spin Up Omega Z Error

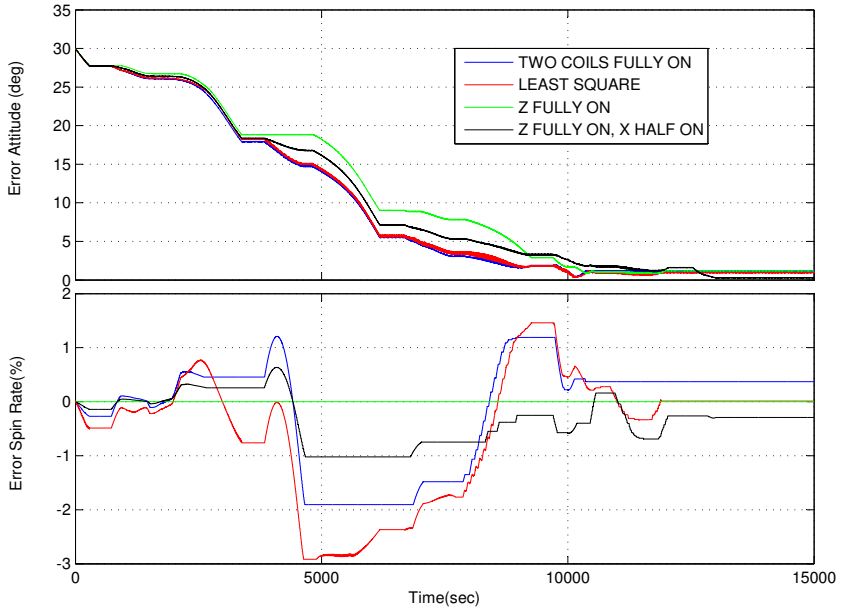

Figure 4.13: Precession Mode

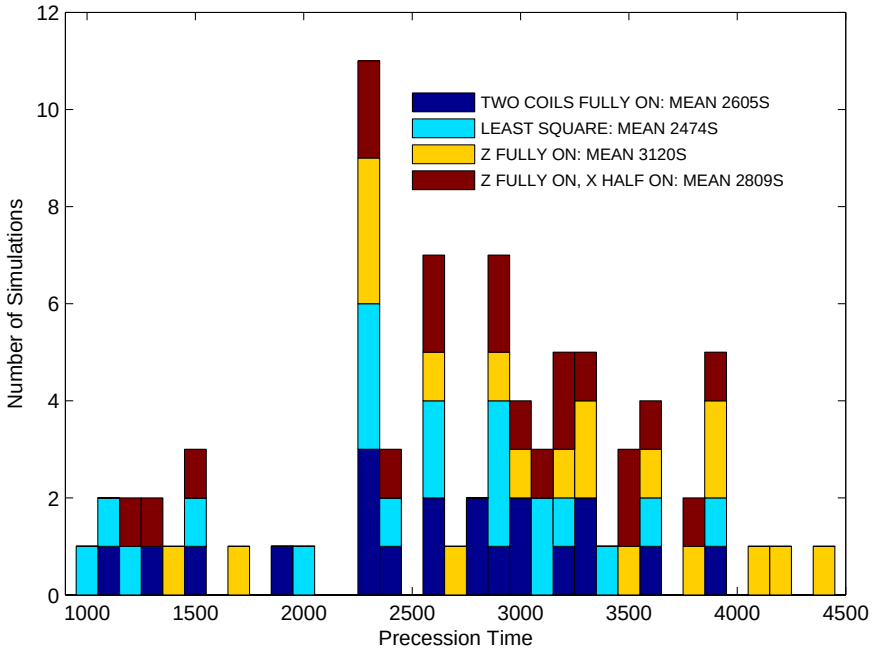

Figure 4.14: Histogram for Precession Mode

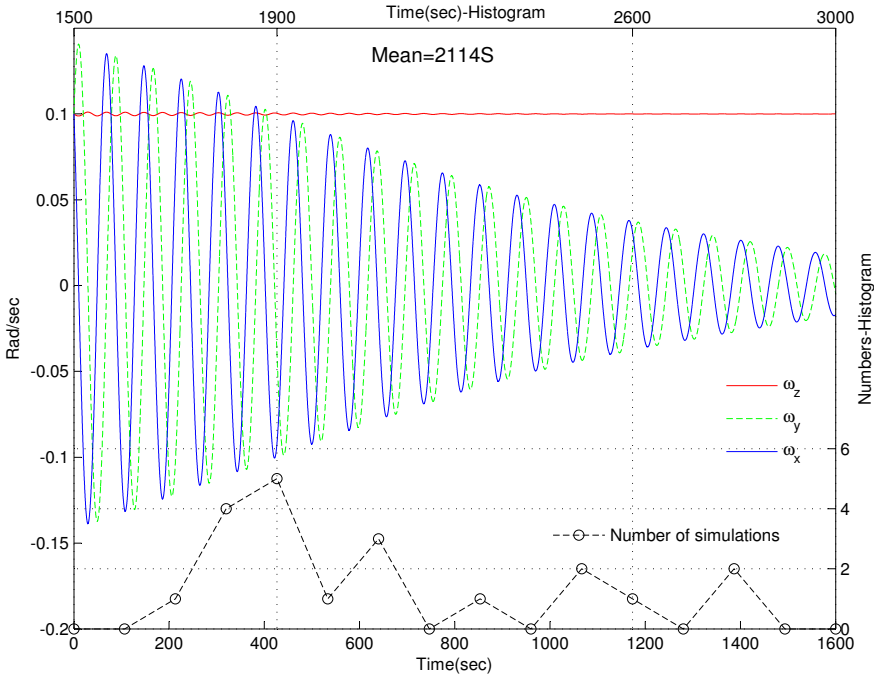

Figure 4.15: Detumble Mode and Histogram

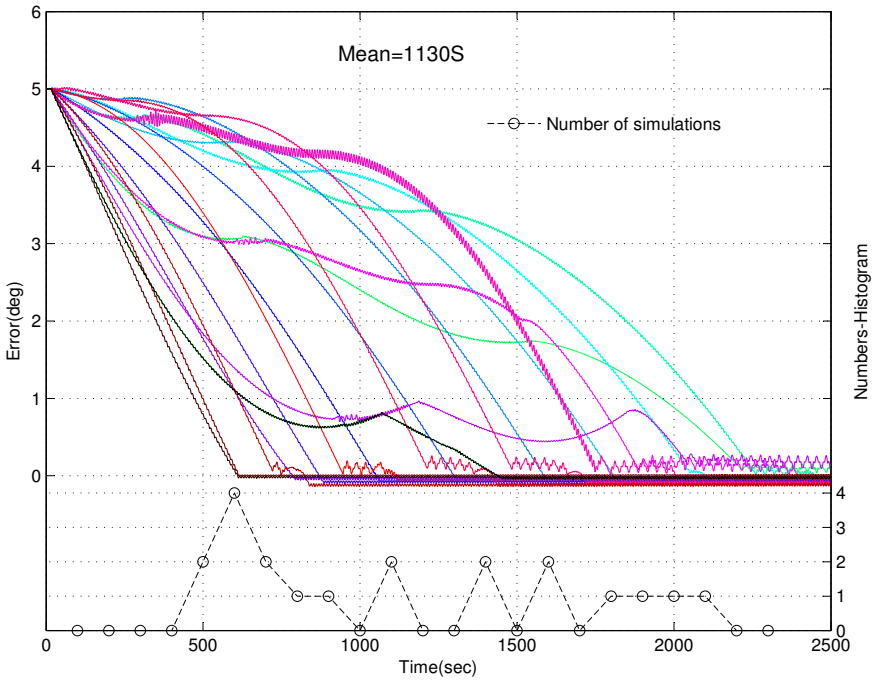

Figure 4.16: Sun Normal Mode and Histogram

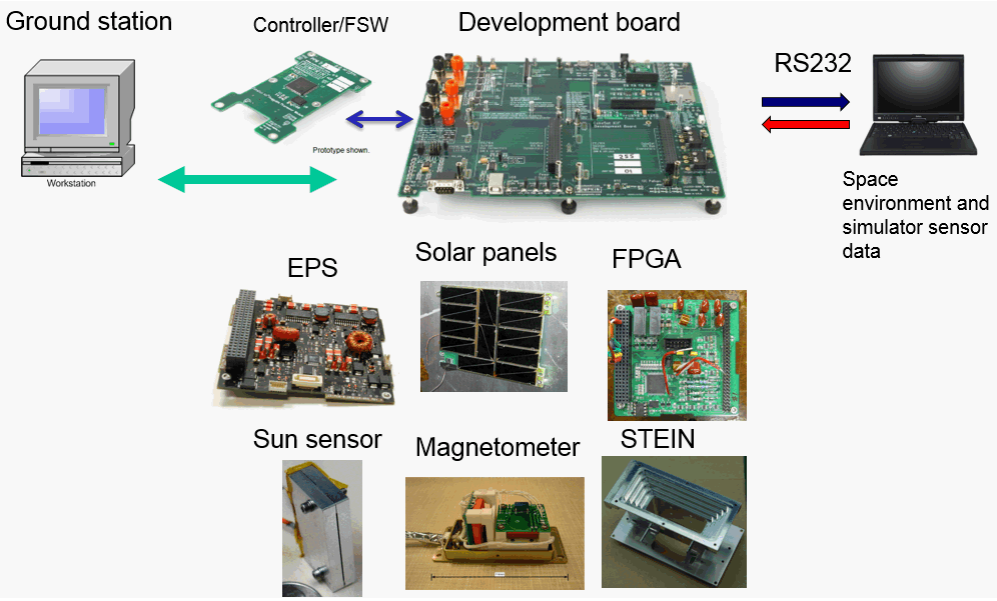

Figure 4.17: The Flight Computer and Peripheral Hardware: EPS: Power System. STEIN:Science Instrument. FPGA: Signal Converter. Ground Station: Simulated Commands and Local Magnetic Field Packages.

Chapter 5

The Stabilization Strategy of a Multibody System - Grotifer Spacecraft

5.1 Mission Initiation

In chapter 4, we describe how to control a rigid body. In this chapter, we present how to stabilize a multibody system from a science mission. There are two controllers implemented in the different bodies for the stabilization.

The microphysics of reconnection, sharp boundaries, shocks and turbulence are at the forefront of space plasma physics research. In all of these cases, the component of the electric field parallel to the local magnetic field (the parallel electric field) plays a key role. To obtain this component, one must measure the three-component electric and magnetic field accurately because the parallel electric field is typically an order-of-magnitude smaller than the perpendicular electric field. Spacecrafts that have measured such electric fields have been spin stabilized, so the spin-axis measurement, made with a much shorter antenna than the spin plane wire boom measurements, does not have the required sensitivity. However, for both field and plasma measurements, it is highly desirable to make measurements in the spin planes of two rotating platforms because major advancements of science are expected from such data. For the purpose of obtaining such measurements, a new spacecraft architecture has been studied. It consists of a fixed center body with one surface, holding solar panels, pointing sunward, magnetometer for the second measurement, with counter-rotating platforms on two other surfaces aligned at 90 degrees to each other. This chapter will review in more detail the science motivations for the spacecraft configuration; a straw-man design of the spacecraft and it will describe the modeling and control of such a system. This chapter also analyzed the dynamics of this structure and proposed a control structure to maintain its attitude to prevent tangle of the booms.

5.2 System Overview

The microphysics of reconnection, sharp boundaries, shocks and turbulence are at the forefront of space plasma physics research. In all of these cases, the component of the electric field parallel to the local magnetic field (the parallel electric field) plays a key role. To obtain this component, one must measure the three-component electric and magnetic field accurately because the parallel electric field is typically an order-of-magnitude smaller than the perpendicular electric field. Spacecraft that have measured such electric fields have been spin stabilized. On such spacecraft, the components of the electric and magnetic field in the spacecraft spin plane have been well-measured because they appear as sine waves at the spin frequency and DC electronic or spacecraft associated offsets, which are constant with time, are easily removed. For electric field measurements, long wire booms, held in their radial positions by the centrifugal force resulting from the rotation, have been used to measure fields smaller than 1 mV/m. The spin axis booms are much shorter than the spin plane booms for dynamics reasons such that the electronic and spacecraft-generated offsets are difficult to separate from the desired signal.

An example of raw electric field data obtained on the Polar satellite, which has produced the best estimates of parallel electric fields to date, is given in Fig. 5.1. The top two panels of this figure give the electric fields measured by long wire booms in the spacecraft spin plane and, as expected, the two signals vary at the spacecraft spin rate, they are 90 degrees out of phase, and their amplitude variations show the temporal variations of the spin plane components of the electric field. The third component, measured by the ten-times-shorter on-axis boom pair, is in the bottom panel.

It exhibits a non-geophysical spin periodicity, which results from the short booms sensing spacecraft potential variations as different elements of the spacecraft rotate in and out of sunlight. After removing this effect, the accuracy of the on-axis component of the electric field is no better than a few mV/m. This is further evidence that more accurate electric field measurements require long wire booms in all three measurement directions. Plasma experiments have typically required one or more spacecraft spin periods for the complete measurement of the plasma distribution. This problem is mitigated by flying many plasma instruments having fields of view in different directions but, even in this case, it is often difficult to measure the plasmas along the spacecraft spin axis because of interference from spacecraft obstacles and near-spacecraft electric fields. Thus, for both field and plasma measurements, it is highly desirable to make measurements in the spin planes of two rotating platforms because major advancements of science are expected from such data. For the purpose of obtaining such measurements, a new spacecraft architecture has been studied. This configuration, called Eggbeater, is described in Fig. 5.2.

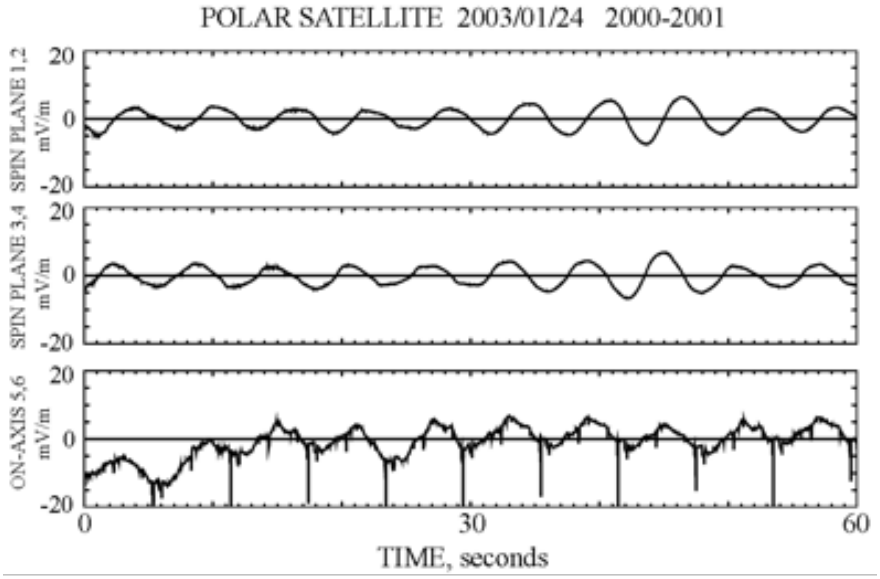

Figure 5.1: Polar Satellite

5.3 Spacecraft Design

A viable mission design generally starts with a well thought out definition of the straw-man concept. For space physics missions, these instruments are sub-divided into fields and particles instruments. Electric and magnetic fields instruments need to be boom mounted so as to avoid the local spacecraft perturbations. These booms also need to be arranged to provide continuous three axis measurements. Particle instruments would like to sample in four pi directions as rapidly as practical. Locating all of the instruments on the platforms also offers an engineering advantage in that greater platform mass will provide greater flywheel effects, useful in moderating spin fluctuations.

Spin or de-spin platforms have been used on a large number of satellites and are extensively studied in the literature. Common motor gear drive synchronization of the platforms is the simplest and appropriate technique. The platforms drive motor is controlled to maintain a constant speed to avoid complex interactions with the primary bus attitude control system. Wire booms are deployed slowly, at a few mm per second, so that the platforms can continue to run at constant speed. Rigid magnetometer booms also need to deploy slowly for the same reason, or be deployed prior to activating the spin platforms. These platforms would be caged for the rigors of the launch environment.

The primary bus is envisioned simply as a meter sized cube that may be later altered to fit specific mission and launch vehicle needs. The primary bus would house all of the traditional spacecraft avionics plus the two platform drive mechanism. One side of the bus will need to

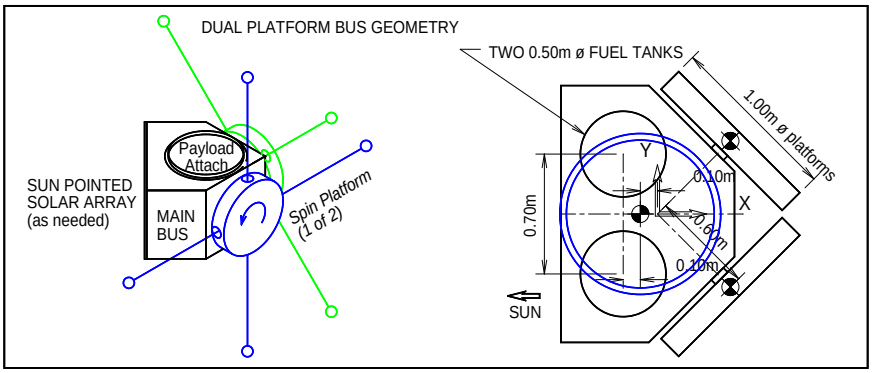

Figure 5.2: Bus Drawing

be sun pointed for electric power generation. Tab. 5.1 provides the breakdown of instruments and avionics selected for this study. The purpose of this figure is developing viable mass, power, surface area, and volume for the straw-man mission concept. For example, more than a square meter of solar array will be needed, which can (with folded extensions) be fit on one face of this cube. In developing the bus avionics suite, specific commercial products, with their advertised performance specifications, have been selected as a baseline for this study. These should not be considered to be the only choice for these purposes, but rather that a known commercial solution does exist.

The attitude control system (ACS) needs the most complete definition for this study. Stable bus reference sensors are needed to avoid random gyrations of the platform appendages. One example might be some combination of sun sensor, horizon sensor and star tracker. The disadvantage in this approach lies in the need for mode switching when inputs drop out, such as when the spacecraft enters shadow. The attractive single technology sensor solution is a gyroscope reference package that will also provide continuous, high data rate outputs. For this application, very modest precision is needed. One attractive choice is the solid state gyro that appears to avoid many of the frailties of traditional mechanical gyroscopes. The Scalable SIRU contains four sensors in a single small package. The sensors are arranged in the desirable redundant tetrahedron configuration such that any one sensor can fail without compromising the mission. This unit is also electrically cross-strapped to deal with potential power interruptions, Northup-Grumman advertizes a SIRU reliability of 99.6% for fifteen

years of operation and claims a heritage of over fifty space missions.

The primary ACS actuators are four momentum, or reaction wheels, where several commercial choices exist. These are oriented to the same tetrahedron geometry as the sensors to provide the desired redundancy. A number of these units are also available with electrical cross-strapping to deal with power interruptions. Momentum wheels must be unloaded to avoid over-speeds, which calls for some secondary form of ACS actuator. This might be either magnetic torque rods or a gas propulsion system. Given the recent orbital debris based mission de-orbit requirements, propulsion is the obvious choice. Adding fuel to any mission also means having to also deal with the complexities of fuel slosh in the tanks. Typical slosh models are included in these studies, where the fuel would be contained in spherical tanks having constraining diaphragms. Wheel unloading usually falls in the category of housekeeping performed by ground controllers. In this context, the thrusting events are assumed to be gentle enough to avoid upsetting the primary ACS control loop. Fig. 5.3 provides illustrations of the selected ACS components.

One very important aspect of ACS is the detailed design is the safe hold plan, where a very simple and robust approach appears plausible. The primary control loop would use only the solid state gyros interacting with the momentum wheels, which locks the spacecraft somewhere in inertial space. The sun sensor and commanded inputs would be in the form of bias commands that, for example, would move the pointing from somewhere in space to sun pointing. One virtue of this approach is that there is no apparent need for ACS safe hold mode switching. If the sun sensor inputs are lost for any reason, the ACS would revert to inertial pointing, which implies that a safe hold could continue for perhaps thirty days before bus power concerns arise.

Figure 5.3: Selected ACS components

5.4 System Modeling and Control

This section is divided into two phases. The first phase includes the modeling of all components of the spacecraft and the verification of the model. The second phase is about the controller design of the bus and the platform.

CROSS SCALE SCIENCE INSTRUMENTS

acronym	mass (kg)	OAP (W)	Measurement
E2D	8.00	3.00	30-50m wire double probe 2D electric field
MAG	1.50	0.50	boom-mounted dc vector magnetic field
ACB	1.75	0.10	boom-mounted ac vector magnetic field
ACDPU	1.50	2.00	Common processor & electronics
	4.75	**2.60**	**Fields Science Sums**
EDEN	0.20	2.50	electron density sounder
EESA	1.50	1.50	Thermal 3D electron electrostatic analyser
IESA	1.50	2.00	Thermal 3D ion electrostatic analyser
CESA	2.50	2.00	Combined 3D ion/electron electrostatic analyser
ICA	5.00	6.00	3D ion composition
ECA	1.00	0.50	3D energetic ion/electron analyser
HEP	1.20	1.00	High energy particle detector
CPP	2.00	2.00	Centralised payload processor
	14.90	**17.50**	**Other Science Sums**
	39.30	**40.20**	**Science on Two Identical Platforms**
	19.65	**20.10**	**Platform ROM (≈ half of live mass)**

MMS bus Mass & Power by systems (from UCB proposal)

acronym	CBE (kg)	OAP (W)	
ACS	*(see below)*	*(see below)*	Attitude Control
EPS	28.48	9.69	Electrical Power
SMS	19.85		Struct. & Mech. - Bus Structure
TCS	4.62	2.63	Thermal Control
C&DH	15.39	43.8	Command & Data Handling
TT&C	5.17	13.92	Telecom
Prop	23.28	12.42	Propulsion
Fuel	50.00		Hydrazine Propellant
	146.78	**82.46**	**MMS Bus Sums**

ACS Unuque Detail

42	88	(4ea) HR14-75 RWAs
2	10	Oerstad ASC Star Tracker
0.2	0.5	Adcole 2DFSS Sun Sensor
44.2	98.5	**Revised ACS Totals**
2.00	2.00	CPP from Cross Scale Table
20.71		**Propulsion Hardware & Tanks**
82.83		**Hydrazine Propellant**

mass (kg)	OAP (W)	
128	139	**Revised Dry Bus (Only)**
187	**199**	**MISSION DRY M&P**
269		**WET LAUNCH MASS**

Table 5.1: straw-man mission mass and power compilation

5.4.1 Assumptions

The spacecraft assumptions and initial conditions are as follows:

- Highly Elliptical Orbit (HEO): 0.5Re x 30Re near Ecliptic Plane
- Three axis stabilize sun pointing main bus (loose pointing of $\pm 30^\circ$ for array power).
- Instrument platforms counter-rotating at five revolutions per minute (5 RPM)
- Main bus spin rate of once per year to account for the regression of nodes
- Two gear-synchronized rotating platforms ($|\omega_1| = |\omega_2|$)
- The assumed mass properties are provided in Table 5.2

Table 5.3 provides the straw-man hardware specifications.

Table 5.2: Mass Properties (kg)

		principal 2nd mass moments		
item	mass (kg)	I_1 (kgm^2)	I_2 (kgm^2)	I_3 (kgm^2)
Primary Bus	166			
Spin Platforms	42	5.24	2.93	2.93
Mag Booms	3	11.5	11.5	0
Wire Booms	8	851	528	305

Wire Boom Properties
Wire Mass Rate (m_w) = 0.003 kg/m
Wire Tip Mass (M_t) = 0.03 kg
Long Dipole (L_1) = 100 m
Short Dipole (L_2) = 80 m
Coloumb Damping (D) = 0.013 J / rad^2

Half Full Fuel Tank (liquid)
Pendulum Length (L_p) = 0.124 m
Pendulum Fuel Mass (M_p) = 12.2 kg
Pendulum Freq. (ω) = 1.57 rad/sec
Damping Coeff (C_θ) = 0.029 Nms / rad

Table 5.3: Straw-man Hardware Specifications

Adcole Two Axis Sun Sensor	Northrop Grumman Scalable SIRU	Honeywell HR-12 RWA
64° Field of View	0.0001° / √hr Random Walk	7 kg Total Mass
0.01° to 0.05° Accuracy	0.003 arc-sec / √Hz White Noise	0.0874 kgm^2 Rotor MOI
0.001° to 0.004° LSB Size	0.0016 deg/hr, 3σ Bias Stability	12 Nms max. Momentum
> 25 yrs of Flight Heritage	0.05 arc-sec / LSB Quantization	0.04 Nm max. Torque

5.4.2 System Modeling Design

This study incorporates several flight validated component modules from previous UCB/SSL missions. Those past mission studies include SNAP, THEMIS, and RBSP. These modules use Newton's law of motion acting on masses, springs and dampers, to build the more complex system models. The spacecraft main bus, magnetometer booms and spinning instrument platforms are all modeled as rigid bodies. The two fuel tanks are represented as 2D pendulums with damping that are attached to bus. The two instrument platforms are constrained to spin at the same rate using a gear-synchronous driver constraint. The spin rate of the platforms is controlled by a simple Proportional, Integral Derivative (PID) controller to maintain constant spin rate of five RPM relative to the bus. This PID controller generates torques in the common platforms drive motor. The reaction wheel models generate torques to maintain the desired pointing attitude of the main bus. These models are all developed in SimMechanics[1]. This software includes constraint and driver block libraries. The constraint tools are used to describe the relative motion of many bodies. Constrained and unactuated driver blocks model scleronomic constraints, and actuated driver blocks model rheonomic constraints. Constrained and driven bodies will respond to external forces and torques, as limited by their constraints. Each SimMechanics body is assigned physical dimensions and mass properties. Body Degrees of Freedom (DOF) are assigned to the bodies by adding joints. These bodies (or body and ground) are connected by joints where each joint is assigned DOFs.

Rigid Bodies

SimMechanics rigid bodies incorporate a body block to represent user-defined body properties. These body properties include: mass, center of mass, inertia tensor, and coordinate orientation for all connections. Users can also assign additional coordinate system to the connections. Fig. 5.4 presents the Eggbeater model. It includes the main satellite body, spinning platforms, booms, and fuel tanks. The small spots are centers of mass for each rigid body. Each coordinate system is represented by three orthogonal line segments.

[1]http://www.mathworks.com/index.html

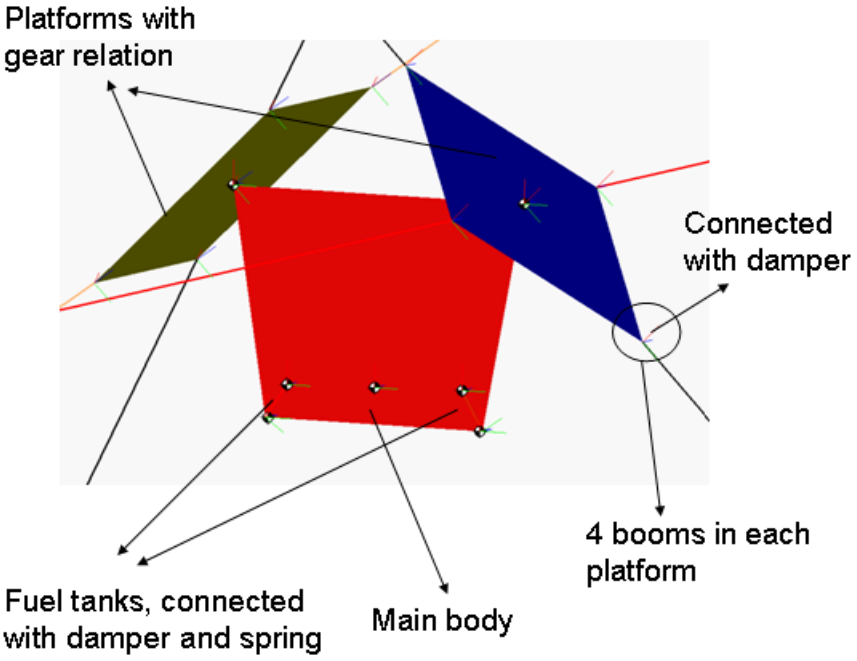

Figure 5.4: Rigid Body Representation in SimMechanics

Fuel tanks as Flexible Bodies

The THEMIS fuel tank model was incorporated into this study. The model assumes that the fuel can be represented as a point mass simple pendulum that oscillates about the fuel tanks geometric center. This approach assumes all of the liquid fuel moves as a single slug, given only modest excitation.

The pendulum mass is a function of the tank fill level and the pendulum length is described by the vector from the tank center to the fuel mass center. In the THEMIS model, the pendulum length is a function of the liquid height. Half of the liquid must above the center of the fuel mass and half below.

L_p is the length of the pendulum and R is the radius of the tank. The model assumes 50% volumetric fill fraction as a worst-case condition. Tab. 5.2 shows the initial parameters for the model of the fuel tanks and Eqn. (5.2) develops γ, ω, k_θ and c_θ. Q factor equals 10.

$$V(L_p) = \frac{1}{2}(1 - \frac{L_p}{R})^2 \cdot (2 + \frac{L_p}{R}) \tag{5.1}$$

$$\begin{aligned} \gamma &= \frac{1}{2Q} \\ \omega_f &= 2\pi f \\ k_\theta &= \omega_f^2 M_p L_p^2 \\ c_\theta &= 2\omega_f M_p L_p^2 \gamma \end{aligned} \tag{5.2}$$

Spin Plane Booms as Flexible Bodies

The instrument platform spin plane booms (SPB) are modeled as simple pendulums with all of their mass positioned at the center of percussion. Tab. 5.2 provides spin plane boom properties derived from RBSP models. Damping is described as energy loss per cycle divided by the motion amplitude squared. The cable damping is a combination of dry friction and hysteretic material behavior. Dry friction is due to small relative motions between the cable components. Hysteretic damping is the result of slightly anelastic behavior of materials. Single pendulum tests of the RBSP SPB cables in air and vacuum provided damping as a function of cable tension. [20] investigated the flexible appendage in a spacecraft with no degree freedom. This chapter assumes each boom attached to the rotation platform has two independent degrees of freedom consisting of two angle of rotation.

Reaction Wheel Assembly

The dynamic angular momentum exchange between rotor and housing is captured in the reaction wheel model. The bus pointing controller provides inputs to the individual wheel controllers. The allowed wheel acceleration is limited by their controllers. The accumulated momentum must be periodically unloaded by the propulsion system thrusters when wheels approach their rated speed. The performance of reaction wheel models is based on published Honeywell HR-12 data[2]. The four reaction wheels are oriented in the traditional tetrahedral vector manner to provide redundancy. This model was developed from the SNAP mission design studies. The reader can get more detail of the reaction wheels design in [2].

5.4.3 Platform Constraint

The constraint between instrument platforms restricts the platforms to equal but opposite angular rates. The SimMechanics library Gear Constraint block in Fig. 5.5(a) was implemented. This constraint uses base and follower bodies (the platforms) to represent meshed gears. The base and follower bodies must be attached to a third carrier body (the spacecraft bus) by a revolute or cylindrical joint. These joint geometric choices define the gear and platform rotation axes. The instrument platform mounted booms and bus mounted fuel tanks use the internal force blocks. These blocks are connected to their respective bodies

[2]http://www51.honeywell.com

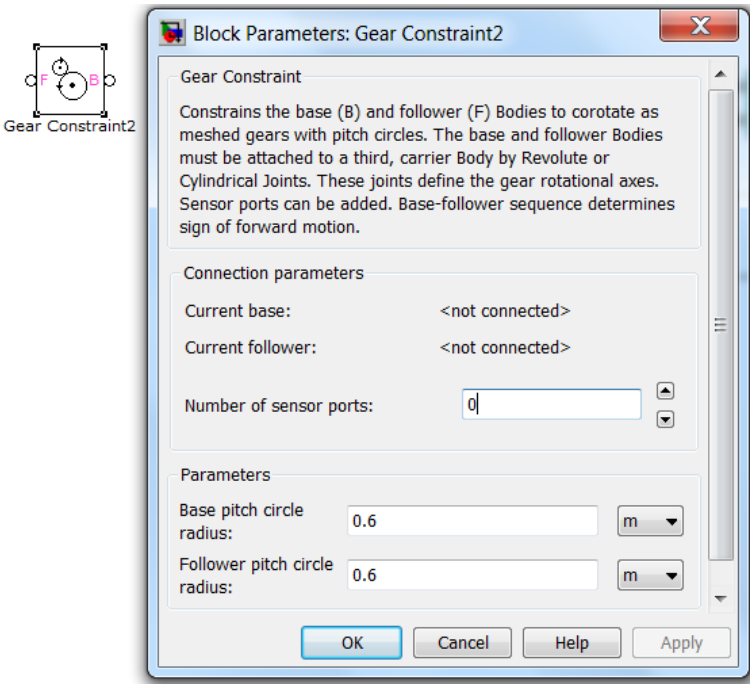

(a) Gear Constraint Block

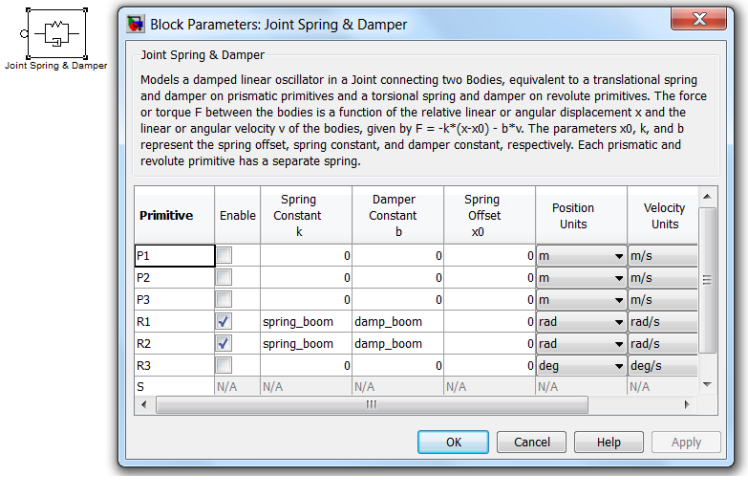

(b) Internal Force block

Figure 5.5: Gear Constraint and Internal Force Block

to represent their known springs and dampers. Fig. 5.5(b) shows an internal force block data module.

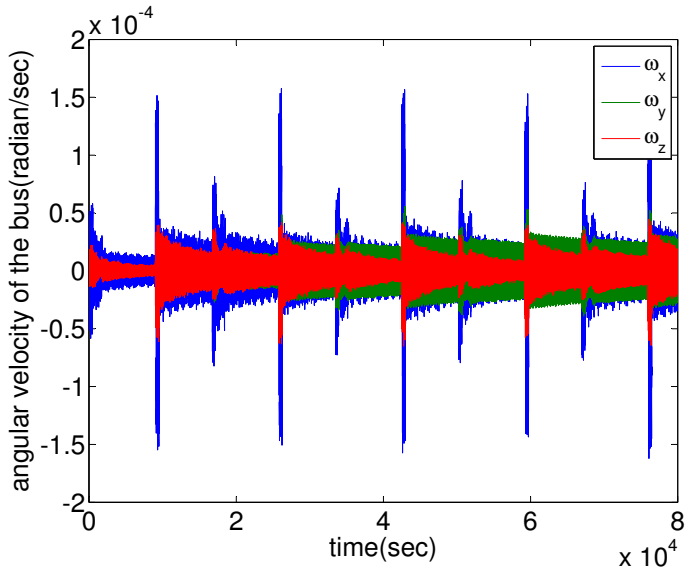

(a) Angular Velocity with Respect to the Body Frame

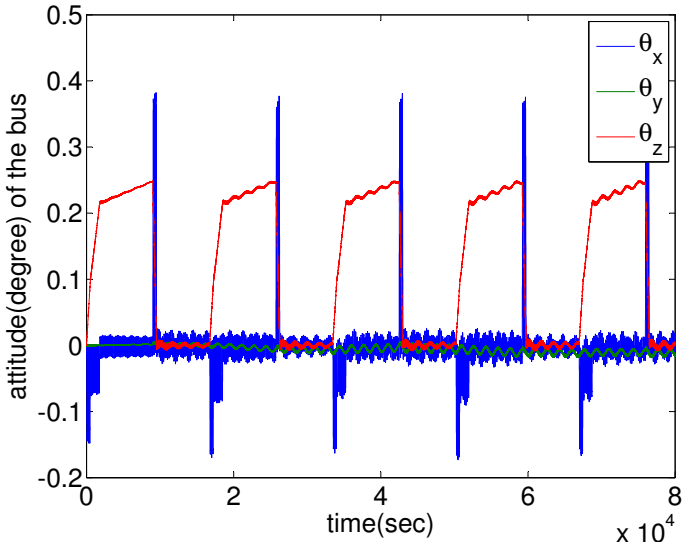

(b) Attitude Change with Respect to the Inertial Frame

Figure 5.6: Bus Control Off and Platform Control Off

5.4.4 The Bus Control Law

The reaction wheels provide the needed vector torques to maintain the bus pointing attitude. The bus controller processes attitude sensor inputs to determine the vector bus pointing error. This data is translated to inertial bus coordinates to establish the $\Delta\omega$ command for each wheel. As previously noted the wheel spin vectors are arranged in a redundant tetrahedron[3], which means there is not a unique $\Delta\omega$ wheel distribution solution. The controller uses the least square optimization of the underdetermined case to translate the input vector command to the four individual $\Delta\omega$ wheel commands. The four vectors from the tetrahedron center to each wheel rotation vectors are:

$$\begin{aligned}
\vec{e_1} &= \begin{pmatrix} \frac{2\sqrt{2}}{3} & 0 & \frac{-1}{3} \end{pmatrix}^T \\
\vec{e_2} &= \begin{pmatrix} \frac{-\sqrt{2}}{3} & \frac{\sqrt{6}}{3} & \frac{-1}{3} \end{pmatrix}^T \\
\vec{e_3} &= \begin{pmatrix} \frac{-\sqrt{2}}{3} & \frac{-\sqrt{6}}{3} & \frac{-1}{3} \end{pmatrix}^T \\
\vec{e_4} &= \begin{pmatrix} 0 & 0 & 1 \end{pmatrix}^T
\end{aligned} \tag{5.3}$$

Those unit vectors form the matrix A:

$$A = \begin{pmatrix} \vec{e_1} & \vec{e_2} & \vec{e_3} & \vec{e_4} \end{pmatrix} \tag{5.4}$$

Using the least square method of the underdetermined case[4], we can get:

$$x_{opt} = A^T(AA^T)^{-1}y \tag{5.5}$$

x_{opt} is the solution of this optimal problem and y is the command from the controller:

$$\begin{aligned}
&minimize\ \|x\| \\
&subject\ to\ Ax = y
\end{aligned} \tag{5.6}$$

The gyroscope and sun sensor provide current bus attitude information to the bus pointing controller. This controller uses states of Gibber parameters from quaternions [69] while the attitude corrections use the Lyapunov function [56]. Gyroscope data is processed for the rotation matrix C, which is expressed as a quaternion [69]:

$$q_4 = \frac{1}{2}(1 + C_{11} + C_{22} + C_{33})^{\frac{1}{2}} \qquad for\ 0 \leq \theta \leq \pi \tag{5.7}$$

$$\mathbf{q} = \begin{pmatrix} q_1 & q_2 & q_3 \end{pmatrix}^T \tag{5.8}$$

[3]the geometry of the tetrahedron: http://www.wretch.cc/blog/febull/8869566

[4]http://see.stanford.edu/materials/lsoeldsee263/08-min-norm.pdf

$$\mathbf{q} = \frac{1}{4q_4}\begin{pmatrix} C_{23} - C_{32} \\ C_{31} - C_{13} \\ C_{12} - C_{21} \end{pmatrix} \qquad if\ q_4 \neq 0 \tag{5.9}$$

The relation of the time derivative of quaternions with angular velocity is:

$$\begin{pmatrix} \dot{q}_1 \\ \dot{q}_2 \\ \dot{q}_3 \\ \dot{q}_4 \end{pmatrix} = \frac{1}{2}\begin{pmatrix} q_4 & -q_3 & q_2 & q_1 \\ q_3 & q_4 & -q_1 & q_2 \\ -q_2 & q_1 & q_4 & q_3 \\ -q_1 & -q_2 & -q_3 & q_4 \end{pmatrix}\begin{pmatrix} \omega_1 \\ \omega_2 \\ \omega_3 \\ 0 \end{pmatrix} \tag{5.10}$$

Gibber parameters from quaternions are:

$$\boldsymbol{g} = \begin{pmatrix} g_1 \\ g_2 \\ g_3 \end{pmatrix} = \begin{pmatrix} q_1/q_4 \\ q_2/q_4 \\ q_3/q_4 \end{pmatrix} \tag{5.11}$$

Define:

$$\mathbf{G} = \begin{pmatrix} 0 & -g_3 & g_2 \\ g_3 & 0 & -g_1 \\ -g_2 & g_1 & 0 \end{pmatrix} \tag{5.12}$$

We can get the time derivative of each component in Eq. (5.11).

$$\begin{aligned} \dot{g_1} =& \dot{q_1}{q_4}^{-1} - q_1{q_4}^{-2}\dot{q_4} \\ =& \frac{1}{2}\frac{q_4(q_4\omega_1 - q_3\omega_2 + q_2\omega_3) - q_1(-q_1\omega_1 - q_2\omega_2 - q_3\omega_3)}{{q_4}^2} \\ =& \frac{1}{2}(\omega_1 + \frac{q_3}{q_4}\omega_2 + \frac{q_2}{q_4}\omega_3 + \frac{{q_1}^2}{{q_4}^2}\omega_1 + \frac{q_1q_2}{{q_4}^2}\omega_2 + \frac{q_1q_3}{{q_4}^2}\omega_3) \\ =& \frac{1}{2}((1 + {g_1}^2)\omega_1 + (g_1g_2 - g_3)\omega_2 + (g_1g_3 + g_2)\omega_3) \end{aligned} \tag{5.13}$$

Take time derivative to g_2 and g_3, we can get:

$$\begin{pmatrix} \dot{g_1} \\ \dot{g_2} \\ \dot{g_3} \end{pmatrix} = \begin{pmatrix} 1 + {g_1}^2 & g_1g_2 - g_3 & g_1g_3 + g_2 \\ g_2g_1 + g_3 & 1 + {g_2}^2 & g_2g_3 - g_1 \\ g_3g_1 - g_2 & g_3g_2 + g_1 & 1 + {g_3}^2 \end{pmatrix}\begin{pmatrix} \omega_1 \\ \omega_2 \\ \omega_3 \end{pmatrix} \tag{5.14}$$

$$\dot{\boldsymbol{g}} = \frac{1}{2}(\boldsymbol{I} + \boldsymbol{G} + \boldsymbol{g}\boldsymbol{g}^{\boldsymbol{T}})\boldsymbol{\omega} = \boldsymbol{Z}(\boldsymbol{g})\boldsymbol{\omega} \tag{5.15}$$

$$\boldsymbol{\omega} = \boldsymbol{Z}^{-\mathbf{1}}\dot{\boldsymbol{g}} \tag{5.16}$$

We assume the gyroscope provide the controller correct feedback signals without the noise at this moment. To deal with the noise, reader can refer the work of McDuffie and Shtessel [42] who used the sliding mode observer to reduce the tracking quaternion errors. The control goal is to stabilize the bus and reject the external disturbances from the platforms and the

internal disturbances from the fuel tanks. We assume the bus is a rigid body. The attitude equation is Euler's Rotational Equation of Motion:

$$\begin{aligned} \boldsymbol{J}\dot{\boldsymbol{\omega}} &= \boldsymbol{J}\boldsymbol{\omega} \times \boldsymbol{\omega} + \boldsymbol{\tau} \\ &= \boldsymbol{p} \times \boldsymbol{\omega} + \boldsymbol{\tau} \end{aligned} \tag{5.17}$$

$$\dot{\boldsymbol{\omega}} = \boldsymbol{J}^{-1}\boldsymbol{p} \times \boldsymbol{\omega} + \boldsymbol{J}^{-1}\boldsymbol{\tau} \tag{5.18}$$

$\boldsymbol{J}$ is the moment of inertia matrix. $\boldsymbol{p}$ is the angular momentum with respect to the body frame. Following the design procedure from Slotine and Li [56], do the time derivative for Eq. (5.15).

$$\ddot{\boldsymbol{g}} = \dot{\boldsymbol{Z}}\boldsymbol{\omega} + \boldsymbol{Z}\dot{\boldsymbol{\omega}} \tag{5.19}$$

Using the Eq. (5.16) and Eq. (5.18), we can get:

$$\ddot{\boldsymbol{g}} = \dot{\boldsymbol{Z}}\boldsymbol{Z}^{-1}\dot{\boldsymbol{g}} + \boldsymbol{Z}(\boldsymbol{J}^{-1}\boldsymbol{p} \times \boldsymbol{Z}^{-1}\dot{\boldsymbol{g}} + \boldsymbol{J}^{-1}\boldsymbol{\tau}) \tag{5.20}$$

Multiply $\boldsymbol{Z}^{-\boldsymbol{T}}\boldsymbol{J}\boldsymbol{Z}^{-1}$ in both sides,

$$\boldsymbol{Z}^{-\boldsymbol{T}}\boldsymbol{J}\boldsymbol{Z}^{-1}\ddot{\boldsymbol{g}} = \boldsymbol{Z}^{-\boldsymbol{T}}\boldsymbol{J}\boldsymbol{Z}^{-1}\dot{\boldsymbol{Z}}\boldsymbol{Z}^{-1}\dot{\boldsymbol{g}} + \boldsymbol{Z}^{-\boldsymbol{T}}\boldsymbol{p} \times \boldsymbol{Z}^{-1}\dot{\boldsymbol{g}} + \boldsymbol{Z}^{-\boldsymbol{T}}\boldsymbol{\tau} \tag{5.21}$$

Let

$$\begin{aligned} &\boldsymbol{\tau} = \boldsymbol{Z}^{\boldsymbol{T}}\boldsymbol{F} \\ &\boldsymbol{H}^*(\boldsymbol{g}) = \boldsymbol{Z}^{-\boldsymbol{T}}\boldsymbol{J}\boldsymbol{Z}^{-1} \\ &\boldsymbol{C}^*(\boldsymbol{g}, \dot{\boldsymbol{g}}) = -\boldsymbol{Z}^{-\boldsymbol{T}}\boldsymbol{J}\boldsymbol{Z}^{-1}\dot{\boldsymbol{Z}}\boldsymbol{Z}^{-1} - \boldsymbol{Z}^{-\boldsymbol{T}}\boldsymbol{p} \times \boldsymbol{Z}^{-1} \end{aligned} \tag{5.22}$$

The governing equations for the bus are:

$$\boldsymbol{H}^*(\boldsymbol{g})\ddot{\boldsymbol{g}} + \boldsymbol{C}^*(\boldsymbol{g}, \dot{\boldsymbol{g}})\dot{\boldsymbol{g}} = \boldsymbol{F} \tag{5.23}$$

$\boldsymbol{F}$ is designed for the control law to stabilize the whole bus, then it is converted to the real torque $\boldsymbol{\tau}$. Eq. (5.5) is responsible for arranging the torque command to each reaction wheels command. The following is a simple expression for $\boldsymbol{Z}^{-1}$:

$$\boldsymbol{Z}^{-1} = \boldsymbol{2}(\boldsymbol{1} + \boldsymbol{g}^{\boldsymbol{T}}\boldsymbol{g})^{-1}(\boldsymbol{I} - \boldsymbol{G}) \tag{5.24}$$

Proof:

$$\begin{aligned} &\boldsymbol{Z}\boldsymbol{Z}^{-1} = \frac{\boldsymbol{1}}{\boldsymbol{2}}(\boldsymbol{I} + \boldsymbol{G} + \boldsymbol{g}\boldsymbol{g}^{\boldsymbol{T}})\boldsymbol{2}(\boldsymbol{1} + \boldsymbol{g}^{\boldsymbol{T}}\boldsymbol{g})^{-1}(\boldsymbol{I} - \boldsymbol{G}) \\ &= (\boldsymbol{I} - \boldsymbol{G}\boldsymbol{G} + \boldsymbol{g}\boldsymbol{g}^{\boldsymbol{T}} - \boldsymbol{g}\boldsymbol{g}^{\boldsymbol{T}}\boldsymbol{G})(\boldsymbol{1} + \boldsymbol{g}^{\boldsymbol{T}}\boldsymbol{g})^{-1} \\ &= (\boldsymbol{1} + \boldsymbol{g}^{\boldsymbol{T}}\boldsymbol{g})^{-1}(\begin{pmatrix} \boldsymbol{1} & \boldsymbol{0} & \boldsymbol{0} \\ \boldsymbol{0} & \boldsymbol{1} & \boldsymbol{0} \\ \boldsymbol{0} & \boldsymbol{0} & \boldsymbol{1} \end{pmatrix} - \begin{pmatrix} -\boldsymbol{g}_3^2 - \boldsymbol{g}_2^2 & \boldsymbol{g}_1\boldsymbol{g}_2 & \boldsymbol{g}_3\boldsymbol{g}_1 \\ \boldsymbol{g}_2\boldsymbol{g}_1 & -\boldsymbol{g}_3^2 - \boldsymbol{g}_1^2 & \boldsymbol{g}_3\boldsymbol{g}_2 \\ \boldsymbol{g}_1\boldsymbol{g}_3 & \boldsymbol{g}_3\boldsymbol{g}_2 & -\boldsymbol{g}_1^2 - \boldsymbol{g}_2^2 \end{pmatrix} + \begin{pmatrix} \boldsymbol{g}_1^2 & \boldsymbol{g}_1\boldsymbol{g}_2 & \boldsymbol{g}_1\boldsymbol{g}_3 \\ \boldsymbol{g}_2\boldsymbol{g}_1 & \boldsymbol{g}_2^2 & \boldsymbol{g}_2\boldsymbol{g}_3 \\ \boldsymbol{g}_3\boldsymbol{g}_1 & \boldsymbol{g}_3\boldsymbol{g}_2 & \boldsymbol{g}_3^2 \end{pmatrix}) \\ &= (\boldsymbol{1} + \boldsymbol{g}^{\boldsymbol{T}}\boldsymbol{g})^{-1} \begin{pmatrix} \boldsymbol{1} + \boldsymbol{g}_1^2 + \boldsymbol{g}_2^2 + \boldsymbol{g}_3^2 & \boldsymbol{0} & \boldsymbol{0} \\ \boldsymbol{0} & \boldsymbol{1} + \boldsymbol{g}_1^2 + \boldsymbol{g}_2^2 + \boldsymbol{g}_3^2 & \boldsymbol{0} \\ \boldsymbol{0} & \boldsymbol{0} & \boldsymbol{1} + \boldsymbol{g}_1^2 + \boldsymbol{g}_2^2 + \boldsymbol{g}_3^2 \end{pmatrix} \\ &= (\boldsymbol{1} + \boldsymbol{g}^{\boldsymbol{T}}\boldsymbol{g})^{-1}(\boldsymbol{1} + \boldsymbol{g}^{\boldsymbol{T}}\boldsymbol{g}) \cdot \boldsymbol{I} \\ &= \boldsymbol{I} \end{aligned} \tag{5.25}$$

We know:

$$\frac{d(ZZ^{-1})}{dt} = 0 = \dot{Z}Z^{-1} + Z\dot{Z}^{-1} \tag{5.26}$$

$$\dot{Z}^{-1} = -Z^{-1}\dot{Z}Z^{-1} \tag{5.27}$$

We know $p\times$ is a skew-symmetric matrix. It can be shown that $\dot{H}^* - 2C^*$ is also the skew-symmetric matrix.
Proof:

$$\begin{aligned}
&\dot{H}^* - 2C^* = \dot{Z}^{-T}JZ^{-1} + Z^{-T}J\dot{Z}^{-1} - 2(-Z^{-T}JZ^{-1}\dot{Z}Z^{-1} - Z^{-T}p \times Z^{-1}) \\
&= \dot{Z}^{-T}JZ^{-1} - Z^{-T}J\dot{Z}^{-1} + 2Z^{-T}p \times Z^{-1} \\
&(\dot{H}^* - 2C^*)^T = Z^{-T}J^T\dot{Z}^{-1} - \dot{Z}^{-T}J^TZ^{-1} - 2Z^{-T}p \times Z^{-1} \\
&= -(\dot{H}^* - 2C^*)
\end{aligned} \tag{5.28}$$

Using the Lyapunov function to find the control rule. Choose the Lyapunov candidate:

$$V = \frac{1}{2}(\dot{g}^T H^* \dot{g} + g^T K_P g) \tag{5.29}$$

This candidate involves all of the attitude states and their time derivatives. K_P is a constant positive definite matrix. The time derivative of the candidate is:

$$\begin{aligned}
\dot{V} &= (\frac{1}{2}\dot{g}^T\dot{H}^*\dot{g} + \dot{g}^T H^*\ddot{g} + g^T K_P\dot{g}) \\
&= (\frac{1}{2}\dot{g}^T\dot{H}^*\dot{g} + \dot{g}^T(F - C^*\dot{g}) + g^T K_P\dot{g}) \\
&= \frac{1}{2}\dot{g}^T(\dot{H}^* - 2C^*)g^* + \dot{g}^T(F + K_P g) \\
&= \dot{g}^T(F + K_P g)
\end{aligned} \tag{5.30}$$

choose a simple PD control law for $\mathbf{F}$.

$$F = -(K_P g + K_D\dot{g}) \tag{5.31}$$

Eq. (5.30) becomes:

$$\dot{V} = -\dot{g}^T K_D\dot{g} \leq 0 \tag{5.32}$$

To check if this candidate get stuck in some point or not, assuming $\dot{g} = 0$ and $\ddot{g} = H^{*-1}K_P g$. It always has the acceleration to drive the states to the origin until $g = 0$. Therefore the bus can be stabilized at origin. In this expression K_P and K_D should be positive definite matrices. The resulting Gibbs vector is not globally singular, so we must assume the bus pointing attitude deviations are small. The controlled states are the bus pointing direction and its angular velocities. This selected bus controller design does not consider the complicating impact of the instrument platforms and wire booms. This assumption is another way of stating that the platform spin and bus pointing controller are completely decoupled.

5.4.5 The Platform Control Law

The platform spin controller uses a canonical PID control law. The input is the spin rate error and the output is the motor torque command. The torque command is applied to the platform bodies through a SimMechanics connected joint, which imposes a reaction counter-torque on the bus body to satisfy the Newton's third law.

5.5 Simulation Results

5.5.1 Doublet Disturbance Response

Some type of input doublet is widely used to explore the open loop local stability of dynamic systems because it does not impose any lasting changes. A torque doublet in body coordinates was selected, to be applied to the main bus. Fig. 5.7(a) shows the open loop bus angular velocities in body coordinates. The resulting angular velocities are around 10^{-13} rad/sec. Fig. 5.7(b), (c) and (d) show this doublet applied to the X, Y and Z axes respectively. The transient response magnitudes correlate well with the moments of inertia about the excited axis. We can find that if the doublet disturbance is applied in the y direction w.r.t. the local frame. The dynamics in x and z don't change much.

The dynamics continuously oscillates if there is no control applied. These collected results suggest this system is neutrally stable. It will have transfer function poles close to the imaginary axis, or when the system is disturbed, oscillations will decay very slowly.

5.5.2 Orbital Earths Shadow Perturbations

Earth shadows are experienced in most orbits, where mission orbit planning typically targets three hours for the maximum period. Prior single spin missions with wire booms have observed small gradual spin increases ($< 1\%$) while in shadow. This is caused by rapid cooling and the subsequent thermal contraction of the long wires. With this dual spin configuration and both controllers off, the shadow response is largely benign. The platform spin rates will increase slightly as the wire 2nd mass moments decrease, while total angular momentum in this system must be conserved. Fig. 5.6 shows the gradual bus yaw to a maximum of 0.24°, which then returns to the sun after orbit sunrise, for a three hour simulated shadow. When both platform spin and bus pointing controllers are in shadow, the controllers dictate the momentum exchanges between the platforms, bus, and reaction wheels to provide the desired attitude and platform performance. Fig. 5.9 shows bus pointing variations of 0.4° and 0.5 milli-rad/sec angular velocity variations caused by these controller interactions. If the bus control off but platform control on, the reaction torques from the platform controller will make the bus attitude drift. Fig. 5.10 shows the bus drift increasing to 26° after 80000 sec. (22 hr.). Figure 5.11 shows very good bus pointing performance with the platform spin controller off. However, with platform spin control off, the platforms rotating friction gradually decreases their spin rate.

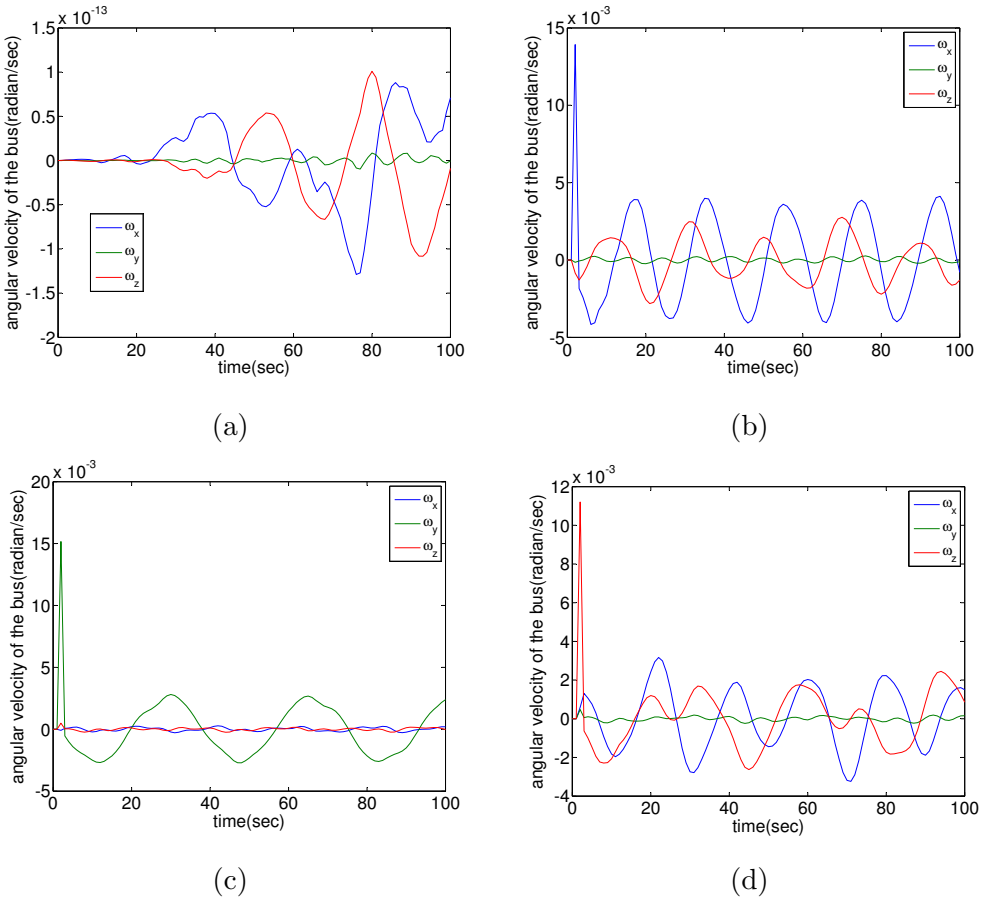

Figure 5.7: Doublet Effects to the Bus Angular Velocity

5.5.3 Unloading the Bus Reaction Wheels

Propulsion system thrusters are used to unload accumulated reaction wheel angular momentum before they exceed their rated maximum speed. A very common mission design has no controller interactions between the propulsion and pointing control systems. The pointing controller simply responds to the thruster torques in the same manner as external disturbances. The known limitation is that thruster torques cannot exceed the rated acceleration of the reaction wheels, which often means that thrusters must be pulse width modulated. Fig. 5.12 illustrates this unloading response using a 1 N thruster with a 10% duty cycle that is located one meter from the bus CG.

5.5.4 Disturbance Settling Times

Maximizing valid science data is a goal of all missions, which means either avoiding known disturbances or minimizing their post event settling time. Wire booms are believed to provide good science data when their excursions are less that $\pm\frac{1}{2}^{\circ}$. Fig. 5.13(a) and (b)

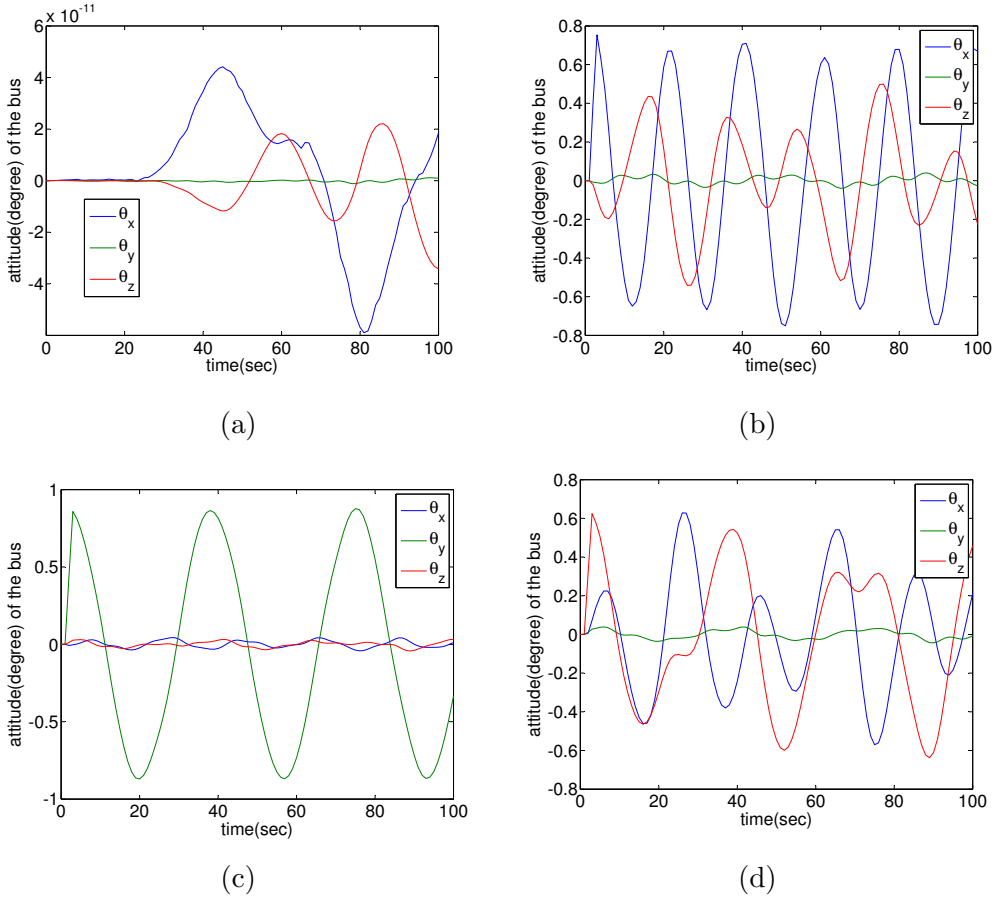

Figure 5.8: Doublets Effects to the Bus Attitude

illustrate the modest settling times associated with the flexible wire booms and fuel tank disturbances.

5.5.5 Stability of This Dual Spin Dynamic System

As previously observed, the idealized system appears neutrally stable. Adding energy dissipation to the model tends to destabilize the system. The modeled energy loss mechanisms include wire boom damping, spin platform drive friction, and fuel slosh. Energy loss on the platforms means their angular momentum is slowly decreasing. The resulting torques must be counteracted by the bus. In normal operation, these torques are countered by gradual speed changes of the four bus reaction wheels. If both the platform spin and bus pointing controllers are off, there is a gradual momentum transfer to the bus. The previously described by bus yaw eventually changes a lot and undesired bus spin which puts the wire booms into ever increasing oscillating helical trajectories. The wires will eventually catastrophically tangle as their spin decreases. Fig. 5.14 shows this degenerating performance,

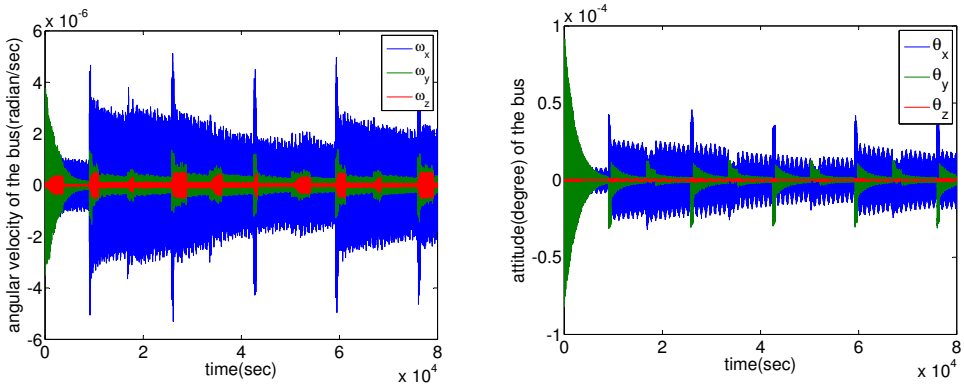

(a) Angular velocities of the Bus (b) Drifting Attitude of the Bus

Figure 5.9: Bus Control On and Platform Control On

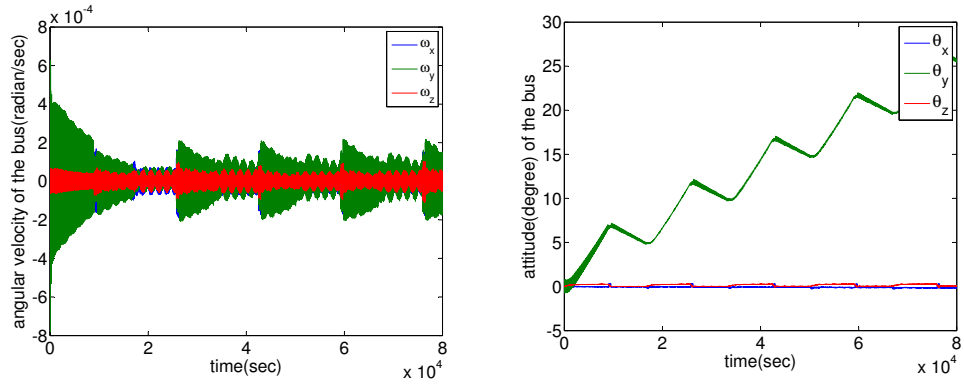

(a) Angular velocities of the Bus (b) Drifting Attitude of the Bus

Figure 5.10: Bus Control Off and Platform Control On

where the mission would be considered at risk after about four hours of loss of control. This means that these controllers should be classified as mission critical and would be included in the safe hold planning.

5.6 Summary

The SimMechanics modeling of the open loop dynamic system indicates that it is neutrally stable, which is the case for most actively pointed space missions. Adding system energy losses in the form of friction, damping, and fuel slosh introduces modest instabilities that can readily be actively controlled. The bus pointing controller design is a multiple input multiple output (MIMO) system. There are three inputs and three outputs. Each of the input and output relations is decoupled in the controller. In this formulation, the states

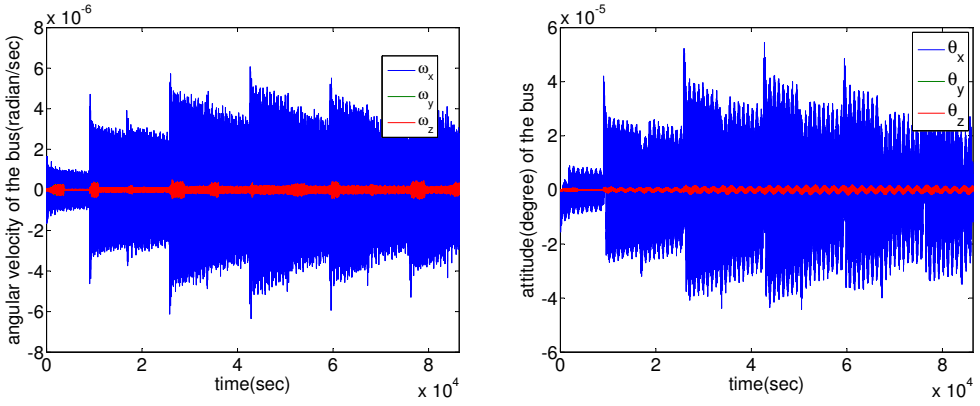

(a) Angular velocities of the Bus (b) Drifting Attitude of the Bus

Figure 5.11: Bus Control On and Platform Control Off

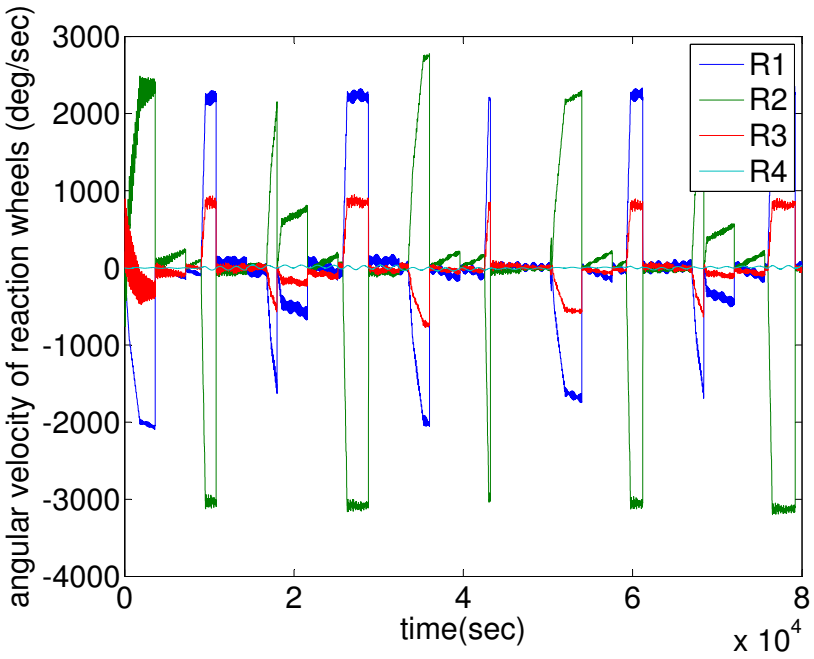

Figure 5.12: The Response of the Reaction Wheels SimMechanics

are described as quaternions. The pointing controller design invokes the Lyapunov function methods. The spin platforms speed is controlled with a classical PID controller while the platform gear drive insures that there is no chance of platform appendage collisions. The typical science requirement for this category of instruments is fractional degree angular stability, where these simulations have demonstrated that this goal can be achieved for known space mission and operational disturbances.

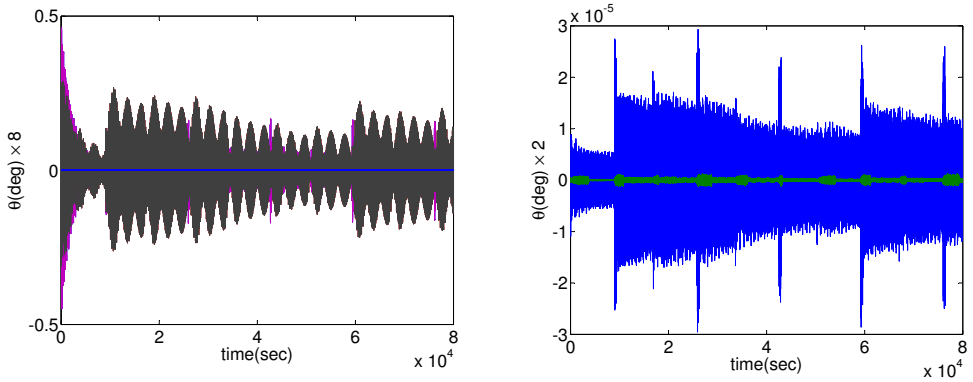

(a) Booms Settling Time (b) Fuel Tank Settling Time

Figure 5.13: Disturbance Settling Time

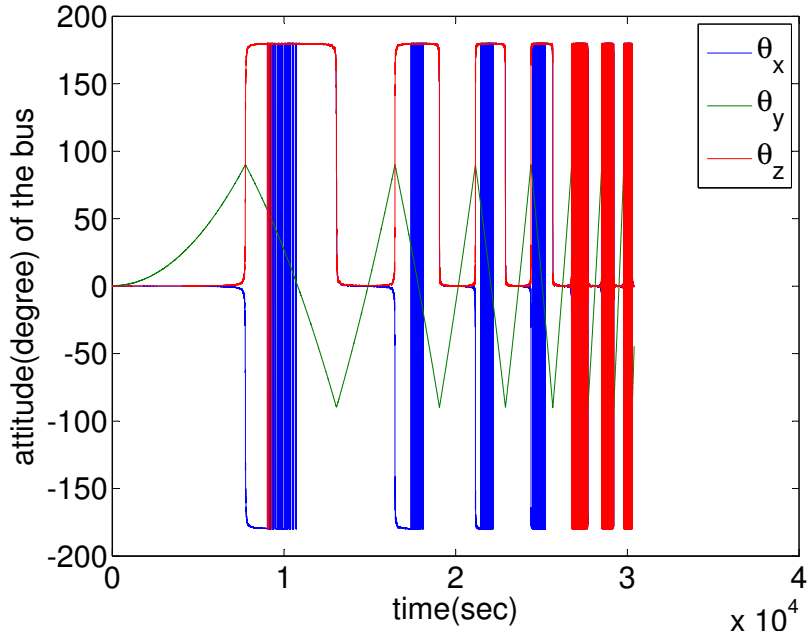

Figure 5.14: Degenerating Performance in Bus Orientation

The identified risk in this mission concept is friction in the platform drives. This friction can be minimized by proper design choices. For example, transferring instrument data by Bluetooth or similar wireless methods would mean that only a few platform slip rings would only be needed for raw platform power. There are several options for the dual platform drive motor, where the (low speed, high torque) direct drive motor is the choice that minimizes friction. This solution has been historically considered an expensive novelty, while they are

now widely used in the robotics industry. As a relevant example, the NASA POLAR satellite (1996) de-spun platform used a 24 pole direct drive motor that consumed only 12W avg. and ran flawlessly for more than ten years on orbit.

A related mission design goal is the maturation of (pointing and spin) controllers that will meet NASAs definition of safe hold systems. In brief, this calls for all (electrical) hardware solutions, or perhaps mostly hardware with modest software. The spin controller is an easy task while the bus pointing control algorithms will prove more challenging. The described pointing control system logic might be achieved by implementing a NASA approved field programmable gate array (FPGA).

These study results suggest that with proper planning and early development, this mission concept could fit into the low to medium risk NASA reviewer categories.

Chapter 6

The Pointing Control of a Multibody System - Balloon-Borne Gondola

6.1 Mission Initiation

In chapter 4 and 5, we present how to control a rigid body and stabilize a multibody system. In this chapter, we describe how to do the pointing control for a multibody system.

A pointing control system is developed for the Gamma-Ray Imager/Polarimeter for Solar flares (GRIPS) balloon-borne instrument which provides a near-optimal combination of high-resolution imaging, spectroscopy, and polarimetry of solar-flare gamma-ray/hard X-ray emissions from ∼20 keV to ∼10 MeV. Within the narrow field of view of its sun sensor, the telescope must track the sun with a 0.5 degrees rms accuracy. This chapter introduces the mechanical structure of the pointing control system and investigates the dynamics and control strategy and presents the simulation and experimental results.

6.2 System Overview

The mechanical structure of the full system is shown in Fig. 6.1. This includes the balloon which is connected to a parachute for gondola recovery . The parachute is connected to the gondola by a ladder line. A gondola rotator is driven by a brushless motor, located between the gondola and the ladder line to generate the torque needed for gondola azimuth control. A Joyce actuator drive is used to control elevation of the telescope. A precision sun sensor with a 12X square field of view (FOV) provides the pointing system input. Prior studies and flight experience have indicated that ladder line torque feedback is needed to stabilize its pointing system. Unfortunately, strain gages are known to be temperamental for sub-PPM measurements. A modified azimuth control method has been developed to replace the strain gage torque cell. System modeling has revealed that dynamic elevation control would need more sensors and actuators, so a quasi-static approach is used. This study develops a

dynamic system model with quasi-static elevation control. Telescope elevation is sensed by an absolute angle encoder supplemented by a more precise incremental encoder on the drive motor. A GPS receiver provides data to calculate the current sun elevation.

6.3 Balloon Point System Dynamics

Experience indicates that the roll angle about the telescope axis will be quite small. This greatly simplifies the modeling by decoupling the telescope pitch and yaw.

6.3.1 Elevation Dynamics

This system has six degrees of freedom. x, y coordinates describe the motion of the balloon center of mass. θ_1 is the elevation of the gondola. θ_2 is the elevation of telescope relative to the gondola. θ_3 is the elevation of the balloon. θ_4 is the elevation of the ladder line and parachute. L_1 is the length from the CG of the gondola to the ladder line bottom. L_2 is the length from the CG of the telescope to the bottom of the ladder line. L_3 is the length from the CG of the balloon to the top of the parachute. L_4 is the length of the parachute and ladder line. J_1, J_2 and J_3 are the second mass moments (MOIs) of the gondola, telescope, and balloon respectively.[1]. m_1, m_2 and m_3 are masses of the gondola, telescope, and balloon respectively. The elevation dynamics can be described using Lagrangian methods Eqn. (6.1). $\mathbb{L}$ is the Lagrangian and equal to $T-U$. T is the kinetic energy and U is the potential energy. q is the generalized coordinate vector.

$$\frac{d}{dt}\frac{\partial \mathbb{L}}{\partial \dot{q}} - \frac{\partial \mathbb{L}}{\partial q} = 0 \tag{6.1}$$

$$q = \begin{pmatrix} x & y & \theta_3 & \theta_4 & \theta_1 & \theta_2 \end{pmatrix}^T \tag{6.2}$$

We assume that θ_1, θ_3, and θ_4 are small. All of the angular velocity $\dot{\theta}_i$ are small.

$$\begin{aligned} \sin(\theta) &\approx \theta \\ \cos(\theta) &\approx 1 - \frac{\theta^2}{2} \end{aligned} \tag{6.3}$$

By ignoring the higher order terms, the kinetic energy can be obtained as

$$\begin{aligned} T =& \frac{1}{2}m_3(\dot{x}^2 + \dot{y}^2) + \frac{1}{2}m_1(\dot{x} + L_3\dot{\theta}_3 + L_4\dot{\theta}_4 + L_1\dot{\theta}_1)^2 + \\ & \frac{1}{2}m_2(\dot{x} + L_3\dot{\theta}_3 + L_4\dot{\theta}_4 + L_2\dot{\theta}_1)^2 + \\ & \frac{1}{2}(m_1 + m_2)\dot{y}^2 + \frac{1}{2}J_3\dot{\theta}_3^2 + \frac{1}{2}J_1\dot{\theta}_1^2 + \frac{1}{2}J_2(\dot{\theta}_1 + \dot{\theta}_2)^2 \end{aligned} \tag{6.4}$$

[1] All J_i are in the out of paper direction

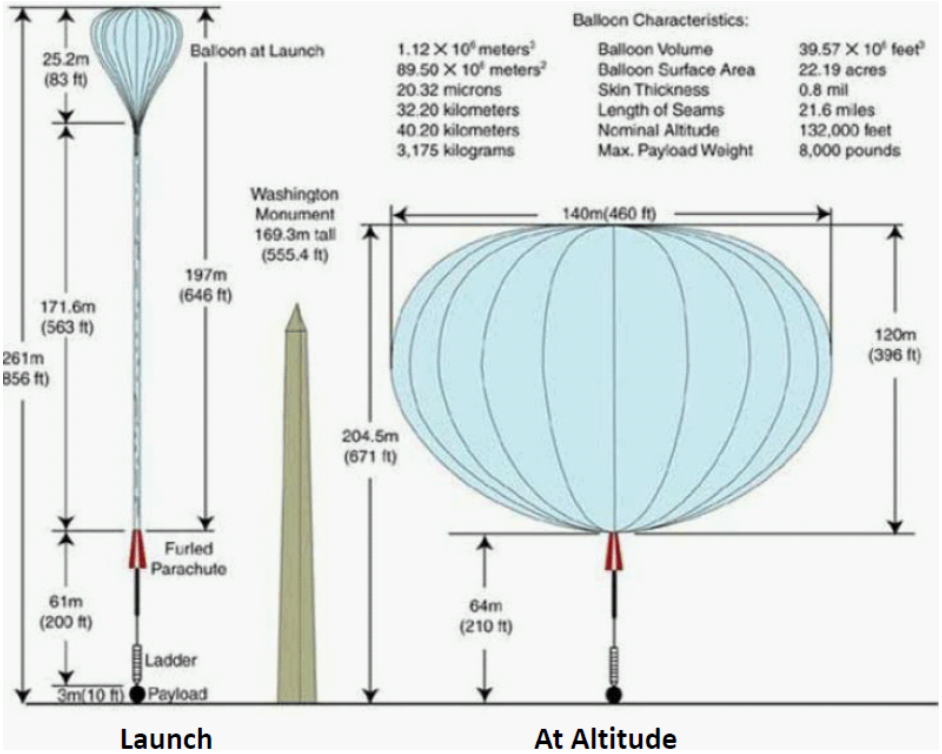

(a) Overview of the Whole System

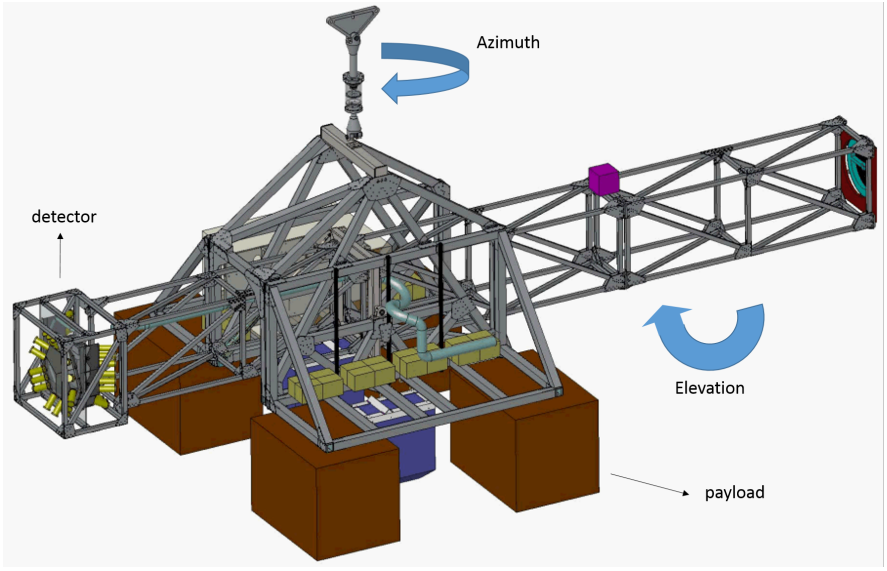

(b) Gondola Structure

Figure 6.1: Mechanical Structure of the whole System

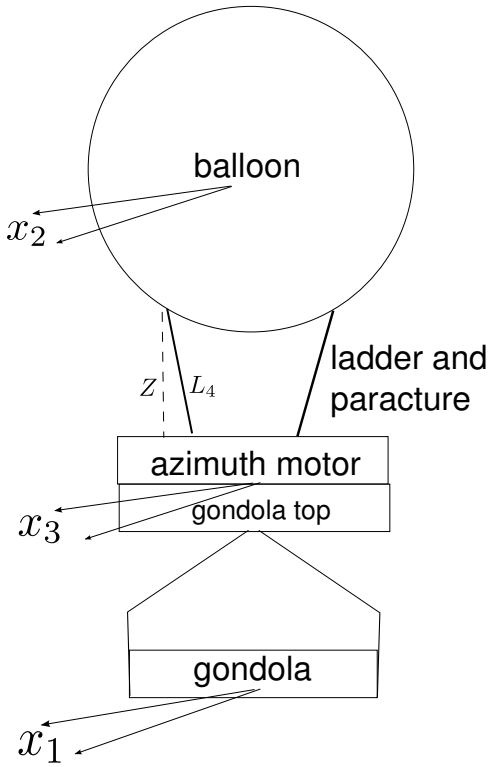

(a) Azimuth System

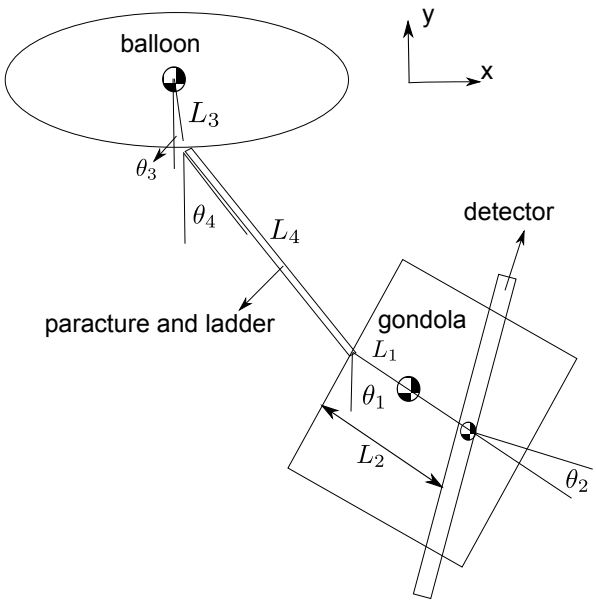

(b) Elevation System

Figure 6.2: The Diagram of Azimuth and Elevation Systems

and the potential energy is given by

$$\begin{aligned} U = &- m_1 g(L_3(1-\frac{\theta_3^2}{2}) + L_4(1-\frac{\theta_4^2}{2}) + L_1(1-\frac{\theta_1^2}{2}))+ \\ &- m_2 g(L_3(1-\frac{\theta_3^2}{2}) + L_4(1-\frac{\theta_4^2}{2}) + L_2(1-\frac{\theta_1^2}{2})) \end{aligned} \tag{6.5}$$

Initially, we assume that the torque control u_{el} is available and $u_{el} = \ddot{\theta}_2$. Use Eqn. (2.86) and Eqn. (2.89) which I propose in chapter 2. Substituting this relation and the physical properties from Tab. 6.1 into Eqn. (6.1) and eliminating the x and y coordinates, we can get the state space representation shown below.

Table 6.1: Physical Properties

Variable*	Value	Variable	Value	Variable	Value
m_1	2196	J_2	5215	L_3	60
I_2	5E6	m_2	554	J_3	5E6
L_4	113	m_3	2500	L_1	2.31
K_s	26	J_1	1480	L_2	2.31
I_1†	2300				

* The unit for each quantity: mass-kilogram; length-meter; MOI-kgm^2; Spring constant-Nm/rad

† The pitch of the detector changes the MOI of gondola in yaw.

$$\begin{pmatrix} \dot{\theta}_3 \\ \dot{\theta}_4 \\ \dot{\theta}_1 \\ \dot{\theta}_2 \\ \ddot{\theta}_3 \\ \ddot{\theta}_4 \\ \ddot{\theta}_1 \\ \ddot{\theta}_2 \end{pmatrix} = \begin{pmatrix} 0 & 0 & 0 & 0 & 1 & 0 & 0 & 0 \\ 0 & 0 & 0 & 0 & 0 & 1 & 0 & 0 \\ 0 & 0 & 0 & 0 & 0 & 0 & 1 & 0 \\ 0 & 0 & 0 & 0 & 0 & 0 & 0 & 1 \\ -0.3237 & 0.3237 & 0 & 0 & 0 & 0 & 0 & 0 \\ 0.1719 & -0.545 & 0.1909 & 0 & 0 & 0 & 0 & 0 \\ 0 & 9.323 & -9.323 & 0 & 0 & 0 & 0 & 0 \\ 0 & 0 & 0 & 0 & 0 & 0 & 0 & 0 \end{pmatrix} \begin{pmatrix} \theta_3 \\ \theta_4 \\ \theta_1 \\ \theta_2 \\ \dot{\theta}_3 \\ \dot{\theta}_4 \\ \dot{\theta}_1 \\ \dot{\theta}_2 \end{pmatrix} + \begin{pmatrix} 0 \\ 0 \\ 0 \\ 0 \\ 0 \\ 0.0159 \\ -0.7789 \\ 1 \end{pmatrix} u_{el} \quad (6.6)$$

The velocity control can be transformed from the torque control and the approach is shown in the controller design section.

6.3.2 Azimuth Dynamics

We first consider the case when external disturbances do not exist. As show in the Fig. 6.2 (a), x_1 is the azimuth of the gondola. x_2 is the azimuth of the balloon. x_3 is the azimuth of the bottom of the ladder and the parachute. The ladder and the parachute are like a spring that connects the azimuth motor and the balloon. The proof is shown in the following equations. The height of the parachute and the ladder is z. w is the width of the ladder. The twisted angle is θ_z. Their relation is as shown in Fig. 6.3. The following relation can be obtained.

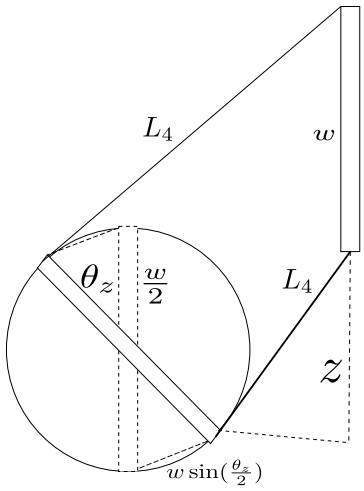

Figure 6.3: Diagram of Ladder Model

$$
\begin{aligned}
z &= -\sqrt{{L_4}^2 - w^2\sin(\frac{\theta_z}{2})^2} \\
\dot{z} &= \frac{1}{4\sqrt{{L_4}^2 - w^2\sin(\frac{\theta_z}{2})^2}} w^2\sin(\theta_z)\dot{\theta}_z
\end{aligned}
\tag{6.7}
$$

The kinetic and the potential energies are:

$$
\begin{aligned}
T &= \frac{1}{2}(m_1+m_2)\dot{z}^2 + \frac{1}{2}I_1\dot{\theta}_z^2 \\
U &= (m_1+m_2)gz
\end{aligned}
\tag{6.8}
$$

Substituting to Eqn. (6.1) with θ_z as generalized coordinate and, ignoring higher order term of θ_z we obtain:

$$
I_1\ddot{\theta}_z \approx \frac{-(m_1+m_2)gw^2\sin(\theta_z)}{4L_4} \approx -K_s\theta_z \tag{6.9}
$$

The above equations prove that the behavior of the ladder is similar to a spring under small twist angle. The balloon has significantly larger moment of the inertia(MOI) than the gondola(750 times higher). The ladder provides the reaction torque to cause the gondola to change its azimuth. If we define a variable called $x_{31} = x_1 - x_3$ [2] to represent the amount of the change of the motor angle, we obtain the following governing equations. The state space

[2] $x_{31} = \theta_z$

representation is shown in Eqn. (6.10).

$$\begin{pmatrix} \dot{x}_1 \\ \ddot{x}_1 \\ \dot{x}_2 \\ \ddot{x}_2 \\ \dot{x}_{31} \end{pmatrix} = \begin{pmatrix} 0 & 1 & 0 & 0 & 0 \\ -\frac{K_s}{I_1} & 0 & \frac{K_s}{I_1} & 0 & \frac{K_s}{I_1} \\ 0 & 0 & 0 & 1 & 0 \\ \frac{K_s}{I_2} & 0 & -\frac{K_s}{I_2} & 0 & -\frac{K_s}{I_2} \\ 0 & 0 & 0 & 0 & 0 \end{pmatrix} \begin{pmatrix} x_1 \\ \dot{x}_1 \\ x_2 \\ \dot{x}_2 \\ x_{31} \end{pmatrix} + \begin{pmatrix} 0 \\ 0 \\ 0 \\ 0 \\ 1 \end{pmatrix} u_{az} \tag{6.10}$$

The physical properties are listed in Tab. 6.1

6.4 Control Algorithm

Two feedback controllers are designed for azimuth and elevation controls. The assumption is that the dynamics of the two are not coupled. The goal of the control is to make the tracking error within 0.5 degree root mean square under the environmental disturbances.

6.4.1 Azimuth Control

Since the balloon has significantly larger MOI than the gondola, for convenience, we ignore the x_2 state, modify Eqn. (6.10), and obtain the following equation:

$$\begin{pmatrix} \dot{x}_1 \\ \ddot{x}_1 \\ \dot{x}_{31} \end{pmatrix} = \begin{pmatrix} 0 & 1 & 0 \\ -\frac{K_s}{I_1} & 0 & \frac{K_s}{I_1} \\ 0 & 0 & 0 \end{pmatrix} \begin{pmatrix} x_1 \\ \dot{x}_1 \\ x_{31} \end{pmatrix} + \begin{pmatrix} 0 \\ 0 \\ 1 \end{pmatrix} u_{az} \tag{6.11}$$

Linear-Quadratic Regulator (LQR) for Eqn. (6.11) is one of the candidates for the control strategy. Based on different criteria, the design parameters, such as rising time, settling time, or weighting cost, are also different. However, the inaccuracy of the dynamics from x_2 needs to be compensated by the addition of integral control. We use Linear-Quadratic-Iintegral (LQI) by augmenting a state for the integral control[72]. LQI systematically finds the gain for integral control rather than the traditional LQR approach.

For the purpose of the stabilization, x_1, $\dot{x}_1$ and x_{31} need to be known for state feedback. Previous mission uses strain gage and sun sensor signals with analog circuitry for feedback. The torque reading from the strain gage relates to the azimuth changes of the entire ladder and parachute. The strain gage has problems with drifting and noise. The error caused by the temperature drift needs to be eliminated by some algorithms in the software. However, it is difficult to know the dynamics of the strain gage. Besides, the initial offset reading needs to be manually tuned in the hardware or be compensated in the software. For state feedback, we also need the information of the azimuth velocity. There is no measurement of $\dot{x}_1$. However, it could be obtained from x_1 indirectly using Euler method.

$$\dot{x}_1(k) \approx \frac{x_1(k) - x_1(k-1)}{T_s} \tag{6.12}$$

T_s is the sampling time and k is the time index. However, the velocity estimation can easily be corrupted by noise. Based on the disadvantages mentioned above and Euler method, we propose an observer to estimate the x_{31} and $\dot{x}_1$. Eqn. (6.13) is dynamics of the estimation. $\hat{x}$ is the vector of the estimator. A and B are the same matrix in Eqn. (6.11). Here, L is the observer gain. $\mathfrak{y}$ is the measurement of x_1.

$$\dot{\hat{x}} = A\hat{x} + Bu + L(\mathfrak{y} - C\hat{x}) \tag{6.13}$$

Subtracting Eqn. (6.11) from Eqn. (6.13) , we obtain

$$\dot{e} = Ae - LCe = (A - LC)e \tag{6.14}$$

$e = x - \hat{x}$ is the error vector. To make the estimation possible, L is chosen to such that A-LC has negative eigenvalues. We use LQR strategy to select the desired L. From the above design procedures, the state feedback gain $K \in \Re^4$ is obtained from LQI and observer gain $L \in \Re^3$ from LQR, Hence, the control output is:

$$u_{az} = -\sum_{i=1}^{3} K_i \hat{x}_i - K_4 \int_0^t \hat{x}_1 dt \tag{6.15}$$

Observer gains from LQR are the solutions:

$$\begin{aligned} &AX + XA^T - XC^TCX + Q_L = 0 \\ &L = CX \end{aligned} \tag{6.16}$$

The state space $(A_{lqi}, B_{lqi}, C_{lqi})$ for the integral term feedback are:

$$\begin{aligned} \begin{pmatrix} \dot{x} \\ \dot{z} \end{pmatrix} &= \underbrace{\begin{pmatrix} A & 0_{3\times 1} \\ -C & 0 \end{pmatrix}}_{=A_{lqi}} \begin{pmatrix} x \\ z \end{pmatrix} + \underbrace{\begin{pmatrix} B \\ 0 \end{pmatrix}}_{=B_{lqi}} u \\ z &= -\int y \cdot dt \\ y &= \underbrace{\begin{pmatrix} C & 0 \end{pmatrix}}_{=C_{lqi}} \begin{pmatrix} x \\ z \end{pmatrix} \end{aligned} \tag{6.17}$$

The controller gains from LQI are the solutions:

$$\begin{aligned} &A_{lqi}^T X + XA_{lqi} - XB_{lqi}R^{-1}B_{lqi}^T X + Q_K = 0 \\ &K = R^{-1}B_{lqi}^T X \end{aligned} \tag{6.18}$$

The natural frequency term $\Omega^2 = \frac{K_s}{I_1}$ in Eqn. (6.11) could be affected by the uncertain weight, MOI of gondola, the ladder and the parachute. The weight and MOI are usually just decided right before the launch and the length of parachute is unknown in the real flight. Moreover, the balloon also has the effects to the spring constant if part of its geometry contributes the

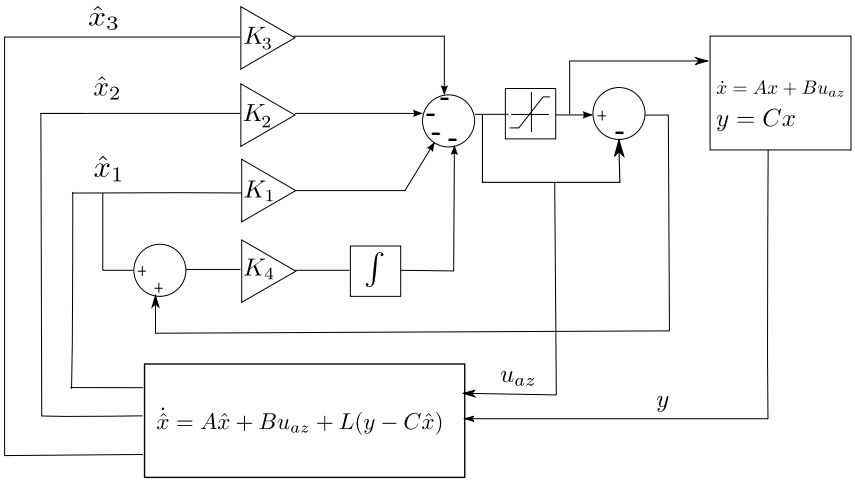

Figure 6.4: Anti-windup Structure

length of the twist angle. Based on those uncertainties, the self-tuning design is necessary. It is not economic for people to tune the system parameters in the real flight moment.

The integral term in the control output will induce stability problem if the actuator saturates. To avoid this issue, the anti-windup strategy is necessary. The structure is shown in Fig. 6.4. Initially, the sun is out the FOV of the sun sensor. The azimuth control provides a constant command for searching purpose. Once, the sun sensor detects the power measured by the sun-sensor exceeds a certain threshold, the feedback azimuth control immediately switches on. The K and L gains are also designed properly to accommodate narrow FOV.

6.4.2 Elevation Control

For any linear state space representation, there is a similarity transformation $\mathcal{T}$, such that:

$$\bar{A} = \mathcal{T}\mathcal{A}\mathcal{T}^T,\ \bar{B} = T\mathcal{B},\ \bar{C} = \mathcal{C}\mathcal{T}^T \tag{6.19}$$

and

$$\bar{A} = \begin{pmatrix} \mathcal{A}_{uc} & 0 \\ \mathcal{A}_{21} & \mathcal{A}_c \end{pmatrix}\ \bar{B} = \begin{pmatrix} 0 \\ \mathcal{B}_c \end{pmatrix}\ \bar{C} = \begin{pmatrix} \mathcal{C}_{uc} & \mathcal{C}_c \end{pmatrix} \tag{6.20}$$

The subscript "uc" means uncontrollable and "c" means controllable. From controllability analysis of Eqn. (6.6), the rank of $\mathcal{A}_{uc}$ is four. This implies that there are four uncontrollable modes in the dynamics of the elevation. For feedback elevation control, the goal is to control the absolute elevation properly. For convenience, we define the absolute elevation as θ_{el}. θ_{el} equal to $\theta_1 + \theta_2$. Therefore, we need to check whether θ_{el} is one of the controllable state or not. The similarity transformation $\mathcal{T}$[3] is:

[3]If the entry is smaller than 10^{-8}, it would be viewed as the numerical error

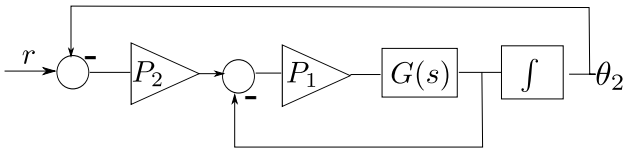

Figure 6.5: Elevation Cascade Structure

$$\mathcal{T} = \begin{pmatrix} 0.635 & 0.77228 & 0.01596 & 0.00011 & 0 & 0 & 0 & 0 \\ 0 & 0 & 0 & 0 & 0.63509 & 0.77228 & 0.01596 & 0.00011 \\ -0.772 & 0.63493 & 0.01402 & 0.0008 & 0 & 0 & 0 & 0 \\ 0 & 0 & 0 & 0 & -0.77244 & 0.63493 & 0.01402 & 0.0008 \\ 0.001 & -0.01712 & 0.78869 & 0.61455 & 0 & 0 & 0 & 0 \\ 0 & 0 & 0 & 0 & 0.00088 & -0.01712 & 0.78869 & 0.61455 \\ 0 & 0.01258 & -0.61442 & 0.78888 & 0 & 0 & 0 & 0 \\ 0 & 0 & 0 & 0 & 0 & 0.01258 & -0.61442 & 0.78888 \end{pmatrix} \tag{6.21}$$

The transformed coordinates is $\bar{x}$=$\mathcal{T}$§. The vector space spanned by rows 5 to 8 of $\mathcal{T}$ is the vector space spanned by all of the controllable states. In other words, if a state is not in this space, then this state is not controllable. The absolute elevation is θ_{el}. It belongs to the following vector v:

$$v = \begin{pmatrix} 0 & 0 & 1 & 1 & 0 & 0 & 0 & 0 \end{pmatrix}^T \tag{6.22}$$

The total independent vectors from rows 5 to 8 of $\mathcal{T}$ and v is five. This implies that v is not in the controllable space. That means the absolute elevation has an uncontrollable mode. The elevation control must not induce the uncontrollable dynamics. One of the controllers is designed by the cascade control. The cascade structure is shown in Fig. 6.5. The idea for the cascade control is to use the secondary loop (internal loop) to control disturbances before they can affect the primary control objective (outside). The feedback signal is the relative elevation θ_2 and the reference signal is the set point from the sun table (which provides actual solar elevation angle in the sky). The absolute elevation calculated from GPS data is a function of local latitude , longitude, and universal time. $G(s)$ is the transfer function from the state space in Eqn. 6.6) and

$$\begin{aligned} \mathcal{C} &= \begin{pmatrix} 0 & 0 & 0 & 0 & 0 & 0 & 0 & 1 \end{pmatrix} \\ \mathcal{D} &= 0 \end{aligned} \tag{6.23}$$

The closed loop transfer function is:

$$\theta_2 = \frac{\frac{P_2 P_1 G(s)}{1+P_1 G(s)} \frac{1}{s}}{1 + \frac{P_2 P_1 G(s)}{1+P_1 G(s)} \frac{1}{s}} r \tag{6.24}$$

We shall fix P_1 and find the most suitable value of P_2. From root locus analysis shown in

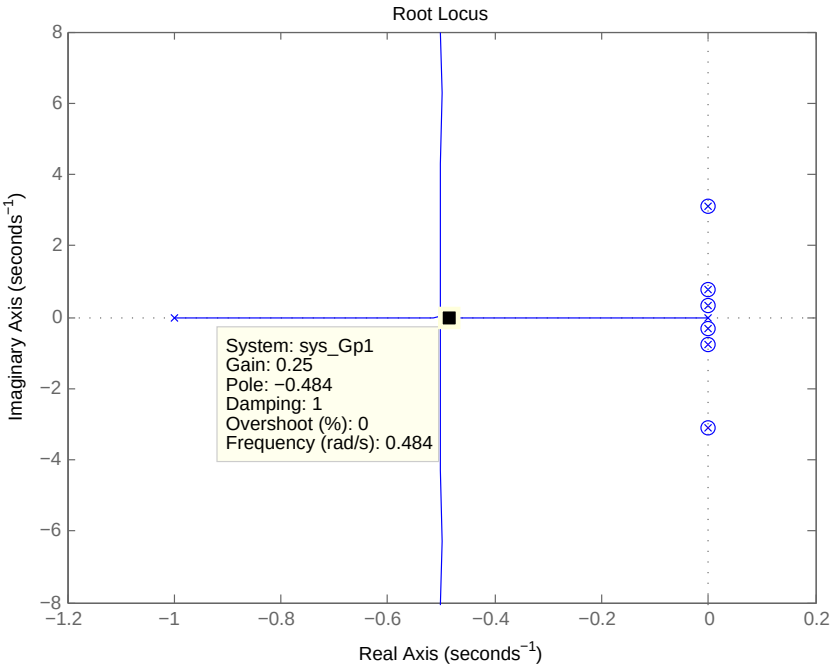

Figure 6.6: The Root Locus Plot for $P_1 = 1$

Fig. 6.6, when $P_2 = 0.25 \times P_1$, two close loop poles satisfy the critical damping condition. There are three pairs of pole- zero cancellation in the imaginary axis. Unfortunately, the elevation control cannot change the close loop poles at those locations. To avoid exciting the dynamics in the uncontrollable mode, the smooth rising speed of the detector is necessary. To satisfy the velocity actuator, the controller needs to integrate the error signal from the output of P_1. The plant $G(s)$ needs to be modified to $sG(s)$ because $G(s)$ receives velocity input instead of torque input. The manufacturing errors may be originated from the following sources: (1) The detector is not balanced well. (2) The pivot joint has small distance relative to the center of the detector. (3) The initial setting point is not calibrated well with absolute encoder. Those errors need to be compensated by the sun sensor. To avoid feeding the compensated signals due to oscillation of the gondola, a low pass filter is implemented for the pitch (vy) feedback. On the other hand, the ground station would also be able to specify the offset for its own purpose. The modified diagram is shown in Fig. 6.7. The elevation is controlled by the jack screw. The structure is shown in Fig. 6.8. The elevation $\angle EOD (= \theta)$ of the detector is indirectly controlled through controlling the length of the $\overline{BG} (= l_a)$ of the jack screw. The relation between θ and l_a is shown in the following equations.

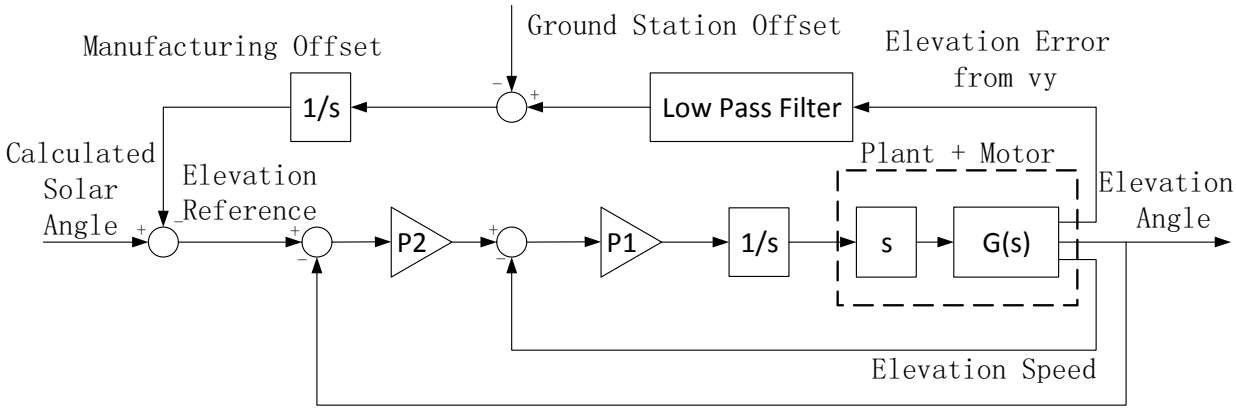

Figure 6.7: Modified Elevation Cascade Structure

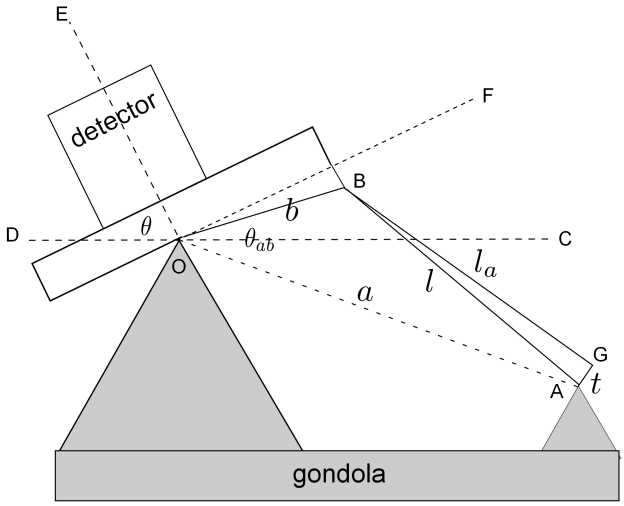

Figure 6.8: Jack Screw Implementation

$$
\begin{aligned}
&\theta = \pi - \angle EOF(=\pi/2) - \angle FOB - \angle AOB(=\theta_{ab}) + \angle AOC \\
&l^2 = \overline{OB}^2 + \overline{OA}^2 - 2\overline{OB}\cdot\overline{OA}\cdot cos(\theta_{ab}) \\
&l^2 = l_a^2 + t^2 \\
&\dot{\theta} = -\dot{\theta}_{ab} \\
&l\dot{l} = \overline{OB}\cdot\overline{OA}\cdot sin(\theta_{ab})\dot{\theta}_{ab} \\
&l\cdot\dot{l} = \dot{l}_a \cdot l_a
\end{aligned}
\tag{6.25}
$$

Typically, there are two stages in the elevation control. One is for the rising mode and the other is for tracking mode. The rising mode is for the initial start-up. The detector is raised

to the setting point with a constant speed based on the current real time calendar which predicts the position of the sun. However, constant angular speed does not imply constant rate of change of the actuator length. Both can change the elevation angle. The former can reduce the oscillation of the gondola in the sense of the conserving angular momentum. The command to the linear actuator $\dot{l_a}$ for constant $\dot{\theta}$ is based on the following calculations:

$$\begin{aligned} \dot{l} &= \frac{\overline{OB} \cdot \overline{OA} \cdot sin(\theta_{ab})\dot{\theta}_{ab}}{l} \\ \dot{l_a} &= \frac{\dot{l} \cdot l}{l_a} \end{aligned} \tag{6.26}$$

When the azimuth control has managed to get the sun in the primary FOV, the tracking mode of the elevation is executed. There is no velocity sensor for the elevation. The velocity is estimated by the Euler method, similar to Eqn. (6.12). The command for the actuator $\dot{l_a}$ for the tracking mode is based on the following calculations:

$$\begin{aligned} \ddot{\theta} &= \ddot{\theta} + (r - \theta) \cdot P_2 - \dot{\theta} \cdot P_1 \\ \dot{l} &= \frac{\overline{OB} \cdot \overline{OA} \cdot sin(\theta_{ab}) \cdot (-\ddot{\theta} \cdot T_s)}{l} \\ \dot{l_a} &= \frac{\dot{l} \cdot l}{l_a} \end{aligned} \tag{6.27}$$

r is the reference signal. The reference is updated by the real time calendar, the compensation from the sun sensor with a low pass filter, and the specified offset from the ground station.

6.4.2.1 Sun Table Calculation

The elevation of the sun is relative to the local time, the latitude and the longitude. Point control system receive the GPS data. To compute the exact elevation of the sun in different location, the pointing control system need to know:

a GPS number of weeks: first week starting January 6, 1980.

b GPS time of weeks: the number of seconds since Sunday at 12:00 AM.

c GPS time offset: should be subtracted from the GPS time to obtain UTC time.

d Balloon geographic location: GPS latitude and GPS longitude.

e time zone: It could be set initially in the flight software. Since the balloon would fly locally, this value is probably a fixed number. If the location of the balloon is the Arctic or the Antarctic, the time zone may frequently change and need to be updated manually with uploaded packages. The time zone maybe change due to the daylight saving time.

Appendix A shows the local solar elevation algorithms from the NOAA [4]. The implementation are programmed with c code style. One should always verify the results if the latitude, the longitude and the time zone changes. Moreover, one should also check if the GPS passes the correct data format and meanings as expected. If the precision of the variable of the processor is limited (ex: float with 32 bits) , one also needs to calculate an offset with the higher precision (ex: double with 64 bits) in PC and insert the results to the modified algorithm in the processor side. The modified algorithm should only keep those algorithms which change frequently.

UTC is adjusted to maintain it within 0.9 s of UT by adding a lead second [5].

6.5 Control Flow

We begin the fully control strategy by setting the elevation of the telescope first, followed by the azimuth direction. Based on current local time, we raise the detector into the known sun elevation angle (we refer this as the raising state). Once the sun gets within the threshold of the set point, we begin performing 360 degree searching in the azimuth direction to find the sun. Meanwhile, the elevation control continues to keep track of the continuously changing set point without any feedback information from sun sensor. Once the sun sensor finds the sun within its FOV, the azimuth tracking mode begins and elevation control begins utilizing the information from sun sensor to keep track of the center of the sun within the specified 0.5 degree rms requirements. The tasks diagram is in the Fig. 6.9. One can refer [3] for designing a control structure of a mechanical system. One can refer [70] for more details of the control software design of GRIPS. All tasks are executed simultaneously. The contents of the task is executed by the dispatcher. Appendix B introduces the ideas of the dispatcher, tasks diagram and states diagram. The tasks are four groups. The first group is responsible for handling the whole control flow with the command from the flight software. The second group is responsible for the outputs computation with feedback inputs or commands. The third group is responsible for data processing from the sensors and voltage outputs. The fourth group is responsible for parsing data package from UDP or TCP/IP.

All tasks which belong the first or second group have the initial state for setting the parameters and state pointer. Azimuth and elevation control states diagrams also have manual state for manually controlling the gondola. Fig. 6.10 is the states diagram of the elevation control. There are several consideration in designing the elevation control states diagram. The angle of the elevation is constrained by the mechanical structure and the balloon geometry. If the angle is too large, the sensor is blocked by the balloon. Once the sun sensor detects the sun, one of the state deals with the manufacturing error compensation. If the sun sensor accidentally loses the sun, elevation control needs to use the exist compensated offset and decide if the outputs command zero or not. The azimuth control state diagram basically is determined by the elevation control state diagram. When the elevation control finishes the raise state, it triggers the azimuth searching state. The sun is supposed to be

[4]NOAA Solar Position Calculator: http://www.esrl.noaa.gov/gmd/grad/solcalc/azel.html

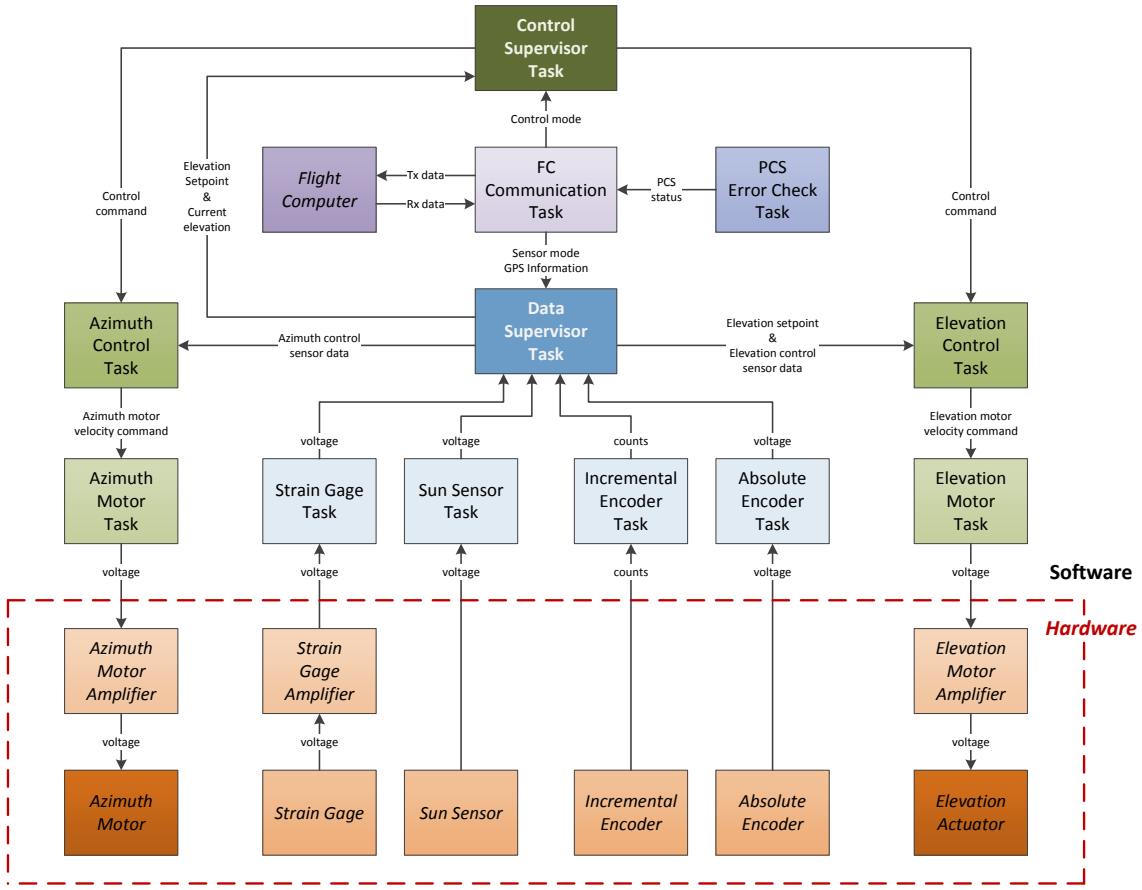

Figure 6.9: Tasks Diagrams of GRIPS

detected after the azimuth searching state. Then the elevation tracking with the sun sensor is triggered.

6.6 Simulation Methods

Fig. 6.11 shows the simulation structure. **absolute time and location** computes the local time and provides the current latitude and the longitude. **sun position** computes the absolute azimuth and the elevation w.r.t. the earth locally. **sensor dynamics and porfile** uses the feed information to generate the corresponding vx, vy and vsum signals. **pointing control system** receives the sensors and the packages of the **simulated flight software** and generates the control signals to the **azimuth motor dynamics** and **elevation actuator mechanical structure and motor dynamics**. **elevation actuator mechanical structure and motor dynamics** includes the geometry of the jack screw implementation

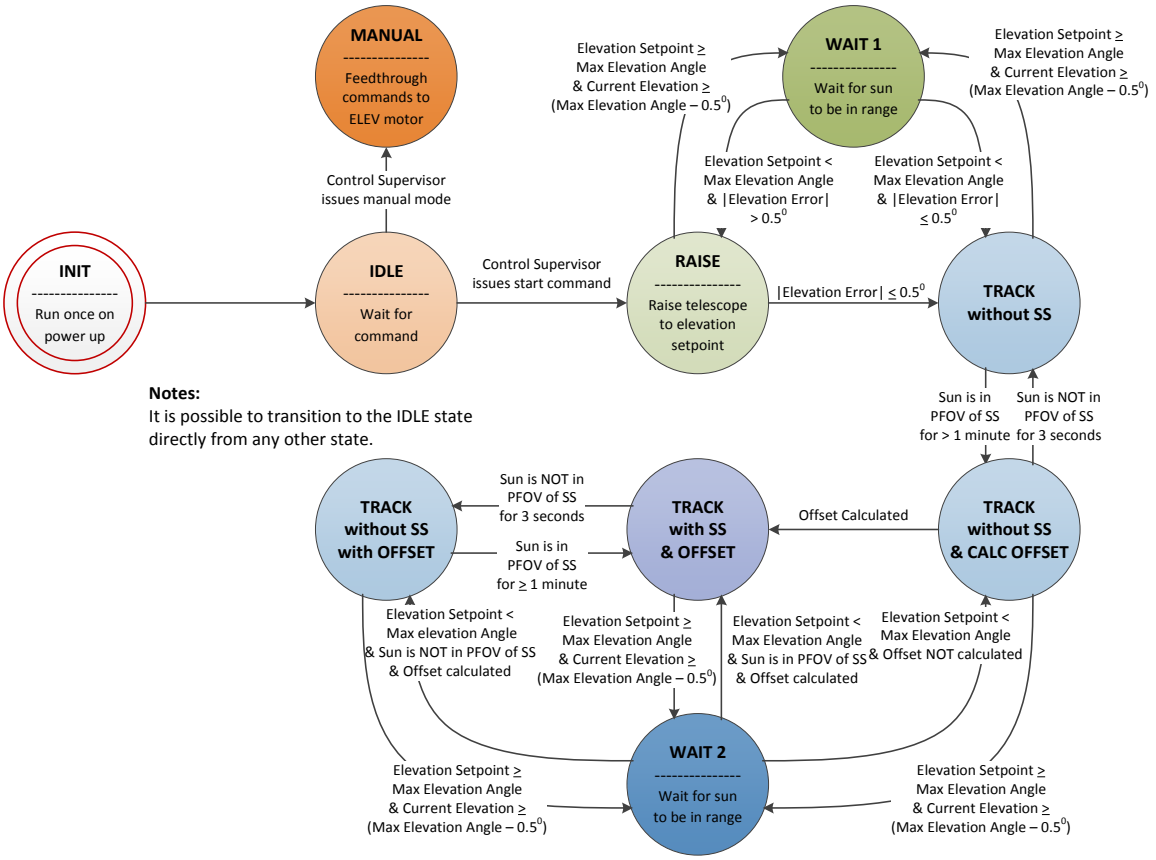

Figure 6.10: States Diagrams of Elevation Control

and produces the corresponding the relative elevation angular velocity to **elevation dynamics**. **azimuth motor dynamics** converts the voltage to motor velocity with units rad/sec and feeds to **azimuth dynamics**. **balloon disturbance** only disturbs the dynamics of the azimuth but not the dynamics of the elevation. The moment of the inertia changes if the elevation of the telescope changes. That makes the azimuth system matrix (A) change. The attitude of the telescope feedback to the **sensor dynamics and porfile**.

6.7 Simulation Results

Figure. 6.12 shows results for different balloon velocities. The azimuth control can stabilize the balloon velocities from 0.0209 rad/sec to - 0.0209 rad/sec. In the transient error figure, we can find some velocities of the balloon that are faster than the searching velocity. This behavior dominates the azimuth of the gondola at that time. However, once the sun is

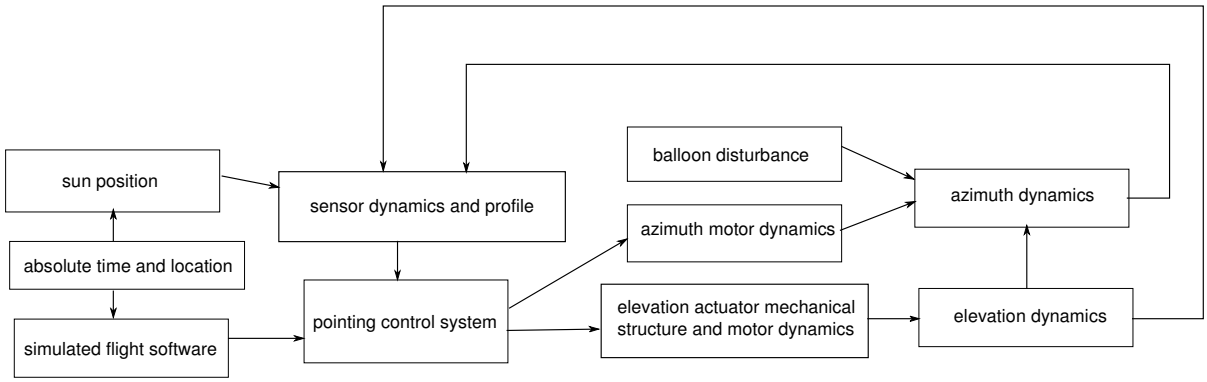

Figure 6.11: GRIPS Simulation Structure

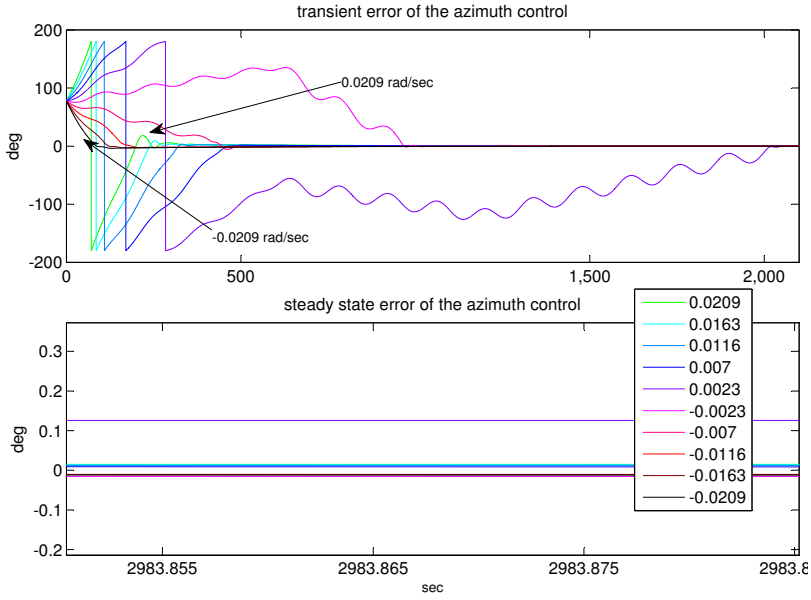

Figure 6.12: Azimuth Simulation: Transient and Steady State Errors

in the FOV. The feedback control begins to execute and stabilize the azimuth. Two balloon velocities are close to the searching velocity. This results in a longer searching time. One of the azimuth states is to search the sun in the opposite direction to reduce the searching time. It can be observed from the figure that the steady state errors are close to 0. One case of steady error exceeds 0.1 degree because the searching time is too long and the integrator control executes a later time. At the initial entry of the FOV, the azimuth commands in Fig. 6.13 are in the saturation region and the twist angles of the ladder and the parachute increases quite significantly, but they are still in the safe range. The commands are adjusted

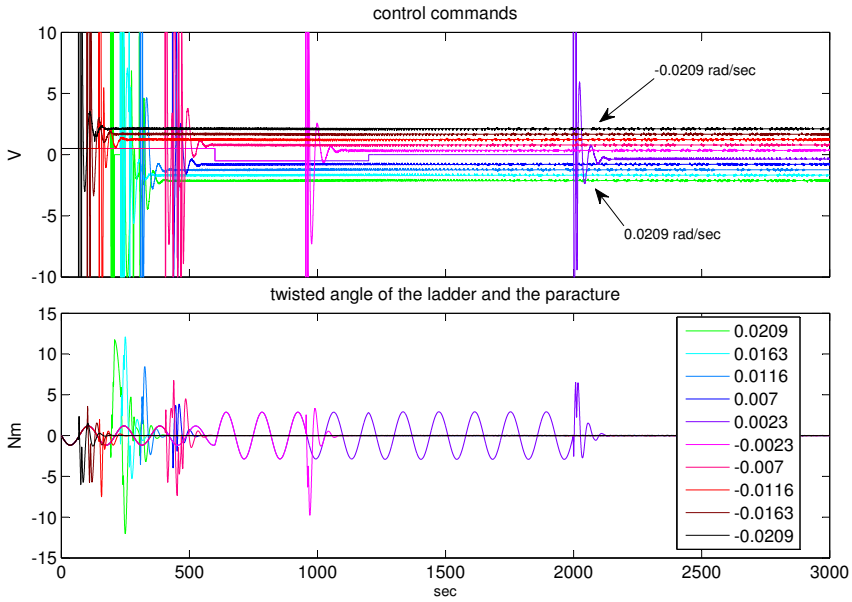

Figure 6.13: Azimuth Simulation: Command and Twisted Angle

by the anti-windup mechanism later and have constant values to overcome the balloon velocity in the end. Fig. 6.14 shows different initial manufacturing errors from 4 degrees to -4 degrees to the elevation control. Initially, the detector is in the rising mode. Once the set elevation is satisfied within a certain threshold, the azimuth control executes and the elevation control continuously tracks the sun by the sun table. After the azimuth control finds the primary FOV, the elevation control calculated the manufacturing error and used it to the reference signal. The amplitude of the steady state error is around 0.05 degree and is dominated by the rising velocity. The rising velocity should be as smaller as possible. However, it should be larger than the rate of change of the elevation of the sun. Fig. 6.15 shows the corresponding commands for the elevation control. Initially, the output is very small due to the small rising speed. Then, the elevation control begins the tracking state using sun table as the reference. Once manufacturing errors update the reference signals, initial peaks shows up in the control command. The bottom figure shows the elevation states in the software. It goes from rising (state 2), tracking with the sun table (state 3), calculation offset (state 4), and tracking with the sun sensor (state 5).

6.8 Small Scale Experiment Setup and Results

We ran the experiment in a small mechanical setup in the lab. The setup in the lab is scaled 1000 times smaller from the actual flight. [5] The actual flight needs to finish the elevation control and azimuth control in one run. In the lab setup, those two controls are

[5]spring constant is similar.

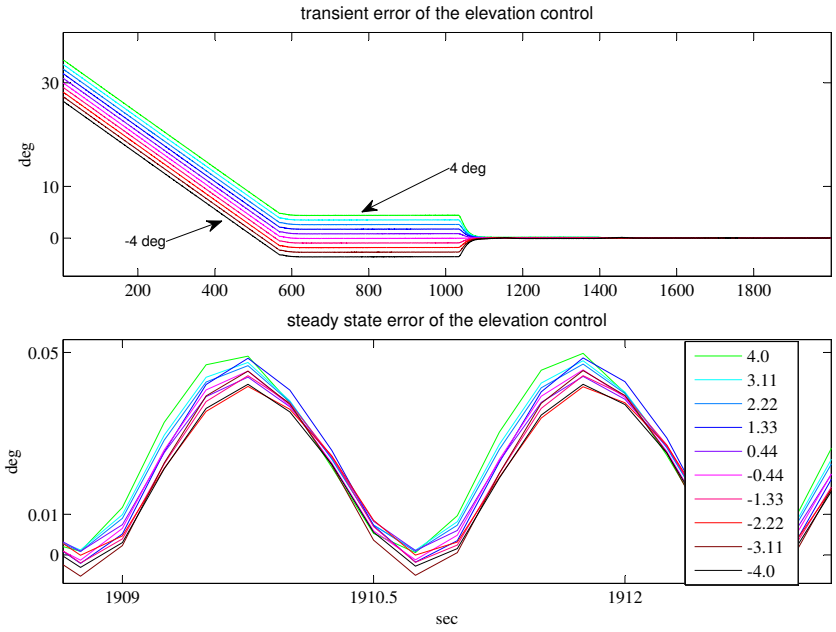

Figure 6.14: Elevation Simulation: Transient and Steady State Errors

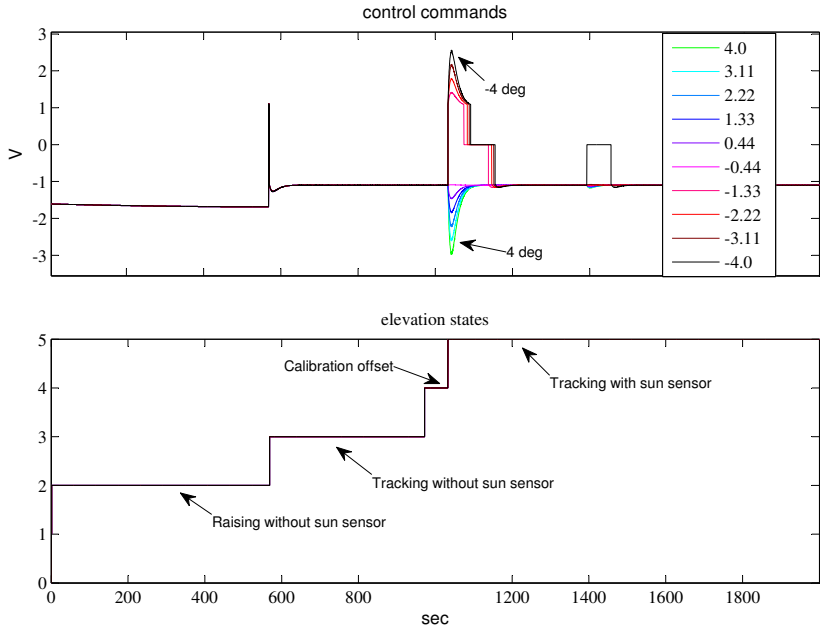

Figure 6.15: Elevation Simulation:Command and Elevation Status

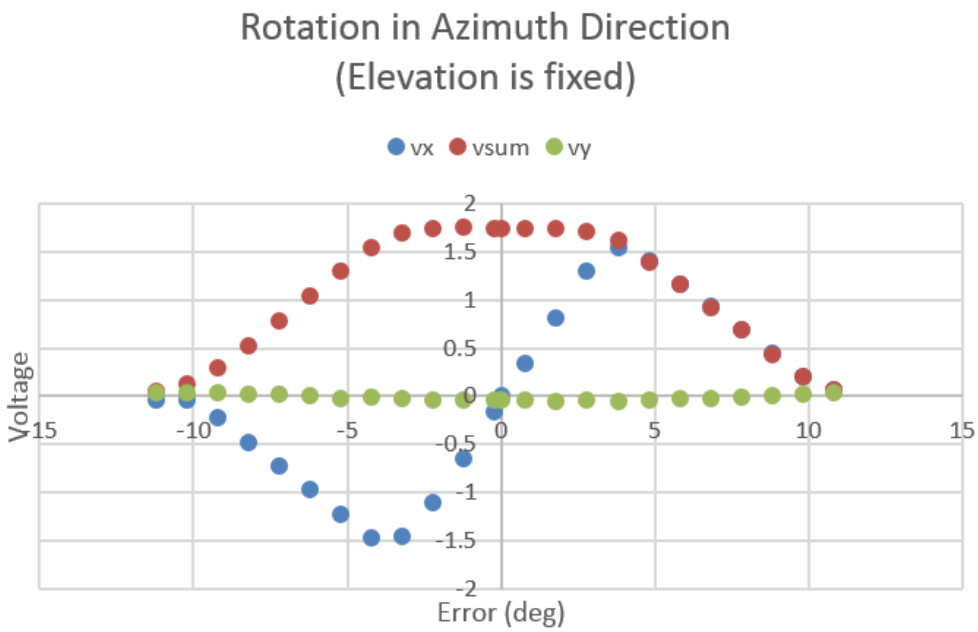

Figure 6.16: The Four-Quadrant Sun Sensor Signal

tested separately. The pointing control system is implemented in a C-Programmable Single-Board Computer(SBC) with Network interface manufactured by Digi International, Inc. SBC has A/D, D/A, real time clock, serial I/O, Ethernet or WIFI connection, and many others. To detect the error signal, a position sensitive four cell detector is used (the sun sensor). Based on the current in each cell, it can indicate the azimuth error signals (named: vx) and elevation (named: vy). Moreover, it also indicates the amount of the receiving power (named: vsum). Fig. 6.16 shows one of the test results to a fixed light resource. We rotated a turn table in the azimuth direction and fixed the elevation in its primary FOV. The total power (vsum) increases after the light enters the secondary FOV and reaches the maximum value in the primary FOV. The error signal (vx) changes its value when the light reaches the secondary FOV and has a linear relationship with the light position in the primary FOV.

6.8.1 Elevation Control Test Setup and Results

Figure 6.17 shows the experiment setup for the elevation control. A change in the length of the linear actuator changes the elevation of the gondola. In order to prevent the frequent switching due to the dead-zone of the actuator, there is a switching logic implemented. Besides, the feedback signals from the sun sensor are averaged for every five minutes to compensate the manufacturing error (as a low pass filter), rather than the sampling time (0.25 sec) of elevation control to avoid inducing the uncontrollable mode. There are two other sensors to indicate the angle of the absolute elevation θ_2 of the detector. Absolute encoder which provides coarse resolution for the elevation angle is used for homing purpose. The

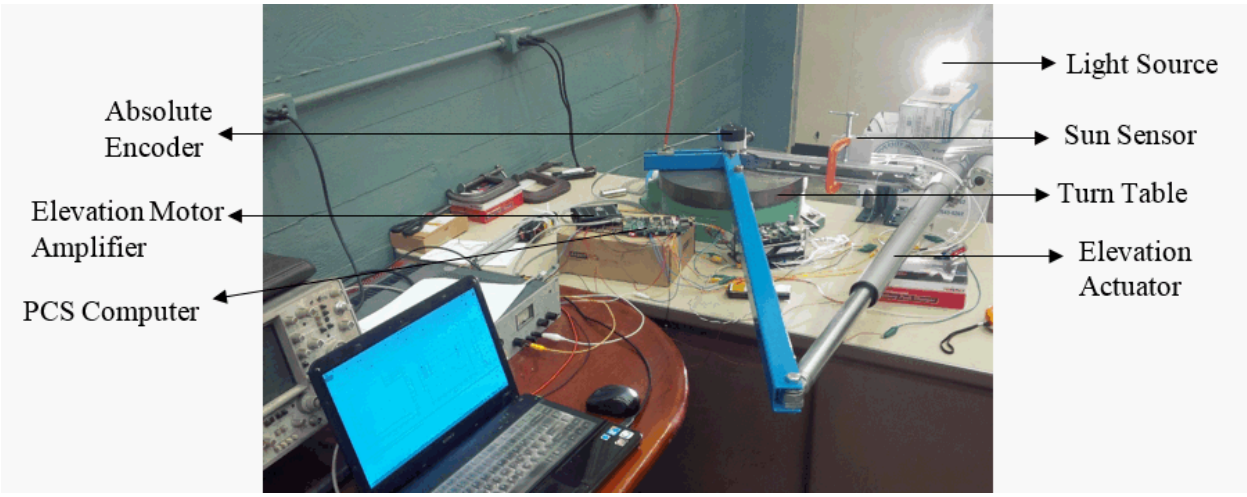

Figure 6.17: Elevation Experiment Setup

incremental encoder is used to provide a finer resolution for the elevation angle and better velocity estimation. Fig. 6.18 (a) shows the values of vy and vsum. Initially, the detector is in the rising mode. The detector changes the elevation based on the real time calendar. Since the sun sensor does not receive any power from the bulb, the vy and vsum are zero initially. As the detector moves, the light enters the secondary field of view. The feedback control executed with a switching logic began to calculate the average manufacturing error. The bump is due to the fact that the average of the manufacturing error doesn't not exactly equal the actual solar elevation. However, as can be observed from the figure, the discrepancy was fully compensated in the end. The error is exactly zero in the flat region. Fig. 6.18 (b) shows the output of the elevation control with the switching logic and the manufacturing error updated every 5 minutes. For most of the times, the output was zero. At some regions, the output is switching frequently because of the dead zone compensation.

6.8.2 Azimuth Control Test Setup and Results

Figure 6.20 shows the experiment setup of the azimuth control. The azimuth actuator uses brushless motor to avoid brush wear from the frequent output switching of azimuth control at high attitude. The weights (Fig. 6.20 (a)) were added to maintain the balance of the simulated gondola. To simulate the disturbances of the balloon, we implemented a brush motor (Fig. 6.20 (b)) to change the azimuth of the top of the ladder line. From frequency analysis from prior Texas flight data, the largest peaks at 1.3e-4 Hz and 6.5e-4 Hz corresponds to 128 min and 25.6 min period. Their amplitudes were 0.001406 rad and 0.000651 rad respectively. We used the worse-case disturbance:, a sinusoidal signal with amplitude of 0.73 rad with 16.6 min period, to simulate the dynamics of the balloon. Fig. 6.19 (a) shows the vx and vsum signals. The gondola starts in the searching mode then changed to the tracking mode immediately after the sun gets within the FOV. The

(a) The Four-Quadrant Sun Sensor Signal for VY and Vsum

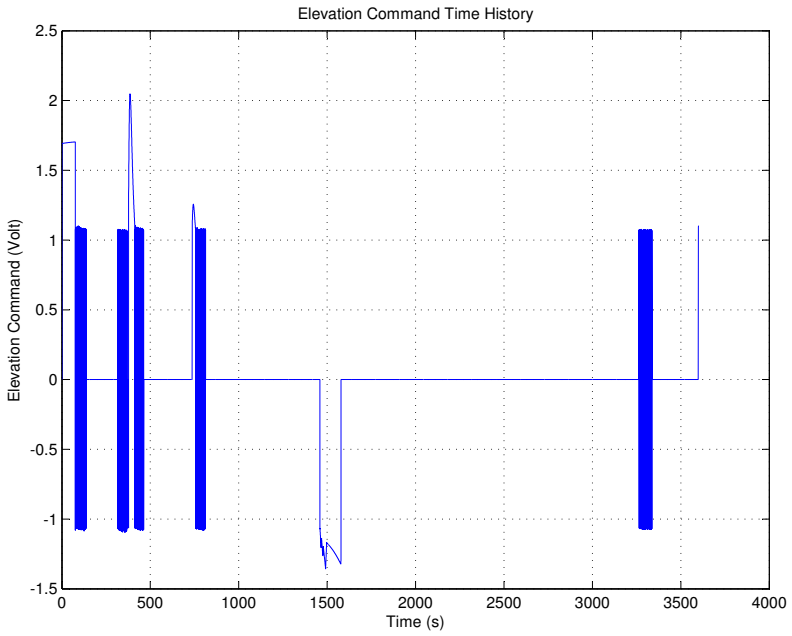

(b) The Output of the Elevation Control

Figure 6.18: Elevation Control Testbed Results

tracking mode continuously increased their gains every 400 hundred seconds until the final gain set is executed (there are four sets of gain values).The amplitude is around 0.24 degree with the worst case disturbance. Fig. 6.19 (b) shows the output of the azimuth control. The amplitude switched frequently because of motor deadzone and increased in magnitude because of the larger gain set.

6.9 Real Scale Experiment Setup and Results

Fig. 6.21 shows the actual size of the gondola. The sun sensor is implemented at the tip of the telescope. Sunlight goes through the whole telescope and is received by the detector. The azimuth brushless motor receives the command from the pointing control system and stirs the ladder for the external torque. The ladder is connected with the parachute and the balloon. The telescope changes its elevation by changing the length of the structure with the elevation brush motor. The mechanism is similar to Fig. 6.8.

6.9.1 Experiment Setup for Actual Gondola

Fig. 6.22 is the diagram for the experiment setup. The orange blocks are implemented in the gondola. The blue blocks are implemented in the ceiling of the building. The green blocks are in a single personal computer (PC) . A wireless router is responsible for the data communication. It uses the Ethernet with the single board computer (SBC) and WIFI with the SBC A and PC. SBC B receives the simulated flight software commands and the feedback signals from encoders and the sun sensors. Then computes the controls signals to the actuators to changes the attitude of the sun sensor. SBC A generates the disturbance signals to distribute the top of the ladder with a power amplifier.

6.9.2 Azimuth Test Results

We generate the disturbance data from the previous experiment in Texas and convert it to the corresponding speed of the ceiling motor. An incremental encoder is fed back to SBC A for PI controller. PI controller regulates the error of the reference count and the actual count. Fig. 6.23 is the simulated disturbance. The ceiling motor has high speed around 1000 sec to 2000 sec and has a larger deceleration around 1500 sec. The azimuth test is inside the building with a light bulb because the strong wind is larger than we expect and the azimuth motor cannot provide the strong enough torques. The amplitude of the wind of the high altitude where the GRIPS operated should be far smaller than the wind on the ground. Before starting the experiment, the sun sensor is implemented at the center of the gondola and is calibrated and needs to have the symmetry profile, like Fig. 6.16. Fig. 6.24 (a) shows that the error of the azimuth is smaller than 0.2 degree under the disturbance effects. vx represents the error of the azimuth. vsum is the total power received by the sun sensor. Fig. 6.24 (b) shows the controls signals. The limit of the control signals is ± 10 volt. The

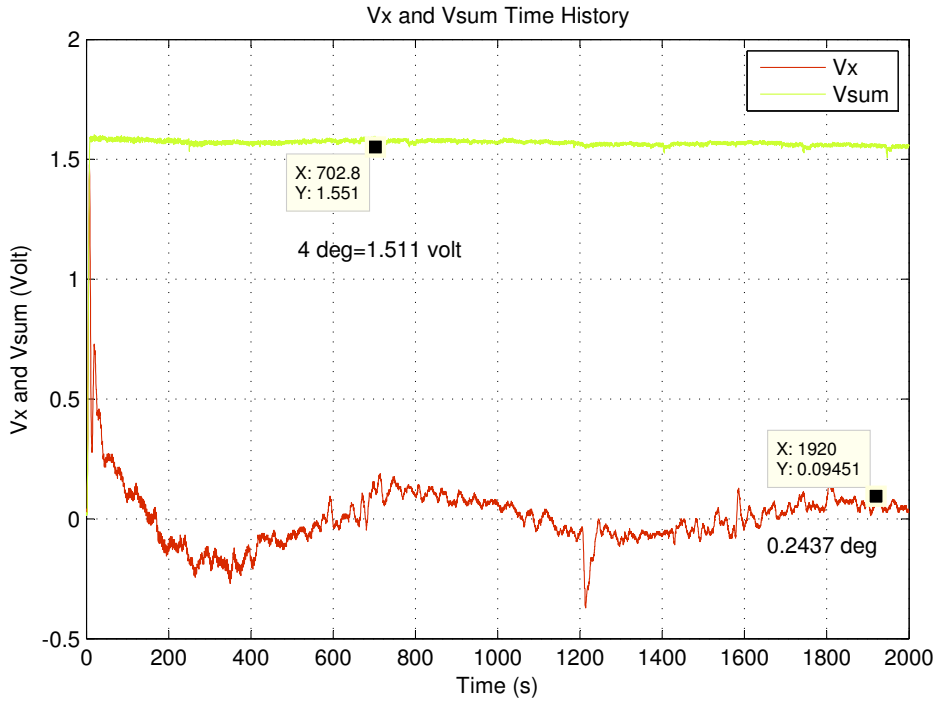

(a) The Four-Quadrant Sun Sensor Signal for Vx and Vsum

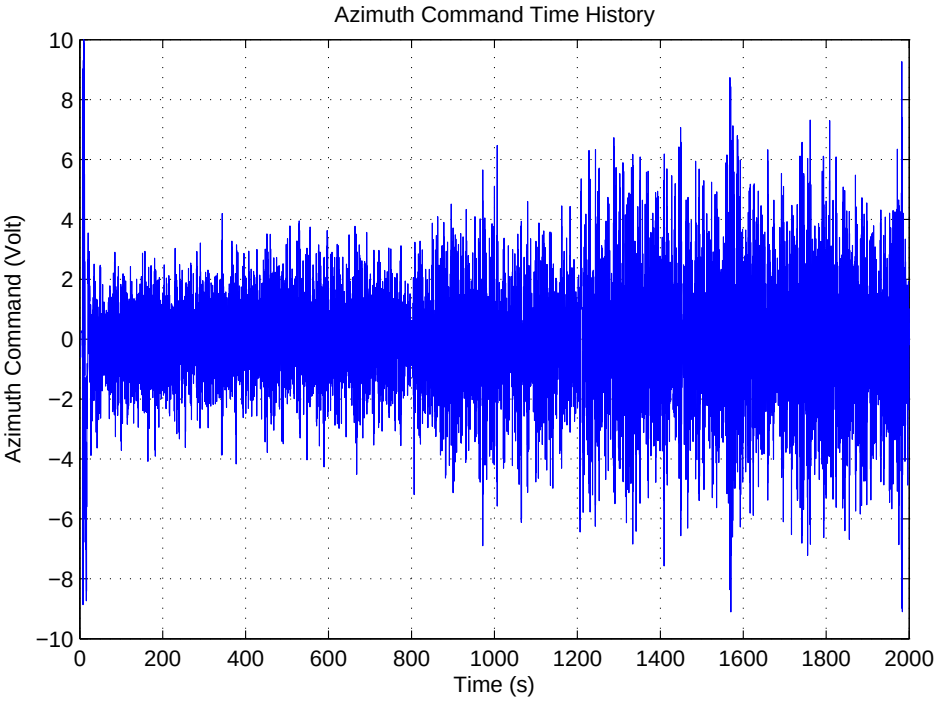

(b) The Output of the Azimuth Control

Figure 6.19: Azimuth Control Testbed Results

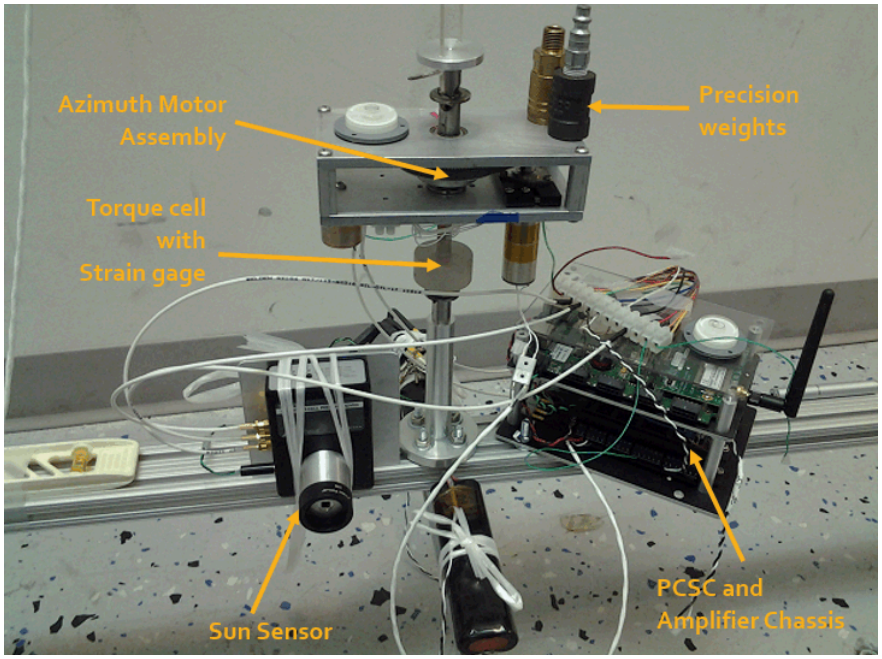

(a) Azimuth Exp. Setup for Computer, Sensor and Actuator

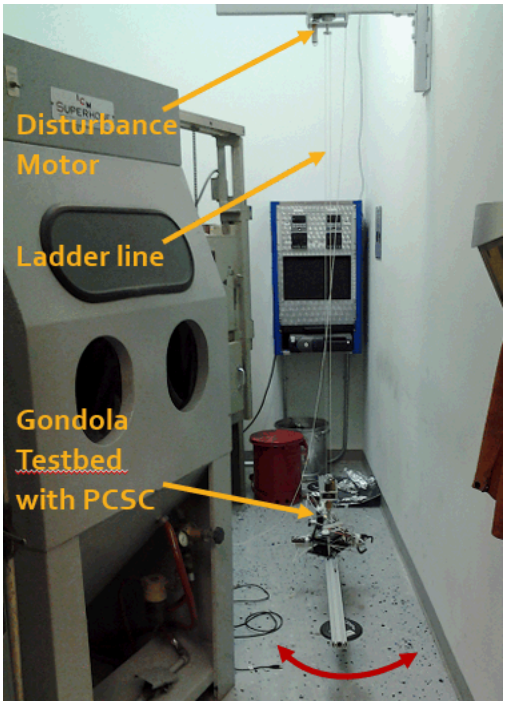

(b) Azimuth Exp. Setup for Ladder Line and Disturbance Motor

Figure 6.20: Azimuth Experiment Setup

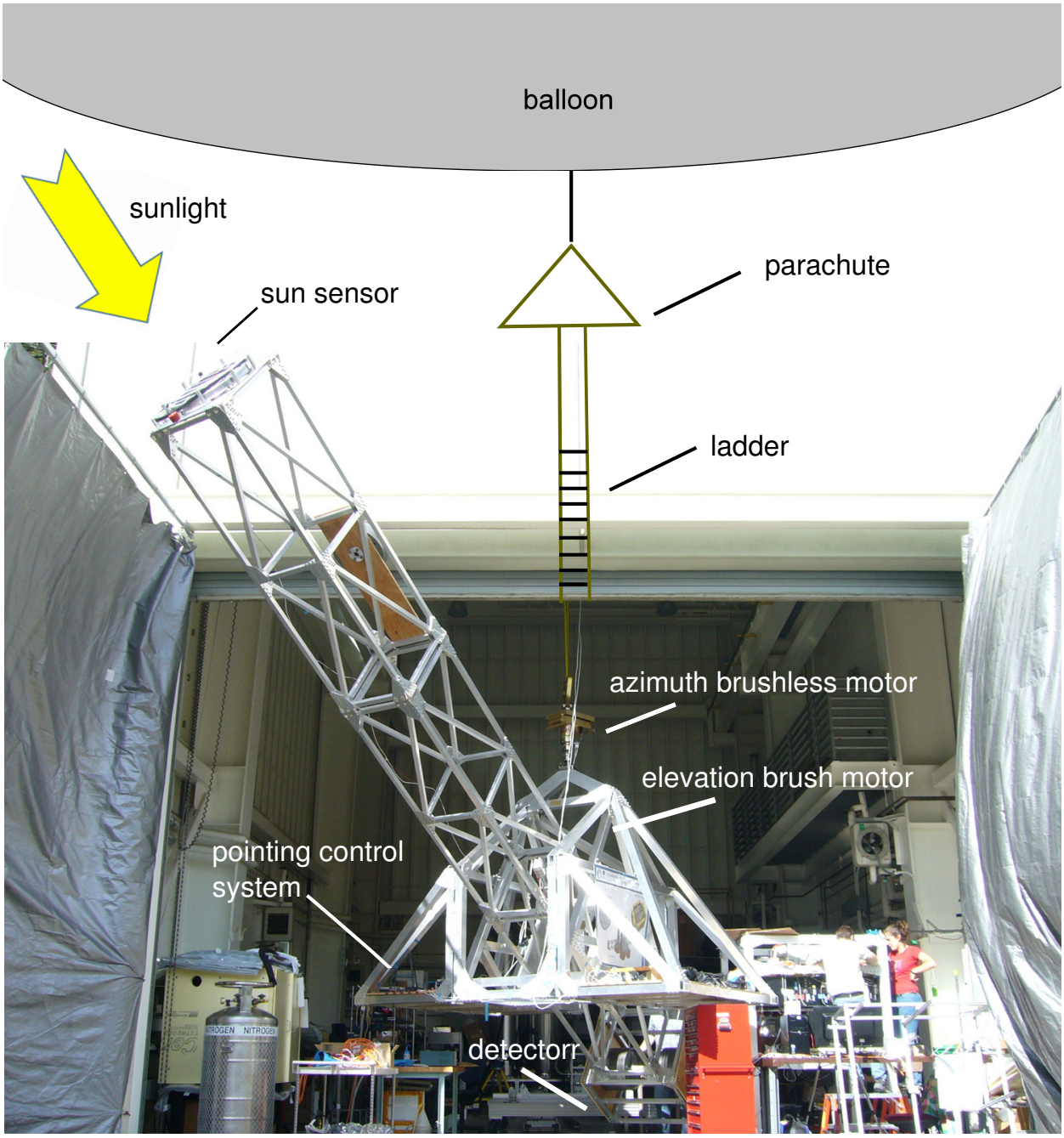

Figure 6.21: Actual Gondola Structure

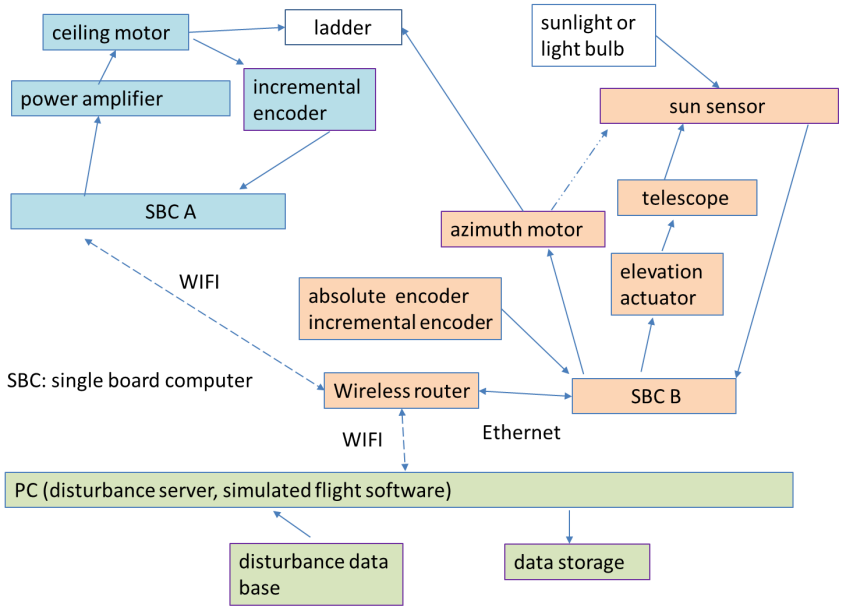

Figure 6.22: Setup for Actual Gondola

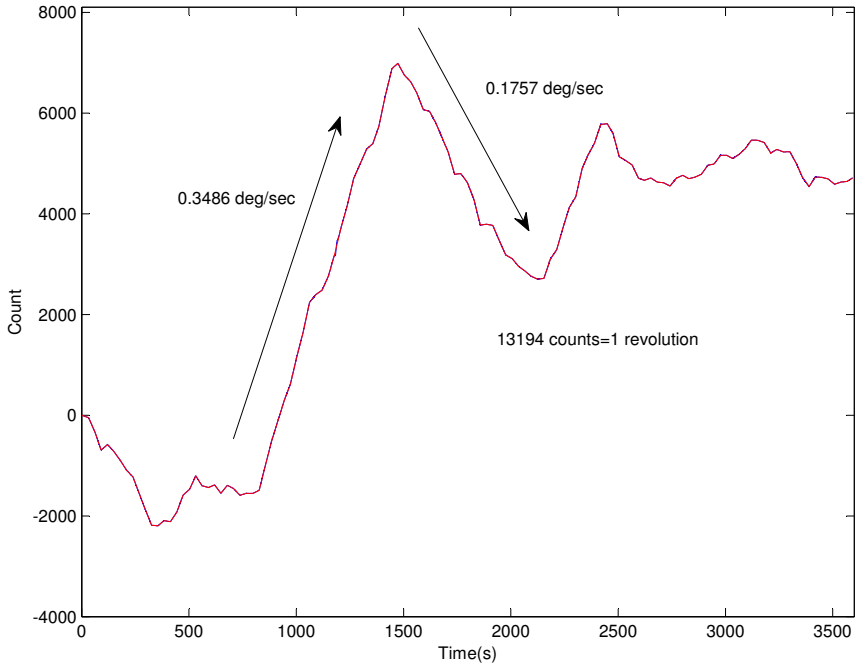

Figure 6.23: Balloon Disturbance Simulator

control signals is oscillating due to the dead zone of the motor. When azimuth control is in the tracking state, the controls gains is increased for every 1 minutes. At the 543 sec, the azimuth gains achieves its highest allowable gains. (i.e. the control signals is the bounded within ± 10 volt). We increased the gains because we want to reduce the tracking error. The system may go outside the FOV of the sun sensor at the transition moment for very strong gains.

6.9.3 Elevation Test Results

The sun sensor is implemented at the tip of the telescope for tracking. Fig. 6.25 (a) shows the reference signal and the incremental encoder. The elevation control initially lower the telescope with an constant angular velocity. The reference signal is updated by the compensated manufacturing error from the sun sensor. Then the controllers changes the elevation with the updated the reference around 120 sec. To avoid the oscillating during the equilibrium point, the controller is turned off when the error within the threshold (0.1 deg) and turned on when the error outside the other threshold (0.4 deg). The difference in the end is around 0.1 deg. Fig. 6.25 (b) shows the sun sensor signals. vy represents the difference between the sun and the center of the sun sensor in the vertical direction. The vsum has a huge decay because the azimuth is effected by a strong gust and the sun is out of the FOV of the sun sensor.

6.10 Azimuth Control with Self-Tuning Parameters

The elevation of telescope would change the spring constant of the whole system. The gains with the different elevations could be recorded in a gain table. The controller loads the gains based on the incremental encoder of the elevation. However, uncertain length of the ladder with parachute or weight make the spring constant change. The uncertain spring constant affects the observers and control outputs. This is a practical issue in the real flight and need to have the strategy to overcome this uncertainty.

6.10.1 Self-Tuning Parameters

Fig. 6.26 shows the self-tuning control (STC) diagram. The STC block includes the observer, a 3 state space with LQR gains, one integral state, and the control command with LQI gains. The plant block is a 5 state space including the dynamics of the balloon. The identification block provides the parameters estimation and feed to STC block for updating the system matrix. The linear regression form [53]:

$$y = \theta^T \phi(t) \tag{6.28}$$

y is the measurement, $\phi(t)$ is the regressor. θ is the parameter needed to be estimated. The linear regression is constructed by using the relation between input u and output y. The

(a) Azimuth Error

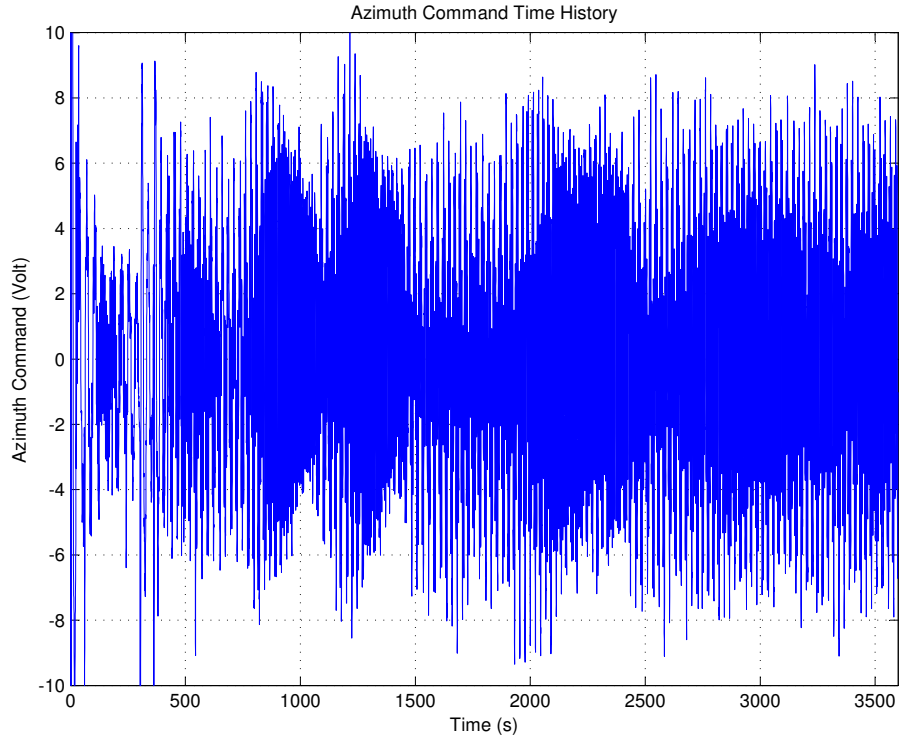

(b) Azimuth Command

Figure 6.24: Actual Gondola Azimuth Test Results with Fixed Light Resource

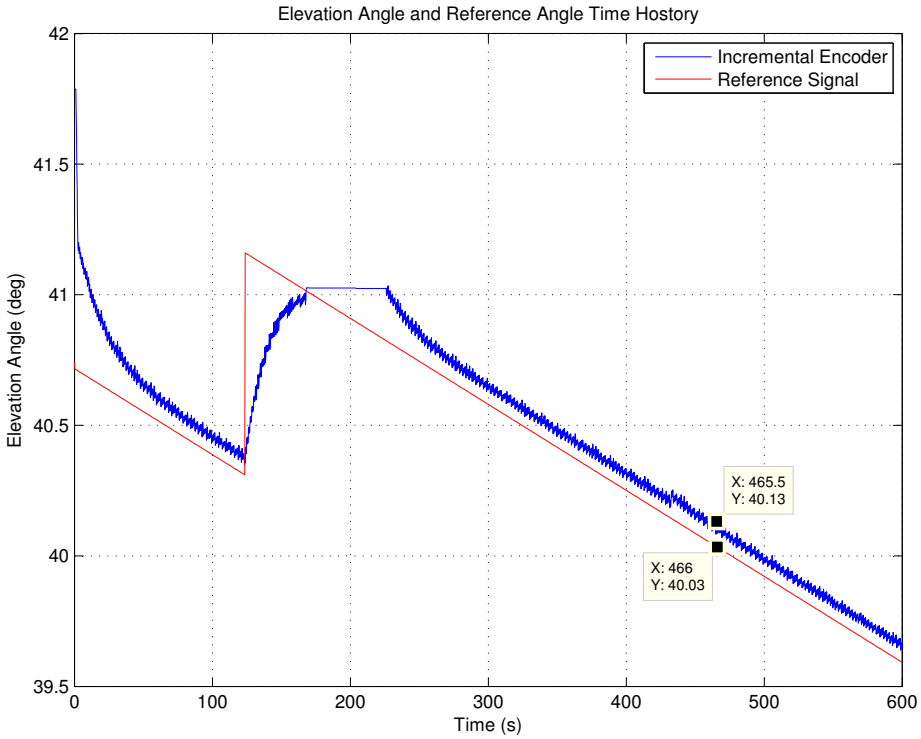

(a) Elevation Error in Incremental Encoder

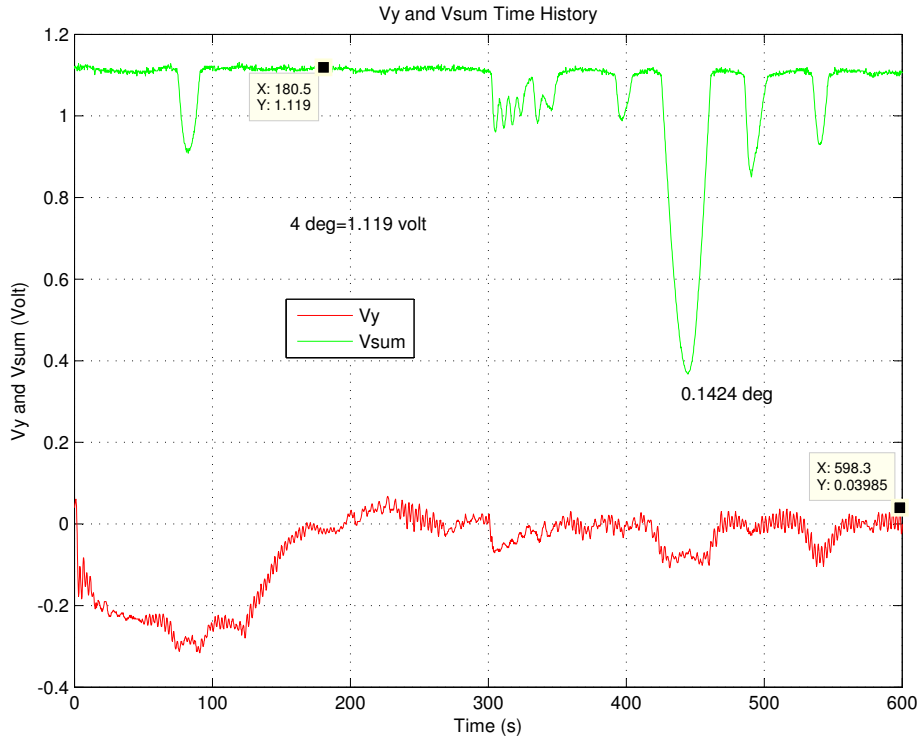

(b) Elevation Error in Sun sensor

Figure 6.25: Elevation Test with the Sun

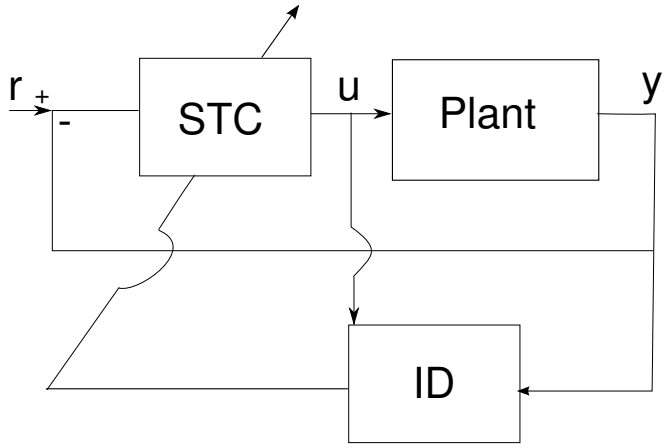

Figure 6.26: Self Tuning Control Diagram

transfer function could be derived from Eqn. (6.11).

$$y = \frac{\Omega^2}{s^3 + \Omega^2 s} u \tag{6.29}$$

There are two main adaptive control schemes. One is the self-tuning, the other is the model reference adaptive control. The self-tuning control can deal with the non-minimum phase system but may have the stability issue. The model reference adaptive control doesn't have stability issues but the system needs to be the minimum phase. We want to feedback the integral term of LQI to overcome the steady state error caused by the balloon, so we choose the self-tuning control. Choose a stable polynomial, like $(s+a)^3, a > 0$ with the same order of the denominator in Eqn. (6.29) and divided it in both side, we obtain:

$$\frac{(s^3 + \Omega^2 s)}{(s+a)^3} y = \frac{\Omega^2}{(s+a)^3} u \tag{6.30}$$

$$y = \frac{3as^2 + (3a^2 - \Omega^2)s + a^3}{(s+a)^3} y + \frac{\Omega^2}{(s+a)^3} u \tag{6.31}$$

Eqn. (6.31) can be converted to the linear regression form or identifier structure [53]. Compare the regression form in Eqn. (6.28), we obtain:

$$\theta^T = \begin{pmatrix} a^3 & 3a^2 - \Omega^2 & 3a & \Omega^2 & 0 & 0 \end{pmatrix} \tag{6.32}$$

$$\begin{aligned} \phi(t)^T &= \frac{1}{(s+a)^3} \begin{pmatrix} y & sy & s^2 y & u & su & s^2 u \end{pmatrix} \\ &= \begin{pmatrix} \phi_y(t)^T & \phi_u(t)^T \end{pmatrix} \end{aligned} \tag{6.33}$$

To realize $\phi_y(t)$ and $\phi_u(t)$, Let

$$\Lambda = \begin{pmatrix} 0 & 1 & 0 \\ 0 & 0 & 1 \\ -a^3 & -3a^2 & -3a \end{pmatrix} \quad \text{and} \quad \bar{B} = \begin{pmatrix} 0 \\ 0 \\ 1 \end{pmatrix} \tag{6.34}$$

We obtain:

$$\begin{aligned} \dot{\phi}_y(t) &= \Lambda\phi_y(t) + \bar{B}y \\ \dot{\phi}_u(t) &= \Lambda\phi_u(t) + \bar{B}u \end{aligned} \tag{6.35}$$

For the identification algorithm, we choose the recursive algorithm with the least square method [1]. [1] also provided the algorithm for the discrete time case.

$$\dot{\hat{\theta}}(t) = \gamma P(t)\phi(t)(y - \phi(t)^T\hat{\theta}(t)) \tag{6.36}$$

$\hat{\theta}(0)$ is an arbitrary vector. We would choose the nominal parameters of the system. γ is a positive number. The covariance matrix $\dot{P}(t)$ is updated with:

$$\dot{P}(t) = -\gamma P(t)\phi(t)\phi(t)^T P(t) \tag{6.37}$$

The parameters estimator vector is:

$$\hat{\theta}(t)^T = \begin{pmatrix} \hat{\theta}_1(t) & \hat{\theta}_2(t) & \hat{\theta}_3(t) & \hat{\theta}_4(t) & \hat{\theta}_5(t) & \hat{\theta}_6(t) \end{pmatrix} \tag{6.38}$$

Ω^2 equals K_s/I_1. $\hat{\theta}_4$ equals $\hat{\Omega}^2$ in Eqn. (6.32) Then $\hat{A}$, estimated state space for the real system A, can be updated by $\hat{\theta}_4(t)$:

$$\hat{A} = \begin{pmatrix} 0 & 1 & 0 \\ -\hat{\theta}_4(t) & 0 & \hat{\theta}_4(t) \\ 0 & 0 & 0 \end{pmatrix} \tag{6.39}$$

Eqn. (6.13) is modified in Eqn. (6.40):

$$\dot{\hat{x}} = \hat{A}\hat{x} + Bu + L(y - C\hat{x}) \tag{6.40}$$

The state feedback gain $K(\hat{A}, B, Q_k) \in \Re^4$ is obtained from LQI and the observer gain $L(\hat{A}^T, C^T, Q_L) \in \Re^3$ from LQR. $Q_{K_{4\times4}} \succ 0$ and $Q_{L_{3\times3}} \succ 0$. We reset the covariance matrix $P(t)$ to improve the convergence rate. The integral term is also reset to avoid the large output due to the initial estimated parameters.

6.10.2 Curve Fitting Self-Tuning Gains

Generating gains in Eqn. (6.16), Eqn. (6.18) for the self-tuning control may consumes a lot of the computing power. We propose use the curving fitting self-tuning gains instead of the normal self-tuning gains. Polynomial coefficients are used to fit the curve of the self-tuning gains with the different system parameters during the off-line process. Then real time controller uses those coefficients to generate corresponding LQR or LQI gains. Furthermore, this idea also accelerates the simulation process for the complicated system with the self-tuning control. We used 6 orders polynomial to fit each gain. $\hat{T}$ is the estimated natural period from $\hat{\theta}_4$. The coefficients c_k are determined in the sense of the least square problem.

$$\underbrace{\begin{pmatrix} 1 & x_1 & x_1^2 & \dots & x_1^{n-1} \\ 1 & x_2 & x_2^2 & \dots & x_2^{n-1} \\ \vdots & \vdots & \vdots & \vdots & \vdots \\ 1 & x_j & x_j^2 & \dots & x_j^{n-1} \\ \vdots & \vdots & \vdots & \vdots & \vdots \\ 1 & x_m & x_m^2 & \dots & x_m^{n-1} \end{pmatrix}}_{=V} \underbrace{\begin{pmatrix} c_0 \\ c_1 \\ \vdots \\ c_k \\ \vdots \\ c_{n-1} \end{pmatrix}}_{=C} = \underbrace{\begin{pmatrix} y_1 \\ y_2 \\ \vdots \\ y_j \\ \vdots \\ y_m \end{pmatrix}}_{=Y} \tag{6.41}$$

x_j is the independent variable and y_j is the dependent variable. The goal is to find the optimal coefficients of C to make $\|VC - Y\|$ as small as possible. V is usually called Vandermonde matrix. Replace x_j with $\hat{T}$, y_j with gains from Eqn. (6.18) and Eqn. (6.16), then we can get the curve fitting coefficients c_k for a_{ik} or b_{ik}.

$$\begin{aligned} \hat{T} &= 2\pi\hat{\theta}_4^{-\frac{1}{2}} \\ \hat{K}_i &= \sum_{k=1}^{6} a_{ik}\hat{T}^{6-k} \\ \hat{L}_i &= \sum_{k=1}^{6} b_{ik}\hat{T}^{6-k} \end{aligned} \tag{6.42}$$

The error percentage plot of each gain is in the Fig. 6.27. Q_k is diag{0.08,0,0,0.08}, R=0.1 and Q_L is diag{1,1,1}, $\hat{T}$ is from 40 sec to 500 sec. The performance of the curve fitting doesn't fit well in the boundary. However, all of the errors are smaller than 0.5 % in the interesting range of the real flight.

6.10.3 Stability Analysis of the Effects of the Balloon

[53] provides the proof for the asymptotically convergence of the estimators $\hat{\theta}$ in recursive formulation and provides the proof of exponential stability for the covariance matrix resetting. That's why we reset the covariance algorithm every 10 seconds to maintain the persistency of excitation (PE). [1] discussed the required orders of PE. [9] provides the linear-time varying observer design and the stability analysis. The state estimator error $\hat{x}(t) - x(t)$

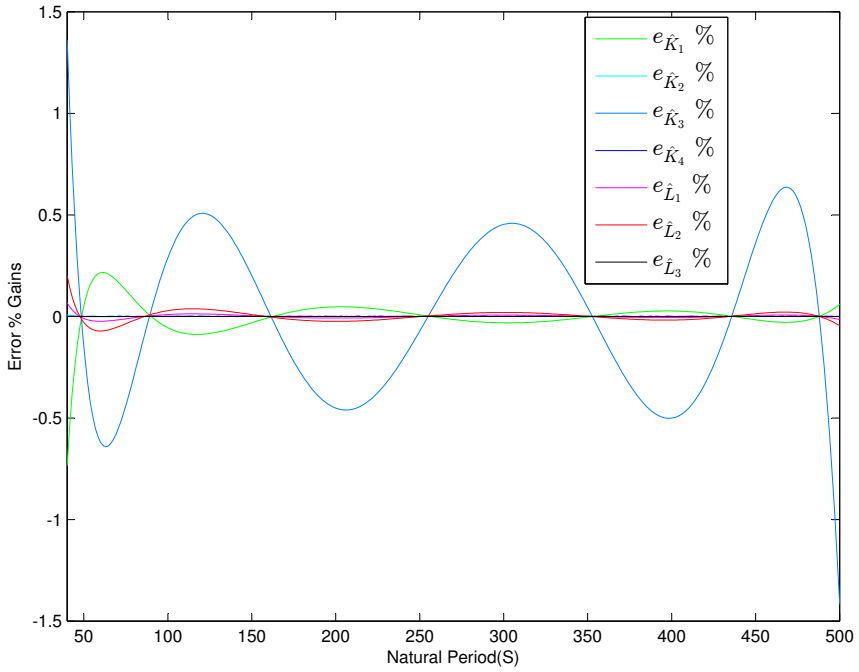

Figure 6.27: Curve Fitting Gains Error Percentage

cannot converge to zero exponentially because of motion of the balloon. At the steady state, the states of observer and the states of the real system have a shift value. Moreover, if the balloon has a constant velocity, the integral term of the control would provide a constant value to overcome the velocity of the balloon and makes the motor angular ($\hat{x}_{31}$) continuously increase. From Eqn. (6.10), Eqn. (6.13), and Eqn. (6.15), we got another state space which includes x, $\hat{x}$ with an addition integral state $\int x_1$.

$$x_{new} = \begin{pmatrix} \int x_1 & x_1 & \dot{x}_1 & x_{31} & \hat{x}_1 & \dot{\hat{x}}_1 & \hat{x}_{31} \end{pmatrix} \tag{6.43}$$

and the state space representation:

$$\mathcal{A} = \begin{pmatrix} 0 & 1 & 0 & 0 & 0 & 0 & 0 \\ 0 & 0 & 1 & 0 & 0 & 0 & 0 \\ 0 & -\Omega^2 & 0 & \Omega^2 & 0 & 0 & 0 \\ 0 & 0 & 0 & 0 & 0 & 0 & 0 \\ 0 & \hat{L}_1 & 0 & 0 & -\hat{L}_1 & 1 & 0 \\ 0 & \hat{L}_2 & 0 & 0 & -\hat{\Omega}^2 - \hat{L}_2 & 0 & \hat{\Omega}^2 \\ 0 & \hat{L}_3 & 0 & 0 & 0 - \hat{L}_3 & 0 & 0 \end{pmatrix} \tag{6.44}$$

The input matrix:

$$\mathcal{B} = \begin{pmatrix} 0 & 0 & 0 & 1 & 0 & 0 & 1 \end{pmatrix}^T \tag{6.45}$$

Consider the state feedback in Eqn. (6.15). The state feedback matrix is $A_{fk} = \mathcal{A} - \mathcal{B}u$

$$\mathcal{A}_{fk} = \begin{pmatrix} 0 & 1 & 0 & 0 & 0 & 0 & 0 \\ 0 & 0 & 1 & 0 & 0 & 0 & 0 \\ 0 & -\Omega^2 & 0 & \Omega^2 & 0 & 0 & 0 \\ -\hat{K}_4 & 0 & 0 & 0 & -\hat{K}_1 & -\hat{K}_2 & -\hat{K}_3 \\ 0 & \hat{L}_1 & 0 & 0 & -\hat{L}_1 & 1 & 0 \\ 0 & \hat{L}_2 & 0 & 0 & -\hat{\Omega}^2 - \hat{L}_2 & 0 & \hat{\Omega}^2 \\ -\hat{K}_4 & \hat{L}_3 & 0 & 0 & -\hat{K}_1 - \hat{L}_3 & -\hat{K}_2 & -\hat{K}_3 \end{pmatrix} \tag{6.46}$$

$\hat{\Omega}^2$, $\hat{K}_i$ and $\hat{L}_i$ are updated by the curve fitting gains with the updated $\hat{\theta}_4$. The disturbance from the balloon is:

$$d = \begin{pmatrix} 0 & 0 & \Omega^2 x_2 & 0 & 0 & 0 & 0 \end{pmatrix}^T \tag{6.47}$$

And the output matrix:

$$\mathcal{C} = \begin{pmatrix} 0 & 1 & 0 & 0 & 0 & 0 & 0 \end{pmatrix} \tag{6.48}$$

We can obtain:

$$\dot{x}_{new} = \mathcal{A}_{fk} x_{new} + d \tag{6.49}$$

and

$$y = \mathcal{C} x_{new} \tag{6.50}$$

The new state space includes the dynamics of the LQI and LQR design. The transfer function from the balloon dynamics to the gondola azimuth is:

$$y(s) = \mathcal{C}(sI - \mathcal{A}_{fk})^{-1} d(s) \tag{6.51}$$

or

$$y(s) = G_{fk}(s) d(s) \tag{6.52}$$

For the nominal value of the system, the period =140 s, the quadratic cost function Q_k is

Table 6.2: Nominal Transfer function $G_{fk}(s)$

zeros	0,0,-1.0031,-0.6315± 0.63355i
poles	-0.002,-0.8654±0.501i,-0.0789± 0.193i,-0.1877±0.0788i

diag{0.08,0,0,0.08}, R=0.1 and Q_L is diag{1,1,1}, the zeros and poles of the the nominal transfer function $G_{fk}(s)$ are in Tab. 6.2.

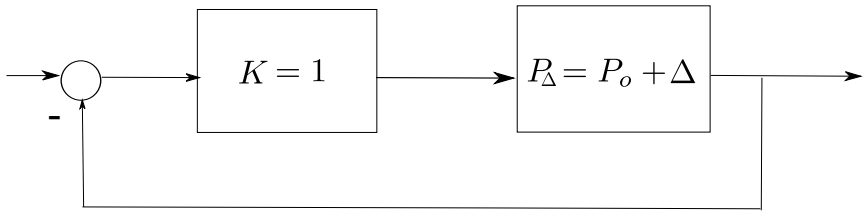

Figure 6.28: Structured Robust Stability Analysis of the Curve Fitting Gains

Remark 1: There are two zeros at the origin. It implies there are two states that cannot be observed explicitly. It was satisfied the previous simulations and the experiments in [39]. $\int x_1$ has the constant value and x_{31} is linearly increasing under the constant disturbance speed of the balloon.
Remark 2: The controller design, observer design, updated system parameters ($\hat{\Omega}^2$) or the real natural period cannot change the zeros at the origin.
Remark 3: pole at -0.002014 cannot be changed by the controller design, the observer design or real system natural period but could be changed by the updated system parameters ($\hat{\Omega}^2$).
Remark 4: A bad guess for the initial $\hat{\Omega}^2(0)$ would make unstable poles appear in the system.
Based on the above reasons, we know that the unobserved dynamics of the balloon and bad guess of the spring constant could make the whole system unstable. We present the simulations to see if the curve fitting gain can overcome those potential issues.

6.10.4 Robust Stability Analysis of the Curve Fitting Gains

We are interested in the robust stability margin of the curve fitting gains. Let state space $\mathcal{A}_{o+\Delta}, \mathcal{B}_{o+\Delta}, \mathcal{C}, \mathcal{D}(=0)$ for the uncertain plant $\mathcal{P}_\Delta$ and $\mathcal{A}_o, \mathcal{B}_o, \mathcal{C}, \mathcal{D}(=0)$ for the nominal plant $\mathcal{P}_o$. Feedback gain $\mathcal{K}$ is a single line for feedback y to stabilize $\mathcal{P}_\Delta$ which has uncertainty internally from the curve fitting gains. The block scheme is shown in the Fig. 6.28

$$\mathcal{A}_{o+\Delta} = \begin{pmatrix} 0 & 1 & 0 & 0 & 0 & 0 & 0 \\ 0 & 0 & 1 & 0 & 0 & 0 & 0 \\ 0 & -\Omega^2 & 0 & \Omega^2 & 0 & 0 & 0 \\ -\hat{K}_4 & 0 & 0 & 0 & -\hat{K}_1 & -\hat{K}_2 & -\hat{K}_3 \\ 0 & 0 & 0 & 0 & -\hat{L}_1 & 1 & 0 \\ 0 & 0 & 0 & 0 & -\hat{\Omega}^2 - \hat{L}_2 & 0 & \hat{\Omega}^2 \\ -\hat{K}_4 & 0 & 0 & 0 & -\hat{K}_1 - \hat{L}_3 & -\hat{K}_2 & -\hat{K}_3 \end{pmatrix} \tag{6.53}$$

$$\mathcal{B}_{o+\Delta} = \begin{pmatrix} 0 & 0 & 0 & 0 & -\hat{L}_1 & -\hat{L}_2 & -\hat{L}_3 \end{pmatrix}^T \tag{6.54}$$

Curve fitting gains update $\hat{K}_i$, $\hat{L}_i$ by the argument $\hat{\theta}_4$. To satisfy the negative feedback structure, a negative sign is put in $\mathcal{B}_{o+\Delta}$ and $\mathcal{B}_o$ for the sign compensation.

Nominal plant: $\mathcal{P}_o = \mathcal{C}(sI - \mathcal{A}_o)^{-1}\mathcal{B}_o$

$$\mathcal{A}_o = \begin{pmatrix} 0 & 1 & 0 & 0 & 0 & 0 & 0 \\ 0 & 0 & 1 & 0 & 0 & 0 & 0 \\ 0 & -\Omega^2 & 0 & \Omega^2 & 0 & 0 & 0 \\ -\bar{K}_4 & 0 & 0 & 0 & -\bar{K}_1 & -\bar{K}_2 & -\bar{K}_3 \\ 0 & 0 & 0 & 0 & -\bar{L}_1 & 1 & 0 \\ 0 & 0 & 0 & 0 & -\bar{\Omega}^2 - \bar{L}_2 & 0 & \bar{\Omega}^2 \\ -\bar{K}_4 & 0 & 0 & 0 & -\bar{K}_1 - \bar{L}_3 & -\bar{K}_2 & -\bar{K}_3 \end{pmatrix} \tag{6.55}$$

$$\mathcal{B}_o = \begin{pmatrix} 0 & 0 & 0 & 0 & -\bar{L}_1 & -\bar{L}_2 & -\bar{L}_3 \end{pmatrix}^T \tag{6.56}$$

Uncertain plant $\mathcal{P}_\Delta$ equals $\mathcal{P}_o(s) + \Delta$. Sensitively function is $S_o = (I + \mathcal{P}_o)^{-1}$. So the robust stability test becomes $\|S_o\Delta\|_\infty$. Fig. 6.29 is the simulation for the robust stability test. The nominal plant was simulated at different natural period: $70, 175.5, 245, 332.5, 420$. Random perturbations are generated of each gain and take uniform on the interval $\pm 1\%$. The maximum amplitude of the total tests in Fig. 6.29 is -27.6 db.

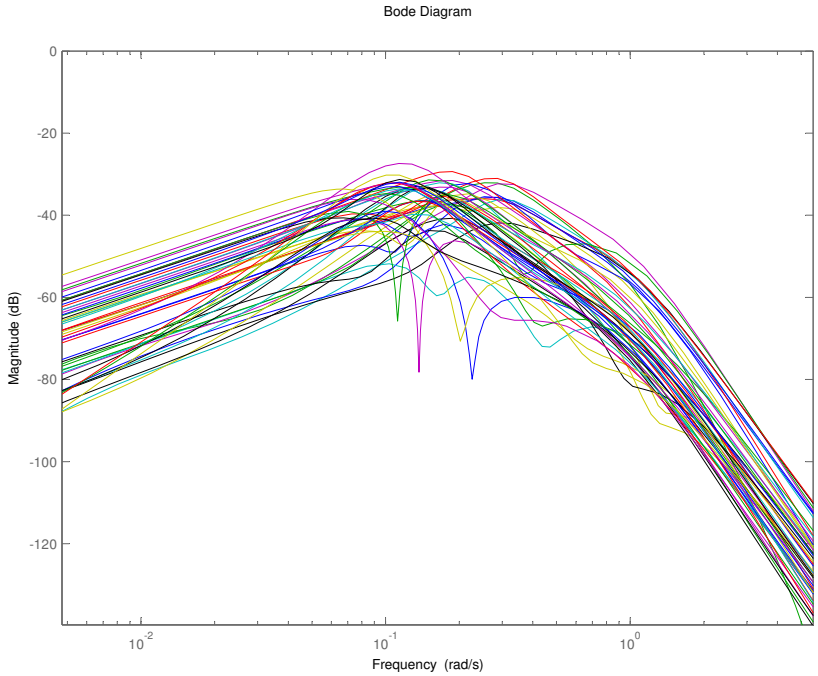

Figure 6.29: $S_o\Delta$ Magnitude Bode Diagram

6.10.5 Curving Gains Simulation Studies

The initial nominal period for the controller is set to 140 seconds. Q_k: diag{0.08,0,0,0.08} $R = 0.1$ and Q_L: diag{1,1,1}. The MOI ratio from the balloon to the gondola is 760. γ in Eqn. (6.36) is 0.001. The pole assignment in Eqn. (6.30) is 0.3. Reset the covarianve matrix P(t) and the integral term every 10 seconds and P(0) is an identity matrix. The initial state of the system is $\begin{pmatrix} \int x_1 & x_1 & \dot{x}_1 & x_2 & \dot{x}_2 & x_{31} \end{pmatrix} = \begin{pmatrix} 0 & 1 & 0 & 1 & 0 & 0 \end{pmatrix}$. The initial observer state is $\begin{pmatrix} \hat{x}_1 & \dot{\hat{x}}_1 & \hat{x}_{31} \end{pmatrix} = \begin{pmatrix} 1 & 0 & 0 \end{pmatrix}$. The curve fitting internal is from 40 seconds to 500 seconds. The order of the polynomial order is 6. The solver is ode45 of MATLAB. Both absolute tolerance and relative tolerance are 1e-10.

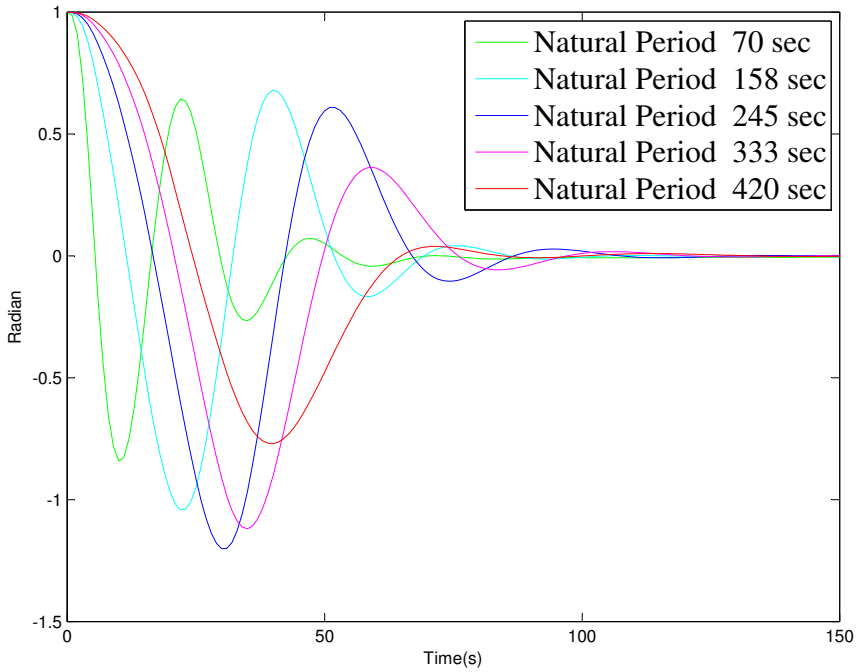

Figure 6.30: Azimuth Error with Curve Fitting Self-Tuning Control

Fig. 6.30 and Fig. 6.31 show that the curve fitting gains can deal with the uncertain natural period. However, constant gains make the system unstable. Fig. 6.32 shows that the natural period 420 second has the largest peak. All of the output converge around 127 second. Fig. 6.33 shows the convergence of the estimating error. $\hat{\theta}_4$ is the only parameter updated in the state space. For the natural period 420 second, the $\hat{\theta}_4$ converges in around 25 second. For the natural period 95 second, $\hat{\theta}_4$ converges around 26 second. In the real flight, the balloon will be disturbed. From the previous flight experiment, the balloon angular velocity was around 1000 seconds period with 0.0013 rad/sec amplitude.[6] Fig. 6.34 shows

[6]1000 seconds is the dominant component of the spectrum of the measurement.

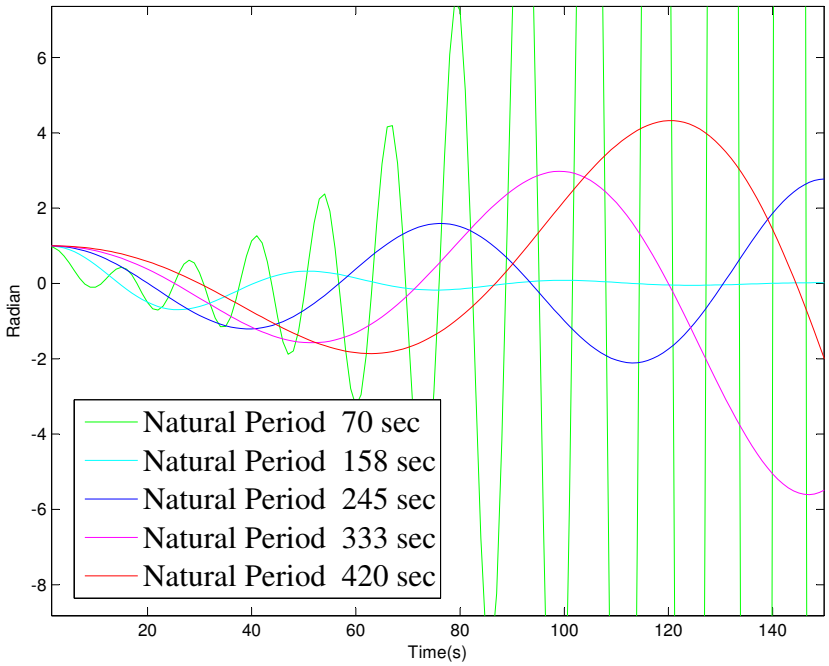

Figure 6.31: Azimuth Error with Constant Gains

Table 6.3: Computation Time

T_{NP}(sec)	70	158	245	333	420	Ave
curve fitting	1.33	1.44	1.76	1.96	2.65	1.8
regular self-tuning	16.33	21.2	27.75	31.55	33.8	26.1

the error of the azimuth at the different spring constants. The errors of the azimuth are still oscillating. However, it still satisfies 0.5 deg rms requirement of the mission.

Curve fitting method can improve the computation time greatly. Tab. 6.3 shows the comparison of the curve fitting method and regular LQR and LQI for the computation time.T_{NP} means natural period. The average of the curve fitting method takes 1.83 seconds. The average of the regular LQR and LQI takes 26.13 seconds. The curve fitting method only takes 7% time computation of the regular computation.

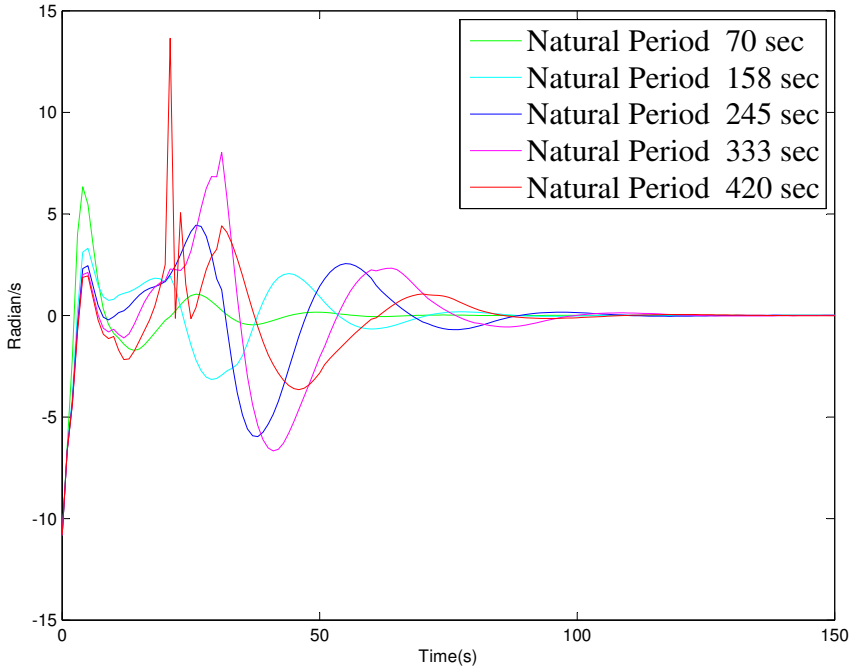

Figure 6.32: Curve Fitting Control Output

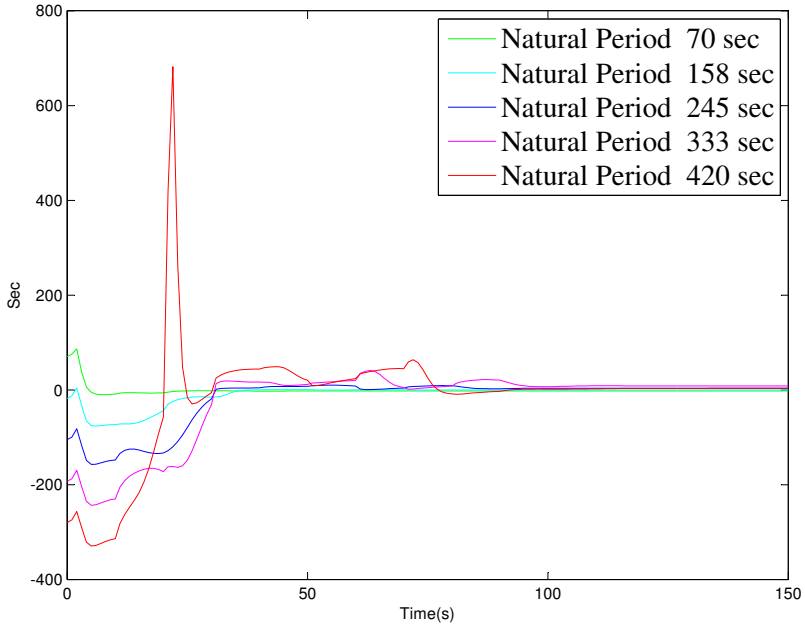

Figure 6.33: Natural Period Estimating Error

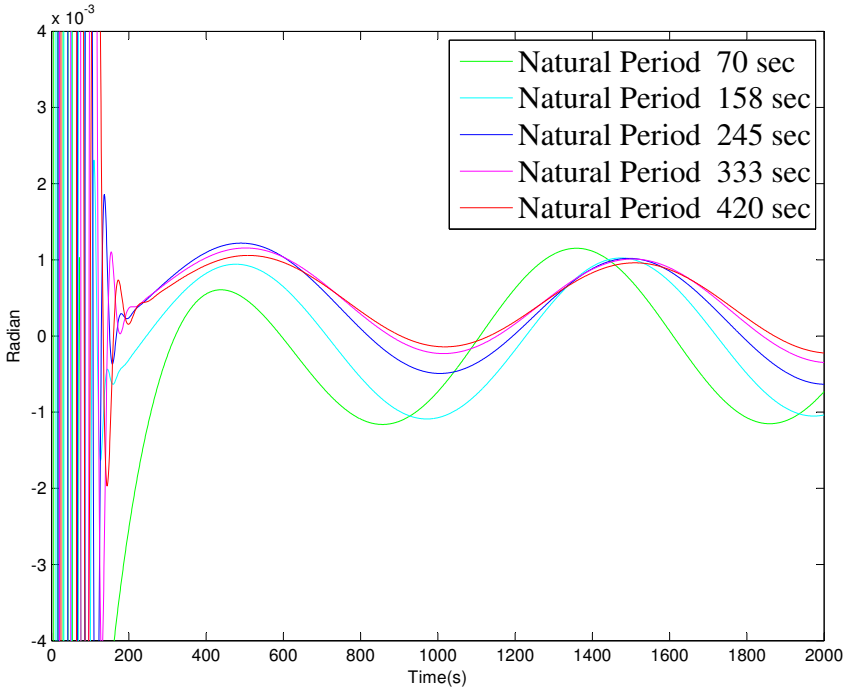

Figure 6.34: Azimuth Error with Curve Fitting Self-Tuning Control and the Disturbance of the Balloon

6.11 Summary

In this chapter, the dynamic analysis and controllers design, for the gondola with non-rigid connections with the flight balloon in high attitude are presented. This chapter can be applied to other similar pointing control systems which control a heavy detector relative to the gondola installed in the bottom of the balloon. The simulation and the experiment results indicate that they satisfy the current requirements of the mission. However, the actual oscillation from the change in elevation can only be observed in the real flight. We expect this oscillation to decay in virtue of the air friction. The best we can do with the current setup, is not inducing the uncontrollable mode by designing a smooth control strategy and small tracking gain. The experiment verifies that these gains are strong enough to track the motion of the sun. This chapter also provides the curve fitting gains for self-tuning in the balloon azimuth control and the robust stability analysis. The simulation results support that the curve fitting gains can overcome the uncertain natural period, the effects of the balloon and the initial errors from the observer. Further more, it improve the simulation time greatly. Any similar vehicle which changes its azimuth by the strings or non-rigid ladder could follow the design procedures in this chapter. The idea of the curve fitting self-tuning gain can be implemented in a digital controller by replacing Eqn. (6.18), Eqn. (6.16) with the

discrete time form. Curve fitting gains for self-tuning is a practical way to get the solutions of LQR or LQI in the embedded systems. Other kinds of complicated controllers could also be realized with this idea to reduce the burden of the computation in the real-time computer.

Chapter 7

Concluding Remarks

7.1 General Conclusions

In this dissertation, the innovated attitude controls are developed for the different types of high altitude stationary platforms. The following describes the relation between the attitude control and the angular momentum transferred.

- In chapter 4, the control algorithms for the spin rate control, the ecliptic normal control, the sun normal control, and the detumble control are proposed. All the control algorithms are developed based on Lyapunov stability and reduce the error of the angular momentum of a rigid body. A rigid body could change its angular momentum by utilizing the magnetic field of the Earth.

- In chapter 5, a stabilization strategy of the multibody system is proposed. The rotation platforms have their own angular momentum and gradually transfer the angular momentum to the bus. The platform controls spin rate and the reaction torques are applied to the bus. The bus control compensates those reaction torques and use the reaction wheels to absorb the angular momentum transferred from the platforms. So far, the whole system obeys the angular momentum conservation principle but not the energy conservation principle. The damping exists in the fuel tanks and joints of the booms. If there is no control, the total energy is decreasing but not the total angular momentum. The whole system must change the motions of each components to compensate for the loss of the energy. When the control is applied, some of the reaction wheels which achieve high spin rate will release the angular momentum to space by injecting the gas. After the releasing, the cycle of transferring the angular momentum begins again.

- In chapter 6, the dynamics of the azimuth and the elevation are analyzed separately. The angular momentum in two directions are also considered individually. In the azimuth direction, the gondola could change its azimuth by the reaction torques of the ladder. Since the angular momentum is conserved, the balloon will change its

azimuth in the opposite direction. Once the azimuth of the gondola is steady, the balloon also stop changing the azimuth because of the angular momentum conservation principle. The same scenario happens with the elevation. When the elevation of the telescope changes, the elevation of the balloon also changes because of the angular momentum conservation. In the elevation direction, some coordinates belong to the uncontrollable mode. The controller cannot eliminate the oscillated angular momentum transferred between the balloon and the gondola. The elevation control tries not to excite the uncontrollable mode. The controller uses a small constant angular velocity for raising. The angular velocity becomes zero immediately once the setting point is achieved. We can design the acceleration and the deceleration for the raising profile. However, those accelerations and the deceleration transfers the angular momentum to the balloon. I propose that the raising control use a constant velocity to avoid the additional excitation to the balloon. It also simplifies the controller design. Besides, the raising speed of the telescope just needs to be higher than the speed of the rising sun. The motor is just operated above the dead zone with a small amount of force. The transient of the raising only excites a very small oscillation and is verified by the simulation.

7.2 Future Research

Based on the work presented in this dissertation, the relative directions for the future are described as follows:

- In chapter 4:
  - The profile of the control signal is bang-bang control for the current science mission. The PWM method could be used for the amplitude variation of the control signals in future satellite missions.
  - Two vectors method of the angular velocity estimation could use Kalman filter for more precise measurement.
- In chapter 5, the following could be included in the future simulation:
  - The model of the booms are assumed rigid bodies. The dynamics of the flexible booms could induce more damping and extra dissipated energy. The effects of the extra dissipated energy to the bus control needs to be studied.
  - The noise effects of the gyro.
  - The mass and the moment of inertia loss after the unloading.
- In chapter 6:
  - Derive a new state space which incorporates the dynamics of the azimuth and the elevation.

- Realize the self-tuning control in future science missions.
- Using the strain gage for an additional measurement to assist the performance of the observer.

Appendix A

Local Solar Elevation Algorithm

The following code is programmed with C style and based on the algorithms from NOAA. This function reads the variables from GPS. Those variables are time of zone, GPS time of week, number of weeks, GPS time offset, and the latitude and the longitude of the interesting location.

```
double SunElevation()
{
    ...
    frac_day = fmod(GPS_timeweek-GPS_timeoffset,86400)/86400;   // Time
    Fraction of the Day
    JD=2415018.5+29221.0+(GPS_numweeks)*7+(GPS_timeweek-GPS_timeoffset)
   /86400+5-time_zone/24.0; //Julian date
    JC = (JD-2451545.0)/36525.0;    // Julian Century
    GMLS = fmod(280.46646+JC*(36000.76983+JC*0.0003032),360);   //
   Geometric Mean Long Sun (deg)
    GMAS = 357.52911+JC*(35999.05029 - 0.0001537*JC);   // Geometric
   Mean Anom Sun (deg)
    epsilon = 0.016708634-JC*(0.000042037+0.0000001267*JC); //
   Eccentricity of Earth Orbit
    SECtr = sin(rad(GMAS))*(1.914602-JC*(0.004817+0.000014*JC))+sin(rad
   (2*GMAS))*(0.019993-0.000101*JC)+sin(rad(3*GMAS))*0.000289;  // Sun
   Eq of Ctr
    STL = GMLS+SECtr;   // Sun True Long (deg)
    SAL = STL - 0.00569-0.00478*sin(rad(125.04-1934.136*JC));   // Sun
   App Long (deg)
    MOE = 23+(26+((21.448-JC*(46.815+JC*(0.00059-JC*0.001813))))/60.0)
   /60.0;    // Mean Obliq Ecliptic (deg)
    OC = MOE+0.00256*cos(rad(125.04-1934.136*JC));  // Oblique Corr (
   deg)
    delta = asin(sin(rad(OC))*sin(rad(SAL)));   // Sun Declination (rad
   )
    vary = pow(tan(rad(OC/2)),2);   // Var y
    EoT = 4*deg(vary*sin(2*rad(GMLS))-2*epsilon*sin(rad(GMAS))+4*
   epsilon*vary*sin(rad(GMAS))*cos(2*rad(GMLS))-0.5*vary*vary*sin(4*rad
   (GMLS))-1.25*epsilon*epsilon*sin(2*rad(GMAS)));    // Equation of
```

```
    Time (minutes)
     TST = fmod(frac_day*1440+EoT+4*-GPS_long-60*time_zone,1440);    //
    True Solar time (minutes)
     if(TST<=0)
     { h = TST/4.0+180;} // Hour Angle (deg)
     else
     { h = TST/4.0-180;} // Hour Angle (deg)
     SEA = asin(sin(rad(GPS_lat))*sin(delta)+cos(rad(GPS_lat))*cos(delta
    )*cos(rad(h)));  // Sun Elevation Angle (rad)
     return SEA;
}
```

Appendix B

Control Software Design

The details of the control software design can be refereed in [3]. The detail of the pointing control system of GRIPS can be refereed in [70]. All of the tasks are executed simultaneously in a single while loop.

```
while(1)
{
  task_1();
  task_2();
  ...
}
```

Each task has its own states diagram. Each task could be executed by checking the current clock and the starting clock. We can also design several dispatchers to coordinate different period of the executions. Here is an example for a dispatcher:

```
int Dispatcher_Flag()
{
  ...
  short delta_t = 250*CLOCKS_PER_SEC/1000; // the relation between
 clock and the real time.
  if(clock()-start_clock<next_dispatcher)
  {return(0);}
  next_dispatcher_+= number_clock_during_250ms;
  return(1);
}
```

Some task could be executed by the binary value of Dispatcher_Flag.

```
void task_i()
{
   ... //some complier only allow local variables definition first in
  a funciton
   if(Dispatcher_Flag==0)
   {return;}
   // contents
   ....
}
```

A state diagram is presented the states, transitions, transition conditions, and entry conditions. When the task is executed, only one state of the task is executed [3]. There are usually three sections inside a state:

- **Entry Section** This section is executed only when the program runs into this state for the first time,
- **Action Section** This section is executed every time when the program runs into this state.
- **Transition Logic Test Section** This section is executed every time and the program decides if it goes to the next state or not.

There exists an initialization state for each task. run_entry is a flag for entering 'Entry Section'. 'Transition Logic Test Section' uses data->next_state to pass the value for the task and the task changes the executed state at the next time. The implementation of the state machine could be found in [70]. It looks like the following code:

```
void task_i(...)
{ ...
  // Check if it is time to run
  if(Dispatcher_Flag==0)
  {return;}
  // content
  // task initialization State
  if(data->state == 0)     // 0: INITIALIZATION
  {
    data->state = 1;       // 1: STATE 1
    data->next_state = 1;   // 1: STATE 1
    return;
  }
  // Audit Section
  if(data->next_state != 99)  // state transition
              // occured
  { data->state = data->next_state;
    data->next_state = 99;  // 99: no state
              // transition occurred
    run_entry = 1;     // execute entry section
  }
  else
  {run_entry = 0;}
  // State Code
  switch(data->state)
  {
  case(1):         // State 1
    // Entry Section
    if(run_entry == 1)
    {EntryFunction();}
    // Action Section
```

```
      ActionFunction();
      // Transition Logic Test Section
      if(logic1 == true)
      {data->next_state = 2; // State 2
       ExitFunction1();
      }
      else if(logic2 == true)
      {data->next_state = 3;  // State 3
       ExitFunction2();
      }
      break;
    case(2):        // State 2
      // Entry Section
      // Action Section
      // Transition Logic Test Function
      break;
    ... // Other states can be inserted here
    }
}
```

Bibliography

[1] Karl J Åström and Björn Wittenmark. *Adaptive control*. Courier Dover Publications, 2013.

[2] Gary F Auclair. *Advanced reaction wheel controller for spacecraft attitude control*. American Institute of Aeronautics and Astronautics, 1969.

[3] David M Auslander, JR Ridgely, and JD Ringgenberg. *Control Software for Mechanical Systems: Object-Oriented Design in a Real-Time World*. Pearson Education, 2002.

[4] Dwightm Bawcom. "International survey of scientific ballooning support organizations". In: *A collection of technical papers: AIAA International Balloon Technology Conference, October 8-10, 1991, Albuquerque, New Mexico*. American Institute of Aeronautics and Astronautics. 1991, p. 149.

[5] Hale Bradt. *Astronomy methods: A physical approach to astronomical observations*. Cambridge University Press, 2004.

[6] Elizabeth Buchen and Dominic DePasquale. "2014 Nano / Microsatellite Market Assessment". In: *SpaceWorks Enterprises, Inc. (SEI)* (2014).

[7] Chi-Tsong Chen. *Linear system theory and design*. Oxford University Press, Inc., 1995.

[8] Min-Shin Chen and Yi-Hsiang Huang. "A state-space approach to the multivariable continuous-time self-tuning control". In: *American Control Conference, 1994*. Vol. 1. IEEE. 1994, pp. 470–474.

[9] Min-Shin Chen and Jia-Yush Yen. "Application of the Least Squares Algorithm to the Observer Design for Linear Time-Varying Systems". In: 44.9 (1999).

[10] Carol J Crannell et al. "A balloon-borne payload for imaging hard x-rays and gamma rays from solar flares". In: *Proceedings of the AIAA International Balloon Technology Conference*. 1991, pp. 8–10.

[11] Peter E Crouch. "Spacecraft attitude control and stabilization: Applications of geometric control theory to rigid body models". In: *Automatic Control, IEEE Transactions on* 29.4 (1984), pp. 321–331.

[12] "CubeSat Design Specification". In: *California State Polytechnic University* (2014).

[13] Ball D. "Long duration ballooning in Antarctica - An operational perspective". In: *International Balloon Technology Conference*. Balloon Systems Conferences. American Institute of Aeronautics and Astronautics, 1991.

[14] "DARPA's Space History". In: *Success Stories in Satellite Systems*. American Institute of Aeronautics and Astronautics, 2009.

[15] Grant Debora and Rand James. "The Balloon Assisted Launch System - A heavy lift balloon". In: *International Balloon Technology Conference*. Balloon Systems Conferences. American Institute of Aeronautics and Astronautics, 1999.

[16] Y Doi et al. "A new Japanese infrared balloon telescope". In: *Advances in Space Research* 25.11 (2000), pp. 2285–2289.

[17] Dan D.V.Bhanderi and Thomas Bak. "Modeling Earth Albedo for Satellites in Earth Orbit". In: (2005).

[18] O Egeland and J-M Godhavn. "Passivity-based adaptive attitude control of a rigid spacecraft". In: *Automatic Control, IEEE Transactions on* 39.4 (1994), pp. 842–846.

[19] Gene F Franklin, Michael L Workman, and Dave Powell. *Digital control of dynamic systems*. Addison-Wesley Longman Publishing Co., Inc., 1997.

[20] Hironori Fujii and Tsutomu Murayama. "Attitude control of space robot with flexible appendage". In: *AIAA Guidance, Navigation and Control Conference, Monterey, CA*. 1993, pp. 1452–1457.

[21] Jessica Gaskin et al. "High Energy Replicated Optics to Explore the Sun: Hard X-ray balloon-borne telescope". In: *Aerospace Conference, 2013 IEEE*. IEEE. 2013, pp. 1–11.

[22] Xin-Sheng Ge and Li-Qun Chen. "Attitude control of a rigid spacecraft with two momentum wheel actuators using genetic algorithm". In: *Acta Astronautica* 55.1 (2004), pp. 3–8.

[23] Carl. Grubin. "Satellite Attitude Determination by Simultaneous Line-of-Sight Sightings". In: *Journal of Spacecraft and Rockets* 13.10 (1977), p. 640.

[24] Carl Grubin. "Satellite attitude determination by simultaneous line-of-sight sightings". In: *Journal of Spacecraft and Rockets* 14.10 (1977), pp. 640–640.

[25] Christopher D Hall. "Spacecraft attitude dynamics and control". In: *Lecture Notes posted on Handouts page [online]* 12 (2003).

[26] J. Karl Hedrick. "Control of Nonlinear Dynamic Systems ME237 Slides". In: *Mechanical Engineering, UC Berkeley* (2010).

[27] Hank Heidt et al. "CubeSat: A new generation of picosatellite for education and industry low-cost space experimentation". In: (2000).

[28] João P Hespanha. *Linear systems theory*. Princeton university press, 2009.

[29] Russell C. Hibbeler. *Engineering Mechanics Dynamics 11th edition in SI units*. Prentice Hall, 2007.

[30] Russell Charles Hibbeler and Peter Schiavone. *Engineering mechanics: statics and dynamics*. Pearson Education India, 2004.

[31] Timothy E Holden and Dale A Lawrence. "A Lyapunov design approach to nutation damping with a reaction wheel". In: *AIAA Conference on Guidance, Navigation and Control, Denver, CO, AIAA Paper*. Vol. 4047. 2000.

[32] Wang Honghui, Yuan Zhaohui, and Chen Qiu. "Attitude control for stratospheric balloon-borne gondola system based on adaptive PID controller". In: *Control Conference (CCC), 2010 29th Chinese*. IEEE. 2010, pp. 2134–2138.

[33] Marshall H Kaplan. "Modern spacecraft dynamics and control". In: *New York, John Wiley and Sons, Inc., 1976. 427 p.* 1 (1976).

[34] Vega Karla, David Auslander, and David Pankow. "Design and Modeling of an Active Attitude Control System for CubeSat Class Satellites". In: *AIAA Modeling and Simulation Technologies Conference* 5812 (2009).

[35] Hariharan Krishnan, Mahmut Reyhanoglu, and Harris McClamroch. "Attitude stabilization of a rigid spacecraft using two control torques: A nonlinear control approach based on the spacecraft attitude dynamics". In: *Automatica* 30.6 (1994), pp. 1023–1027.

[36] Alan R Krull. "A History of the Artificial Satellite". In: *Journal of Jet Propulsion* 26.5 (1956), pp. 369–383.

[37] Ascani Livio, Rosa Diego De, and Curti Fabio. "Autonomous Attitude Control Strategies for a Nanosatellite with a Momemtum Wheel". In: *AIAA/AAS Astrodynamics Specialist Conference and Exhibit*. Guidance, Navigation, and Control and Co-located Conferences. American Institute of Aeronautics and Astronautics, 2006.

[38] Fernando Lizarralde and John T Wen. "Attitude control without angular velocity measurement: A passivity approach". In: *Automatic Control, IEEE Transactions on* 41.3 (1996), pp. 468–472.

[39] Yao-Ting Mao et al. "Dynamic Analysis and Controller Design of the Balloon Point Control System of Gamma-Ray Imager/Polarimeter for Solar Flares". In: (2014).

[40] Riccardo Marino and Patrizio Tomei. *Nonlinear control design: geometric, adaptive and robust*. Prentice Hall International (UK) Ltd., 1996.

[41] F Landis Markley and Daniele Mortari. "How to estimate attitude from vector observations". In: *Proceedings of the AAS/AIAA Astrodynamics Specialist Conference*. Vol. 103. 3. 1999, pp. 1979–1996.

[42] James H McDuffie and Yuri B Shtessel. "A sliding mode controller and observer for satellite attitude control". In: *AIAA Guidance, Navigation, and Control Conference*. 1997.

[43] Farman Michael and Barsic John. "A Semi-Automatic Parachute Release System for Balloon Payloads". In: *AIAA's 3rd Annual Aviation Technology, Integration, and Operations (ATIO) Forum*. Aviation Technology, Integration, and Operations (ATIO) Conferences. American Institute of Aeronautics and Astronautics, 2003.

[44] Therese Moretto. "CubeSat mission to investigate ionospheric irregularities". In: *Space Weather* 6.11 (2008).

[45] T. Nakano and Y.Shoji. "The Pointing Control Method of Balloon Borne Telescope Compensating the Motion of Flexible Base". In: *IEEE/SICE International Symposium on System Integration* (2012), pp. 313–318.

[46] Isaac Nason, Jordi Puig-Suari, and Robert Twiggs. "Development of a family of picosatellite deployers based on the CubeSat standard". In: *Aerospace Conference Proceedings, 2002. IEEE*. Vol. 1. IEEE. 2002, pp. 1–457.

[47] Oliver M. O'Reilly. *Intermediate Dynamics for Engineers: A Unified Treatment of Newton-Euler and Lagrangian Mechanics*. Cambridge University Press, 2008.

[48] Yaakov Oshman and Francois Dellus. "Spacecraft Angular Velocity Estimation Using Sequential Observations of a Single Directional Vector". In: *Journal of Spacecraft Rockets* 40.2 (2003), pp. 237–247.

[49] Mark L Psiaki. "Magnetic torquer attitude control via asymptotic periodic linear quadratic regulation". In: *Journal of Guidance, Control, and Dynamics* 24.2 (2001), pp. 386–394.

[50] Jordi Puig-Suari, Clark Turner, and William Ahlgren. "Development of the standard CubeSat deployer and a CubeSat class PicoSatellite". In: *Aerospace Conference, 2001, IEEE Proceedings*. Vol. 1. IEEE. 2001, pp. 1–347.

[51] Douglas E Rowland et al. "The NSF Firefly CubeSat mission: Rideshare mission to study energetic electrons produced by lightning". In: *Aerospace Conference, 2011 IEEE*. IEEE. 2011, pp. 1–12.

[52] Jon Seddon and Alexandre Pechev. "3-D Wheel: A Single Actuator Providing Three-Axis Control of Satellites". In: *Journal of Spacecraft and Rockets* 49.3 (2012), pp. 553–556.

[53] Sastry Shankar and Marc Bodson. *Adaptive Control: Stability, Convergence and Robustness*. Courier Dover Publications, 2011.

[54] Masamichi Shigehara. "Geomagnetic Attitude Control of an Axisymmetric Spinning Satellite". In: *Journal of Spacecraft and Rockets* 9.6 (1972), pp. 391–398.

[55] Malcolm David Shuster and SD Oh. "Three-axis attitude determination from vector observations". In: *Journal of Guidance, Control, and Dynamics* 4.1 (1981), pp. 70–77.

[56] Jean-Jacques E Slotine, Weiping Li, et al. *Applied nonlinear control*. Vol. 199. 1. Prentice-Hall Englewood Cliffs, NJ, 1991.

[57] Robert F Stengel. "Lecture 5: Rigid-Body Dynamics Slides". In: *Robotics and Intelligent Systems MAE 345 Slides* (2013).

[58] A Craig Stickler and KT Alfriend. "Elementary magnetic attitude control system". In: *Journal of Spacecraft and Rockets* 13.5 (1976), pp. 282–287.

[59] Jeremy Straub et al. "OpenOrbiter: A low-cost, educational prototype cubesat mission architecture". In: *Machines* 1.1 (2013), pp. 1–32.

[60] Gang Tao. *Adaptive control design and analysis*. Vol. 37. John Wiley & Sons, 2003.

[61] Armen Toorian, Ken Diaz, and Simon Lee. "The cubesat approach to space access". In: *Aerospace Conference, 2008 IEEE*. IEEE. 2008, pp. 1–14.

[62] P Tsiotras, M Corless, and JM Longuski. "A novel approach to the attitude control of axisymmetric spacecraft". In: *Automatica* 31.8 (1995), pp. 1099–1112.

[63] Panagiotis Tsiotras, Haijun Shen, and Chris Hall. "Satellite attitude control and power tracking with energy/momentum wheels". In: *Journal of Guidance, Control, and Dynamics* 24.1 (2001), pp. 23–34.

[64] David A Vallado. *Fundamentals of astrodynamics and applications*. Vol. 12. Springer, 2001.

[65] Karla Patricia Vega. "Attitude Control System for Cubesat for Ions, Neutrals, Electrons and Magnetic Fields (CINEMA)". MA thesis. University of California, Berkeley.

[66] Stephen Waydo, Daniel Henry, and Mark Campbell. "CubeSat design for LEO-based Earth science missions". In: *Aerospace Conference Proceedings, 2002. IEEE*. Vol. 1. IEEE. 2002, pp. 1–435.

[67] JT-Y Wen and Kenneth Kreutz-Delgado. "The attitude control problem". In: *Automatic Control, IEEE Transactions on* 36.10 (1991), pp. 1148–1162.

[68] Thomas W.Flatley et al. "A B-Dot Acquisition Controller for the RADARSAT Spacecraft". In: *NASA Conference Publication* (1997).

[69] Bong Wie. *Space vehicle dynamics and control*. Aiaa, 1998.

[70] Eduardo Wiputra. "Balloon Pointing Control System Embedded system Code Development and Testing". MA thesis. University of California, Berkeley.

[71] Rafał Wiśniewski and Mogens Blanke. "Fully magnetic attitude control for spacecraft subject to gravity gradient". In: *Automatica* 35.7 (1999), pp. 1201–1214.

[72] Peter Colin Young and JC Willems. "An approach to the linear multivariable servomechanism problem". In: *International journal of control* 15.5 (1972), pp. 961–979.

[73] Sikandar Zaman. "Low-cost satellites and satellite launch vehicles". In: *Space commercialization: Launch vehicles and programs* (1990), pp. 227–234.

[74] Kemin Zhou, John Comstock Doyle, Keith Glover, et al. *Robust and optimal control*. Vol. 40. Prentice Hall New Jersey, 1996.